The Changing Characteristics of Precipitation Extremes in a High-Resolution Climate Model Ensemble

Zur Erlangung des akademischen Grades einer

DOKTORIN DER NATURWISSENSCHAFTEN (Dr. rer. nat.)

von der KIT-Fakultät für Physik des

Karlsruher Instituts für Technologie (KIT)

genehmigte

DISSERTATION

von

Marie Hundhausen, M.Sc.

aus Bietigheim-Bissingen

Tag der mündlichen Prüfung:	31.01.2025
Referent:	Prof. Dr. Joaquim G. Pinto
Korreferentin:	Prof. Hayley J. Fowler, PhD

Karlsruher Institut für Technologie

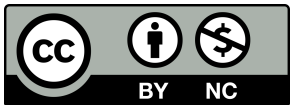

Abstract

The intensity of extreme precipitation is projected to increase with global warming, increasing the risk of flooding. To effectively adapt to this risk, it is essential to understand regional changes in extreme precipitation, including the frequency, duration and temporal profile of precipitation events. Conventional regional climate models parametrise convection, which severely limits their ability to accurately simulate extreme precipitation events. High-resolution simulations at the convection-permitting scale (1-4 km) offer improvements, but due to the high computational demands, previous convection-permitting simulations for Germany have been limited to time slice simulations, typically with single realisations and a temporal resolution of 1 h.

This thesis presents a detailed analysis of the KIT-KLIWA ensemble, to improve the understanding of extreme precipitation in a warming climate, in particular for short duration events. The KIT-KLIWA ensemble consists of four global climate models downscaled with the regional climate model COSMO-CLM to a convection-permitting scale of 2.8 km. This ensemble provides the first transient convection-permitting model (CPM) projections for southern Germany from 1971 to 2100, including unique 5-minute precipitation simulations for selected periods.

In line with practical engineering requirements, we assess changes in future extreme precipitation across a range of scales (return periods from 1 to 100 years and durations from 1 hour to 3 days). The CPM ensemble projects an increase in return levels of up to 8.5 % per 1 °C increase in global warming level, with the largest changes for short durations and long return periods. Our analysis highlights the importance of transient datasets, as opposed to time-slice experiments, to increase confidence in the climate change signal, especially for precipitation intensities over long durations.

Given the limitations of conventional extreme value analysis, we developed an event-based analysis method that assesses the temporal precipitation event profile. By evaluating the historical CPM simulations with observational station and radar data, this method reveals a tendency for CPMs to overestimate longer events and a bias in the representation of heavy, short-duration convective events. For extreme events leading to 1-hour and 6-hour annual maximum precipitation intensities, simulated 5-minute peak intensities agree with the radar data, but remain below the intensity maxima in the station data. The CPM ensemble reproduces the dominant front-loaded shape of the temporal profile of 1-hour annual maximum events in agreement with observations.

Applying the event-based method to future projections, the CPM ensemble shows an increase in the mean intensity of a precipitation event (total event precipitation sum/duration). Moreover, unprecedented events with record-breaking mean intensity for all event durations occur with global warming. Seasonal changes reveal fewer long (12-24 h) and medium (3-12 h) duration events in summer, but more in winter, and a slight increase in short duration events (1-3 h) across the year. The frequency of extreme precipitation events increases, particularly in summer.

Our analysis of precipitation event profiles shows that warmer conditions lead to more peaked and front-loaded profiles, likely due to a shift from stratiform to convective precipitation. This apparent scaling relationship does not necessarily translate into a distinct climate change signal for extreme summer events, as they are already predominantly convective. We note that the event-associated temperature – evaluated over the 2-m air temperature on the day of the event – increases more rapidly with global warming for extreme events than for moderate events. We thus emphasise the importance of assessing the evolution of atmospheric conditions associated with extreme precipitation events to understand the projected changes.

The analysis of the novel KIT-KLIWA ensemble highlights the need for updated heavy precipitation products for climate adaptation that are also valid in a warmer future climate. Using a resolution of 5 min, we show that CPMs reproduce precipitation event profiles, which represents a significant advance in the practical application of CPMs. The integration of CPMs into impact models could be key to facilitating effective adaptation measures for resilient drainage design and flood protection in a warmer world.

Kurzfassung

Die Intensität von Starkniederschlägen hat in den letzten Jahrzehnten als Folge des Klimawandels zugenommen und Projektionen sagen eine weitere Zunahme voraus. Um effektive Anpassungsmaßnahmen an das dadurch zunehmende Hochwasserrisiko entwickeln zu können, ist es entscheidend, die regionalen Veränderungen von Starkniederschlagsereignissen nicht nur hinsichtlich ihrer Intensität, sondern auch hinsichtlich ihrer Häufigkeit, Dauer und ihres zeitlichen Profils zu verstehen. Regionale Klimamodelle basieren auf einer Parametrisierung von Konvektion und können Starkniederschlagsereignisse daher nicht mit der notwendigen Genauigkeit abbilden. Hochauflösende, so genannte konvektionserlaubende Modelle (CPM, 1-4 km Auflösung) können Niederschlagsereignisse deutlich realistischer abbilden. Aufgrund der hohen Rechenzeiten beschränken sich diese für Deutschland verfügbaren Simulationen derzeit auf Simulationen von Zeitscheiben, und in der Regel auf Simulationskonfigurationen mit einer einzigen Realisierung und Beschränkung der zeitlichen Auflösung auf eine Stunde.

Um das Verständnis zukünftiger Starkniederschlagsereignisse, insbesondere solcher von kurzer Dauer, zu verbessern, stellen wir das KIT-KLIWA Ensemble vor. Es besteht aus vier COSMO-CLM Modellläufen mit einer Auflösung von 2,8 km, die mit vier globalen Klimamodellen angetrieben werden. Dieses Ensemble liefert die ersten transienten konvektionserlaubenden Ensembleprojektionen für Süddeutschland, mit einem Simulationszeitraum von 1971 bis 2100 sowie derzeit einzigartige 5-min Niederschlagssimulationen für ausgewählte Zeiträume.

Basierend auf den Anforderungen der Praxis untersuchen wir das Klimaänderungssignal von Starkniederschlägen auf verschiedenen Skalen (Wiederkehrperioden von 1 bis 100 Jahren und Dauerstufen von 1 Stunde bis 3 Tage). Das CPM Ensemble projiziert eine Zunahme der Wiederkehrwerte von bis zu 8,5 % pro 1 °C Anstieg des globalen Erwärmungsniveaus, mit den größten Änderungen für kurze Dauerstufen und lange Wiederkehrperioden. Die Sensitivitätsanalyse zeigt den Mehrwert von transienten Datensätzen gegenüber Zeitscheiben-Experimenten, mit einer zuverlässigeren Abschätzung des Klimaänderungssignals, insbesondere für Intensitäten langer Dauerstufen.

Um die Einschränkungen der klassischen Extremwertanalyse zu überwinden, die auf Intensitäten einer festen Dauerstufe basiert, haben wir eine ereignisbasierte Analysemethode entwickelt. Diese zeigt in den historischen Simulationen im Vergleich zu Beobachtungsdaten eine Tendenz zur Überschätzung lang andauernder Ereignisse im CPM Ensemble und Defizite in der Simulation der Häufigkeit kurz andauernder konvektiver Ereignisse. Für Extremereignisse, die zu 1-stündigen und 6-stündigen Jahresmaxima führen, stimmen die simulierten 5-min Spitzenintensitäten mit den Radardaten überein, liegen aber unter den Intensitätsmaxima der Stationsdaten. Das CPM Ensemble reproduziert die dominant auftretenden frontbetonten zeitlichen Niederschlagsprofile der 1-stündigen Jahresmaxima.

Bei Anwendung der ereignisbasierten Methode auf die Klimaprojektion zeigt das CPM Ensemble eine Zunahme der mittleren Niederschlagsintensität der Ereignisse, sowie das Auftreten von Ereignissen mit Rekordwerten der mittleren Niederschlagsintensität für alle Ereignislängen. Die Veränderungen im Jahresgang führen zu einer Abnahme der langen (12-24 h) und mittleren (3-12 h) Ereignisse im Sommer und einer Zunahme im Winter. Kurze Ereignisse (1-3 h) nehmen über das Jahr hinweg leicht zu. Die Häufigkeit von Starkniederschlägen nimmt vor allem im Sommer zu.

Unsere Analyse der Charakteristika der zeitlichen Niederschlagsprofile zeigt, dass wärmere Bedingungen zu einem höheren Anteil der Spitzenintensität am Gesamtniederschlag und zu mehr frontbetonten Profilen führen, was durch eine Verschiebung von stratiformem zu konvektivem Niederschlag erklärt werden kann. Dieser Zusammenhang spiegelt sich jedoch nicht in einem Klimaänderungssignal für sommerliche Extremereignisse wider, da diese bereits überwiegend konvektiv sind. Die Analyse der Temperaturbedingungen, unter denen Niederschlagsereignisse auftreten – ausgewertet über die 2-m Lufttemperatur am Tag des Ereignisses – zeigt, dass diese Event-Temperatur für Extremereignisse mit der globalen Erwärmung schneller ansteigt als für moderate Ereignisse. Das Ergebnis unterstreicht die Bedeutung der Entwicklung der atmosphärischen Bedingungen im Zusammenhang mit Extremereignissen für das Verständnis von Starkniederschlägen im Klimawandel.

Die Analyse des neuen KIT-KLIWA Ensembles verdeutlicht die Notwendigkeit aktualisierter Starkregengefahrenprodukte, die auch in einer wärmeren Welt Bestand haben. Durch die Verwendung einer hohen zeitlichen Auflösung von 5 Minuten zeigen wir, dass zeitliche Niederschlagsprofile in CPMs mit der erforderlichen Genauigkeit wiedergegeben werden. Dies stellt einen bedeutenden Fortschritt in der praktischen Anwendung von CPMs dar. Die Integration von CPMs in die hydrologische Modellierung bietet das Potential für die Entwicklung effektiver Anpassungsmaßnahmen für eine resiliente Siedlungsentwässerung und den Hochwasserschutz in einer wärmeren Welt.

PREFACE

The PhD candidate confirms that the research presented in this thesis contains significant scientific contributions by herself. This thesis reuses material from the following publications:

> Hundhausen, M., H. Feldmann, N. Laube & J. G. Pinto (2023). Future heat extremes and impacts in a convection-permitting climate ensemble over Germany. Natural Hazards and Earth System Sciences, 23(8), 2873-2893, doi: 10.5194/nhess-23-2873-2023.
>
> Hundhausen, M., H. Feldmann, R. Kohlhepp, & J. G. Pinto (2024). Climate change signals of extreme precipitation return levels for Germany in a transient convection-permitting simulation ensemble. International Journal of Climatology, 44(5), 1454-1471, doi: 10.1002/joc.8393.
>
> Hundhausen, M., H. J. Fowler, H. Feldmann, and J. G. Pinto, 2025: Sub-hourly precipitation and rainstorm event profiles in a convection-permitting multi-GCM ensemble. Weather and Climate Extremes, 48, doi: 10.1016/j.wace.2025.100764.

The concept of Hundhausen et al. (2023) was developed by the candidate, Hendrik Feldmann, and Joaquim G. Pinto. Natalie Laube performed the preliminary analysis. The candidate is responsible for the analysis and wrote the original draft. All authors contributed to discussions, comments, and revisions. Hundhausen et al. (2023) is reused in the description of the simulation ensemble in Chapter 4.

The concept of Hundhausen et al. (2024) was developed by the candidate, Hendrik Feldmann and Joaquim G. Pinto. The candidate performed the analysis and wrote the original draft. All authors contributed to discussions, comments, and revisions. Hundhausen et al. (2024) is the basis for the result Chapter 5.

The concept of Hundhausen et al. (2025) was developed by the candidate, Hayley J. Fowler, Hendrik Feldmann and Joaquim G. Pinto. The candidate is responsible for the development of the event-based analysis method, performed the analysis, and wrote

the original draft. All authors contributed to discussions, comments, and revisions. Hundhausen et al. (2025) is the basis for the result Chapter 6.

The analysis in Chapter 7 is based on the following article in preparation for re-submission in Geophysical Research Letters:

> Hundhausen, M., H. J. Fowler, H. Feldmann, & J. G. Pinto (in preparation). Unprecedented precipitation events and seasonal shifts over Germany revealed by sub-hourly ensemble. Geophysical Research Letters – in preparation for re-submission.

The concept of the article was developed by the candidate, Hayley J. Fowler, Hendrik Feldmann, and Joaquim G. Pinto. The candidate is responsible for the analysis. The candidate wrote the original manuscripts with advice and revisions from the co-authors.

The candidate performed the analysis for Chapter 8. The chapter was written by the candidate with advice from Hayley J. Fowler, Hendrik Feldmann, and Joaquim G. Pinto. The content of Chapter 8 has not yet been submitted as a journal article.

The remaining Chapters 1, 2, 3 & 9 were authored by the candidate with advice from Joaquim G. Pinto, and Hendrik Feldmann.

The candidate has also contributed to the following publications, which, while not directly included in this thesis, have enriched their expertise and provided valuable context:

> Mohr, S., U. Ehret, M. Kunz, P. Ludwig, A. Caldas-Alvarez, J. Daniell, F. Ehmele, H. Feldmann, M. J. Franca, C. Gattke, M. Hundhausen, P. Knippertz, K. Küpfer, B. Mühr, J. G. Pinto, J. Quinting, A. M. Schäfer, M. Scheibel, F. Seidel, C. Wisotzky (2023). A multi-disciplinary analysis of the exceptional flood event of July 2021 in central Europe – Part 1: Event description and analysis Natural Hazards and Earth System Sciences, 23 (2), 525–551, doi: 10.5194/nhess-23-525-202.

> Ludwig, P., F. Ehmele, M. J. Franca, S. Mohr, A. Caldas-Alvarez, J. E. Daniell, U. Ehret, H. Feldmann, M. Hundhausen, P. Knippertz, K. Küpfer, M. Kunz, B. Mühr, J. G. Pinto, J. Quinting, A. M. Schäfer, F. Seidel, C. Wisotzky (2023). A multi-disciplinary analysis of the exceptional flood event of July 2021 in central Europe – Part 2: Historical context and relation to climate change. Natural Hazards and Earth System Sciences, 23 (4), 1287–1311, doi: 10.5194/nhess-23-1287-2023.

In Ludwig et al. (2023) the candidate took the lead on section 4.2 “High-resolution future climate projections” and otherwise contributed to discussions, comments, and revisions for both manuscripts.

The work was carried out by the candidate with funding from the Federal Ministry of Education and Research (BMBF) as part of the ISAP project (01LR2007B

& 01LR2007B1). This work was supported by additional funding from the GRACE Graduate School to enable a research visit to the UK Met Office in Exeter and Newcastle University.

CONTENTS

LIST OF FIGURES

LIST OF TABLES

ACRONYMS

AM	Annual Maximum
CAPE	Convective Available Potential Energy
CC	Clausius-Clapeyron
CCS	Climate Change Signal
CDF	Cumulative Distribution Function
CF	Change Factor
CIN	Convective Inhibition
CMIP	Coupled Model Intercomparison Project
CORDEX-FPS	Coordinated Regional Downscaling Experiments Flagship Pilot Studies
COSMO-CLM	COnsortium for Small-scale MOdelling in CLimate Mode
CPM	Convection-Permitting climate Model
CSR	Climate Scaling Rate
DWA	Deutsche Vereinigung für Wasserwirtschaft, Abwasser und Abfall e. V. (German Association for Water, Wastewater and Waste)
DWD	Deutscher Wetterdienst (German weather service)
ECS	Equilibrium Climate Sensitivity
ED	Event Duration
ETCCDI	Expert Team on Climate Change Detection and Indices
GCM	Global Climate Model
GEV	Generalized Extreme Value Distribution
GWL	Global Warming Level
HYRAS	Dataset “Hydrometeorologische Rasterdaten” (Hydrometeorological raster dataset)
IDF curve	Intensity-Duration-Frequency curve
IPCC	Intergovernmental Panel on Climate Change

ISAP	Project “Integrative stadt-regionale Anpassungsstrategien in einer polyzentrischen Wachstumsregion: Modellregion – Region Stuttgart” (Integrative urban-regional adaptation strategies in a polycentric growth region: Model region - Stuttgart Region
KLIWA	Project “Klimaveränderung und Wasserwirtschaft” (Climate change and water management)
KOSTRA	“Koordinierte Starkniederschlagsregionalisierung und -auswertung des DWD” (Coordinated heavy precipitation regionalisation and evaluation)
LCL	Lifted Condensation Level
LFC	Level of Free Convection
LNB	Level of Neutral Buoyancy
MCS	Mesoscale Convective System
POT	Peaks-over-threshold
PPT	Percentage points
RCM	Regional Climate Model
RCP	Representative Concentration Pathway
RL, RL10	Return Level, 10-year Return Level
RP	Return Period
TKE	Turbulence Kinetic Energy
WMO	World Meteorological Organization

1 | INTRODUCTION

From 12 to 15 July 2021, a severe flood event struck western Germany and the neighbouring regions in the Netherlands, Belgium, Luxembourg, and France. An extensive slowly-moving low-pressure centre over Central Europe advected extremely humid air masses to the region, resulting in local extreme rainfall of 100 to 150 mm during the event. The precipitation over the complex terrain with steep valleys led to record-breaking discharges between 400 and 700 m^3/s, which were reconstructed in the river Ahr. The flood event claimed 170 lives, left over 800 people seriously injured and caused an estimated total damage of 32 billion euros (Mohr et al., 2023). The public discourse quickly turned to the question of whether climate change has shaped the event. Indeed, an attribution study confirmed that global warming had increased the likelihood of such an event by a factor between 1.2 and 9 compared to a 1.2 K colder climate (Kreienkamp et al., 2021).

This event is not an isolated case. The sixth Assessment Report of the Intergovernmental Panel on Climate Change (IPCC) concluded that the frequency and intensity of extreme precipitation in Europe has "likely" increased and will "likely" increase further with additional global warming to a global warming level of 2 °C (IPCC, 2021). This change is primarily driven by the increasing capacity of warmer air to hold more moisture, a thermodynamic effect that leads to approximately 6 to 7 % more precipitable water per degree of temperature increase at constant relative humidity. As a second mechanism, dynamic processes – from small, cloud-scale to large-scale circulation patterns – impact the climate change signal of extreme precipitation (Fowler et al., 2021a). Dynamic effects dampen or amplify the change signal and can cause regionally substantial differences from the global increase (Fowler et al., 2021a; Pfahl et al., 2017; Santos et al., 2016).

The importance of understanding past and future changes in extreme precipitation arises from the fact that extreme precipitation is a multifaceted hazard: It serves as the key driver of flooding, can trigger landslides and especially urban areas are vulnerable to flash floods. The risk assessment frameworks in place often rely on historical data (Wasko et al., 2021). For instance, the Germany-wide rainfall risk dataset KOSTRA, provided by the national weather service, Deutscher Wetterdienst (DWD), is based on

observations from 1951 to 2020. KOSTRA provides estimates of precipitation intensities of events with return periods of up to 100 years and serves as a foundation for many heavy rainfall risk frameworks on the state-level in Germany (DWA, 2012). However, past observed data may no longer represent the increasing frequency and intensity of extreme weather events and fails to represent future climate risks. Updated guidelines and infrastructure design standards are therefore urgently needed (Wasko et al., 2021).

Some countries have taken steps to address these gaps by incorporating "climate uplifts" – or amplification/allowance factors – into their infrastructure planning (Wasko et al., 2021). For example, in Europe, the UK (UK Environment Agency, 2022), Belgium (Willems, 2011), and Denmark (Arnbjerg-Nielsen, 2008) have adopted guidelines that account for projected increases in precipitation under future climate scenarios. In Germany, while some states have started to include climate change factors in flood guidelines (Hennegriff, 2007), there is still no formal consideration of climate intensification of heavy precipitation in drainage system design (DIN EN 752; DIN 1986-100).

While these approaches are promising, the scientific uncertainty surrounding regional changes in precipitation remains high. Observational data are often limited, especially at high temporal resolution, and natural variability confounds the analysis (e.g. Willems, 2013). Model projections are therefore essential to assess future changes in precipitation extremes. However, regional climate simulations, typically with grid spacings of 12 to 50 km, rely on the parametrisation of convection. This leads to deficiencies in the representation of key processes involved in precipitation extremes. These simulations tend to produce precipitation that is too spatially diffuse, too persistent in time, and with too low intensity maxima of precipitation extremes (Kendon et al., 2021).

High-resolution climate simulations are a promising tool to advance the understanding of future extreme precipitation changes. The climate models at the so-called convection-permitting scale with a grid resolution of 1 to 4 km can explicitly resolve deep convection and have been shown to improve the representation of precipitation in comparison to convection parametrization in conventional coarser regional climate models (Prein et al., 2015; Lucas-Picher et al., 2021). These improvements comprise especially the intensities and frequencies of extreme precipitation, the diurnal cycle, and orographically-enhanced extreme precipitation (Kendon et al., 2012; Hohenegger et al., 2008; Sato et al., 2009; Prein et al., 2013; Ban et al., 2014, 2021). Further, the very high resolution allows the derivation of relevant data fields for impact assessment or the coupling of the convection-permitting climate models (CPMs) with data-driven impact models, making them a promising tool for the development of climate adaptation measures. On the downside, CPMs come with a high computational cost, and only recently has it become feasible to perform longer simulations (e.g. Kendon et al., 2021). Previous CPM projections are generally limited to time slices and/or single realisations. First ensemble simulations exist that improve the understanding of the uncertainty of extreme precipitation changes (Coppola et al., 2018; Kendon et al., 2020; Pichelli et al., 2021). In 2023, the first transient CPM ensemble simulations were released for the UK (Kendon et al., 2023)

and southern Germany (Hundhausen et al., 2023). The analysis of record precipitation events in Kendon et al. (2023) shows that indeed changes in extreme precipitation do not follow a steady upward trend of increase over time, highlighting the limitations of time-slice approaches.

One particularly underexplored area in the assessment of future precipitation changes is spatio-temporal shifts within precipitation profiles. As illustrated by Trenberth et al. (2003): "Steady moderate rains soak into the soil and benefit plants, while the same rainfall amounts in a short period of time may cause local flooding and runoff, leaving soils much drier at the end of the day.", highlighting the importance of precipitation characteristics beyond quantity. Specifically, the profile characteristics of the peak intensity and the timing of the peak intensity, have been identified to modify the peak runoff rates, their timing, and runoff volumes (Ball, 1994; Lambourne and Stephenson, 1987; Ochoa-Rodriguez et al., 2015; Cristiano et al., 2017; Dullo et al., 2017; Hettiarachchi et al., 2018; Pochwat et al., 2017). Despite the critical importance of linking precipitation volume to its temporal profile, most analyses of extreme precipitation – in observation as well as models – rely on fixed-duration periods, often daily or hourly precipitation sums. This fixed-duration approach imposes artificial constraints on rainstorm duration and therefore fails to capture the full range of precipitation characteristics that drive hydrological and hydraulic impacts. Early studies show an enhanced increase of the peak fraction of an event compared to its mean intensity (Wasko and Sharma, 2015; Ghanghas et al., 2024). To our knowledge, the first systematic study of the timing of the bulk precipitation or "event loading" in climate change by Visser et al. (2023) found a trend towards more front-loaded event profiles in the last decades in Australia. While supporting the finding by investigating day-to-day variability in temporal event profiles, Ghanghas et al. (2024) showed significant dependence on geographic location and dominant precipitation mechanisms. The limited literature available shows that potential changes in the temporal pattern of precipitation with increasing temperature aspects have not been sufficiently addressed in climate change impact studies (Visser et al., 2023).

One reason for this research gap is that assessing changes in precipitation profiles requires high-resolution precipitation time series, which are often scarce or unavailable over extended time periods. Previous analysis in CPM studies analysing extreme precipitation has often been limited to hourly model output, and little is known about sub-hourly extremes. A limited pool of sub-hourly CPM projections is available (Chan et al., 2016b; Meredith et al., 2020; Vergara-Temprado et al., 2021; Purr et al., 2021). Their evaluation provides promising results, indicating similar errors in sub-hourly data than in hourly precipitation extremes (Meredith et al., 2020; Vergara-Temprado et al., 2021), as well as an adequate representation of precipitation cell characteristics in Purr et al. (2021). Testing how well climate models reproduce the sub-hourly scale is of significant importance to increase confidence in predicted climate change signals on the sub-hourly scale as well as for the analysis of potential future change signals of the

temporal profile of precipitation events. Understanding future changes in precipitation patterns is critical, particularly for making the necessary adjustments to storm profiles used in hydrological applications, such as drainage design, to support climate adaptation.

The research gap to facilitate the development of informed climate adaptation measures regarding extreme precipitation can be summarized in three main points: (1) The limited availability of high-resolution climate model data constrains projections of changes in extreme precipitation intensity. (2) There is a lack of understanding of how high-resolution climate models reproduce sub-hourly features of extreme precipitation. (3) There is a missing assessment of the future changes of extreme precipitation on an event-based scale, specifically changes in the temporal event profile.

The overall aim of this thesis is to bridge the existing research gap and enhance the current understanding of climate change's impact on precipitation events with an emphasis on the short-duration time scale. To achieve this, we introduce the novel KIT-KLIWA ensemble, a transient CPM projection over Germany. The ensemble is driven by four CMIP5 GCMs (Coupled Model Intercomparison Project 5, Global Climate Models), representing a range of climate sensitivities from 3.28 to 4.64 degrees of global warming per doubling of CO_2 concentrations. The data is downscaled with the regional climate model COSMO-CLM (Baldauf et al., 2011) to a grid resolution of 2.8 km, which is on the convection-permitting scale at which deep convection is explicitly resolved by the model. The transient CPM simulation period covers 1971-2005 (historical) and 2006-2100 (projection). With 5-min precipitation output in the historical period as well as in selected future time slices, the ensemble presents a unique source of 5-min precipitation simulation data at the convection-permitting resolution.

We approach the topic in four steps. First, we use the transient projection period of the KIT-KLIWA projection to evaluate climate change signals of intensities down to the hourly resolution. The uncertainties arising from internal variability, the driving GCM and spatial patterns are assessed. After identifying the most sensitive return levels to global warming - namely short duration extremes - we focus on the sub-hourly scale in a second step. Based on the unique 5-min data from climate simulations, we develop a novel event-based approach to evaluate the characteristics of extreme precipitation events, including their sub-hourly features. The evaluation of the model data is based on the high-resolution station and radar observations of the DWD in Germany. The analysis reveals too persistent events in the CPM projection, but an adequate representation of the temporal profile of extreme events. In the third step, the event-based analysis is used to identify changes in the climatology of precipitation events, focusing on event duration and seasonal changes. In the final step, we focus on the dependence of event characteristics on temperature and explore the climate change signal of the event characteristics peak fraction and timing of the peak precipitation.

1.1 Thesis structure

The thesis is structured in 9 chapters. Following this introduction (Chapter 1), Chapter 2 provides the theoretical background to the research on the drivers of precipitation, and provides the state of the art on convection-permitting climate models and extreme precipitation in a warming world - its description, the mechanisms of change, and a review of the climate change signal. Chapter 3 outlines the research gaps and formulates four research questions targeted in the thesis. The data used in the study are presented in Chapter 4 with a focus on the KIT-KLIWA ensemble. Further, the reference data is described. Chapters 5 to 8 address the four research topics:

- Assessment of the climate change signal of extreme precipitation return levels from hourly to multi-day scale and associated uncertainties (Chapter 5)
- Development of an event-based analysis and evaluation of 5-min precipitation data and temporal precipitation event profiles in CPM (Chapter 6)
- Assessment of the climate change impact on the climatology of precipitation events (Chapter 7)
- Analysis of the scaling relation and the climate change signal of the profile characteristics peak intensity and timing of the peak intensity (Chapter 8)

The conclusion in Chapter 9 summarizes the findings, discusses the implications, and provides an outlook.

2 | THEORY AND LITERATURE REVIEW

In order to contextualise the topic of extreme precipitation in climate projections, this chapter outlines the underlying mechanisms of precipitation (Section 2.1) and the climatology of precipitation in Germany (Section 2.2). Then it reviews the simulation of precipitation in numerical climate models (Section 2.3), and concludes with an overview of the climate change signal of extreme precipitation (Section 2.4).

2.1 The driving mechanisms of precipitation

Precipitation is the result of a series of physical processes. It begins with water vapour in the air. This water vapour condenses around nucleation sites such as dust particles and aerosols as the air rises, forming clouds. Cloud droplets grow and eventually precipitation falls from these clouds due to gravity. This section provides a theoretical background to the formation of precipitation. The section is structured in first an overview of atmospheric moisture saturation and adiabatic processes, then it introduces the concept of atmospheric stability, and finally explains the mechanisms behind convective and stratiform precipitation.

2.1.1 The Clausius-Clapeyron relation

Water vapour saturation is a key condition for condensation in the atmosphere. As described by the Clausius-Clapeyron relation, which defines the relationship between vapour pressure and temperature during phase transitions, water vapour saturation is closely tied to temperature. The following derivation of the Clausius-Clapeyron equation is based on Vallis (2017).

We consider water in chemical equilibrium between the liquid phase – liquid water (denoted as phase l) – and the gas phase – water vapour (denoted as phase v). In an enclosed system, the gas and liquid phases exchange mass and energy and will eventually come to an equilibrium, with the same mass of liquid evaporating into vapour and vapour condensing into the liquid. The energy required for the phase change is given

by the latent heat of evaporation L, which is defined by the difference between the enthalpies (h) of both phases:

$$L(T) = h_v - h_l \tag{2.1}$$

L is dependent on temperature, T, and has a magnitude of approximately 2.5×10^6 J/kg (at 0 °C) for water. The energy E of the phase change of a mass M is given Eq. 2.2 and can be related to the entropy, η with the specific entropy η_v and η_l for vapour and liquid. T is constant in this consideration at equilibrium, as the energy for condensation equals the energy for evaporation.

$$E = ML = M(h_v - h_l) = MT(\eta_v - \eta_l) \tag{2.2}$$

Rearranging and application of the definition of the specific Gibbs function, $G = h - T\eta$, leads to the following relationship, stating that the specific Gibbs functions for the liquid and water phases at equilibrium are equal:

$$h_v - T\eta_v = h_l - T\eta_l \tag{2.3}$$

$$G_l = G_v \tag{2.4}$$

If equilibrium is maintained along the phase boundary as the temperature or pressure changes, the changes in Gibbs function will also be the same for each phase:

$$dG_l = dG_v \tag{2.5}$$

From the fundamental thermodynamic equation for Gibbs Energy, the change in the Gibbs function can be expressed as:

$$dG = -\eta dT + \alpha dp \tag{2.6}$$

with the specific entropy η, temperature T, specific volume $\alpha = 1/\rho$ which is the inverse of the density ρ, and pressure p. Using Eq. 2.5 and Eq. 2.6, re-arranging gives an expression of dp/dT which describes the conditions along the phase boundary. For the phase boundary between the liquid and vapour phase, the difference $\eta_l - \eta_v$ can be expressed over L (as in Eq. 2.2):

$$-\eta_l dT + \alpha_l dp = -\eta_v dT + \alpha_v dp \tag{2.7}$$

$$\frac{dp}{dT} = \frac{\eta_l - \eta_v}{\alpha_v - \alpha_l} \tag{2.8}$$

$$\frac{dp}{dT} = \frac{L}{T\,(\alpha_v - \alpha_l)} \tag{2.9}$$

Since we consider the water vapour in equilibrium with the liquid water phase, p is the saturation water vapour pressure (e_s) to arrive at the Clausius–Clapeyron equation (Eq. 2.10). For the phase transition between the vapour and liquid phase, $\alpha_v >> \alpha_l$

applies and $\Delta\alpha = \alpha_v - \alpha_l$ can be approximated by α_v.

$$\frac{de_s}{dT} = \frac{L}{T(\alpha_v - \alpha_l)} \approx \frac{L}{T\alpha_v} \tag{2.10}$$

In the atmosphere, we further consider that the relationship between saturation vapour pressure and the absolute humidity is given by the ideal gas law with the specific gas constant R (Eq. 2.11) – written for water vapour with the specific water vapour gas constant $R_v = 462\text{Jkg}^{-1}\text{K}^{-1}$ in Eq. 2.12:

$$p = \rho RT = \frac{RT}{\alpha} \tag{2.11}$$

$$e_s = \frac{R_v T}{\alpha_v} \tag{2.12}$$

This reduces to the following form of the Clausius-Clapeyron equation, which is typically used in atmospheric applications:

$$\frac{de_s}{dT} \approx \frac{e_s L}{R_v T^2} \tag{2.13}$$

Assuming a constant $L(T)$ – which is only valid as an approximation – the Clausius-Clapeyron equation can be integrated by introducing the constants e_0 and T_0 (Eq. 2.14). Further approximations exist that partially account for the temperature dependence of L. However, instead of integrating the equation, empirical approximations to the vapour pressure curve are often used, such as the Magnus Equation (Eq. 2.15, Alduchov and Eskridge, 1996). The Magnus Equation uses temperature T^C in °C as input, and the output e_s^{hPa} is in hPa.

$$e_s = e_0 \exp\left(-\frac{L}{R_v}\left(\frac{1}{T_0} - \frac{1}{T}\right)\right) \tag{2.14}$$

$$e_s^{hPa} = 6.1094 \exp\left(\frac{17.625 T^C}{T^C + 243.04}\right) \tag{2.15}$$

For typical conditions in the atmosphere, the denominator changes only slightly with temperature and the saturation vapour pressure thus behaves approximately exponentially with temperature. The non-linear relationship implies that warmer air can hold substantially more moisture than colder air: for example absolute moisture content at 10 °C is 7 g/kg, but is 14 g/kg at 20 °C. Inserting reasonable values for our atmosphere, saturation pressure increases by ~7 % per degree at 0 °C and ~6 % per degree at 24 °C, referred to as the Clausius-Clapeyron rate (CC-rate or CC-scaling).

2.1.2 Adiabatic processes in the atmosphere

In our atmosphere, air typically reaches water vapour saturation when it ascends to a higher altitude which is accompanied by a decrease in pressure and consequently temperature. In this section, we will use the lifted parcel theory to explain the tem-

perature change during the ascent of air that leads to condensation in the atmosphere. Derivations in this section are based on Stull (2015).

The lifted parcel theory tracks the characteristics of a parcel of air as it rises or sinks in the atmosphere. Several underlying assumptions are made. No radiative or other heat transfer occurs with the surrounding air and the process is thus adiabatic. The parcel is assumed to have no finite size and does not exchange mass with the surrounding air. The pressure of the air parcel is considered equal to that of the surrounding environment and no solid phase of water is considered. Assuming that the air in the atmosphere behaves like an ideal gas, the ideal gas law applies (Eq. 2.11). We further consider that the column of air is in hydrostatic balance (Eq. 2.16), where the pressure gradient, dp, with altitude, dz, is determined by the air density, ρ, and gravitational acceleration, g.

$$\frac{dp}{dz} = -\rho g \tag{2.16}$$

The following sections consider two examples of atmospheric ascent for an air parcel. First is the dry adiabatic ascent, defined as vertical ascent without any phase change of water, occurring below the condensation level. The second example is the moist adiabatic ascent, which includes phase changes as the parcel rises.

Unsaturated (dry) lifting

The consideration of a dry adiabatic ascent is based on the first law of thermodynamics, which states that energy is conserved:

$$dU = \delta Q + \delta W \tag{2.17}$$

A change in internal energy, U, can occur through the addition or removal of heat, δQ, as well as through work done on the system, δW. The notation d signifies a total differential, while δ represents a path-dependent differential.

For a dry adiabatic process, there is no heat exchanged with the surroundings, so:

$$\delta Q = 0 \tag{2.18}$$

$$dU = \delta W \tag{2.19}$$

The work performed is given by:

$$\delta W = -p d\alpha \tag{2.20}$$

For an ideal gas, the internal energy U is related to temperature T by Eq. 2.21 with the specific heat capacity at constant volume c_v:

$$dU = c_v dT \tag{2.21}$$

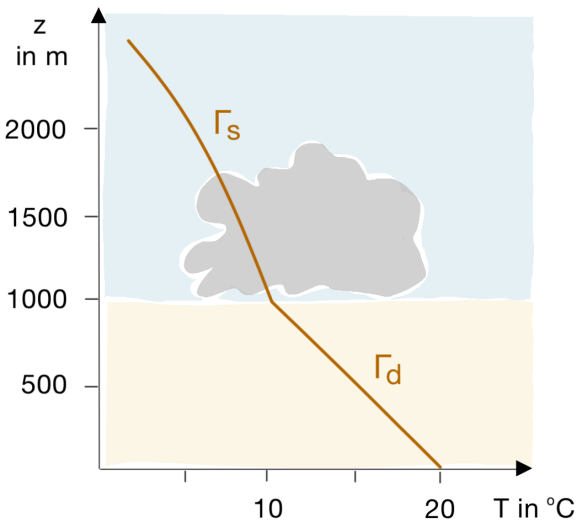

Figure 2.1: Temperature trajectory of a parcel of moist air lifted from the surface.

Substituting Eq. 2.20 and Eq. 2.21 in the first law of thermodynamics for adiabatic processes, we get:

$$c_v dT = -p d\alpha \tag{2.22}$$

For application in the atmosphere, the equation is typically rearranged using the product rule $pd\alpha = d(p\alpha) - \alpha dp$ and the ideal gas law $p\alpha = RT$:

$$0 = c_v dT + p d\alpha \tag{2.23}$$

$$0 = c_v dT + R dT - \alpha dp \tag{2.24}$$

With the relationship $c_v + R = c_p$, introducing the specific heat capacity at constant pressure c_p, we can rewrite this as:

$$c_p T = \alpha dp \tag{2.25}$$

We use the hydrostatic equation (Eq. 2.16) to rewrite to:

$$dT = -\frac{g}{c_p} dz \tag{2.26}$$

Rearrangement leads to an expression for the temperature change with altitude, defined as the dry adiabatic lapse rate, Γ_d:

$$\Gamma_d = -\frac{dT}{dz} = -\frac{g}{c_p} \tag{2.27}$$

Γ_d is constant with height, and is approximately $1\,\mathrm{K}/100\,\mathrm{m}$. It describes the rate of temperature change with altitude for a rising parcel of air below the water vapour saturation (Fig. 2.1).

Saturated (moist) lifting

If a lifted parcel contains moisture, it will eventually cool to saturation, and water will start to condense. The latent heat released due to condensation reduces the cooling of an ascending parcel significantly (Fig. 2.1). The moist adiabatic lapse rate, Γ_s, describes the temperature change of an ascending saturated parcel:

$$\Gamma_s = \frac{g}{c_p} \cdot \frac{1 + \left(\frac{r_s L_v}{R_d T}\right)}{1 + \left(\frac{L_v^2 r_s \frac{R_d}{R_v}}{c_p R_d T^2}\right)} \tag{2.28}$$

The variables are defined as gravitational acceleration g, specific heat capacity of air at constant pressure c_p, saturation mixing ratio r_s, latent heat of evaporation L_v, gas constant for dry air R_d, gas constant for water vapour R_v, air temperature T. Γ_s depends non-linearly on temperature and pressure or altitude. It is higher at higher pressure and temperature (close to the Earth's surface) and asymptotically approaches the dry adiabatic lapse rate for low temperatures and low pressure – at high latitudes (Fig. 2.1).

2.1.3 Atmospheric stability

The environmental conditions within the troposphere are essential for the formation of precipitation. This section introduces the concept of air masses and provides the theoretical background to atmospheric stability.

Air masses are large bodies of air with relatively uniform temperature and humidity characteristics. They develop over large, homogeneous areas where they reside for long periods of time, allowing them to adopt the thermal and moisture characteristics of the underlying surface (Spiridonov and Ćurić, 2021). For example, air masses forming over oceans (maritime) are typically moist, while those forming over continents (continental) are generally dry. Similarly, air masses forming over polar regions are cold, while those forming over tropical regions are warm. Advection of air masses over large distances results in changes in the temperature or humidity of an air mass as it passes over different surfaces. The vertical temperature profile of an air mass is critical in determining its characteristics, and classifies the atmospheric stability of the air mass.

Atmospheric stability is determined by the environmental lapse rate, which is the rate at which temperature decreases with altitude (e.g. Lutgens and Tarbuck, 2019). A stable environment is characterised by an environmental lapse rate below Γ_s. In such conditions, a parcel of air lifted to a higher altitude cools at the dry or moist adiabatic lapse rate and becomes denser than the surrounding air, inhibiting further upward movement unless forcefully lifted. Conversely, instability occurs when the environmental lapse rate is greater than Γ_d (absolute instability) or between Γ_d and Γ_s (conditional instability). When a parcel of air is displaced in an absolutely unstable atmosphere, the temperature of the parcel changes with Γ_d or Γ_s depending on its saturation. The parcel

becomes warmer, therefore lighter, than the surrounding air, and becomes buoyant. The same applies to a saturated parcel of air in a conditionally unstable environment.

The buoyant force per unit mass depends on the density difference between the parcel (subscript p) and the environment (subscript e). Using the ideal gas law, the buoyant force can be related to the temperature of the parcel and the environment (Stull, 2015):

$$\frac{F}{m} = \frac{\rho_p - \rho_e}{\rho_p} g \tag{2.29}$$

$$\frac{F}{m} = \frac{T_{ve} - T_{vp}}{T_{ve}} g \tag{2.30}$$

The virtual temperature T_v is introduced here, based on the definition that dry air of the temperature T_v has the same density as the actual moist air of temperature T. This approach includes the effects of water vapour and allows the application of the ideal gas law with the specific gas constant of dry air R_d. T_v is approximated based on the specific humidity q:

$$T_v \approx T(1 + 0.608q) \tag{2.31}$$

In essence, the characteristics of an air mass determine the prevailing conditions, including temperature, moisture content, and atmospheric stability. The following sections will outline how the stability of an air mass affects cloud formation and precipitation.

2.1.4 Stratiform and convective precipitation

Precipitation can be categorized into two main types: stratiform precipitation and convective precipitation. In the following sections, we will explore the characteristics of stratiform and convective precipitation and discuss the atmospheric conditions that support their development. The following background theory is based on Lutgens and Tarbuck (2019) and Houze (1993), unless stated otherwise. The microphysics of cloud formation are out of the scope of this work and not detailed here.

Stratiform precipitation

The precipitation type can be defined in terms of the vertical velocity scale. Stratiform precipitation is defined over the condition that the vertical movement of air, w, is small compared to the fall velocity of ice crystals or snow, v_{ice}:

$$|w| < v_{\text{ice}} \tag{2.32}$$

Stratiform clouds are typically formed in a stable environment, where the upward movement of the air is inhibited and the air will not rise unless forcefully lifted (Fig. 2.2a).

Lifting processes in a stable environment are observed, for example, at a warm front, where warmer (lighter) air masses meet cooler (denser) air masses, and the

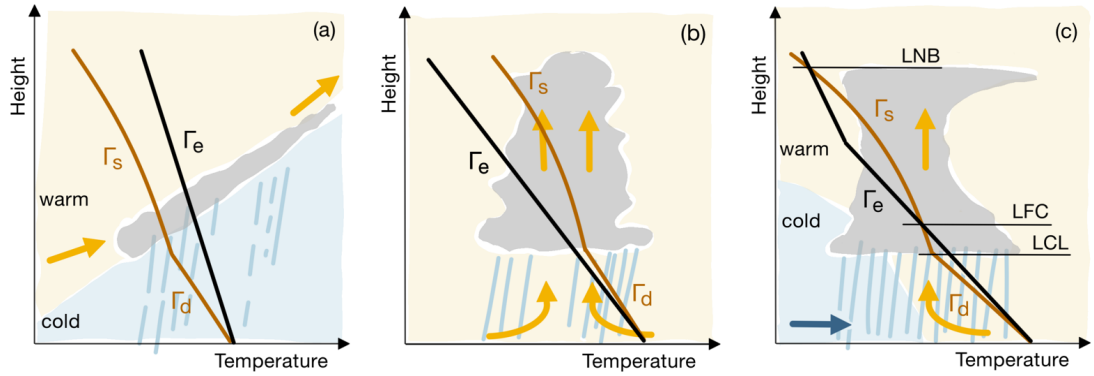

Figure 2.2: Temperature trajectory of a parcel of moist air lifted from the surface in (a) a stable environment, (b) absolutely unstable environment, and (c) conditionally unstable environment with the lifted condensation level, LCL, the level of free convection, LFC, level of neutral buoyancy, LNB. Γ_d is the dry adiabatic lapse rate, Γ_s the moist adiabatic lapse rate and Γ_e the environmental lapse rate (Based on Lutgens and Tarbuck, 2019).

warm air glides up the colder air mass (Fig. 2.2a). In addition, orographic lifting can lead to stratiform precipitation. Extensive cloud layers form when the air becomes saturated with moisture. Stratiform precipitation often covers a large area, resulting in widespread but relatively uniform, rainfall. Characteristics are steady, light to moderate precipitation, that may persist for several hours.

Convective precipitation

Convective precipitation is characterised by a fast vertical movement of air, w, compared to the fall velocity of ice crystals or snow, v_{ice}, which occurs in cumulus clouds.

$$|w| > v_{\text{ice}} \tag{2.33}$$

Convective cloud formation requires instability. When a parcel of air is displaced in an absolutely unstable atmosphere, the temperature of the parcel changes with the dry lapse rate until the water vapour saturation is reached and condensation leads to cloud formation (Fig. 2.2b). Free convection in an absolutely unstable atmosphere over land is primarily driven by localized heating of the Earth's surface, which warms the lower layers of the atmosphere and generates rising columns of warm air. This phenomenon is commonly observed in the mid latitudes during the summer months, or in the tropics the whole year round.

In a conditionally unstable atmosphere (Fig. 2.2c), a moist parcel of air that is lifted from the surface, will expand and cool according to the dry adiabatic lapse rate until saturation pressure is reached at the lifted condensation level (LCL). Cooling above the LCL is associated with condensation and therefore along the moist adiabatic lapse rate. Forced above the level of free convection (LFC), the parcel becomes buoyant. Hence, conditional stability requires a specific amount of energy, referred to as Convective

Inhibition (CIN), to initiate convective processes (Eq. 2.34 with p_{bot} the pressure at the bottom or in a boundary layer, Vallis, 2017). In the thermodynamic diagram (Fig. 2.2c), CIN can be related to the area between the environmental temperature T_e and the lifted parcel's temperature T_p below the LFC, plotted with logarithmic pressure as the vertical axis. This energy must be invested to lift an air parcel to the LFC. Unstable conditions leading to precipitation are typically connected with unstable maritime air masses. Lifting air above the LFC can occur through mechanisms such as orographic lifting or frontal lifting along a cold front (Fig. 2.2c).

$$\text{CIN} = -R \int_{p_{\text{bot}}}^{\text{LFC}} (T_p - T_e) \frac{dp}{p} \tag{2.34}$$

$$\text{CAPE} = -R \int_{\text{LFC}}^{\text{LNB}} (T_p - T_e) \frac{dp}{p} \tag{2.35}$$

CIN is opposed by the energy released during the convective process, the convective available potential energy (CAPE), which determines the strength of the convection (Eq. 2.35, Vallis, 2017). In a thermodynamic diagram with logarithmic pressure as the vertical axis, CAPE is proportional to the area between the environmental temperature T_e and the lifted parcel's temperature T_p integrated from the LFC to the level of neutral buoyancy (LNB), where its density is equal to the surrounding air (Fig. 2.2c).

Convective precipitation is often intense and short-lived, with high rainfall rates that, depending on the strength of convection, can lead to heavy downpours, thunderstorms, and hail.

Stratiform and convective precipitation in our atmosphere can occur separately but also coexist within the same precipitation system (Houze, 1993). Stratiform clouds can for example form near the outflow of active deep convective clouds, or from previously active deep convective clouds. The coexistence of the two types of precipitation is observed, for example, in large mesoscale convective systems (MCSs). MCSs are ensembles of convective storms with diameters of several hundred kilometres and contain both stratiform and convective subregions.

In summary, two distinct forms of precipitation occur in the atmosphere, whereby stratiform precipitation mostly originates from a stable atmosphere and forced, relatively slow lifting, convective precipitation is produced by strong upward motion in an unstable atmosphere. Stratiform precipitation tends to be light to moderate and widespread, while convective precipitation is more localised and can lead to deep convective clouds with intense precipitation, hail and thunderstorms at high CAPE. Both precipitation types can coexist in the same precipitation system.

2.2 Overview of Germany's precipitation climatology

Germany is located in the mid-latitudes in the zone of westerly winds. The region is characterised by alternating low and high pressure systems with the associated warm

and cold fronts. The advected air masses from different origins influence the weather in Germany.

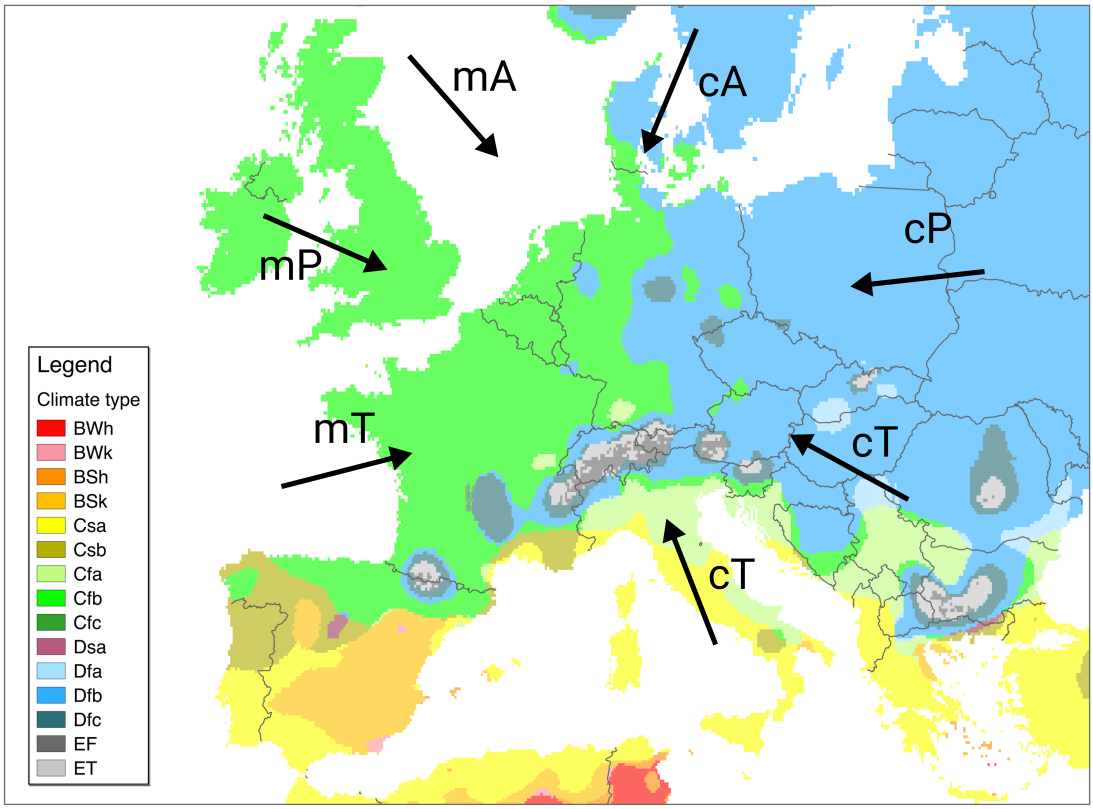

Figure 2.3: Air masses influencing the weather in Germany. The first letter c denotes continental air masses, while m denotes maritime air masses. The source regions are denoted with T for tropical, P for polar, A for Arctic. The climate zones in Europe according to the Köppen-Geiger Climate Classification are shown in the background. The following notation is used in the legend: Hot climates (BWh: Hot desert climate, BWk: Cold desert climate, BSh: Hot semi-arid climate, BSk: Cold semi-arid climate), temperate climates (Csa: Hot-summer Mediterranean climate, Csb: Warm-summer Mediterranean climate, Cfa: Humid subtropical climate, Cfb: Temperate oceanic climate, Cfc: Subpolar oceanic climate), continental climates (Dsa: Mediterranean-influenced hot-summer humid continental climate, Dfa: Hot-summer humid continental climate, Dfb: Warm-summer humid continental climate, Dfc: Subarctic climate), polar and alpine climates (ET: Tundra climate, EF: Ice cap climate). The classification is based on Peel et al. (2007), the raster data used is available from `http://www.hydrol-earth-syst-sci.net/11/1633/2007/hess-11-1633-2007-supplement.zip`, last access October 2024.

Based on Spiridonov and Ćurić (2021) and Kurz (1990), southwesterly, westerly, and northwesterly winds bring humid air masses with maritime origin from the Atlantic to Central Europe (Fig. 2.3). Air masses of Atlantic origin dominate the weather in Central Europe, leading to a wet climate with year-round precipitation. The further north these air masses originate, the colder they are. Cold, polar maritime air masses (mP) rise in temperature during their passage over the relatively warm waters of the North Atlantic, becoming unstable. Weather with prevailing polar maritime air masses is characterised by frequent showers at any time of the year. In winter, cold arctic

maritime air masses (mA) can lead to heavy snowfall. Warm, subtropical and tropical maritime air masses (mT) can carry a lot of moisture, which can lead to heavy rainfall. In particular, extreme precipitation in Germany can occur when a low pressure system over the Mediterranean moves northwards towards north-eastern Europe (in a so-called "Vb pattern"), advecting extremely humid air masses that lead to prolonged and intense precipitation in Germany (e.g. Seibert et al., 2006). In contrast, the advection of air masses from the east is less frequent. The polar continental air masses (cP) lead to mostly dry weather in Central Europe, which is associated with heat in summer and cold in winter.

Overall, the climate in Germany is classified as temperate climate (Cfb) in the west to cold climate (Dfb) in the east with warm summers and precipitation in all seasons according to the Köppen-Geiger climate classification (Fig. 2.3, Peel et al., 2007).

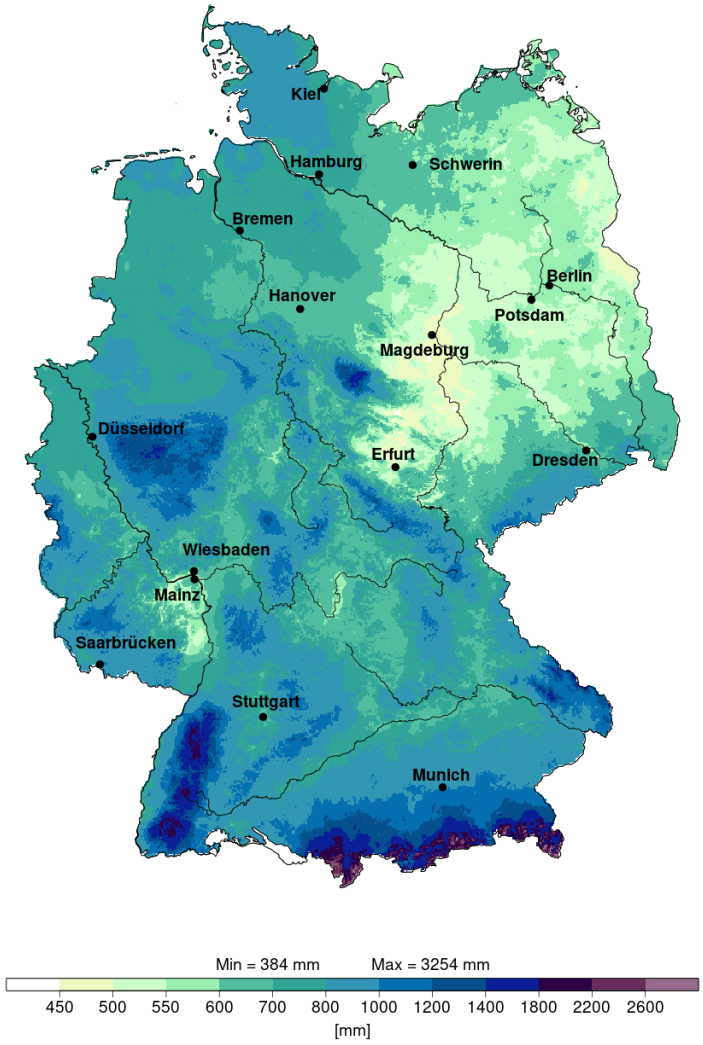

Figure 2.4: Annual precipitation sum averaged over the period 1971 to 2000 (German Climate Atlas, a service by the German weather service, Deutscher Wetterdienst, URL: `www.dwd.de/klimaatlas`, last access October 2024).

The annual precipitation sums in Germany are on average around 800 mm. The spatial distribution is mainly dependent on the orography (Fig. 2.4). While in the low mountain range in the southwest of Germany, the Black Forest, annual precipitation totals of up to 2000 mm are observed, precipitation sums of less than 700 mm are reached in the eastern part of the domain, the Elbe basin. In the western regions, annual precipitation of 1000 mm is common. The highest precipitation totals are observed in the Alps in the south of Germany, with precipitation totals above 3000 mm.

The type of precipitation depends on the season. In summer, there are predominantly convective events and in the winter mostly large frontal systems associated with stratiform precipitation (Lengfeld et al., 2019). The most intense precipitation events in Germany tend to be associated with convective precipitation events in summer (Berg et al., 2013; Gatzen et al., 2020). MCSs that typically span several hundred kilometres in diameter, dominate the convective precipitation yield (Da Silva and Haerter, 2023, and Supporting Information therein).

In summary, moisture transport from the North Atlantic Ocean drives precipitation throughout the year in Germany, averaging about 800 mm annually, with local variations shaped by orography. Seasonal patterns influence the type of precipitation: summer is dominated by convective precipitation, while winter features widespread stratiform precipitation from frontal systems. Extreme events with high precipitation rates are primarily associated with intense summer convective systems.

2.3 The state of the art of convection-permitting climate modelling

To project future climate change, numerical climate models simulate the Earth's climate using mathematical equations to represent the physical processes in the Earth's climate system. Numerical climate modelling has undergone considerable advancements in recent decades, evolving from coarse-resolution models that rely heavily on parametrisations, to increasingly finer grid spacings that more accurately resolve atmospheric processes. Increasing the resolution to the km scale, typically 1 to 4 km (Prein et al., 2015), so-called convection-permitting climate models (CPMs, alternative terms are convection-resolving, convection-allowing, storm-resolving, storm-permitting and storm-allowing, Kendon et al., 2021) can partly resolve convective processes. This section clarifies how CPMs represent convection compared to conventional regional models, reviews the added value of those CPM simulations, and gives an overview of the emerging ensemble simulations on the convection-permitting scale.

2.3.1 Convection in numerical climate models

In numerical climate modelling, the principles of conservation of mass, conservation of energy, and conservation of momentum provide the basis for the description of processes

in the Earth's atmosphere. Together with the ideal gas law, they form the fundamental model equations. Different numerical methods exist, to solve the complex set of model

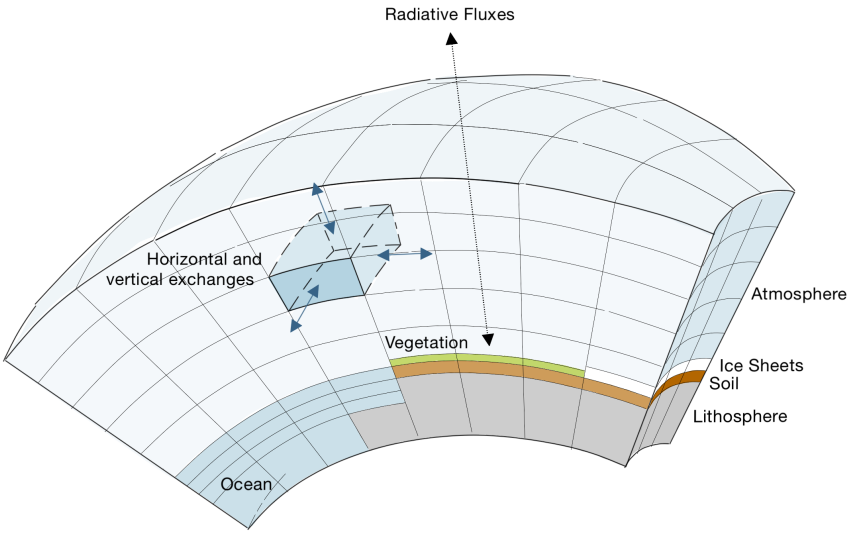

Figure 2.5: Schematic of a numerical climate model.

equations. In today's climate models – so-called grid point models – the atmosphere of the Earth is divided into a 3D grid and the underlying differential equations – with implementations specific to the model – are solved on a grid of horizontal and vertical extension for each time step, followed by vertical and lateral interchange of energy, momentum, and mass between the boxes (Fig. 2.5). The grid resolution of the model limits processes that the model can explicitly resolve.

The grid resolution of today's global climate models (or general circulation models, GCMs), that are used in the current IPCC report, have a resolution of approximately 0.5 to 3 degrees in latitude and longitude. To achieve higher resolution, regional climate models (RCMs) are used to dynamically downscale the coarse global simulation to a grid with higher resolution in a spatially limited area. Typically, nesting techniques are used to drive the regional simulations using boundary conditions from the GCM.

Parametrisation of convection in RCMs

The physical processes in the atmosphere occur on a wide range of scales, from micro-scale phenomena to large-scale circulations and planetary waves (Fig. 2.6). Convection ranges from shallow convection in the range of about 1 km to deep convection in cumulonimbus clouds, which can extend to tens of kilometres.

The grid resolution of RCMs ranges typically from 12 to 50 km (Kendon et al., 2017). Consequently, convection is a process that generally occurs on a length scale

[1]Adapted from Mahgue (`http://commons.wikimedia.org/wiki/User:Mahgue`), 2012. Atmospheric motions and their typical scales in time and space according to Heinz Fortak: Meteorologie. Retrieved October 2024, from: `https://commons.wikimedia.org/wiki/File:Atmosphere_motion_scale.svg`

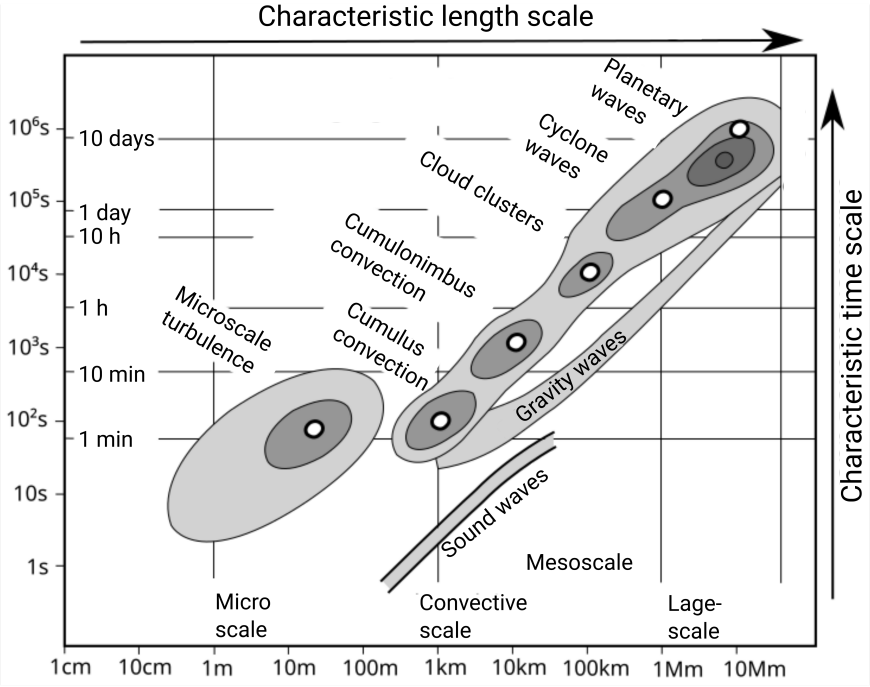

Figure 2.6: Atmospheric motions and their typical scales in time and space based on Fortak (1982)[1].

smaller than the grid resolution, on the so-called sub-grid scale (Fig. 2.6). Convection is therefore not explicitly resolved by RCMs. To represent subgrid-scale processes, they are parametrised in the model formulation.

In practice, convection parametrisation includes three steps (Bechtold, 2017):

- Determine the initialization of convection, referred to as "Trigger of convection".
- Determine the vertical distribution of heating, moistening, and momentum changes, generally by a cloud model.
- Determine the overall amount of convective precipitation from the converted energy, referred to as "Closure".

Various approaches exist for implementing parametrisation in climate models, ranging from schemes based on moisture budgets, over adjustment schemes, to mass flux schemes. A comprehensive review of these methods is provided by Bechtold (2017). Today's RCMs, including the regional climate model COSMO-CLM used in this thesis, predominantly utilize the mass flux scheme. The basic concept of the mass flux scheme is that the vertical mass flux at the base of a convective cloud can be derived from grid-scale variables, as described by Bechtold (2017).

Convection parametrisation is a major source of uncertainty in climate models. The largest uncertainties in projected climate sensitivity in GCMs are associated with the parametrisation of deep convection (Knight et al., 2007; Sherwood et al., 2014). Deficiencies in the convective parametrisation schemes are amplified by their interaction

with various parametrisation schemes, such as microphysical, radiative and boundary layer schemes, implying non-linear error growth of the deficiencies (Prein et al., 2015). Common errors of convection parametrisation in RCMs include the diurnal cycle of convective precipitation, underestimation of the frequency of dry days, overestimation of the frequency of low precipitation events, and underestimation of hourly precipitation extremes (Prein et al., 2015).

Explicit resolution of convection in CPMs

Increasing the grid resolution to the kilometre scale, at grid resolutions of 1 to 4 km, the convection-permitting scale is reached at which deep convection is explicitly resolved by the model (Prein et al., 2015). Shallow convection is however still parametrised in the model (Fig. 2.6).

2.3.2 The added value of convection-permitting climate models

CPM climate projections profit not only by avoiding error-prone convection parametrisation of deep convection but also by improving the representation of orography and other surface forcing (Prein et al., 2015). Indeed, the climate simulations on the convection-permitting scale were shown to have an added value compared to conventional convection-parametrising RCM simulations.

Precipitation

CPM simulations have been shown to improve the onset and peak of the diurnal precipitation cycle in several studies, e.g. in Fosser et al. (2015); Knist et al. (2018); Meredith et al. (2021); Berthou et al. (2020) for Germany and the finding is robust for other regions (Lucas-Picher et al., 2021). Improvements in the diurnal cycle are attributed to the explicit resolution of deep convection, allowing atmospheric instabilities to build up during the day and their more realistic release in the form of precipitation in the late afternoon (Leutwyler et al., 2016; Lucas-Picher et al., 2021). Spatial patterns of precipitation events were found to be more realistically reproduced by e.g. Prein et al. (2013), showing more intense smaller events in the CPM simulation compared to the coarser RCM simulation. Pichelli et al. (2021) find a more realistic simulation of regional patterns of precipitation over the Alps in CPMs compared to RCMs.

There is no clear indication of an added value in the representation of daily mean precipitation in CPMs and daily extreme precipitation is generally found to be overestimated in the CPM simulations (e.g. Prein et al., 2013; Chan et al., 2013; Fosser et al., 2015). However, major improvements were found in precipitation on a short time scale. Mostly examined at hourly resolution, there is a significant improvement in the representation of heavy precipitation compared to the underestimation of hourly extreme intensities in RCMs (e.g. Ban et al., 2014; Fosser et al., 2015; Berthou et al., 2020; Knist et al., 2018). In general, CPMs are able to more realistically reproduce the

relevant smaller-scale phenomena, such as mesoscale convective systems, geographic precipitation, or squall lines (Lucas-Picher et al., 2021). Ban et al. (2021) and Pichelli et al. (2021) assessed spatial patterns in a multi-model ensemble over Europe, and found a more realistic simulation of regional patterns, especially the orographic features of the Alps in heavy precipitation of hourly extremes in the CPM ensemble compared to the coarser RCM counterpart. In addition, the improved representation of convective precipitation events in CPMs is expected to improve the diagnostic for high-impact weather such as hail produced by microphysics schemes (Kendon et al., 2017)

Comparing the change signal of precipitation between CPM and RCM shows that the climate change signal of extreme precipitation is dependent on the model resolution and there is a stronger intensification of extreme precipitation in CPM projections compared to coarser RCM projections (Chan et al., 2014a; Kendon et al., 2014). Fosser et al. (2024) do not only find a stronger intensification of local extreme precipitation in CPMs but also that an ensemble of CPM projections reduces the uncertainties for future changes in comparison to the RCM ensemble. They conclude that there is greater confidence in projected changes in CPM compared to RCM projections. The improvement is attributed to the more realistic representation of local dynamical processes in CPMs. Kendon et al. (2014) argue that CPMs should be used in the assessment of the climate change signal in contrast to RCMs to avoid underestimating the future climate change signal in extreme precipitation, particularly for warm seasons.

Temperature

Regarding the representation of temperature, there is not yet a consensus on the added value in convection-permitting simulations. Prein et al. (2013) and Brisson et al. (2016) attribute improvements in the temperature output to the better resolution of orography. Further the better spatial representation of local atmospheric circulations and land-atmosphere interactions in CPMs are expected to lead to improvements of temperature simulations, particularly in coastal areas (Soares et al., 2022). Ban et al. (2014) found an increasing bias in temperature on the convection-permitting scale in a domain covering the alpine region. In contrast, an improvement of mean temperature was found in Hohenegger et al. (2008) for most of her study area and in investigations by Hackenbruch et al. (2016) over Germany. In addition, Tölle et al. (2018) found added value for temperature extremes. Sangelantoni et al. (2023) highlights the role of soil moisture fluxes, noting that a multi-model ensemble reveals lower latent and higher sensible heat fluxes in CPMs compared to RCMs. This results in drier and hotter heat waves. However, this cannot be generally attributed to an added value in the CPMs.

From an extensive assessment of a multi-model ensemble over Europe, the CORDEX-FPS on convection (Coordinated Regional Downscaling Experiments Flagship Pilot Studies program on convection, Coppola et al., 2018), Soares et al. (2022) conclude that the added value of CPM simulations for maximum and minimum temperatures is limited, and the gain of the high resolution is dependent on the region, season and

model evaluated. The diurnal cycle of temperature is generally found to be improved in CPM compared to RCM simulations (Hohenegger et al., 2008; Ban et al., 2014; Tölle et al., 2018).

The added value of CPM simulations over RCM simulations, beyond the temperature and precipitation parameters, includes the representation of clouds and radiation, local wind systems such as lake and sea breezes, foehn and wind channelling, and the representation of urban land use, reviewed by Lucas-Picher et al. (2021).

Bridging the gap between climate model and practical application

A broader benefit of the very high resolution of the CPM model output is that it enables the derivation of relevant data fields for impact assessment or the direct coupling of the CPM with data-driven impact models. The use of CPM data for impact studies has been demonstrated for hydrological applications, such as river run-off and flooding (Lackmann, 2013; Kay et al., 2015; Lee et al., 2019; Rudd et al., 2019), or flash flood predictions (Reszler et al., 2018; Dougherty and Rasmussen, 2020). Further impact studies tackle the simulation of renewable energy production – mainly wind energy (e.g. Carvalho et al., 2012; Fernández-González et al., 2018), and solar energy (e.g. Jimenez et al., 2016; Losada Carreño et al., 2020). Several CPM-based studies focus on the thermal comfort in cities and the effect of the urban heat island (e.g. Argüeso et al., 2015; Wouters et al., 2017; Ramon et al., 2020). More recently, the representation of the urban environment and the improvement of the urban parametrisation schemes in CPMs have been brought into focus (Langendijk et al., 2024). The wide range of examples gives an insight into how convection-permitting projections have the potential to facilitate tailored impact studies and can help narrow the gap between climate research and the needs of end users.

2.3.3 Convection-permitting ensemble simulations

The increase in resolution in CPM compared to RCM simulations is accompanied by an increase in computational costs. As a rule of thumb, the runtime increases by factor 10 with double the horizontal grid resolution (Kendon et al., 2021). While the convection-permitting scale is already routinely used for weather forecasts, it has only been possible in recent years to model sufficient areas and long enough simulation periods for climate studies. The computational costs are still the limiting factor in the design of CPM model studies (Kendon et al., 2021).

To reduce the computational time to reasonable amounts (Fig. 2.7), CPM projections are generally performed as limited area simulations in which GCM simulations are downscaled in the area of interest. Furthermore, CPM projections are largely limited to decadal or multi-decadal time slices and to single realisations. However, the availability of ensemble projections with multiple realisations is crucial to assess the uncertainty in the projected changes.

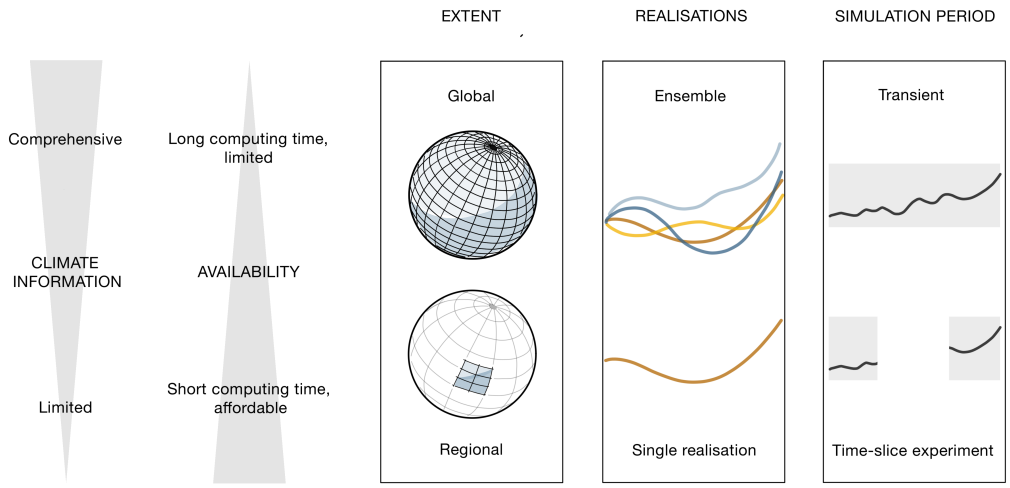

Figure 2.7: The trade-off between comprehensive climate simulation output and computational costs in CPM simulation strategies.

The first ensemble of CPM projections was presented by Kendon et al. (2020) in the UKCP project with 12 members of a perturbed parameter ensemble at 2.2 km resolution over the UK. The first multi-model CPM ensemble simulations have been carried out over Central Europe in the CORDEX-FPS (Coordinated Regional Downscaling Experiments Flagship Pilot Studies program) on convection (Coppola et al., 2018; Pichelli et al., 2021). Here, five different regional climate models were downscaled from selected CMIP5 GCMs under the emission scenario RCP8.5, resulting in an ensemble of 12 members. The projections provide three 10-year time slices (historical, mid-21st century and end of 21st century).

These current ensemble projections of the CPM are all based on simulations of relatively short time slices. However, short time slices limit the analysis because they do not sufficiently sample natural variability, including long-term variability modes such as the North Atlantic and El Niño Southern Oscillations (Lucas-Picher et al., 2021). In addition, simulations of long time periods are a prerequisite for robust statistics, especially when assessing extremes (Kendon et al., 2017).

The first transient ensemble simulations at convection-permitting resolution have recently been performed by Kendon et al. (2023) for the UK. Their analysis of record precipitation events shows that changes in extremes do not follow a smooth trend, highlighting the limitations of time-slice approaches. This demonstrates the potential of transient data and represents a pioneering step towards a more robust analysis of climate change signals. However, the perturbed parameter ensemble used in their study is based on a single global and regional model, and thus does not fully capture the range of model uncertainty. Moreover, the scope of their analysis is limited to the UK. Extending the local results to other regions is vital. Transient multi-model approaches for a more comprehensive exploration of both internal variability, as well as model uncertainty are needed.

In summary, CPMs operating at high resolutions of 1 to 4 km explicitly resolve deep convection, reducing errors associated with traditional convection parametrisation schemes. They represent a significant advancement in the projection of future climate change at local scales, especially for precipitation extremes on short timescales, and provide valuable, tailored climate information to end-users. However, the availability of CPM projections remains limited due to their high computational cost. This scarcity of CPM ensemble projections limits the assessment of uncertainties due to climate variability and model deficiencies, and highlights the need for more ensemble projections to improve understanding of future climate change signals.

2.4 The climate change signal of extreme precipitation

The sixth IPCC assessment report provides strong evidence that climate change significantly impacts extreme precipitation and highlights the complexity of these changes. To contextualize the analysis this section summarises the necessary background information on the quantification of extreme precipitation (Section 2.4.1), and the mechanisms through which global warming influences these events (Section 2.4.2). Then the chapter addresses observed and projected changes in extreme precipitation patterns: The climate change signal based on daily to hourly intensity is discussed in Section 2.4.3 with a focus on the region of Germany and, more broadly, Central Europe. The climate change signal on the precipitation event scale is discussed in Section 2.4.4 with an emphasis on the very high temporal resolution.

2.4.1 Describing extreme precipitation

According to IPCC (2021), an extreme weather event is defined as "an event that is rare at a particular place and time of year". However, there are various approaches to quantifying extreme precipitation, with the method chosen often depending on the purpose of the analysis. Because extreme precipitation is addressed by various disciplines, this can lead to inconsistencies in the definitions and types of rainfall statistics used (Westra et al., 2014). Three commonly used concepts in risk management are extreme precipitation indices including warning levels, return levels and design storm profiles, as described below.

Extreme precipitation indices and warning levels

The simplest form of definition is based on fixed levels of precipitation intensity over a defined period. In Germany, the DWD provides three levels of warnings for heavy precipitation, based on the following thresholds:

- >15 to 25 mm in 1 h or >20 to 35 mm in 6 h (Warning of significant weather, "Markante Wetterwarnung")

- >25 to 40 mm in 1 h or >35 mm to 60 mm in 6 h (Warnings of severe weather, "Unwetterwarnung")
- >40 mm in 1 h or >60 mm in 6 h (Warnings of extreme weather, "Warnung vor extremem Unwetter")

Work by the Expert Team on Climate Change Detection and Indices (ETCCDI) developed a set of standard indices, including the number of heavy precipitation days (>10 mm) and the number of very heavy precipitation days >20 mm (Peterson and Manton, 2008). Further ETCCDI indices tailored to extreme precipitation include the annual maximum 1-day and 5-day precipitation amounts. Building on the ETCCDI indices, Pritchard et al. (2023) developed sub-daily indices together with prospective users. These GSDR-Indices describe precipitation variability and precipitation extremes in terms of intensity, duration, and frequency properties.

Extreme value theory and return levels

In a more general approach, extreme precipitation can be described in terms of probabilities. A commonly used statistical approach to estimate low-probability events and even to analyse the probability of occurrence of events outside the range of observed data are extreme value statistics. Extreme value statistics consider the distribution of events and derive extreme values from the tail of a probability distribution. Based on Coles et al. (2001), the largest independent samples from a fixed distribution will converge to follow the generalized extreme value distribution (GEV), with the cumulative distribution function (CDF), provided in Eq. 2.36.

$$F(x) = \exp\left(-\left(1+\frac{\xi\,(x-\mu)}{\sigma}\right)^{-\frac{1}{\xi}}\right) \tag{2.36}$$

μ is the location parameter, σ is the scale parameter and ξ is the shape parameter.

The case of ξ approaching zero is referred to as the Gumbel distribution (Wilks, 2011). The Gumbel distribution describes data drawn from a tail, where density distribution decays exponentially, and is suitable for datasets that e.g. follow a normal or gamma distribution (Wilks, 2011). The CDF of the Gumbel distribution reads:

$$F(x) = \exp\left(-\exp\left(-\frac{x-\mu}{\sigma}\right)\right) \tag{2.37}$$

The quantiles x of the respective probabilities p can be estimated over the inverted CDF:

$$x_p = \mu + \frac{\sigma}{\xi}\left(\left(-\ln\left(p\right)\right)^{-\xi} - 1\right), \qquad \text{for } \xi \neq 0 \tag{2.38}$$

$$x_p = \mu - \sigma\ln(1-\ln(1-p)), \qquad \text{for } \xi = 0 \tag{2.39}$$

The parameters of the extreme value distribution are usually determined numerically. There are several practical approaches to determining the choice of extreme data to which the distribution is fitted. In the analysis of extreme precipitation, the block maximum approach is commonly used, where the analysis is drawn from the maximum values of successive blocks of a time series, usually years (Wilks, 2011). Another common method is the peaks-over-threshold (POT) approach, where estimation is based on events exceeding a certain threshold, e.g. the 95th percentile of the distribution (Seneviratne et al., 2012). Similar to POT, there are further modified approaches that select the n largest independent values and are referred to as partial duration or partial series data (Wilks, 2011; DWA, 2012).

Extreme precipitation intensity is commonly expressed in terms of a return level (RL) associated with a return period (RP). The RP is typically interpreted to be the average time between the occurrence of precipitation events of that magnitude or greater (Wilks, 2011). The RP is the inverse of the probability p. For example, for annual maximum data, the intensity x_p will have the probability $p = 1 - F(x_p)$ of being exceeded in any given year. x_p with an annual probability of $p = 0.01$ is the RL associated with an RP of RP $= \frac{1}{0.01} = 100$ years, and would be called a 100-year event (Wilks, 2011).

In practical applications, varying durations of precipitation spells are of interest. Therefore, the evaluation is carried out over different sampling time windows of the precipitation time series, referred to as duration or event duration (ED). It is important to note that ED does not correspond to the actual duration of a precipitation event but to the sampling period of the precipitation intensity. The results are typically presented as intensity-duration-frequency (IDF) curves, which show the relationship between RLs for different EDs and RPs (Fig. 2.8). IDF curves are widely applied in engineering applications and for stormwater management (e.g. Martel et al., 2021).

Design storm profiles

For several engineering applications, it is not sufficient to quantify extreme precipitation by intensity over a fixed time window; the temporal profile of a precipitation event, also known as a hyetograph, is also required. This profile is central to the design of urban drainage systems, stormwater infrastructure and flood management. Sub-hourly resolution for the temporal profile is necessary to capture precipitation peaks and effectively drive impact models (Markolf et al., 2021; Peleg et al., 2024).

The standardised event profiles for use in the design of a hydrologic system are referred to as design storm profiles (Chow et al., 1988). Different types of design storm profile approaches exist today and the method is often based on available guidelines, often at a national level. They can be derived either from observed event profiles or derived synthetically from IDF curves, generally constructed so that the intensities correspond to the rainfall intensities in the IDF curve. An overview of the different concepts is given in Chow et al. (1988). A commonly used method in Germany is the

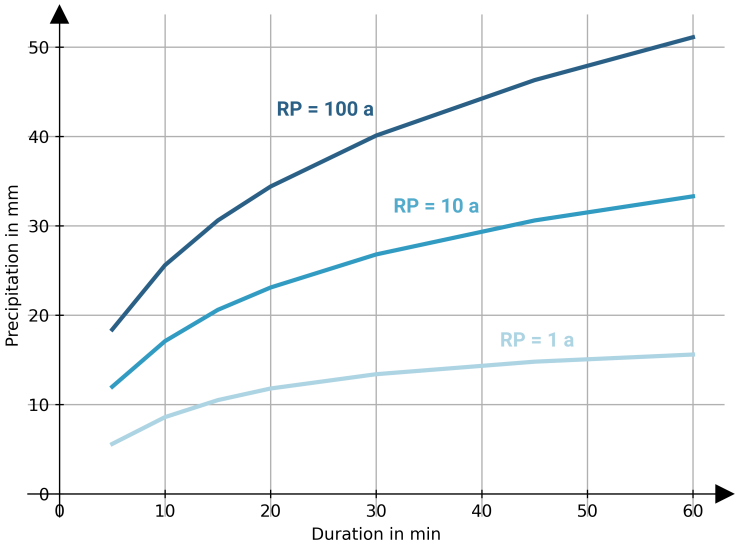

Figure 2.8: IDF curve constructed from the heavy precipitation dataset KOSTRA (see Chapter 4, for details of the dataset) for the example grid point of Karlsruhe (longitude 8.39, latitude 49.02).

Euler Typ II design storm (Fig. 2.9). This front-loaded profile – a profile where the bulk of the precipitation occurs towards the beginning of the event – is recommended by the German Association for Water, Wastewater and Waste (DWA-A 118E) and is widely used in Germany and Austria (Krvavica and Rubinić, 2020). The profile is similar to the internationally applied Chicago Design Storm (Keifer and Chu, 1957). Centred design storm profiles are used in the UK, with variations for summer and winter storms (Villalobos Herrera et al., 2023a).

There are indications that hyetographs derived from IDF curves overestimate peak discharge and flooding, compared to observed hyetographs (Krvavica and Rubinić, 2020; Balbastre-Soldevila et al., 2019). In addition to total precipitation depth, the characteristics of peak intensity and timing of the peak intensity are identified as key features of the design profile that also influence the hydrological response (Ball, 1994; Dullo et al., 2017). Recent observational analysis in the UK has shown that real rainstorms have a number of different temporal profiles - front-loaded, centred and back-loaded, the frequency of which depends on the duration of the event (Villalobos Herrera et al., 2023a). A step towards assessing uncertainty has been taken in Australia, where the latest iteration of the Australian Rainfall and Runoff Guidelines avoids synthetic profiles and instead uses a range of observed profiles (Ball et al., 2019).

In summary, several methods are available to quantify extreme rainfall. The common approaches are extreme indices or statistical methods based on extreme value statistics. The latter associates extreme RLs with an RP and provides an improved estimation of very rare events. Although regularly applied in climate science, IDF curves alone do not fully meet practical needs and for the assessment of the hydrological response in impact

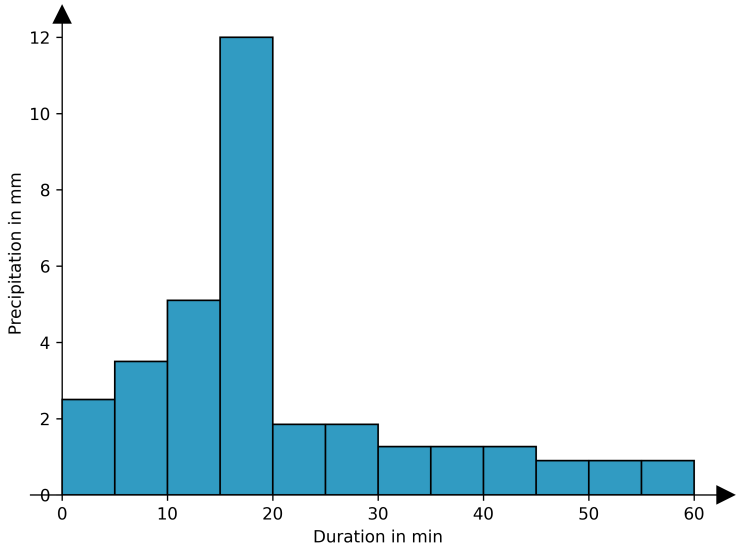

Figure 2.9: Euler Typ II design storm profile according to the guideline DWA-A 118E, constructed from the heavy precipitation dataset KOSTRA (details in Chapter 4) for the return level of 10 years at the example grid point of Karlsruhe (longitude 8.39, latitude 49.02).

models, high-resolution temporal precipitation profiles are essential. So-called design storm profiles provide standardised profiles of extreme events and are a well-established method in practical application, though their use is not without controversy.

2.4.2 Climate change drivers of extreme precipitation

Global warming affects extreme precipitation primarily through two processes: increases in the availability of moisture in the atmosphere with increasing temperature, and changes in the frequency of atmospheric circulation patterns and the mechanisms that generate precipitation (Westra et al., 2014). While the former is based on thermodynamics, the latter can be summarised as a dynamic contribution. The two mechanisms are outlined below.

Thermodynamic component

A theoretical upper limit to the water-holding capacity of the atmosphere as a function of temperature is provided by the Clausius-Clapeyron relation (details are in Section 2.1.1). The saturation water vapour pressure increases approximately exponentially by ~7 % per degree at 0 °C and ~6 % per degree at 24 °C, referred to as the CC-rate. Assuming a constant relative humidity in a warming world, this would lead to an increase in the actual precipitable water to scale with the CC-rate (Westra et al., 2014). If we anticipate that the most intense events are mainly determined by precipitable water, the intensity of extremes is expected to increase with the CC-rate over large regions (Allen and Ingram, 2002).

The assumption of CC scaling of extreme precipitation is based on the constraints that relative humidity remains relatively constant, that extreme precipitation is mainly

determined by the precipitable water in the atmosphere, and that atmospheric circulation does not change significantly with global warming (Lenderink and Van Meijgaard, 2008). However, dynamic changes can either dampen or amplify the change signal of extreme precipitation with global warming, leading to regionally significant deviations from the global trend determined by thermodynamics (Pfahl et al., 2017).

Dynamic contribution

Dynamic contributions range from large-scale atmospheric circulation to local cloud dynamics (Westra et al., 2014; Fowler et al., 2021a). An overview is given below.

Large-scale circulation Water vapour transport in the atmosphere primarily occurs through advection, driven mostly by large-scale atmospheric circulation (Vallis, 2017). With altering large-scale circulation patterns, climate change affects the frequency and intensity of synoptic and subsynoptic phenomena, including extratropical cyclones, fronts, mesoscale-convective systems and thunderstorms (IPCC, 2021). However, the actual changes to the large-scale circulation patterns are not as well understood as the thermodynamic components.

Relevant for the mid-latitudes, are for example projected changes to the Hadley cell. A weakening and broadening of the Hadley cell with a poleward movement of tropical dry zones and mid-latitude jets are expected (IPCC, 2021). This is in agreement with projected future trends in GCM simulations with high-end emission scenarios (Gillett and Fyfe, 2013), but projections are highly model-dependent and effects depend strongly on the region (Stephenson et al., 2006; McKenna and Maycock, 2022). Moreover, it is still unclear to what extent a shift of the jet is associated with changes in the total storm track activity (Seneviratne et al., 2012; Shaw et al., 2016).

Dynamic responses and feedbacks within storms Furthermore, extreme precipitation is altered by dynamic responses and feedbacks within convective storms. Warming leads to an increase in CAPE, which is associated with enhanced convection (Romps, 2016; Barbero et al., 2019). The resulting increased latent heat release in a convective cloud would therefore enhance the updraft motions in the cloud, causing more air and moisture from the surrounding environment to converge into the cloud (Trenberth et al., 2003). Stronger cloud feedback has been suggested as one way of inducing an increase in precipitation above the CC-rate (Loriaux et al., 2013; Westra et al., 2014).

Other factors that influence storm dynamics and may be altered by climate change include entrainment, cold pool formation, depth of convection, wind shear, and cloud organization (Fowler et al., 2021a). The effects are expected to reach down to the microscale and affect cloud microphysics, particularly for ice and mixed-phase processes (Singh and O'Gorman, 2014; Fowler et al., 2021a). A higher proportion of graupel and hail in the cloud is expected with more intense convection, which can increase downdraft velocities and precipitation rates (Fowler et al., 2021a).

In summary, an interplay of thermodynamic and dynamic contributions determines the effects of global warming on extreme precipitation. While the thermodynamic component leads to an overall increase of the available moisture per degree temperature increase, following the CC-rate of 6-7 %, dynamics lead to regionally significant deviations from the CC-rate. The dynamic contribution includes changes to atmospheric circulation patterns, storm dynamics, and cloud microphysics and the projections are uncertain.

2.4.3 The observed and modelled climate change signal of extreme precipitation intensities in Central Europe

Observation

Over the past decade, there has been growing evidence from long-term observational time series, that daily extreme precipitation intensities have increased over Europe (IPCC, 2021). A significant increase in daily annual maximum precipitation derived from European station data was found by Sun et al. (2021); Westra et al. (2013); Madsen et al. (2009). For Central Europe, Zeder and Fischer (2020) derive scaling of daily annual maximum in the range of CC-scaling with Northern Hemisphere Temperature. Several studies report stronger changes for longer return periods compared to moderate extremes (van den Besselaar et al., 2012; Myhre et al., 2019; Madsen et al., 2009). Regional and seasonal variability is emphasised (e.g. Willems, 2013; van den Besselaar et al., 2012).

Less certain is the development of extreme precipitation on the sub-daily scale (IPCC, 2021). This is mainly due to the limited availability of long time series with good accuracy, which is required to analyse a robust change signal due to the strong natural variability (Willems, 2013). Several regional studies have explored the relationship between sub-hourly precipitation intensity and temperature or humidity coinciding with the event to derive so-called apparent scaling rates. Apparent scaling of short, hourly precipitation intensities is found to be higher than for daily precipitation, though mostly consistent with CC-scaling over regions (Ali et al., 2021). However, (Lenderink and Van Meijgaard, 2008) found apparent scaling to exceed the CC-scaling rate. Further studies in Europe support the finding of apparent super-CC scaling (Lenderink and Van Meijgaard, 2010; Berg and Haerter, 2013; Loriaux et al., 2013; Formayer and Fritz, 2016; Da Silva and Haerter, 2024). Super-CC scaling is likely to be extended to even shorter, sub-hourly timescales (Loriaux et al., 2013). Super-CC scaling of extreme precipitation is argued to originate from a change in the type of rainfall (Haerter and Berg, 2009; Berg and Haerter, 2013; Da Silva and Haerter, 2024): While precipitation extremes are predominantly stratiform at low temperatures, at high temperatures convective extremes become dominant. In the transition zone of stratiform – lower intensities – to convective events with generally higher intensities, super-CC scaling is expected, even if each rainfall type scales with CC-rate (Fig. 2.10). Although still under debate (Moseley et al., 2013; Berg et al., 2013; Lenderink et al., 2017), super-CC scaling seems to be mainly attributed to the shift in rain type (Da Silva and Haerter, 2024).

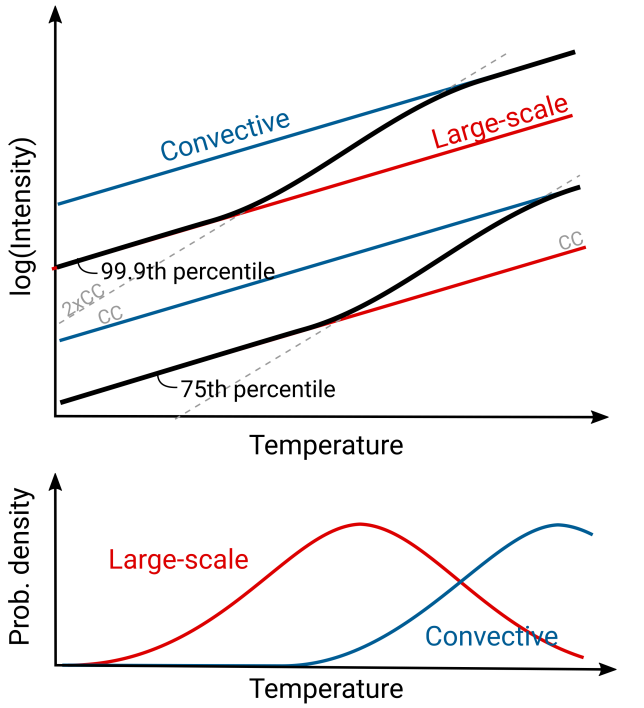

Figure 2.10: Apparent super-CC scaling due to a shift in the precipitation type, based on Haerter and Berg (2009). The lower plot shows the weighting functions for large-scale/stratiform (red) and convective (blue) precipitation as a function of temperature. In the upper panel, the corresponding 99.9th and 75th sub-daily precipitation intensity percentile of large-scale (red), convective (blue) and total precipitation (black) is shown. Double CC-scaling is shown in dashed grey.

With many storms in Central Europe involving a combination of precipitation types, this super-CC shift is vital for evaluating future extreme precipitation (Da Silva and Haerter, 2024). However, it is uncertain to what extent the observed apparent scaling will translate into a climate change signal (Fowler et al., 2021a). In particular, dynamic changes may limit extrapolation of the observed apparent scaling rates of short-duration intensities into a warmer future (Chan et al., 2016a; Pfahl et al., 2017; Zeder and Fischer, 2020).

Convection-permitting model projections

To assess the transfer of observed scaling to future climate, projections are inevitably required. As discussed in Section 2.3, CPMs provide a more realistic characterisation of precipitation extremes compared to coarser RCMs and were found to reduce the model uncertainty in the climate change signal (Chan et al., 2014a; Kendon et al., 2014; Fosser et al., 2024). The following results on the projection of precipitation extremes are therefore limited to CPM studies.

In general, the dynamical downscaling of GCM projections to the convection-permitting scale supports the observed results in Central Europe of intensification of rainfall extremes in frequency and intensity with global warming (IPCC, 2021). Un-

certainty in the magnitude and regional differences are detected. Whereas Kendon et al. (2014) and Lenderink et al. (2021) find super-CC scaling, Ban et al. (2015), Ban et al. (2020), and Hodnebrog et al. (2019) find scaling approaching the CC-rate. Regional differences in the climate change signal across Europe are highlighted e.g. by Hodnebrog et al. (2019); Pichelli et al. (2021); Fosser et al. (2024), with Pichelli et al. (2021), showing an increase in extreme precipitation mostly in the alpine region and northwards. Moreover, CPM studies generally find higher intensification for the most extreme events compared to moderate extremes (Helsen et al., 2020; Lenderink et al., 2021; Hodnebrog et al., 2019).

Due to their high computational cost, CPM projections are typically based on time slices of decadal duration (Ban et al., 2015, 2020; Pichelli et al., 2021; Hodnebrog et al., 2019; Lenderink et al., 2021) to longer, multi-decadal time slices (Kendon et al., 2014; Saeed et al., 2016). Ensemble approaches are rarely considered (Helsen et al., 2020; Pichelli et al., 2021). Indeed, when analysing record precipitation events in the first transient CPM ensemble for the UK, the authors emphasise that changes in extremes are not realised in a smooth trend, highlighting the limitations of time-slice approaches due to internal variability (Kendon et al., 2023). Nevertheless, it is expected that the perturbed parameter ensemble based on a single global and regional model will still not sample the full range of model uncertainty (Tebaldi and Knutti, 2007; Caillaud et al., 2024).

In summary, the trend of increasing precipitation intensities and frequencies with climate change is supported by observations in Central Europe. CPMs were shown to adequately represent extreme precipitation changes with temperature. They reinforce that the change signal is higher for the most extreme events compared to moderate extreme events. There is no consensus on the magnitude, with climate scaling generally simulated to be similar to or higher than the CC-scaling rate with regional variations. The previous limitation of time slice experiments and often single simulation realisations limits the analysis due to sensitivity to internal variability and there is a lack of uncertainty estimation. The recent development towards transient CPM data offers promising derivation of more robust trends.

2.4.4 The climate change signal of precipitation event profiles

Although multiple studies predict the increase of precipitation extremes with temperature, little is known about how these intensity increases will impact the temporal characteristics of precipitation events. Indeed, the hydrological response to a precipitation event depends not only on the total volume of rainfall but also on the duration over which it occurs and its temporal distribution. The profile characteristics of peak intensity and the timing of peak intensity, have been identified to modify the peak runoff rates and their timing, as well as runoff volumes (Ball, 1994; Lambourne and Stephenson, 1987; Ochoa-Rodriguez et al., 2015; Cristiano et al., 2017; Dullo et al., 2017; Hettiarachchi et al., 2018; Pochwat et al., 2017). This is especially true for small and

urban catchments, which are more sensitive to changes in rainstorm profiles (Lambourne and Stephenson, 1987; Cristiano et al., 2017; Ochoa-Rodriguez et al., 2015). Despite the critical importance of linking precipitation volume to its temporal profile, most analyses of extreme precipitation rely on fixed-duration periods, often daily or hourly precipitation sums. This fixed-duration approach imposes artificial constraints on rainstorm duration and therefore fails to capture the full range of precipitation characteristics that drive hydrological impacts. Potential changes in the temporal pattern of precipitation with increasing temperature aspects have not been sufficiently addressed in climate change studies (Trenberth et al., 2003; Visser et al., 2023).

Recent studies in regions with long-term data availability have started to explore event-based analyses of precipitation events under a changing climate. The characteristics of the temporal profile of interest generally fall into two categories: the steepness or peakedness of the profile and the timing of the bulk precipitation. Although spatial variability also plays an important role in hydrological responses, this aspect is beyond the scope of this work and will not be discussed in depth here.

Profile steepness

First findings of a less uniform temporal pattern of precipitation within precipitation events were derived by Wasko et al. (2015) based on 6-min station recordings of precipitation in Australia. Sub-dividing single precipitation events in 5 equal-duration embedded bursts, scaling with coinciding temperatures revealed more intense peak precipitation and weaker precipitation of off-peak intensities. Their finding of a steeper or "peakier" event profile with temperature is most pronounced in the tropics. Long et al. (2021) confirm the finding of a steeper or peakier event profile with temperature studying station data in China, and show a concentration of precipitation intensity with temperature in both space and time within a range of 5 to 24 °C and plateauing at higher temperatures. Also in the UK, intensification of peak rainfall fraction with temperatures is confirmed in the analysis of 28 gauges with a 15-min resolution (Fadhel et al., 2018).

To our best knowledge the first attempt to globally assess extreme precipitation profile structure was done by Ghanghas et al. (2024). The study is based on rather coarse satellite data and a temporal resolution of only 30 min. Introducing a metric of the combined spatio-temporal characteristics of extreme precipitation events they find "spatio-temporally peakier" storms with higher temperature – meaning intense precipitation bursts over a smaller area and shorter duration – mainly in the tropics as well as in parts of western Europe (including England, France, Portugal, and Spain), in parts of the midwestern United States and northern Australia. However, other areas in the Northern and Southern temperate regions – including parts of Central Europe – observe the opposite trend with storms generally tending to expand in space and time.

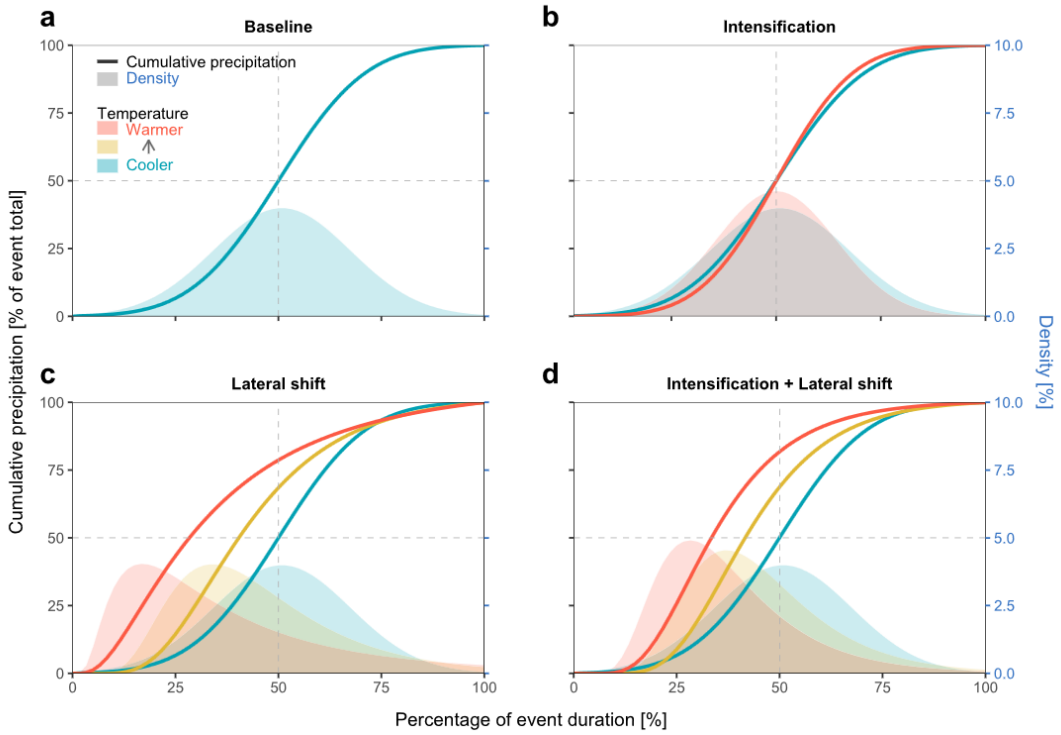

Figure 2.11: Potential modes of climate change signal to the temporal precipitation profile (reprinted from Visser et al., 2023, ©American Meteorological Society. Used with permission.).

Timing of the bulk precipitation

A systematic study of the climate change signal of the timing of the bulk precipitation or "event loading" of precipitation profiles in climate change was done by Visser et al. (2023). Introducing the D50 measure – defined as the percentage of event duration after which 50% of the rain volume has fallen – they analyse the changes in event loading of extreme storms in Australia. Profiting from long sub-hourly time series, they derive not only positive apparent scaling relations between coinciding temperature and front-loading of events but can derive a climate change signal with a significant increase in front-loading per decade.

The global analysis in Ghanghas et al. (2024) confirms an increase in front-loaded storms in the tropics and southern temperate regions with higher temperatures. Conversely, temperate regions, especially in the northern temperate regions including Central Europe show a slight tendency toward more back-loading with coinciding temperature in extreme precipitation events. Irrespective of geographical location and consistent with Visser et al. (2023)'s findings for tropical regions in Australia, Ghanghas et al. (2024) show higher sensitivity of front-loading with temperature for shorter duration events, with maximum for events of 6 to 12 h.

Based on Visser et al. (2023), Fig. 2.11 visualizes the potential modes of change of how the two parameters, profile steepness and timing of the peak intensity, impact the

temporal precipitation profile. The limited studies available point out regional differences and indicate that dominant precipitation mechanisms and geographic locations play a key role in how storm structures change. Hypothesised by Ghanghas et al. (2024) and Visser et al. (2023), the observed changes in extreme precipitation event profiles could be an indication of modifications in the characteristics of a typical storm event at increased temperatures: With increasing temperature, a precipitation event tends to exhibit increased convective properties, resulting in enhanced peak intensity and an increasingly asymmetric precipitation profile.

Modelling of sub-hourly precipitation

One reason for this research gap is that the analysis of precipitation profiles relies on the limited availability of high spatial and temporal resolution precipitation time series over long periods. While global advancements have improved access to observed hourly-scale rainfall data (Lewis et al., 2019), enabling better analysis of high-intensity events, this resolution is still insufficient for capturing the full temporal evolution of short, intense storms. Sub-hourly data remains scarce and is typically limited to regional observational networks, often on the national level. Long, multi-decadal time series are rare.

High-resolution model projections on the sub-hourly scale are a promising tool to overcome the shortcomings of limited data availability of long observational periods and limited applicability of apparent scaling rates from observations to derive the climate change signal of precipitation event characteristics. However, the representation of the sub-hourly scale in climate models is not well understood yet.

First CPM simulations on the sub-hourly scale exist and provide promising results: Chan et al. (2016b) project an intensification of sub-hourly rainfall with global warming for the UK but the study lacks evaluation of the model due to missing adequate observational data. Meredith et al. (2020) performed multi-decadal CPM simulations over Catalonia and find the bias in sub-hourly precipitation similar to hourly precipitation. 10 years-long simulations of current and future climates in Vergara-Temprado et al. (2021) for a domain over the Alps can capture the observed percentiles of extreme sub-hourly precipitation. An event-based analysis by Purr et al. (2021) for Germany shows that sub-hourly precipitation in a convection-permitting downscaling of the GCM EC-EARTH adequately reproduces convective cell characteristics including precipitation sum, area, and peak intensity. The derived climate change signal comprises a shift towards larger and more intense events, increasing the precipitation sums per cell. Existing studies reveal the limited pool of sub-hourly model data as well as a lack in multi-model comparison, and to date no analysis of temporal profile characteristics.

In summary, sub-hourly precipitation and the temporal profile of a precipitation event have an impact on the hydrological response to an extreme event. However, research

on a climate change signal of the temporal event profile is still in its infancy. Early studies hypothesise a trend towards a stronger peakedness and more front-loaded events in a warmer climate. The analysis is limited by the scarcity of high temporal resolution precipitation data. To address future risks, it is important to test how well climate models deal with these features, and the first CPM studies at the sub-hourly scale show a promising representation of the sub-hourly features of precipitation events.

3 | RESEARCH QUESTIONS

The overall aim of this work is to improve the current understanding of the representation of precipitation extremes in CPMs as well as to pinpoint the possible changes to extreme precipitation in a warmer future climate over Germany, with an emphasis on the high temporal resolution. The novel high-resolution 4-member KIT-KLIWA ensemble is the basis of our analysis. It provides the first transient CPM ensemble projections for southern Germany and the Alpine region for the period 1971-2100. Furthermore, this dataset is a unique source of sub-hourly precipitation with a resolution of 5 min. The following section outlines the research gaps addressed by the thesis and formulates the four corresponding research questions to be answered in the thesis.

3.1 The climate change signal of precipitation return levels

Multiple studies have addressed the intensification of extreme precipitation in Central Europe and Germany (Chapter 2). The scientific literature underscores the complexity of the local changes, including strong regional differences (Hodnebrog et al., 2019; Pichelli et al., 2021), larger changes for the most extreme events compared to moderate extremes (Hodnebrog et al., 2019; Helsen et al., 2020; Lenderink et al., 2021), and enhanced intensification for short-duration precipitation intensities – partially above the CC-rate (Loriaux et al., 2013; Kendon et al., 2014; Lenderink et al., 2021). These changes imply a strong need to update infrastructure design strategies to account for the intensification of extreme precipitation.

However, uncertainty in the magnitude of the climate change signal remains high, especially at the short, sub-daily timescale. This is partly because long observational time series are rare and the ability to infer a future climate change signal of precipitation extremes from day-to-day variability is limited. Climate models of coarse resolution are deficient in representing the key processes associated with precipitation extremes (Kendon et al., 2014). High-resolution modelling improves the reliability of projections of extreme precipitation but data availability is limited due to the high computational costs. Missing transient simulation data enhances uncertainties in the projections of extreme precipitation. Past research has mostly relied on time slice approaches that are

sensitive to the internal variability of the climate system. So far, transient ensemble simulations of very high resolution are only available in the UK (Kendon et al., 2023). However, the UKCP perturbed parameter ensemble is expected to not sample the whole range of model uncertainty (Tebaldi and Knutti, 2007) and to our knowledge to date, no assessment of transient multi-GCM ensemble is available.

In addition, a variety of approaches have been used in the scientific literature to assess changes to extreme precipitation in Europe, including assessments of changes in frequency, changes in intensity of extremes above different thresholds, or the use of different extreme value statistics. This not only limits the comparability of the different results but also makes it difficult to translate the valuable information into practical applications (Fowler et al., 2021b).

We address the research gap of the limitations of high-resolution projections in the assessment of climate change signals by using the novel KIT-KLIWA ensemble for Germany. To our knowledge, this is the first analysis of a transient multi-GCM ensemble and the first transient CPM ensemble over Germany. This permits assessing the uncertainty in the change signals due to internal variability, which has been a limitation of previous time-slice approaches for Germany.

Our aim is to provide climate change signals that are as close as possible to the practical needs of climate adaptation. Therefore, we base this analysis on methods originally developed for practical applications in the German guideline DWA (2012). In addition, the analysis covers a wide range of precipitation extremes at different scales: from hourly to 3-day duration and for return periods from 1 year to 100 years. Specifically, we address the central research question:

> **Research question 1: How do precipitation return levels evolve under global warming as a function of duration and return period?**

The analysis addresses this research question in three sequential steps, aligned with the following research objectives:

a) Evaluation of return levels in CPM historical simulations with observations and observation-based precipitation risk products.

b) Assessment of climate change factors for return levels of different durations and return periods from the transient projection period.

c) Quantification of uncertainties of the derived climate change signal.

This analysis is the subject of Chapter 5. The chapter is based on Hundhausen et al. (2024).

3.2 Temporal precipitation profiles in CPM

A key finding from the first part of the analysis on changes in return levels (Chapter 5) is that intensities over short temporal aggregations are expected to exhibit the strongest

changes in a future climate. Accordingly, we further focus on short-scale precipitation. There is little knowledge on the sub-hourly scale in CPM and ensemble evaluations are missing (Chapter 2, Chan et al., 2016b; Meredith et al., 2020; Vergara-Temprado et al., 2021; Purr et al., 2021). Studies tackling the projected precipitation characteristics beyond intensity on sub-hourly resolution are rare (Purr et al., 2021).

In this second part of the analysis in the thesis, we therefore evaluate the unique 5-min resolution CPM dataset in the KIT-KLIWA ensemble. For three ensemble members, precipitation of a temporal resolution down to 5-min during the historical simulations (1971-2000) is compared with the dense station and radar observational network over Germany. An event-based analysis approach for the characterization of event profiles is developed and the ability of the ensemble to reproduce precipitation event profile characteristics is tested.

The following research question is central to the analysis:

> **Research question 2: How well does the CPM ensemble reproduce the temporal profiles of extreme precipitation events compared to observations?**

The analysis approaches the research question in three steps:

a) Assessment of the 5-min precipitation frequencies in the CPM historical simulations evaluated with station and radar observations.

b) Development of a precipitation event-based analysis method based on 5-min precipitation time series.

c) Characterisation of extreme precipitation events in the historical CPM simulations and assessment of bias by comparison with observational data.

The analysis is the subject of Chapter 6. The chapter is based on Hundhausen et al. (2025).

The analysis in Chapter 6 provides an evaluation of the representation of precipitation events in the CPM ensemble. The event-based method is the basis for the following analysis: The event-based approach is applied in a more general way to study the projected changes in event climatology in Chapter 7, and to study the scaling of precipitation characteristics in Chapter 8.

3.3 The climate change impact on the climatology of precipitation events

Event-based assessments of precipitation intensity changes in Europe in CPM were previously performed (e.g. Kendon et al., 2014; Kahraman et al., 2021; Fosser et al.,

2020; Müller et al., 2023; Purr et al., 2021). However, the analysis is in general based on a temporal resolution of 1 h. This constrains the accuracy of the output, especially for the assessment of short events. To our knowledge, the only sub-hourly event-based CPM analysis based on multi-decadal projections was done in Purr et al. (2021) using a Lagrangian cell tracking scheme. The analysis is based on a single model realization and no consideration of seasonality was made.

To advance the understanding of the event climatology of precipitation events, we apply the event-based analysis method to the 5-min projection data. The analysis addresses the research question:

> **Research question 3: What is the projected climate change signal for the frequency of precipitation events and how does the climate change signal manifest seasonally?**

The research question is addressed in two steps:

a) Evaluation of mean intensity in the ensemble in the historical CPM simulations and projection of the climate change signal of the mean event intensity with a focus on record-breaking events.

b) Assessment of the seasonality of the climate change signal.

The analysis is the subject of Chapter 7. The chapter is based on the article Hundhausen et al. (2024 – in preparation for re-submission).

3.4 The scaling relation of event profile characteristics

In the final analysis, we zoom in on the temporal profile and assess how it is affected by global warming. Studies of the temporal profile changes due to warming are in their infancy (Visser et al., 2023; Ghanghas et al., 2024) and to our knowledge not available for Germany. This contrasts with the need to quantify potential changes within the temporal profiles of extreme precipitation events as a basis for how hydrological applications should accommodate the changes induced by a warming climate.

We address this gap with an investigation of the profile characteristics 5-min peak intensity (Imax), the 1-h peak intensity (I1h) and mean event intensity (Imean), and the timing of the bulk precipitation, parametrised over D50. Specifically, we ask the research question:

> **Research question 4: How do the precipitation event profile characteristics Imax, I1h, Imean, and D50 depend on temperature and does this apparent scaling relationship translate into a climate change signal?**

We approach the topic in three steps:

a) Evaluation of the apparent scaling rates for Imax, I1h, Imean, and D50 in the historical CPM simulations.

b) Comparison of the established apparent scaling relations in the historical time slice with the apparent scaling rates in the future time slice to test whether the relationships hold in a warmer future.

c) Assessment of the climate change signal of Imax, I1h, Imean, and D50 in the CPM projection.

The analysis is the subject of Chapter 8.

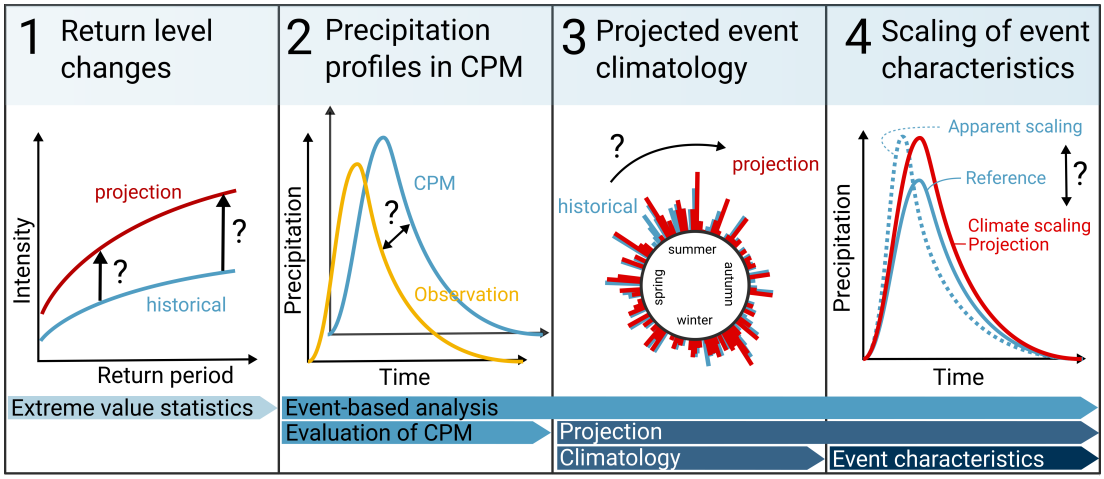

Figure 3.1: Schematic overview of the research questions posed in the thesis.

In this thesis (Fig. 3.1), we transition from a statistical description of extreme precipitation based on intensities over fixed durations (Topic 1: Return Level Changes), to an event-based analysis of extreme precipitation (Topic 2: Event profiles in CPM). Utilizing the event-based analysis method, we zoom into various aspects of the climate change signal on precipitation events, examining changes in the climatology of rainfall events (Topic 3) and the scaling of temporal event profile characteristics (Topic 4).

Building on these four steps, the analysis of the novel KIT-KLIWA ensemble improves our scientific understanding of how precipitation extremes are represented in CPMs and provides insights into future climate change signals over Germany. With a focus on high temporal resolution and an event-based approach, the analysis advances the use of CPMs for sub-hourly precipitation and provides a detailed understanding of future climate change signals of precipitation at the event scale.

4 | DATA

The analysis in the thesis is based on the KIT-KLIWA ensemble. The simulations have been generated in the context of the project KLIWA (Klimaveränderungen und Konsequenzen für die Wasserwirtschaft) and extended within the project ISAP (Integrative urban-regional adaptation strategies in a polycentric growth region: Model region Stuttgart). This chapter describes the simulation ensemble. Further, the observational reference data is presented.

The chapter reuses parts of the publications Hundhausen et al. (2023), licensed under a Creative Commons Attribution 4.0 License, and Hundhausen et al. (2024):

> Hundhausen, M., H. Feldmann, N. Laube & J. G. Pinto (2023). Future heat extremes and impacts in a convection-permitting climate ensemble over Germany. Natural Hazards and Earth System Sciences, 23(8), 2873-2893, doi: 10.5194/nhess-23-2873-2023.
>
> Hundhausen, M., H. Feldmann, R. Kohlhepp, & J. G. Pinto (2024). Climate change signals of extreme precipitation return levels for Germany in a transient convection-permitting simulation ensemble. International Journal of Climatology, 44(5), 1454-1471, doi: 10.1002/joc.8393.

4.1 The KIT-KLIWA ensemble

4.1.1 The regional climate model COSMO-CLM

The convection-permitting climate projections are simulated with the climate model COSMO-CLM (COnsortium for Small-scale MOdelling in CLimate Mode) of version COSMO5.0-CLM9 (Rockel et al., 2008). COSMO-CLM originates from the German weather service forecast model COSMO (Baldauf et al., 2011), which is a three-dimensional, non-hydrostatic, fully compressible numerical model for the atmosphere including a multi-layer soil–vegetation transfer model TERRA-ML (Schrodin and Heise, 2001). The model uses a radiative transfer scheme based on Ritter and Geleyn (1992), the convection parameterisation of Tiedtke (1989) and solves the vertical

turbulent diffusion with the prognostic TKE scheme from Raschendorfer (2001). The physical parameterisation is described in further detail by Doms et al. (2013) and the dynamics and numerics by Doms and Baldauf (2013).

COSMO-CLM has been previously applied in multiple studies over different CORDEX domains (Sørland et al., 2021) and on the kilometre scale within the CORDEX Flagship Pilot Study on Convection (Ban et al., 2021; Pichelli et al., 2021). The source code of the COSMO-CLM is available for scientific purposes after registering with the CLM community[1].

4.1.2 Setup

Boundary conditions for the downscaling in the KIT-KLIWA ensemble are projections of four GCMs from the CMIP5 generation: CNRM-CM5, MPI-ESM-LR, EC-EARTH, and HadGEM2-ES. The global simulations are based on the emission scenario RCP8.5. The RCP (Representative Concentration Pathway) scenarios are defined over time series of greenhouse gas emissions, aerosol emissions, and land use-pattern (Van Vuuren et al., 2011; IPCC, 2021). They are labelled by the approximate additional radiative forcing reached at the year 2100 compared to the pre-industrial values from 1850. The additional radiative forcing is 8.5 W/m^2 for RCP8.5. RCP8.5 is a high emissions scenario in the absence of policies to combat climate change, leading to continued and sustained growth in atmospheric greenhouse gas concentrations (IPCC, 2021). Although the likelihood of high emissions scenarios is considered low in light of recent developments in the energy sector, the simulated global warming based on the high-emission scenario cannot be ruled out (IPCC, 2021).

The GCMs downscaled in the KIT-KLIWA ensemble were selected to cover a range of climate sensitivities (Nijsse et al., 2020). The climate sensitivity is parametrised over the equilibrium climate sensitivity (ECS) which is defined as the global mean surface air temperature increase that results from a doubling of atmospheric CO_2. The ECS in the downscaled GCMs ranges from 3.28 °C (lowest ECS in CNRM-CM5) to 4.64 °C (highest ECS in HadGEM2-ES). The overview of the ECSs in the ensemble is provided in Table 4.1. The CMIP5 driving data are publicly available at World Data Center for Climate (WDCC) at Deutsches Klimarechenzentrum (DKRZ). The realisations used for the downscaling and the according references are provided in Table 4.1. In addition to the four ensemble members driven by the GCMs, an evaluation simulation was carried out, by downscaling of the reanalysis dataset ERA40 (Uppala et al., 2005) over the period 1971–2000 (see Hundhausen et al., 2023), which is not analysed within this thesis.

The downscaling was performed in a three-step nesting approach (Fig. 4.1). Each nesting step was calculated on a grid with rotated geographical coordinates. The first nest is centred over Europe with a horizontal grid resolution of 0.44 ° (approximately 50 km). An intermediate nest is over Central Europe with a grid resolution of 0.0625 °

[1]CLM community: https://www.clm-community.eu/, last accessed September 2024

Table 4.1: Overview of the CMIP5 GCMs downscaled in the KIT-KLIWA ensemble.

GCM & realisation	ECS	Reference historical	Reference RCP8.5
CNRM-CM5, r1i1p1	3.28 °C	Sénési et al. (2014a)	Sénési et al. (2014b)
MPI-ESM-LR, r1i1p1	3.66 °C	Giorgetta et al. (2012a)	Giorgetta et al. (2012b)
EC-EARTH, r12i1p1	4.18 °C	EC-Earth Consortium (EC-Earth) (2014a)	EC-Earth Consortium (EC-Earth) (2014b)
HadGEM2-ES, r1i1p1	4.64 °C	Jones et al. (2014)	Sanderson et al. (2014)

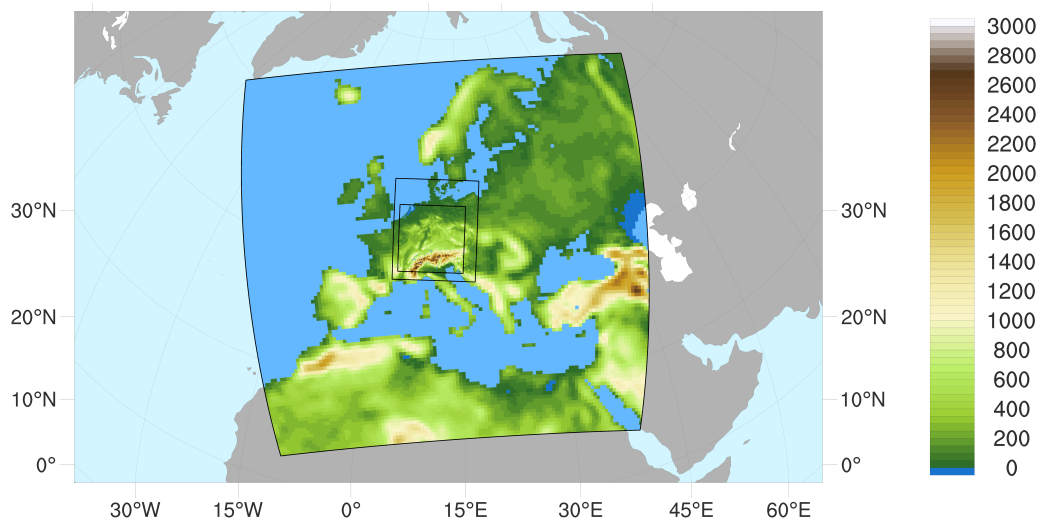

Figure 4.1: Three nesting levels of the KIT-KLIWA simulation: outer 50 km grid, second 7 km grid and final 2.8 km convection-permitting domain.

(7 km) resolution, and an inner nest encompasses the area of central and southern Germany and the Alpine area with a resolution of 0.025 ° (2.8 km). The first two coarser nests are calculated over a convection-parametrised RCM simulation with COSMO-CLM using the Tiedtke convection scheme (Tiedtke, 1989). The model versions for these coarser simulations are sub-versions of COSMO5.0-CLM (COSMO5.0-CLM9 and COSMO5.0-CLM3) due to the available versions at the time of the calculation of the simulation. The inner convection-permitting simulation is done with the COSMO-CLM version COSMO5.0-CLM9. The convection parametrisation is only used for shallow convection as in Hackenbruch et al. (2016). The setup of the convection-permitting model run is based on the setup of the COSMO-DE standard at the time of the model calculations (Laube, 2019). Further information on the model setup is provided in the Supporting Section A.1.

The first two coarser nesting levels were performed transiently from 1971-2100 with a spin-up of three years (1968-1970). The third nest was originally performed in 30-year time slices preceded by a 3-year spin-up (1968–2000, 2018–2050, 2068–2100; Schädler et al., 2018). These time slices were later extended (2001–2020, 2051–2070) to provide a quasi-transient ensemble for the whole period 1971-2100 – except for the

ensemble member driven by HadGEM2-ES, where only data until 2099 is available. The overlapping periods (2018–2020 and 2068–2070) were compared for a consistency check (not shown). No relevant differences were found several months after the simulation start, in agreement with the findings from Lavin-Gullon et al. (2022). The downscaled CPM simulations driven by specific GCMs are referred to with an appended -C (GCM-Name-C).

Sub-hourly, 5-min precipitation is available for three ensemble members EC-EARTH-C, HadGEM2-ES-C, and MPI-ESM-LR-C for the historical period, 1971-2000. In the projection period, 5-min data is transiently available to 2100 for MPI-ESM-LR-C and for the time slices 2000-2021 and 2050-2071 for EC-EARTH-C and HadGEM2-ES-C.

In the current setup, the boundary zone between the inner nests is relatively narrow. However, there is a relatively small horizontal resolution step (less than a factor of 3) between the nests, which is smaller than common convection-permitting setups used today (Ban et al., 2021). This likely decreases boundary effects and enables tighter nesting. Nevertheless, the boundary zone that was excluded from the analysis of the innermost domain was relatively large (48 grid points). The assessment of the boundary effects in the innermost domain indeed revealed that anomalies of temperature, as well as mean and extreme precipitation, occur well outside the evaluation area.

The final CPM domain covers southern and central Germany as well as the Alps in the south and parts of France in the west of the domain (Fig. 4.2). The analysis in the thesis focuses mainly on the German part of the domain. The largest part of the domain extends over the German region of low mountain ranges – the Western Uplands, the Eastern Uplands, and the South German Scarplands. The altitude of most of the low mountain ranges is between 500 and 1500 m - below the tree line. The mountain ranges are mostly rounded and forested. The Alpine Foreland covers the area in the southeast of Germany. It is a gently hilly area with altitudes of around 300 to 800 m.

4.1.3 Global warming levels

The transient projection data enables an analysis based on global warming levels (GWLs). GWLs are generally defined as the anomaly of the global mean temperature averaged over a climatological period, compared to pre-industrial conditions. The analysis of GLWs allows improved comparability from the downscaling of GCMs with differing climate sensitivities or different emission scenarios (IPCC, 2021). Moreover, the analysis of GWLs benefits from the mitigation of parts of the GCM and scenario uncertainties and provides information about the effects of climate change given a certain threshold of warming.

Slightly different approaches to the definition of global warming levels from GCM data exist in the literature. The reference period from which the anomaly is calculated is either from 1850-1900 (IPCC, 2021) or a more recent period (Vautard et al., 2014; Teichmann et al., 2018). To better capture the recent developments of global warming,

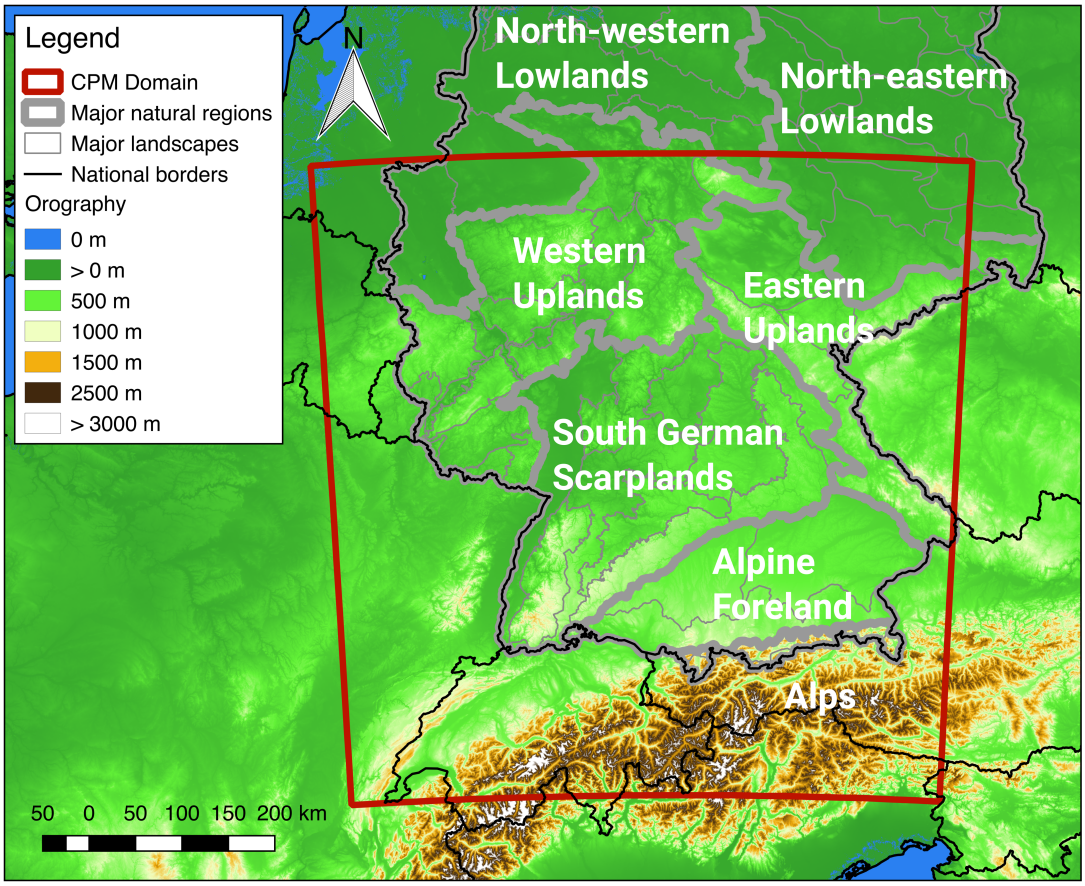

Figure 4.2: Major natural areas in the CPM domain of the KIT-KLIWA ensemble. The model domain with the boundary zone truncated is displayed in red. Further information on the major landscapes indicated here with thin black lines is detailed in Fig. A.1. Shapefiles of the major landscapes: Bundesamt für Naturschutz (BfN) (2011); digital elevation model, EarthEnv-DEM90: Robinson et al. (2014).

the thesis follows the approach in Vautard et al. (2014) and Teichmann et al. (2018), using the period 1971-2000 as a historical reference period, to which a GWL of 0.46 K is assigned.

Projected global warming is analysed over the anomaly of a 30-year running window of global mean surface temperature in the GCM projection, centred around the year in which the threshold is exceeded. The GWL for the four ensemble members is shown in Fig. 4.3: The projected increase in GWL since 1971-2000 is relatively similar for MPI-ESM-LR, EC-EARTH, and CNRM-CM5. For HadGEM2-ES a stronger warming is found which is partly based on a higher climate sensitivity, in addition, the realisation in HadGEM2-ES has a relatively cold period in 1971-2000. In this thesis, specifically the 30-year periods centred around 2 and 3 K of global warming are analysed, hereafter referred to as GWL2 and GWL3. Table 4.2 provides the years of the respective 30-year time slices.

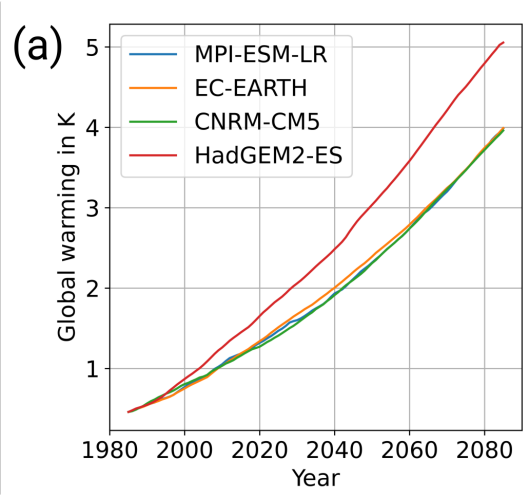

Figure 4.3: Global warming levels in the four driving GCMs displayed over time (reprinted from Hundhausen et al., 2024).

Table 4.2: 30-year periods corresponding to GWL2 and GWL3 relative to pre-industrial conditions.

GCM	GWL2	GWL3
CNRM-CM5	2029 - 2058	2052 - 2081
MPI-ESM-LR	2029 - 2058	2052 - 2081
EC-EARTH	2026 - 2055	2051 - 2080
HadGEM2-ES	2016 - 2045	2037 - 2066

4.2 Reference data

To evaluate the model output of precipitation and temperature within the thesis, the following observational datasets are analysed: Station data, radar observation and aggregated gridded products - namely the HYRAS dataset and the KOSTRA dataset. An overview of all datasets is provided in Tab. 4.3, and a description of the datasets is provided below.

4.2.1 Station observations

The DWD operates a Germany-wide station network providing in-situ precipitation recordings. Since the nineties, the first automated stations have operated routinely on hourly and sub-hourly resolution (Kaspar et al., 2013, Fig. 4.4a). Stations are operated in accordance with the WMO guidelines and quality control data are provided by the DWD. The complete station metadata, such as station relocations, and instrument changes are available from the DWD Climate Data Center.

In contrast to the model simulations that are representative of an area, station data is a point measurement, leading to a different footprint of the precipitation output in the contrasting datasets. Even though approaches for the transfer of data from different spatial footprints are vastly examined in literature with so-called areal reduction factors,

the uncertainty associated with those factors is large (e.g. Wright et al., 2014). The dependence of those factors on different storm types is not well understood yet (Wright et al., 2014). In order not to introduce additional uncertainty and potentially systematic errors across the temporal resolutions analysed and focused on in the thesis, no area reduction factors are applied in the analysis. This shortcoming is detailed in the associated error analyses within the relevant results sections.

Table 4.3: Overview of the observational datasets and observation-based products.

Dataset	Parameter	Reference
Station data	Hourly precipitation	Hourly station observations of precipitation for Germany[2]
Station data	5-min Precipitation	5-minute station observations of precipitation for Germany[3]
Station data	Hourly air & dew point temperature	Hourly station observations of moisture parameters for Germany[4]
Radolan	5-min precipitation	RADKLIM Version 2017.002: Reprocessed quasi gauge-adjusted radar data, 5-minute precipitation sums (YW) DOI: 10.5676/DWD/RADKLIM_YW_V2017.002, Winterrath et al. (2018)
KOSTRA	Return levels of precipitation	DWD Climate Data Center (CDC): Grids of return periods of heavy precipitation (design precipitation) over Germany (KOSTRA-DWD), version 2010R, Malitz and Ertel (2015) & Junghänel et al. (2017)
HYRAS	Daily precipitation	Raster dataset of daily sums of precipitation in mm for Germany - HYRAS-DE-PRE, Version v5.0[5], Rauthe et al. (2013)
HYRAS	Daily maximum temperature	Raster dataset of daily maximum temperature in °C for Germany - HYRAS-DE-TASMAX, Version v5.0[6], Razafimaharo et al. (2020)

Within the thesis, two subsets of station precipitation records are used, tailored to the specific research question: Chapter 5 analyses station record long time series down to hourly resolution, while Chapter 6-8 use sub-hourly station data, but also of shorter time series length. The criteria for data selection are described in the respective chapters. In addition, air temperature and dew point temperature recorded at the DWD stations are analysed in Chapter 8.

4.2.2 Radar

To complement the station point measurements of precipitation, we use the radar dataset, Radolan, provided by the DWD on a grid with a resolution of 1 km×1 km (Winterrath et al., 2018). Radolan provides 5-min resolution precipitation over Germany since 2001, and is a composite of 17 radars today (Fig. 4.4b). The correction of the

[2]Dataset-ID: urn:x-wmo:md:de.dwd.cdc::obsgermany-climate-hourly-precipitation
[3]Dataset-ID: urn:x-wmo:md:de.dwd.cdc::obsgermany-climate-5min-rr
[4]Dataset-ID: urn:x-wmo:md:de.dwd.cdc::obsgermany-climate-hourly-moisture
[5]Dataset-ID: urn:x-wmo:md:de.dwd.cdc::GRD_DEU_P1D_RR_HYRAS-DE
[6]Dataset-ID: urn:x-wmo:md:de.dwd.cdc::GRD_DEU_P1D_T2M-X_HYRAS-DE

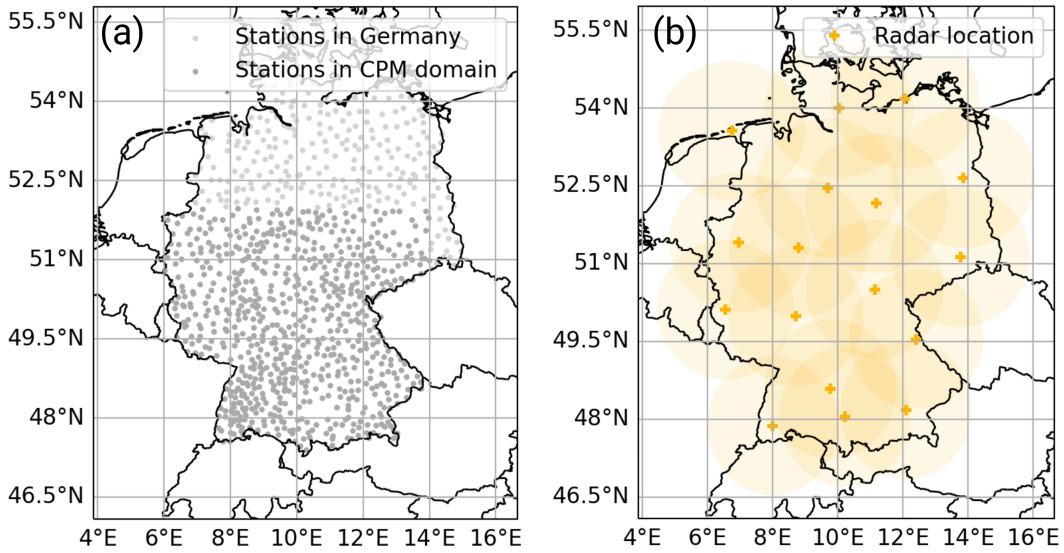

Figure 4.4: (a) Station locations in Germany with sub-hourly precipitation data available. (b) Radar coverage with yellow shading showing the theoretical coverage of the radars.

radar data and the transformation of the raw data into precipitation is performed by the DWD. Central to this process is the adjustment of radar-based precipitation estimates using station measurements (Bartels et al., 2004).

Due to the sparse data coverage in the first years of operation of the radar network, the thesis only analyses data for the 20 years from 2003 to 2022. For the analysis in Chapter 6 to Chapter 8, the radar data are conservatively remapped onto the model grid at 2.8 km resolution. The interpolated data are hereafter referred to as the "radar model grid". As in the simulations, the interpolated radar data are analysed only over Germany to match the station measurements and to avoid sparse data coverage outside of Germany. Secondly, the radar data are analysed at the original resolution of 1 km×1 km in the grid cell corresponding to allow a direct comparison between the two datasets (notation "radar station grid").

4.2.3 Aggregated gridded data products

The high-resolution gridded daily dataset, HYRAS

The HYRAS dataset (short for "Hydrometeorologische Rasterdaten") processed and provided by the DWD is an observation-based gridded dataset on a grid resolution of 1 km for precipitation and 5 km for the temperature variables daily mean temperature (Tmean), daily maximum temperature (Tmax), and daily minimum temperature (Tmin). We use the HYRAS dataset of version 5.0, which covers the observation period from 1931 to 2020.

Precipitation in HYRAS is based on daily station measurements of precipitation totals (6 UTC to 6 UTC of the following day). The regionalisation is done according to

the REGNIE method (Rauthe et al., 2013). Central to this method is an interpolation of the observed precipitation anomalies to a regular grid. The interpolation relies on monthly background climatological fields that are calculated based on data from 1971-2000. The background fields are based on a multiple linear regression taking longitude, latitude, altitude, direction and exposure into account. To derive daily precipitation totals, precipitation anomalies defined as daily precipitation at a station divided by the value of the background field are calculated at each station. The anomalies are then interpolated onto the regular grid using inverse distance weighting. Finally, the daily precipitation at each grid point is determined over the multiplication of the anomaly with the background field. Details regarding the method are in Rauthe et al. (2013).

A similar approach is applied in the HYRAS dataset of daily mean, minimum and maximum temperature. This method also accounts for the urban heat island effect and cold pools. Details are in Razafimaharo et al. (2020).

Daily precipitation from the HYRAS dataset for the period 1971 to 2005 is used for the evaluation of simulated precipitation in Chapter 5. Tmax from HYRAS is used in Chapter 8, providing an estimate of the temperature conditions associated with the radar soundings. For the assessment, HYRAS data is interpolated conservatively onto the simulation's grid.

An observation-based rainfall risk product - KOSTRA

As a reference for extreme precipitation return levels (RLs), we use the KOSTRA dataset, the "Coordinated heavy precipitation regionalisation and evaluation" (originally "Koordinierte Starkniederschlagsregionalisierung und -auswertung des DWD") of the version KOSTRA-DWD-2010R (Junghänel et al., 2017). The dataset is available from the DWD and provides RLs of precipitation intensities for return periods (RPs) of 1 a to 100 a with an event duration (ED) of 5 min to 3 days. The horizontal resolution of the gridded dataset over Germany is 8.2 km×8.2 km.

The data basis for the evaluation of long EDs (ED = 24 h to ED = 72 h) is the regionalised daily precipitation sums by the DWD according to the REGNIE method (Junghänel et al., 2017; Rauthe et al., 2013). The evaluation of short ED<24 h is primarily based on DWD station recordings and additionally high-quality partner observational networks (Junghänel et al., 2017).

Extreme precipitation in KOSTRA-DWD-2010R is derived in the form of RLs with the method outlined in the following, the details can be found in Malitz and Ertel (2015); Junghänel et al. (2017). In a first step, the strongest independent intensity recordings over the respective ED are selected. The sample size is defined as e = 2.718 times the number of available years. To assure independence between the individual elements of the series, they must be separated by a precipitation-free period of at least four hours. For ED > 4 h, the minimum interval is equal to the ED (Refer to DWA, 2012, for reference and example of the construction of a partial series). An exponential

distribution is fitted to the data to derive RLs (as discussed in Section 2.4.1). To avoid discontinuities in intensities, an adjustment across different EDs was applied. The results are regionalised using location as well as orographic information (Malitz and Ertel, 2015; Junghänel et al., 2017). Uncertainties of the extreme value statistical evaluation due to regionalisation, the long-term natural climate variability, the measurement error, and the limitations of the station-based extreme value statistical approach are expected. The DWD provides the following error range (Junghänel et al., 2017):

- 10 % for 1 a $<$ RP $<$ 5 a,
- 15 % for 5 a $<$ RP $<$ 50 a
- 20 % for 50 a $<$ RP $<$ 100 a

The main application for KOSTRA in Germany is the dimensioning of water management structures, for example, the dimensioning of drainage systems, sewage treatment plants, and retention basins (Malitz and Ertel, 2015). KOSTRA therefore presents an essential reference for an application-tailored evaluation of extreme precipitation in Germany. Even though KOSTRA was developed for practical application it has also been previously evaluated in the peer-reviewed literature to assess extreme events in climate models (Berg et al., 2019; Poschlod et al., 2021). We use KOSTRA in Chapter 5 as a reference for simulated extreme precipitation intensities.

5 | CLIMATE CHANGE SIGNAL OF EXTREME PRECIPITATION RETURN LEVELS

This chapter is an edited version of the peer-reviewed article:

> Hundhausen, M., H. Feldmann, R. Kohlhepp, & J. G. Pinto (2024). Climate change signals of extreme precipitation return levels for Germany in a transient convection-permitting simulation ensemble. International Journal of Climatology, 44(5), 1454-1471, doi: 10.1002/joc.8393.

Minor changes have been made to make the article coherent in the context of this thesis.

5.1 Introduction

The 6th IPCC assessment report provides broad evidence that heavy precipitation events are expected to become more frequent and intense with global warming (IPCC, 2021). However, the magnitude of the regional changes in extreme precipitation intensities remains uncertain. The previous CPM analysis of extreme precipitation changes in Germany is so far based on time slice approaches that are sensitive to the internal uncertainty of the climate system. Furthermore, previous CPM analysis is mostly based on single CPM simulation runs and high-resolution ensemble data are rare.

To address these shortcomings, we use the KIT-KLIWA ensemble to track for the first time the evolution of future heavy rainfall in a transient convection-permitting, multi-GCM ensemble with a simulation period from 1971 to 2100. We investigate precipitation return levels (RLs) of different scales: from hourly to multi-day (3 d) duration (ED) and for different return periods (RPs) up to 100 a, to cover the wide range of scales relevant to various stakeholder applications, such as urban drainage design or regional planning.

Specifically, this chapter addresses the research question: How do return levels evolve under global warming as a function of duration and return period? To answer the question, the analysis is subdivided into the following three parts:

a) Evaluation of RLs in CPM historical simulations with observations and observation-based precipitation risk products.

b) Assessment of climate change factors for RLs of different EDs and RPs from the transient projection period.

c) Quantification of uncertainties of the derived climate change signal.

The chapter is structured as follows: Section 5.2 describes the extreme value statistics to derive RLs from the simulations and observations, as well as the calculation of the climate change signal. Sections 5.3, 5.4, and 5.5 present the results corresponding to the three parts of the analysis. The discussion and conclusion are provided in Section 5.6.

5.2 Methods

5.2.1 Evaluation of precipitation return levels

The analysis of RLs in the CPM ensemble is based on the simulated hourly precipitation time series. For each grid point, we derive RLs for RPs from 1 a to 100 a, over EDs from 1 h to 3 days. It should be noted that ED refers to a fixed sampling interval here, and is not tied to the actual duration of a precipitation event. We analyse the EDs of 1 h, 6 h, 12 h, 24 h, and 72 h in the projection period and additionally, the ED 2 h, 4 h, 9 h, and 48 h in the historical period. Various procedures for event selection and extreme value distributions are used in the literature. As elaborated by Pendergrass (2018), deciding which definition of extreme precipitation to use is critical, especially when communicating climate change information to other sectors. As our work integrates the KOSTRA dataset (details are in Sec. 4.2) and is intended to be close to the hydrological application for Germany, the method is based on the German DWA-A 531 guideline (DWA, 2012), which is the basis for the KOSTRA-DWD-2010R dataset.

A partial series is generated to select extreme events from the time series. This is done over the selection of the $e = 2.72$ times the number of analysed years' strongest precipitation peak intensity over the respective ED. To save computational time, the hourly time series are aggregated over a running window of the respective length of the ED prior to the event selection and individual rain events are separated from each other by a rain-free period in the aggregated time series of one day.

According to DWA (2012), we derive plotting positions of the events of the partial series using Eq. 5.1, with L sample size, M length of the time series in a and k running index of the sorted samples ($k = 1$ largest, $k = L$ smallest intensity). An exponential function in the logarithmic form of Eq. 5.2 is fitted to the data using a least square polynomial fit. The fit parameter slope w_p and offset u_p define the intensity distribution for different RP (DWA, 2012).

$$\mathrm{RP}(k) = \frac{L + 0.2}{k - 0.4} \frac{M}{L} \tag{5.1}$$

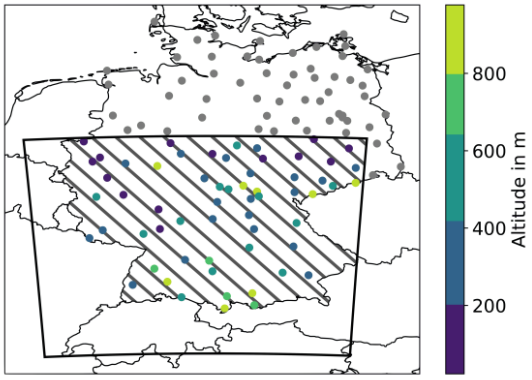

Figure 5.1: Study area with the simulation domain indicated in thick black line. The dots locate the DWD stations that have been recording hourly precipitation since 1995 and have a data coverage of at least 9 years from 1995-2005 - the coloured station locations within the simulation domain are evaluated in the study. The hatched area covers the German part of the domain considered in the analysis. Reprinted from Hundhausen et al. (2024).

$$\mathrm{RL}(\mathrm{RP}) = u_p + w_p \cdot \ln \mathrm{RP} \tag{5.2}$$

To correct for systematic underestimation of precipitation intensities due to an equidistant sampling window for ED similar to the sampling frequency, the suggested correction factors from guideline DWA-A 531 were applied to increase precipitation depth for small ED: correction factor 1.14, 1.07, 1.04, and 1.03 for the number of 1, 2, 3, and 4 measurement points per ED (DWA, 2012). In our case, an hourly resolution of the simulation and the observation is available, which leads to corrections for ED ≤ 4 h.

The method is applied to the time series for each ensemble member and at each grid point individually. For the reference period, the analysis of the CPM simulations is conducted for the years 1971-2005, which is the historical period of the driving GCMs. In the projection period, consecutive 30-year running time slices are evaluated, starting from 2006-2035, and ending with 2071-2100. In addition, RLs are calculated from the CPM simulations at the model grid cells closest to the station location and for the respective available measurement period, usually 1995 to 2005.

5.2.2 Evaluation against reference data

The derived RLs from the CPM historical period are evaluated against station data and KOSTRA. Refer to Chapter 4 for details regarding the observational datasets. For the analysis, the KOSTRA dataset has been truncated to the simulation domain (hatched area in Fig. 5.1). The comparison of median RLs as well as the distribution of RLs in CPM and KOSTRA was conducted using data on their respective original grids. This approach avoids any potential bias introduced by interpolation during the comparison. We interpolate KOSTRA data onto the CPM grid to visualise spatial comparisons. The interpolation was performed using the radial basis function method, implemented via the function scipy.interpolate.RBF in Python.

The station observations of hourly precipitation are available from the DWD since 1995 (details are in Chapter 4). We restrict the analysis to stations with large data coverage in the model historical period, defined as at least 9 years of observations from 1995 to 2005 and stations that are located within the model domain. The locations of the stations used are shown in Fig. 5.1b. The same method for the calculation of RLs as described above for CPM data is applied to the available time series for each station individually.

5.2.3 Climate change signal of extreme precipitation

We evaluate changes in extreme precipitation RLs based on 30-year running time slices in the projection period. A GWL is attributed to each 30-year time slice (details are in Sec. 4.1). To evaluate changes in RLs in the CPM projection with global warming, we make use of the concept of relative climate change signals (or change factors/uplifts) similar to Chan et al. (2022) to become more independent of the absolute precipitation intensities that are subject to model bias (Ho et al., 2012).

We evaluate the change factor (CF) according to Eq. 5.3 as the absolute change in precipitation normalised by the simulation's value in the reference period 1971-2005 ($\mathrm{RL}_{\mathrm{hist}}$). To derive a robust change signal, the CF is evaluated over the slope of a linear regression to the respective trajectory of RL over GWL (ΔRL in mm/(K GWL)). CFs are evaluated for the median RL of the grid points in the evaluation domain (hatched area in Fig. 5.1b), except for the spatial analysis in Fig. 5.11 where the procedure is applied to the model output at each grid point individually.

$$\mathrm{CF}(\mathrm{RP}, \mathrm{ED}) = 1 + \frac{\Delta\mathrm{RL}(\mathrm{RP}, \mathrm{ED})}{\mathrm{RL}(\mathrm{RP}, \mathrm{ED})_{\mathrm{hist}}} \tag{5.3}$$

5.3 Comparison of simulation and observation-based data

5.3.1 Comparison with station data

The observation of hourly precipitation intensity from stations considered within this study ranges from 0 to 67 mm h^{-1}. The largest fractional contribution is expected for small intensities (I), with approximately equal contribution for $I \leq 1\,\mathrm{mm\,h^{-1}}$ (Fig. 5.2a). With increasing I, the fractional contribution declines. For large I, scattering due to sparse data coverage is visible.

Comparing those observational results to the fractional contribution of intensities in the corresponding grid point of the 2.8 km resolution CPM simulations, the simulations replicate the shape of the curve: a plateau from 0.01 mm to 1 mm and a declining contribution for $I > 1$ mm. However, there is a systematic bias between the ensemble and the observations (Fig. 5.2b). All ensemble members overestimate the contribution of small intensities, with the largest overestimation seen in HadGEM2-ES-C (solid

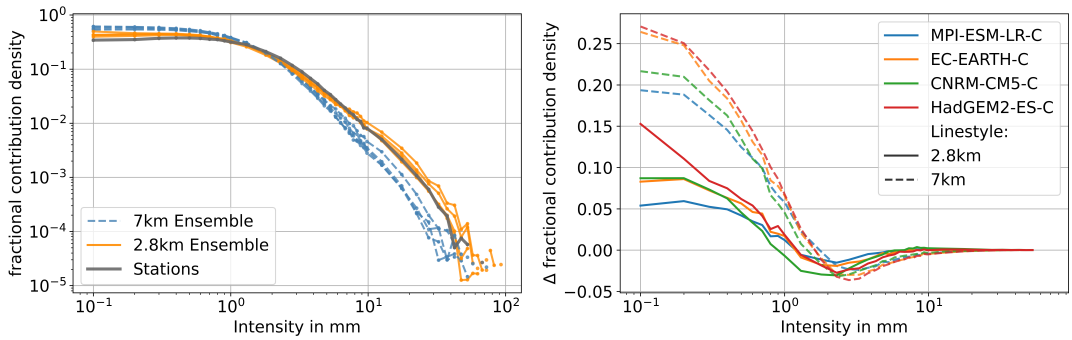

Figure 5.2: (a) The density distribution of fractional contributions of hourly rainfall from station measurements and the according results in the corresponding grid cell of 2.8 km and 7 km simulation output. Coloured single lines correspond to the single ensemble members. (b) provides the differences between observation and simulations for the 4 ensemble members. The bin width for both panels is 0.1 mm for the intensity range from 0 to 1 mm aligned with the resolution of the station measurement. Bin width is 0.5 mm for the intensity range from 1 to 10 mm and 5 mm for the intensity range from 10 to 100 mm. Reprinted from Hundhausen et al. (2024).

red line) and the most realistic representation for MPI-ESM-LR-C (solid blue line). Medium intensities exceeding 0.9 mm (CNRM-CM5-C) or 1.2 mm (MPI-ESM-LR-C, EC-EARTH-C, and HadGEM2-ES-C) are systematically underestimated by the simulations. The maximum underestimation occurs around 2 mm precipitation, with the largest underestimation in CNRM-CM5-C and again the best representation in MPI-ESM-LR-C (Fig. 5.2b). Observations and simulations converge for higher values, and show a slight overestimation of extreme events exceeding 6–8 mm (the interval corresponds to the ensemble range).

The coarser, convection-parameterising simulations on the 7 km grid show similar patterns of over- and underestimation of small to medium intensities as the 2.8 km simulations, but the differences with respect to the observation are amplified and the overestimation for small I is extended to larger intensities of 1.5–1.8 mm, above which the frequency of the respective intensity is underestimated. This underestimation at higher I is also amplified, with the maximum deviation occurring around $I = 3$ mm. This underestimation persists for the highest intensities, and there is no full convergence between the coarser simulations and the observations (Fig. 5.2a).

In the analysis, data with different horizontal resolutions are compared. As precipitation statistics are related to horizontal resolution the shown improvement of the high intensities from 7 to 2.8 km is partly attributed to the finer grid resolution in the CPM. Especially the intensity of short and intense (convective) precipitation extremes is sensitive to resolution (Eggert et al., 2015). To assess the effect of different resolutions alone, a comparison on a common grid, the 7 km grid, is made and the results are provided in Supplementary Fig. B.1. As expected, the difference in the CPM compared to the 7 km simulation decreases when the comparison is made on a common grid. However, the improvement in the regridded CPM simulation compared to the convection parametrised

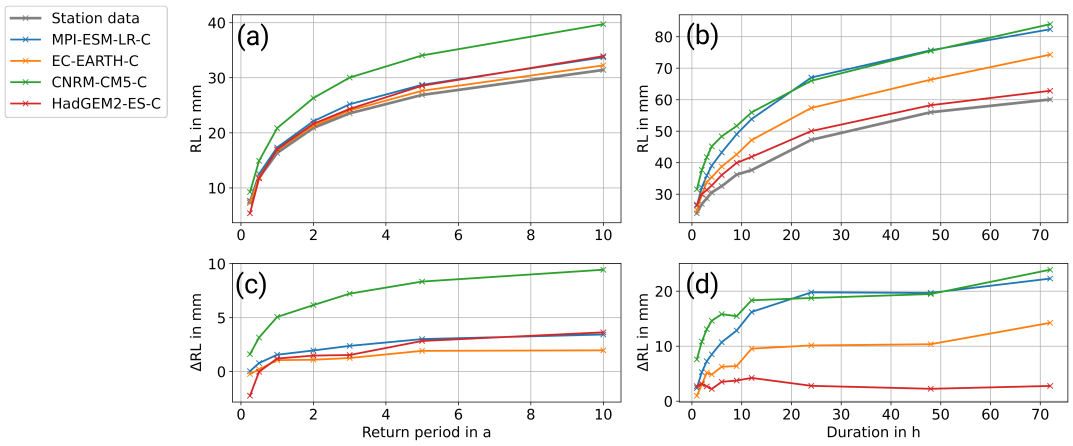

Figure 5.3: Median RLs in station observations and CPM simulations at the nearest neighbour grid point (a) for different RPs with fixed ED of 1 h and (b) for different ED with fixed RP of 5 a. In the second row, the differences between simulations and observations for the above are shown. Reprinted from Hundhausen et al. (2024).

simulations is reproduced for both, low and high intensities. Therefore, we conclude that an additional improvement comes from the CPM and is attributed presumably to a more realistic representation of precipitation due to the explicit resolution of deep convection.

In summary, the CPM simulations better represent the whole spectrum of precipitation intensities than the coarser 7 km resolution simulations. The features of the density distribution at high intensities are especially more realistically reproduced on the CPM scale. However, a slight overestimation of the most extreme events has to be expected using CPM. This finding holds for a short temporal resolution of 1 h. For longer aggregation times, the CPM simulations tend to systematically overestimate the contribution of high intensities and there is an increased bias compared to the coarser grid. This was tested with aggregated station data as well as using the gridded daily dataset HYRAS. The results are provided in the appendix in Fig. B.2 and revisited in more detail in Chapter 6.

Comparison of RLs in station and CPM data

The statistically derived RLs from the time series of the station data compared to the results of the CPM simulations at the respective grid points show the following patterns (Fig. 5.3):

For different RPs: The CPM simulations generally reproduce the RLs derived from the station data within a deviation of 4 mm for the three ensemble members MPI-ESM-LR-C, EC-EARTH-C and HadGEM2-ES-C as shown for the duration of 1 h (Fig. 5.3a). The function RL(RP) has a slightly steeper slope in all CPM simulations leading to an increasing overestimation of RL with increasing RP. Thus, the differences are smallest for small RPs, and sub-yearly results tend to be underestimated by EC-EARTH-C and

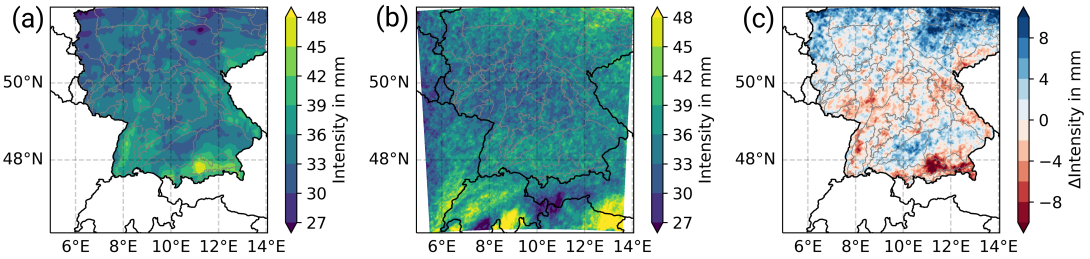

Figure 5.4: Spatial distribution of the return level with RP=10 a, ED=1 h in (a) KOSTRA, (b) the median of the ensemble results and (c) the differences (KOSTRA subtracted from the simulations). Reprinted from Hundhausen et al. (2024).

HadGEM2-ES-C (Fig. 5.3c). The largest error is found for CNRM-CM5-C, with an overestimation of up to 10 mm for large RP.

For different EDs: Taking the example of a 5-year RP and evaluating different ED (Fig. 5.3b and d), the overestimation of RL is generally smallest for the shortest duration (1 h) and increases with accumulation time. The trend is most prominent for MPI-ESM-LR-C, where the overestimation ranges from 2 to 22 mm. Only in HadGEM2-ES-C, the described pattern is not visible. Here, the overestimation is similar across all EDs, with approximately 3 mm.

5.3.2 Comparison with aggregated observations in KOSTRA

Spatial analysis of the 10-year return level

The aggregated rainfall hazard dataset KOSTRA provides gridded RLs covering Germany. In Fig. 5.4a, the hourly 10-year RL (RL10) is shown as an example. RL10 ranges from 27 to 48 mm. Higher values are visible in the Black Forest and the alpine foreland in the south, while flatter regions in the north generally show a smaller RL10. An overview of the geographical regions in Germany is provided in Chapter 4 and Fig. 4.2 therein.

The ensemble median of RL10 of the CPM simulations during the reference period (1971–2005) ranges from 28 to 50 mm in the German part of the domain (Fig. 5.4b). There is no clear dependence on orographical structures within this domain for the ensemble median. There is no clear dependence on orographical structures within this domain for the ensemble median. Same is true for the single ensemble members (Supplementary Fig. B.3). The ensemble median shows a slight pattern of lower values in the centre of the domain, with RL slightly increasing towards the north and south. Strong spatial patterns in the CPM results are detected only outside the evaluation domain in the Alps.

The lack of spatial structures for short EDs is consistent with the analysis of observational data, for example, radar data in Lengfeld et al. (2019), who concluded that the intensity of precipitation intensities of short compared to longer durations is less

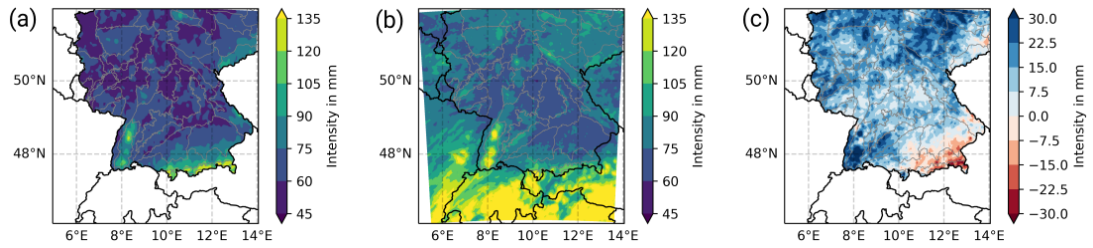

Figure 5.5: Spatial distribution of the RL with RP=10 a, ED=24 h in (a) KOSTRA, (b) the median of the ensemble results, and (c) the differences. Reprinted from Hundhausen et al. (2024).

dependent on orography. Therefore, we attribute the lack of spatial patterns mainly to uncertainty due to the relatively short time series length compared to the RP of interest. We expect that longer time series are needed or that using a regression model, such as that used to derive the KOSTRA dataset, could improve the representation of the expected patterns associated with orography, and likely explain the differences with KOSTRA.

The differences between hourly RL10 in KOSTRA and the CPM ensemble lead to an underestimation of RL10 for areas with high KOSTRA values (Alpine foreland and low mountain ridges in the southwest of the domain) and a general overestimation in the north of the domain (Fig. 5.4c). Seemingly random spatial deviations between CPM and KOSTRA appear superimposed on this pattern. Moreover, exceptionally high RL10 in KOSTRA in the Alpine foreland stand out (lon $\approx$ 11°E, lat $\approx$ 48°N). At this location, there is no orographic feature that could explain a mechanism for such a strong local maximum, but it is assumed that either an error in the data or a strong observed local event has biased the statistics. This is thus an example of how the method can depend on individual events even for comparatively short RP (as in the example of 10 years) and shows that the available, finite observation time series do not always permit a robust estimate.

For longer ED, spatial patterns of extreme precipitation associated with elevation become apparent in the CPM ensemble. For example, all ensemble members reproduce higher daily RL10 in mountainous regions such as the Black Forest compared to the flat surroundings (Fig. 5.5). This pattern is slightly more pronounced in the CPM simulations than in observations, leading to an overestimation of daily RL10 in these mountainous areas.

Evaluation across different RPs and EDs

Based on the finding of random spatial deviations in the CPM results for short ED, we use the median of the grid point results for the comparison of the full range of extreme intensities over different RPs and EDs between the historical CPM simulations (1971-2005) and KOSTRA. Both datasets are evaluated over the shared, German, part of the model domain. The following patterns emerged from the comparison and are

visualised in Fig. 5.6 and Fig. 5.7. The values of the relative differences displayed in Fig. 5.7 are provided in the appended Table B.1.

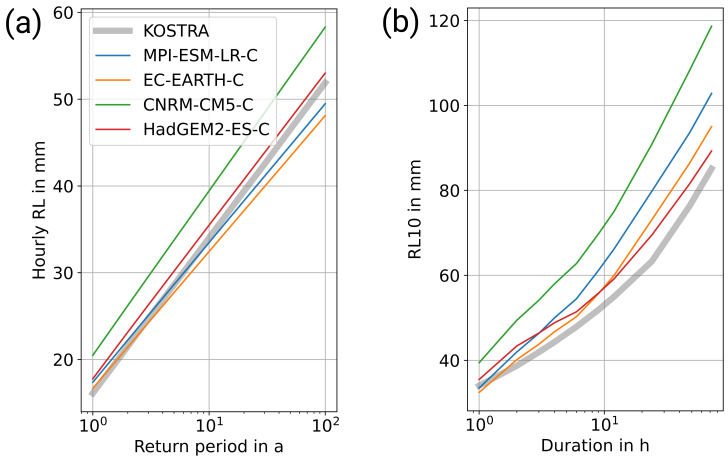

Figure 5.6: RLs in KOSTRA and CPM are shown in (a) for different RPs keeping ED constant with 1 h and in (b) for different ED with constant RP of 10 a. Reprinted from Hundhausen et al. (2024).

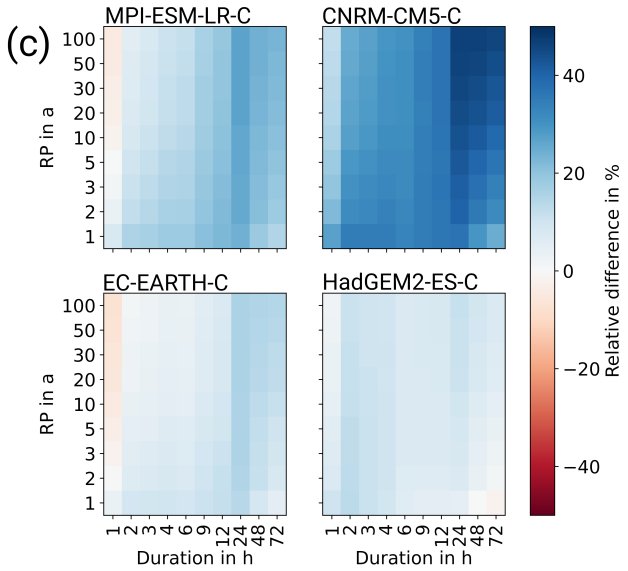

Figure 5.7: The relative differences in RLs for all analysed RPs and EDs are shown for the four ensemble members separately – top left: MPI-ESM-LR-C, top right: CNRM-CM5-C, bottom left: EC-EARTH-C, bottom right: HadGEM2-ES-C. Reprinted from Hundhausen et al. (2024).

For different RPs, constant ED: two different regimes are apparent. For ED<24 h (small-scale or predominantly convective events), the relative difference between CPM simulations and KOSTRA decreases (becomes more negative) with increasing RP (Fig. 5.7). This behaviour is determined by the underestimation of the slope of the fitted function RL(RP), which tends to be too small for the ensemble members MPI-ESM-LR-

C and EC-EARTH-C (Fig. 5.6). For HadGEM2-ES-C and CNRM-CM5-C, the slope agrees well with KOSTRA, resulting in a roughly constant absolute overestimation in the simulations. Apart from ED=1 h, the absolute differences almost always increase with RP, except for further few sub-daily events in EC-EARTH-C. The absolute values are provided in the appendix in Fig. B.4. In the range of ED≥24 h (large-scale events), the pattern in the relative differences is reversed for all GCM: the overestimation increases with RP.

For different EDs, constant RP: Generally, the difference between KOSTRA and CPM is smallest for ED=1 h, with negative values for the realizations driven by MPI-ESM-LR and EC-EARTH. For ED<24 h, the difference becomes larger with increasing ED, leading to an increasing overestimation of RL projected by MPI-ESM-LR-C, EC-EARTH-C and CNRM-CM5-C. No continuous increase is visible in the HadGEM2-ES-C realization and in CNRM-CM5-C for low RP. For ED≥24 h, a reversal of the pattern is again apparent. Overestimation is largest for ED=24 h and decreases with higher aggregation times. For ED=72 h, a negative bias is found in HadGEM2-ES-C for low RP. Exceptionally large deviations between simulation and KOSTRA are found for daily ED.

The deviation between the spatial median in KOSTRA and CPM ensemble ranges from -7 % to 10 % for hourly duration, excluding the outlier CNRM-CM5-C with significantly higher deviations (up to 27 %). For sub-daily events with ED>1 h, a positive bias/overestimation is expected for the model (2 to 23 %, excluding CNRM-CM5-C). Longer events (ED≥24 h) show the largest overestimation and variance with -2 to 27 % deviation – excluding CNRM-CM5-C with up to 47 % overestimation.

Distribution-based evaluation

The best agreement and no systematic over-/underestimation compared to KOSTRA was found in the ensemble for hourly ED and medium RP, which is in this case around an RP of 10 a, which corresponds to one third of the analysed time series length. Therefore, hourly RL10 serves as an example for more detailed analysis of the distribution in Fig. 5.8. Both KOSTRA and the four ensemble members exhibit a positive skew, with the CPM ensemble displaying more pronounced tailing and larger values for the most extreme events. The distribution of CPM simulation results is generally smoother than in KOSTRA. RLs derived from station data are generally lower than KOSTRA or CPM ensemble results. Station results show larger scattering, which is mainly attributed to shorter time series which increase uncertainty in extreme value statistics.

5.3.3 Implications

We conclude that there is adequate agreement between the CPM ensemble and station measurements for hourly rainfall intensities, with an added value in the CPM simulations beyond the mere higher resolution compared to coarser simulations. Confidence in RLs

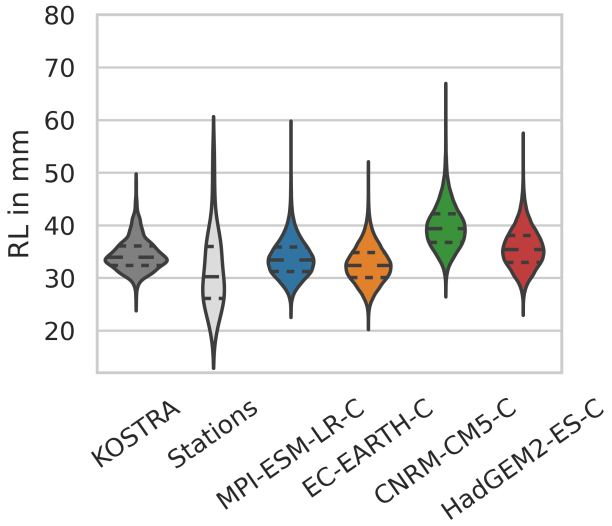

Figure 5.8: RLs for ED=1 h and RP=10 a in KOSTRA, derived from the available station data and from the four ensemble members in the CPM ensemble for 1971-2005. The distribution is evaluated over the German part of the model domain for KOSTRA and CPM simulations, and over all available stations within this domain for station data. Reprinted from Hundhausen et al. (2024).

in the CPM simulations is higher for short ED (hourly to sub-daily), as they are in better agreement with the observations (station and KOSTRA). The mean bias is not necessarily smaller with short RP. In general, there is an overestimation of the RL by the CPM simulations, except for ED=1 h. The positive skew of the distribution of hourly RL10 is represented by the simulations, but there is a greater magnitude of the largest possible extreme events. We find higher confidence in the ensemble members driven by MPI-ESM-LR, EC-EARTH and HadGEM2-ES. CNRM-CM5-C is likely to overestimate extreme precipitation.

Our analysis implies that we have more confidence in the simulated values that are similar to those in KOSTRA. However, it is important to consider the limitations of this comparison. KOSTRA and the CPM ensemble consider different time periods. Moreover, also observational datasets come with limitations in accurate, high-resolution rainfall measurements, especially for intense events accompanied by strong winds (e.g. Sieck et al., 2007). Data retrieval and interpolation in complex terrain is challenging due to sparse observations (e.g. Henn et al., 2018). Systematic errors can be expected in the observations, especially for short events and complex terrain. Moreover, the large bias between the model and KOSTRA associated with daily ED raises the question whether this effect could originate from a discontinuity in the data source in KOSTRA or is an impact of applied corrections in KOSTRA. The bias compared to the simulations is therefore treated here as a reference rather than the ultimate truth. Based on these considerations, observational data was therefore not used for bias correction but to account for systematic model errors; change signals of percentage increase are derived in the following similar to Chan et al. (2022).

5.4 Future development of heavy precipitation

The projection period 2006 to 2100 of the CPM ensemble covers global warming levels from 1 to 5 K, depending on the driving GCM (details are in Sec. 4.1). The following patterns are derived from the change signal of the RLs over global warming level in the projection period (Fig. 5.9).

If ED is kept constant and RP is varied, the main change is an increased slope with greater RP. The shape of the curve (local maxima and minima) remains independent of RP (Fig. 5.9a). This is as expected for the displayed values from the same underlying extreme value fits. For the relative increase with global warming, approximated by a linear regression over the normalised RL-GWL curves, three out of four ensemble members project an enhanced increase of RL with RP for ED<24 (Fig. 5.9c). Only CNRM-CM5-C shows an approximately constant change factor for all RPs for ED=1h. For large ED=72 h, a reverse pattern is observed for the majority of the ensemble members (MPI-ESM-LR-C, EC-EARTH-C and HadGEM2-ES-C), where the relative increase is slightly larger for small RPs than for large RPs. There is no agreement on a common trend in the projections at ED=24h and the change signal is approximately constant, especially for EC-EARTH-C and HadGEM2-ES-C.

If RP is kept constant and ED is varied, the projected increase is substantially affected, altering the shape of the intensity trajectory with GWL (Fig. 5.9b). Different local maxima and minima emerge. However, similarities in the curves indicate that the same event appears to be partially sampled at several EDs. In terms of the relative change signal (Fig. 5.9c), increasing ED generally leads to decreasing change factor for DS<24 h. Only CNRM-CM5-C shows lower values for ED=1 and thus no steady decrease. For ED=72h, there is no common trend in the ensemble. While in EC-EARTH-C and MPI-ESM-LR-C, the pattern is visible throughout all EDs and the change factors are smallest for ED=72 h, CNRM-CM5-C and HadGEM2-ES-C show similar or slightly higher magnitudes for ED=72 h compared to ED=12 h.

The climate change signal is therefore expected to be largest for short ED and long RP. The projected increase in extreme precipitation per degree warming, in this case, reaches up to 8.5 % (EC-EARTH-C) or up to 5.9 % and 6.1 % (MPI-ESM-LR-C and HadGEM2-ES-C). CNRM-CM5-C shows a maximum change signal of 8.1 % for sub-daily events, which is well within the range of other models assigned higher confidence due to better agreement with observations and similar projected development of RLs. The change signal is in the range of the CC-scaling. Super-CC scaling is projected by EC-EARTH-C and CNRM-CM5-C. Events with longer EDs also increase with GWL but to a lesser extent from 0.8 % (MPI-ESM-LR-C) over 2.3 % (EC-EARTH-C) to 4.3 % (HadGEM2-ES-C) for 3-day ED and large RP. CNRM-CM5-C indicates that also for those long ED larger change signals may be expected (up to 6.8 %). Please refer to Tab. B.2 for an overview of all extracted change signals.

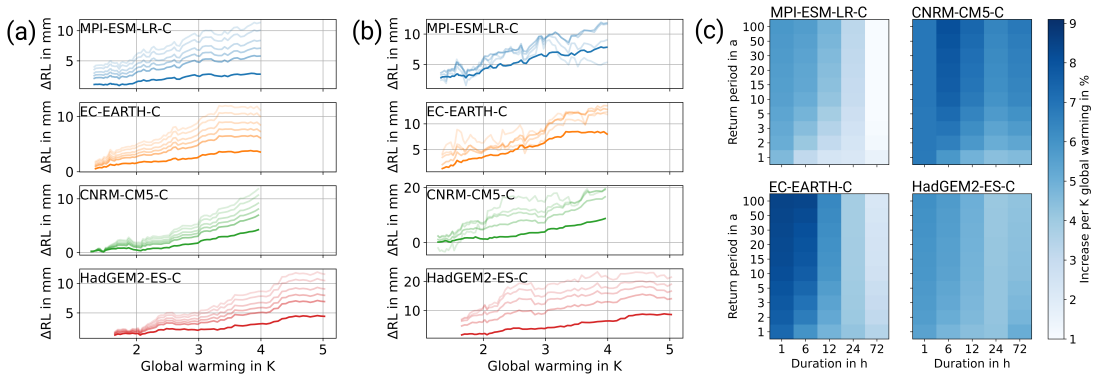

Figure 5.9: (a) Projected change compared to the reference period (1971–2005) for ED=1 h and variable RP=1, 5, 10, 20, 50 and 100 a (with increasing transparency) for MPI-ESM-LR-C, EC-EARTH-C, CNRM-CM5-C and HadGEM2-ES-C (from top to bottom), (b) for RP=10 a and variable ED=1, 6, 12, 24 and 72 h (with increasing transparency). (c) Relative percentage increase of RL, normalised to the corresponding value in the reference period 1971–2000. The increase is evaluated over a linear regression in the projection period – top left: MPI-ESM-LR-C, top right: CNRM-CM5-C, bottom left: EC-EARTH-C and bottom right: HadGEM2-ES-C. Reprinted from Hundhausen et al. (2024).

In summary, for sub-daily events, the change signal increases with RP, whereas for large-scale multi-day events (ED=72 h), the change signal decreases with RP. The highest climate change signals, ranging from 6 to 9 %, are associated with the shortest ED, falling within the range of CC-scaling and partly super-CC scaling.

5.5 Uncertainty in the climate change signal

Apart from identifying the major patterns of change in extreme precipitation, the continuous assessment over GWL using a running 30-year window reveals the inherent variance in the increase in extreme events, visible as local minima and maxima in the trajectories of RLs over GWL (Fig. 5.9a and b). This variance is approximated by the residual standard deviation of the linear fit, which is a measure of how well a linear relationship describes the future development of RLs with GWL. The residual standard deviation ranges from 0.8 and 2 percentage points (PPT) (10th to 90th percentile) for most RP-ED combinations (Fig. 5.10a). The highest residual standard deviations are found for large EDs in MPI-ESM-LR-C, HadGEM2-ES-C, and CNRM-CM5-C. However, the magnitude differs for the individual ensemble members. CNRM-CM5-C and HadGEM2-ES-C reach maximum residual standard deviation of 3.5 and 3.0 PPT for long ED and large RP, while MPI-ESM-LR-C and EC-EARTH-C show maximum values of 1.4 and 1.7 PPT for all tested configurations. For ED>6 h, all GCMs show an increasing residual standard deviation with increasing RP. However, this pattern is reversed for most ensemble members (MPI-ESM-LR-C, CNRM-CM5-C, and HadGEM2-ES-C) for ED=1 h. No consistent result within the ensemble is found for ED=6 h. The derived trends at large ED, as the apparent decreasing change signal with RP for

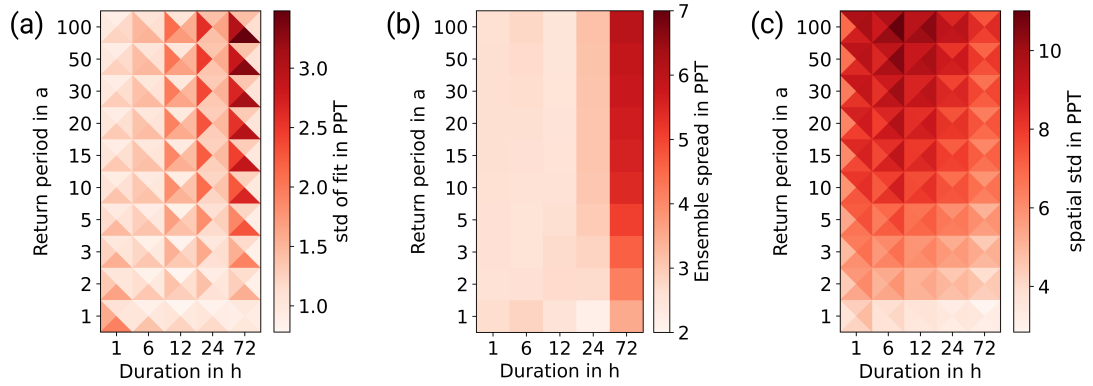

Figure 5.10: Different types of uncertainty in the climate change signal of extreme precipitation for different RP and ED. (a) The residual standard deviation is calculated for the linear regression that was used to approximate the change signal of extreme precipitation with global warming. (b) The ensemble spread corresponds to the range between the minimum and maximum ensemble member projections of the relative change signal. (c) The spatial standard deviation is calculated over the increase at each grid point in the domain. For (a) and (c), the sections in the graph correspond to the ensemble members, top: MPI-ESM-LR-C right: EC-EARTH-C, bottom: CNRM-CM5-C, left: HadGEM2-ES-C. Reprinted from Hundhausen et al. (2024).

ED=72 h, are thus associated with greater uncertainty. These findings suggest that a linear regression describes the trend better for short EDs and less accurately for large ED and large RP. The availability of a transient simulation allowed local minima and maxima in the climate change signal to be smoothed. The analysis suggests that caution should be taken when applying a linear assumption to the analysis of time slice experiments, as significant stochastic errors can be expected, in contrast to transient data series.

Further uncertainties arising from differences in GCM formulation are expected and can be estimated from the ensemble spread (Fig. 5.10b). The ensemble range in the relative increase with GWL depends mainly on the ED and is between 2 and 3 PPT for the majority of the EDs studied up to 24 h and is relatively independent of RP for ED<24 h. The range is significantly higher for ED=72 h up to 6 PPT, mainly due to the exceptionally low RL changes projected by MPI-ESM-LR-C. The spread increases with RP for ED=24, 72 h. The relationship found indicates that the spread is particularly pronounced for long events (72 h), which are thought to depend on large-scale circulation patterns predetermined by the GCM and propagated into the RCM domain. Events of shorter duration, for which little spread is found here, are likely to be mainly controlled by the RCM, which is identical for all ensemble members in our analysis.

In contrast, the spatial variance depends mainly on the RP (Fig. 5.10c). For all ED, it increases with RP up to 9 PPT (HadGEM2-ES-C), 10 PPT (MPI-ESM-LR-C, CNRM-CM5-C) and 11 PPT (EC-EARTH-C) for RP=100 a. MPI-ESM-LR-C tends to show higher variance for shorter durations, while HadGEM2-ES-C shows the highest variance for longer durations of 12 and 24 h. For CNRM-CM5-C and EC-EARTH-C, the

maximum spatial variance is centred around ED=6 h, and ED=12 h. The magnitude of the spatial variance is similar for all ensemble members. For large RP (approximately RP>15 a), the spatial variance is in the order of magnitude of the change signal itself. The results highlight uncertainties in estimating RLs from time series with a length close to or smaller than the RP. This implies that the robustness of a single grid point result is not given and that information can be derived from the consideration of multiple points only.

Analysis of the spatial patterns with respect to the climate change signal shows no dependence on the geographic location or orographic features (Fig. 5.11). Because of this stochastic nature of the climate change signal across the domain, we treat the spatial distribution of the individual grid point results as an estimate of uncertainty. On examination of the evolution of RL10 with ED=1 h and RP=10 a at GWL2 and GWL3 in Fig. 5.12, the main feature is a shift of the distribution. All ensemble members project a positive shift of the median from historical, over GWL2 to GWL3 (Tab. 5.1). The distribution is right-skewed, with longer tailing towards higher RLs, indicating the possibility of local exceptionally high RLs. The skewness does not show a clear climate change signal, remaining relatively constant for the ensemble members EC-EARTH-C, and HadGEM2-ES-C, slightly increasing for CNRM-CM5-C, and decreasing for MPI-ESM-LR-C (Tab. 5.1). The distribution widens for all ensemble members from historical to GWL2 to GWL3, as indicated by the increase in the interquartile range (Tab. 5.1). This effect is strongest for CNRM-CM5-C (increase of 1.5 mm) and EC-EARTH-C (increase of 1.2 mm) and less pronounced for MPI-ESM-LR-C and HadGEM2-ES-C with 0.9 and 0.7 mm. The broadening of the distribution indicates that extreme precipitation will become more variable in the future. These patterns derived from hourly RL10 are largely consistent for events of further RPs and duration, and are provided in the appendix for RPs between 5 and 30 years in both hourly and daily EDs (Table B.3). The median increases consistently for all configurations. The interquartile range shows an increase except for the ensemble member MPI-ESM-LR-C for the daily ED in GWL2. In general, the change in RP alone has little effect on the observed patterns within the ensemble, but amplifies the changes for the median and interquartile range. The skewness shows no common projected patterns even in further configurations.

Table 5.1: Statistics of the distribution of hourly 10-year RL sampled over all grid points in the domain.

Driving GCM	Median in mm			Interquartile range in mm			Skewness		
	hist	GWL2	GWL3	hist	GWL2	GWL3	hist	GWL2	GWL3
MPI-ESM-LR	33.5	37.4	39.2	4.7	5.5	5.6	0.68	0.52	0.38
EC-EARTH	32.4	35.7	38.6	4.7	5.7	6.2	0.32	0.29	0.33
CNRM-CM5	39.4	40.6	43.8	5.4	6.1	6.7	0.50	0.55	0.63
HadGEM2-ES	35.5	37.5	39.3	5.1	5.6	5.8	0.37	0.43	0.40

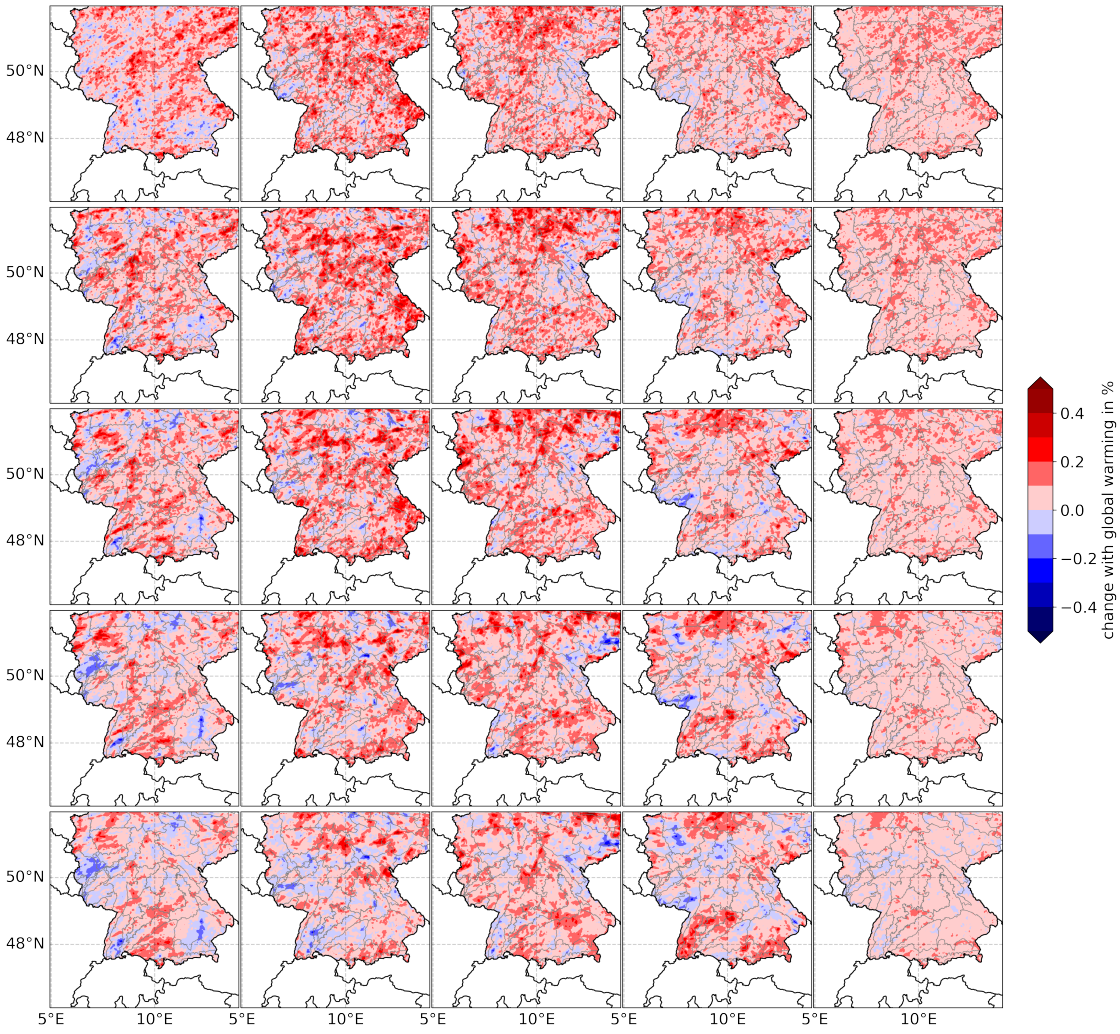

Figure 5.11: Climate change signal for the single grid points displayed as contour plots. The RP is 10 a. Different EDs are arranged in rows for ED=1, 6, 12, 24, 72 h (from top to bottom). Columns show the ensemble members MPI-ESM-LR-C, EC-EARTH-C, CNRM-CM5-C, HadGEM2-ES-C, and Ensemble median (from left to right). Reprinted from Hundhausen et al. (2024).

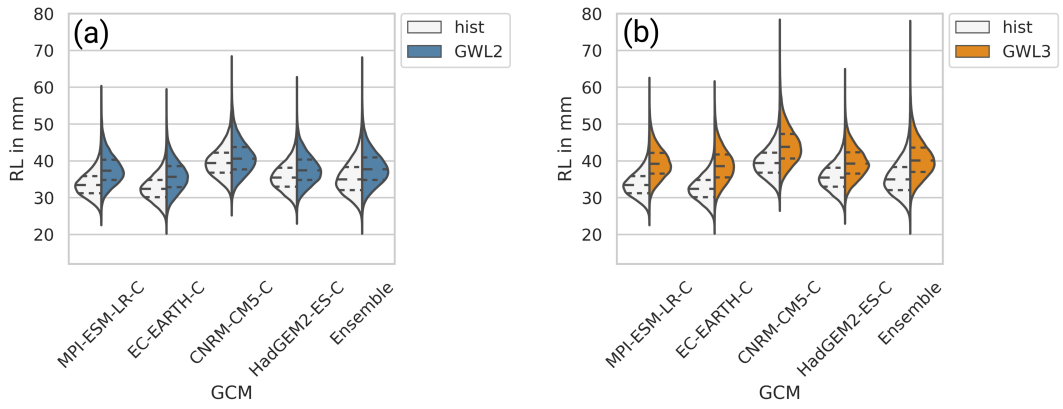

Figure 5.12: Distribution of hourly 10-year RL over the evaluation area for (a) GWL2 and (b) GWL3. The distribution in white represents the results from the reference period 1971-2005. Reprinted from Hundhausen et al. (2024).

In summary, sensitivity analysis provides evidence that there is a substantial residual standard deviation in the linear fit (5 % confidence interval from 0.8 to 2 PPT) and that uncertainty is expected especially for large-scale events. The ensemble spread in the multi-GCM, single-RCM ensemble is significantly smaller for small-scale events (2–3 PPT) than for large-scale events (up to 6 PPT). Analysis of the spatial distribution of the climate change signal revealed a standard deviation in the order of magnitude of the climate change signal itself for large RP. Further analysis of the spatial distribution shows that the change in mean RL is accompanied by an increase in variance.

5.6 Discussion and conclusion

Based on the analysis of extreme precipitation in the transient CPM climate ensemble over Germany, we compare simulated RLs to observation-based extreme values, derive climate change signals of RLs, and assess their uncertainties. The chapter draws three main conclusions:

- The CPM simulations show a good coverage of the range of hourly precipitation intensity observed at the stations. Compared to the station observations and to KOSTRA, a better agreement with the CPM simulations is found for RLs with short EDs. In general, the simulations overestimate the RL for EDs longer than 1 h.
- The CPM simulations project climate change signals of extreme precipitation intensities of up to 6 or 8.5 % increase per K increase in GWL depending on the ensemble member. Events with short duration and long RPs are expected to change the most.
- Analysis of the uncertainty in the climate change signal revealed a substantial residual standard deviation of the linear approximation of RLs with GWL. The

model spread is significantly smaller for short ED. The apparent spatial uncertainty implies that estimates for long RP are only possible for pooled spatial information. Furthermore, the spatial variance is expected to increase with climate change.

The comparison of the CPM ensemble with station data shows the agreement of the hourly intensity range in CPM and an added value in the fractional contribution of precipitation intensities compared to conventional, convection parametrised simulations (here 7 km). This more realistic representation of rain events, especially of short duration, is consistent with previous research (Ban et al., 2014; Chan et al., 2014b; Fosser et al., 2015; Ban et al., 2020). Also the tendency to overestimate observed heavy rainfall in the CPM aligns with previous analyses (Kendon et al., 2012; Fosser et al., 2015).

Spatial patterns of extreme precipitation associated with orography are represented in the CPM ensemble for longer, daily durations. However, likely due to the relatively short time series length, shorter (hourly) extremes do not reflect spatial patterns without the application of regionalization techniques. Still, our confidence in RLs from CPM is higher for short (hourly to sub-daily) events than for daily to multi-day events due to better agreement with station data and KOSTRA. The mean absolute bias is usually – but not necessarily – smaller for short RPs. The relative mean bias generally decreases with RP for sub-daily (except hourly) ED and increases for daily to multi-day events. In general, RLs are overestimated by CPM. An underestimation of the RL was only found for the shortest evaluated ED of 1 h and high RP. We have higher confidence in the three ensemble members driven by MPI-ESM-LR, EC-EARTH, and HadGEM2-ES, due to a larger overestimation for the simulation driven by CNRM-CM5. We expect a mean bias in the order of ±10 % for hourly ED, up to 23 % for sub-daily events with ED>1 h and up to 27 % for daily and longer events in the CPM ensemble, excluding CNRM-CM5-C. The findings complement previous comparisons of simulations with KOSTRA or observations by Berg et al. (2019); Poschlod et al. (2021); Ban et al. (2020), who described increasing overestimation with ED by the simulations but for coarser resolution. As we assume a systematic bias in the simulations and shortcomings in the observations, we support the concept of climate change factors or uplifts (Chan et al., 2022) for a more robust assessment of future extreme precipitation.

There is agreement among the ensemble members that extreme precipitation increases with GWL on all time scales considered. Fig. 5.13 summarizes the main patterns in the ensemble regarding the relative climate change signal: For sub-daily events, the change signal increases with RP. In contrast, for large-scale events (ED=72 h), the change signal is relatively constant or decreases with RP. The strongest change signals are associated with the shortest ED and tend to decrease with larger ED for sub-daily events. For daily to multi-day events, no consistent pattern could be derived. The highest change signals are therefore associated with the shortest ED (hourly) and large RP, where an increase of 6 to 8.5 % is projected, which is in the range of CC-scaling to slightly super-CC scaling. This strongest increase of extreme precipitation for short

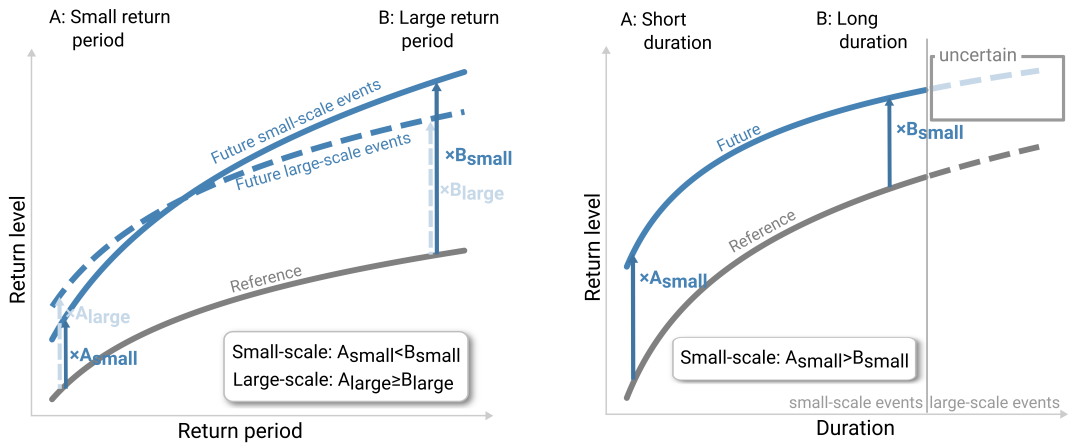

Figure 5.13: Schematic for the development of future intensity and duration curves. Changes are expressed in terms of relative change factors. The dependency of those change factors $A_{\text{small/large}}$ and $B_{\text{small/large}}$ on return period and duration is illustrated. The absolute values are not the subject of the diagram. Reprinted from Hundhausen et al. (2024).

rainfall events is in agreement with previous research (Lenderink et al., 2021; Hodnebrog et al., 2019; Berg et al., 2019; Rajczak and Schär, 2017; Ban et al., 2020, 2015).

The finding of a larger increase for more rare events from hourly to daily duration is consistent with previous findings based on regional climate projections (e.g. Li et al., 2019; Rajczak and Schär, 2017; Helsen et al., 2020; Ban et al., 2015). For very long, multi-day events, we could not identify an increase in the change signal with RP. Ban et al. (2020) found a similar behaviour of 5-day events in winter over the Alpine region. This behaviour of long events is likely influenced by shifts in the large-scale circulation patterns.

The sensitivity analysis showed that there is a substantial residual standard deviation for the linear fit of the intensity trajectories over GWL, especially for long EDs. The ensemble spread is significantly smaller for small-scale, sub-daily events (2–3 PPT) than for large-scale, multi-day events (up to 6 PPT). This difference is attributed to the influence of large-scale circulation patterns on long events (Kautz et al., 2022) carried by the GCM, while small-scale events depend more on the thermodynamic representation in the CPM. The spatial distribution of the climate change signal was shown to have a standard deviation in the range of the magnitude of the change signal itself for large RP. This suggests that robust estimates can only be derived from the distribution of results or pooled spatial information. Moreover, the width of this spatial distribution is found to increase with global warming, indicating an increasing variability of extreme events.

Limitations of the analysis are that our conclusion is based on CMIP5 simulations and only four ensemble members and thus results potentially differ for other CMIP-based ensembles. Comparing daily extremes of annual RPs, Seneviratne and Hauser (2020) did not find different climate change signals in CMIP6 compared to CMIP5 in

Central Europe. However, there are indications of an added value of CMIP6 simulations, including a better representation of blocking for some models (Schiemann et al., 2020). Furthermore, our analysis is limited to one RCM, which is suggested to largely determine the representation of short events. The uncertainty in the change signal for small-scale events may not be fully captured in the multi-GCM and single-RCM ensemble used. A matrix of CMIP6 GCMs and RCMs, such as is currently being targeted in the project NUKLEUS (Actionable local climate information for Germany), could be key to clarifying the robustness of trends in future ensembles.

The analysis also highlighted uncertainties in the methods used to estimate future extreme precipitation statistics. The variability in the results of individual grid points was discussed and is probably determined by short time series and therefore limited occurrence of rare events. Future investigations making use of the increasing number of CPM simulations available will show whether the uncertainty can be reduced with additional model data. In addition, spatial pooling approaches could reduce uncertainty in RL estimates. For example, Chan et al. (2022) were able to resolve spatial patterns of short events using a regression model.

Overall, the analysis emphasises that new products for rainfall risk management are needed today for sustainable (future/long-term) planning and management of climate adaptation and gives an indication of which thresholds are particularly sensitive to climate change, namely short-duration and long RPs. Moreover, we found an increased variability of future extreme precipitation. This is expected to pose a challenge for the application as the incorporation of uncertainty, also in impact modelling, may become more important. To avoid underestimating the risk, more conservative approaches that consider higher percentiles than the median may be reasonable.

In addition, the chapter emphasises the considerable standard error associated with evaluating individual time slices as it is common practice in CPM downscaling. By utilizing a transient projection and considering inherent variance, we obtained a more robust change signal. This highlights the benefits of conducting long transient ensemble simulations and underscores the necessity for such simulations.

6 | EVALUATION OF PRECIPITATION EVENT PROFILES IN THE CPM ENSEMBLE

This chapter is an edited version of the following article in Weather and Climate Extremes:

> Hundhausen, M., H. J. Fowler, H. Feldmann, and J. G. Pinto, 2025: Sub-hourly precipitation and rainstorm event profiles in a convection-permitting multi-GCM ensemble. Weather and Climate Extremes, 48, doi: 10.1016/j.wace.2025.100764.

Minor changes have been made to make the article coherent in the context of this thesis.

6.1 Introduction

The findings from Chapter 5 indicate that the intensification of extreme precipitation in a warming climate in Germany is strongest for short and intense precipitation spells. The largest climate change signal was indeed found for intensities over the shortest temporal window analysed in Chapter 5 of 1 h. This prospect is a major concern because short and heavy precipitation peaks have the potential to trigger flash floods (Archer and Fowler, 2018). Their short response time, rapid water level rise and great runoff peak depths can lead to high mortality (Archer and Fowler, 2018) and cause significant damage, especially in urbanized areas (Darwish et al., 2018).

Besides the precipitation depth and the peak precipitation, the impacts of an extreme event are also influenced by its temporal profile, including the timing of the peak intensity (Hettiarachchi et al., 2018; Lambourne and Stephenson, 1987; Müller et al., 2017; Ng et al., 2020; Zhu et al., 2018), which often occur on sub-hourly time scales. Accurately representing sub-hourly time scales in climate models, including the temporal profiles of extreme precipitation events, is crucial for adjusting design storm profiles for climate adaptation and for confidence in the projected climate change signals. However, previous CPM studies analysing extreme precipitation events have often been limited to daily or, less frequently, hourly model output (Kendon et al., 2012; Chan et al., 2023a; Fosser

et al., 2020, 2024; Müller et al., 2023), and little is known about sub-hourly extremes in CPMs (Chan et al., 2016b; Meredith et al., 2020; Purr et al., 2021).

Therefore, this chapter investigates sub-hourly precipitation in the KIT-KLIWA ensemble. For three ensemble members, we compare extreme precipitation at a temporal resolution down to 5-min for the historical simulations (1971-2000) with the dense observation network over Germany. This represents the most comprehensive, and the only multi-model, study of sub-hourly precipitation in a convection-permitting climate ensemble to date. While common analytical approaches remove the natural temporal correlation structure of precipitation events, we develop an event-based approach to improve the understanding of the precipitation biases in CPM simulations by examining the representation of (sub-hourly) characteristics of rainstorms in CPM historical simulations.

This chapter addresses the research question: How well does the CPM ensemble reproduce the temporal profiles of extreme precipitation events compared to observations? To address the research question, the analysis is built on the following three steps:

a) Assessment of the 5-min precipitation frequencies in the CPM historical simulations evaluated with station and radar observations.

b) Development of a precipitation event-based analysis method based on 5-min precipitation time series.

c) Characterisation of extreme precipitation events in the historical CPM simulations and assessment of bias by comparison with observational data.

The chapter is structured as follows: Section 6.2 provides a description of the methods with a focus on the development of the event-based analysis. Section 6.3 presents the results of the 5-min frequency analysis in the CPM and observational data. Section 6.4 presents the first results of the event-based analysis with an overview of the detected events. Section 6.5 evaluates the simulated event characteristics against observational data. The discussion and conclusions are provided in Section 6.6.

6.2 Methods

6.2.1 Development of an event-based analysis

In an event-based analysis, a rain event is defined as a series of precipitation recordings separated from the next event by a sufficiently long rain-free period, which is referred to as the inter-arrival time.

The inter-arrival time

Event-based approaches often rely on a subjectively defined interval based on expert knowledge of the climatology of precipitation in the region of interest (Villalobos Herrera

et al., 2023b). Statistical approaches have been proposed to provide a more objective definition of inter-arrival time. We follow the approach formulated by Restrepo-Posada and Eagleson (1982) and successfully implemented and applied to rainstorm observations in the UK by Villalobos Herrera et al. (2023b).

When events of "point" or "instantaneous" occurrence occur randomly over time, their arrivals are described by a Poisson process. For such events, the distribution of intervals, t_a, between Poisson arrivals is distributed exponentially:

$$f(t_a) = \omega e^{-\omega t_a} \tag{6.1}$$

with $t_a \geq 0$ and the average arrival rate ω. However, in contrast to the mathematical concept, precipitation events have a finite event duration t_r. Restrepo-Posada and Eagleson (1982) argue that the arrivals of independent rainstorms are still adequately described by a Poisson process if the following condition holds:

$$\omega \overline{t_r} \ll 1 \tag{6.2}$$

Given the additional condition is maintained, the time between precipitation events, t_b, is exponentially distributed with the same goodness-of-fit as Eq. 6.1. The respected relationship is provided by Eq. 6.3.

$$f(t_b) = \beta e^{-\beta t_b}, t_b \geq 0 \tag{6.3}$$

We expect that two precipitation records separated by a small t_b have a high probability of being embedded within the same synoptic or even mesoscale event - and the two recordings are not considered independent. The probability of small t_b is therefore high. Increasing the t_b, we expect the dependence of the events to vanish. Consequently, only t_b above a certain threshold $t_{b,\min}$ is expected to follow an exponential distribution (Restrepo-Posada and Eagleson, 1982). $t_{b,\min}$ refers to the minimum inter-arrival time above which precipitation events are assumed to be independent. Based on Villalobos Herrera et al. (2023b), $t_{b,\min}$ can be increased iteratively until an exponential distribution is reached. For details on implementation, see the supporting information in Villalobos Herrera et al. (2023b).

For our study, we evaluated the minimum inter-arrival time for station observation as well as for radar data and CPM simulations. The calculation was conducted for each station separately. For the radar and CPM simulations, the minimum inter-arrival time was evaluated on a sparse matrix of every 50th grid point only due to computational resources. This sub-sample is assumed to be representative of the full grid. To avoid low rainfall amounts present in the gridded data, every 5-min recording below 0.01 mm is set to zero before the calculation. We find a dependence of the minimum inter-arrival time on the dataset as well as geographic location. However, to ensure comparability, a constant inter-arrival time was chosen across all datasets. As a compromise to best

represent all datasets, the average value of $t_{b,\min}$ in the radar dataset 7.5 h was chosen. Detailed results for the estimation of the inter-arrival time are provided and discussed in Section 6.4.

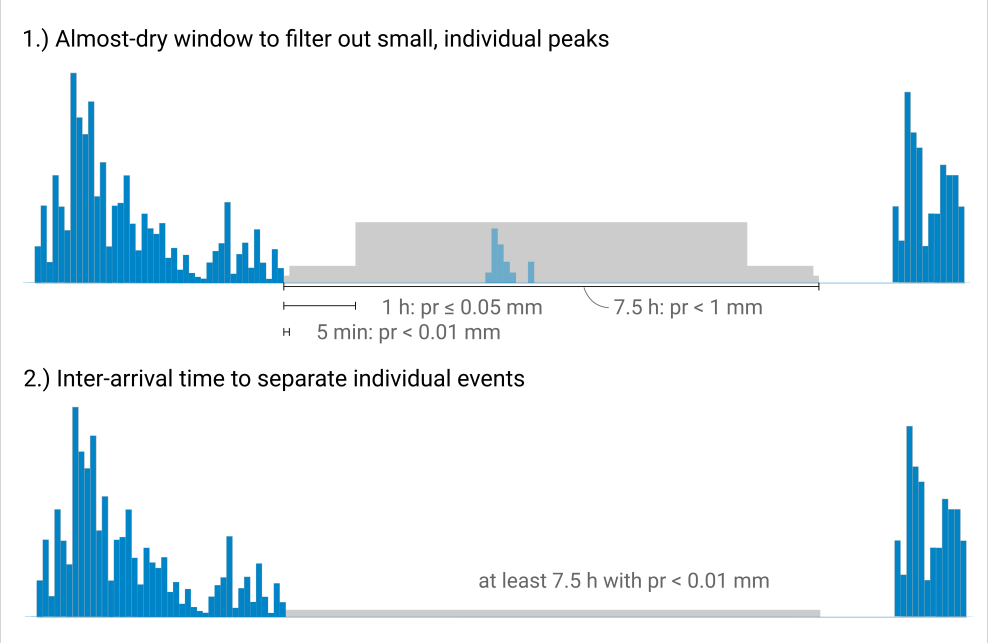

Figure 6.1: Schematic of the event selection procedure: Application of the almost-dry window in the first step, and separation of the independent events over the inter-arrival time in the second step.

In addition to defining independent events by minimum inter-arrival time, we introduce an almost-dry window – a period with little rain, where precipitation is set to 0 – to avoid very long precipitation events with large dry fractions (Fig. 6.1). The almost-dry window is defined as an interval of 7.5 h with precipitation intensities below 1 mm. To ensure not to cut off the tail or front of a precipitation event, the condition was imposed that precipitation has to be below 0.01 mm (approximated value of zero precipitation in the gridded data) directly adjacent to the main event and ≤ 0.05 mm in the 1 h before/after the main event to be considered an almost-dry window. The method is similar to the approach in Villalobos Herrera et al. (2023b) but uses user-defined windows. A schematic of the method is provided in Fig. 6.1. In addition, as shown in Fig. 6.2 for the 2016 heavy precipitation event in southern Germany, leading to a flash flood in the Braunsbach catchment (e.g., Piper et al., 2016), the almost-dry window removes individual peaks before and after the main event and reduces the precipitation event to a reasonable length.

Event characterization

After the extraction of the independent precipitation events from the time series, several event characteristics are assessed (Fig. 6.2).

- The event duration refers to the time from the first to last 5-min precipitation interval recorded during the event.

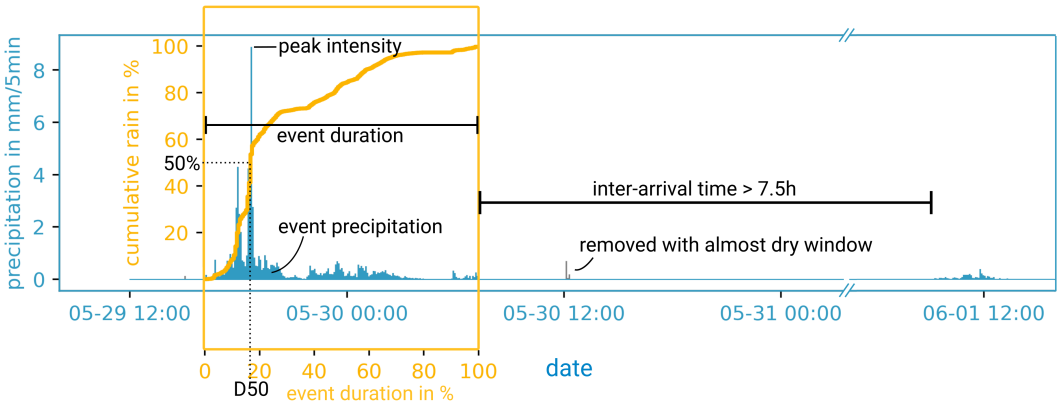

Figure 6.2: Example event analysis for the DWD station Kupferzell-Rechbach during the flood event in the Braunsbach catchment in 2016. The detected precipitation event extends over the yellow box. Grey precipitation records are filtered out by the almost-dry window. The event characteristics of event duration, peak intensity, event precipitation, and D50 are shown in the schematic. Reprinted from Hundhausen et al. (2025).

- The precipitation event sum describes the total precipitation summed over the entire duration of the event.
- The mean intensity, I_{mean}, is defined as the ratio between the precipitation event sum and the event duration.
- The maximum peak intensity, I_{max}, is the maximum 5-min precipitation recorded.
- The temporal profile or shape of an event is parametrised by the measure D50 (Visser et al., 2023). D50 is the percentage of the event's duration at which 50 % of the cumulative precipitation sum of the event is reached (Fig. 6.2). Events with a small D50 describe a front-loaded event, while events with a large D50 describe a back-loaded event. We further refer to events with a D50≤20 % as very front-loaded, 20 %<D50≤40 % as front-loaded, 40 %<D50≤60 % as centred, 60 %<D50≤80 % as back-loaded, and D50>80 % as very back-loaded.

The code for event-based analysis was implemented in Python. Parts of the code for event selection are based on Pichler (2024). The code for the calculation of the inter-arrival time was implemented by Villalobos Herrera et al. (2023b).

6.2.2 The event catalogue

We apply the method developed for event selection and characterization to CPM simulations and observational data. For the CPM simulations, we use the KIT-KLIWA ensemble members EC-EARTH-C, HadGEM2-ES-C, and MPI-ESM-LR-C, for which 5-min precipitation data are available. This analysis focuses on the historical period 1971–2000. The final domain of the KIT-KLIWA ensemble was truncated for this study in the south to exclude mountainous terrain in the Alps and in the west to align with the German border (Fig. 6.3). The analysis is limited to the German part of the domain to match the available observational data coverage.

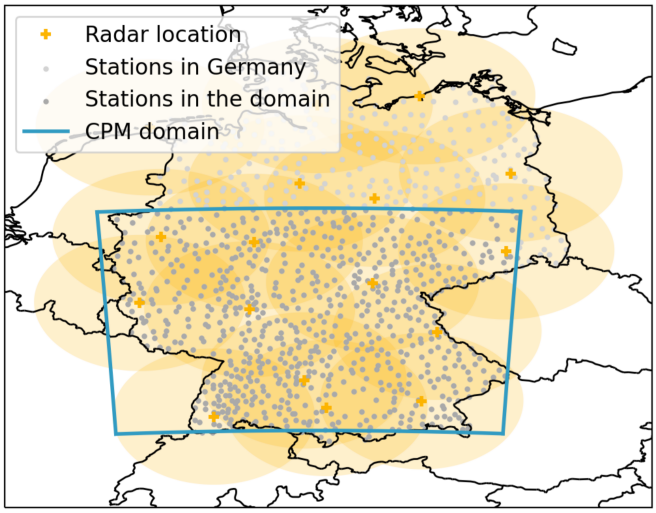

Figure 6.3: Overview of the data analysed in this chapter with simulation domain, stations, and data coverage of the measurements. Yellow shading shows the theoretical coverage of the 17 radars.

For comparison, we analyse precipitation events in station and radar data. Refer to Chapter 4 for details regarding the two datasets. We analyse precipitation recordings from stations within the model domain (Fig. 6.3). The quality control of the station measurements is carried out by the DWD and only quality-controlled data are used. For the event-based analysis, only years with data availability of >80 % data are included. The analysis encompasses data up to 2022, the most recent year with complete availability at the time of the study. The first 5-min station data are available from 1995. The first station recordings that fulfil the criteria to be included in the event-based analysis are in 2002. A summary of data availability is provided in Table 6.1, with detailed information on the specific years analysed available in Supplementary Fig. C.1.

Table 6.1: Overview of the event catalogue analysed. The data availability for the observational data indicates the total number of analysed years, and does not reflect sub-annual data gaps. Data coverage in the radar model grid is calculated as analysed years at all grid points / (18 years in the full dataset × number of grid points).

Data	Period	Data availability
Stations	available data until 2022	686 stations, in average 16.6 years analysed
Radar station grid	2003-2022	677 grid cells, in average 16.4 years analysed
Radar model grid	2003-2022	96 %
KIT-KLIWA ensemble	1971-2000	EC-EARTH-C, HadGEM2-ES-C, MPI-ESM-LR-C

The second observational dataset used is the Radolan radar data (details are in Chapter 4). Due to limited data coverage during the initial years of radar operation, the present study focuses on the 20-year period from 2003 to 2022. For this analysis, the

radar data are interpolated conservatively to the model grid at 2.8 km resolution. The interpolated data are hereafter referred to as the "radar model grid". The interpolated radar data are analysed only over Germany to match the station measurements and to avoid sparse data coverage outside of Germany (Fig. 6.3). For the event-based analysis of the gridded radar data, the maximum missing data per year and grid cell was restricted to 5 %. Additionally, radar data were analysed at their original 1 km×1 km resolution, using the nearest-neighbour grid cell to station locations. This approach was applied only for the years in which station data were available, facilitating direct comparisons between the two datasets (notation "radar station grid"). An overview of the data availability is given in Table 6.1, with detailed information on the specific years analysed available in Supplementary Fig. C.1. We note the different periods compared in CPM simulations and observations.

6.3 Sub-hourly precipitation frequency in the CPM ensemble

The frequency distributions of the precipitation datasets are first analysed from the precipitation sum over a running window for the four different durations of 5 min, 15 min, 1 h and 6 h. This conventional analysis in this section is therefore based on the continuous time series, while the *event-based* analysis is presented later in Sections 6.4 and 6.5. The distributions shown are composites over all stations or grid points in the analysis domain. The frequency analysis shows high occurrence of low intensity precipitation and a decreasing occurrence with increasing intensity (Fig. 6.4a-d). Comparing the two observational datasets, there is good agreement between the station and radar observations for low to moderate precipitation intensities. Low intensities are slightly underestimated in the radar data for sub-hourly aggregations (Fig. 6.4a-b). Equally, the radar data underestimate the frequency of high and extreme intensities compared to the station measurements for all aggregations. This is particularly the case for short aggregations, where the underestimation is larger if the radar dataset is at coarser resolution (i.e. radar on model grid with 2.8 km×2.8 km resolution compared to radar on station grid with 1 km×1 km resolution). In general, this difference can be attributed to the different characteristics of the datasets: while stations provide point measurements, the radar output is a gridded dataset and thus representative for an, albeit limited, area. As expected for a short temporal resolution, local high-intensity precipitation bursts, captured by local, point-like measurements, provide higher extreme values, in contrast to the larger spatial aggregations of precipitation provided by radar products.

In general, the CPM ensemble members reproduce the shape of the observed precipitation frequency curves and there is close agreement of the frequency distributions within the ensemble members (Fig. 6.4a-d). A systematic bias in the overestimation of low intensities compared to observations is apparent across all temporal resolutions from 5 min to 6 h. For the extremes, the model bias differs depending on the temporal

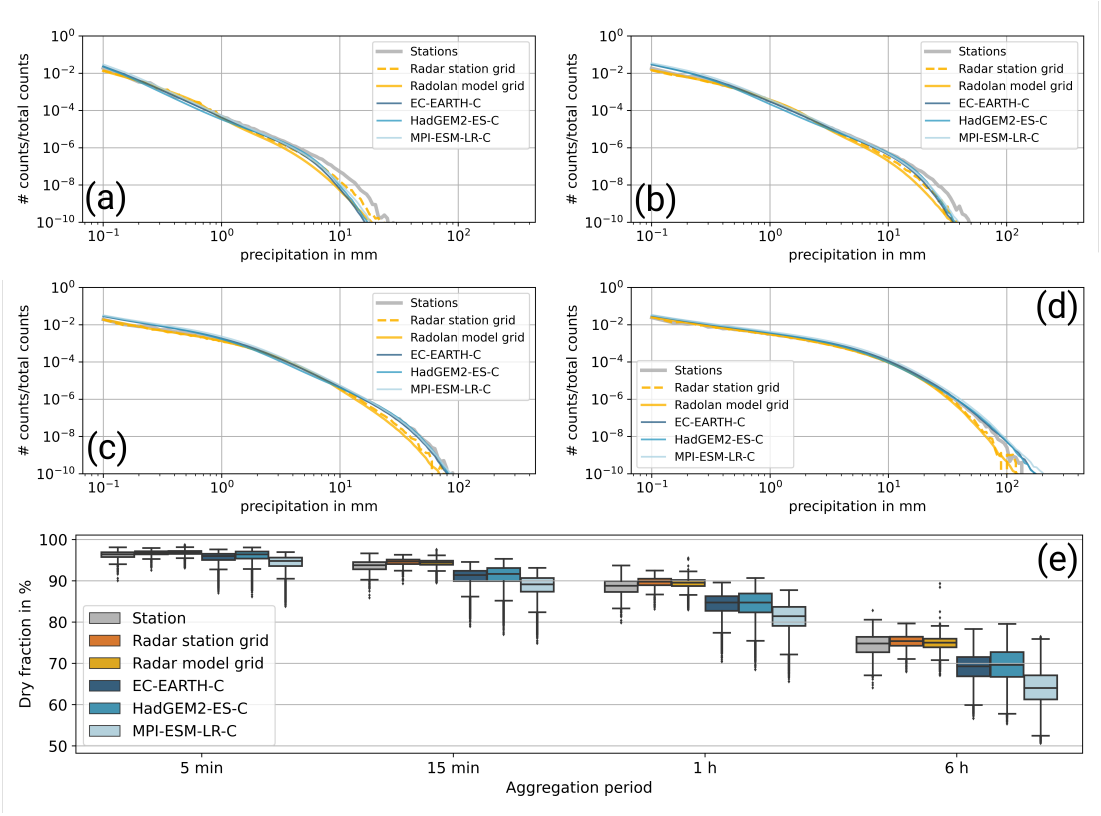

Figure 6.4: Normalised frequency distribution for observational datasets and CPM simulation outputs over all grid points/stations in the evaluation domain for (a) 5-min, (b) 15-min, (c) 1-h, and (d) 6-h durations. Panel (e) shows the dry fraction in the respective datasets and durations. Samples with <0.05 mm within the aggregation period are defined as dry. Reprinted from Hundhausen et al. (2025).

aggregation. Extreme values in the 5-min simulations mainly agree with the results of the radar dataset, while using a temporal resolution of 6 h, there is an overestimation of extreme intensities compared to the observations. Therefore, extreme precipitation intensities in the CPM simulations seem to increase in comparison to the observations for increasing temporal aggregation.

The percentage dry fraction is highest at the shortest temporal resolution of 5-min and decreases with increasing duration (Fig. 6.4e). Comparing the two observational datasets, the radar data show slightly higher dry fraction compared to the station data. This difference appears less pronounced at higher temporal resolutions. In general, there is a close agreement in the simulation of percentage dry fraction between the two radar dataset resolutions, on the station grid (1 km×1 km) and on the model grid (2.8 km×2.8 km), with the coarser resolution dataset showing a slightly lower dry fraction. The differences result from both, the different resolutions and the smaller number of locations sampled in the radar station grid. Within the CPM ensemble, agreement is good for members driven by EC-EARTH and HadGEM2-ES. MPI-ESM-LR-C shows a significantly lower dry fraction, which is consistent with the much higher precipitation totals simulated in MPI-ESM-LR-C (cf. following Table 6.2). In general, all simulations

show a systematically lower dry fraction compared to observations, with wet bias increasing with increasing temporal aggregation.

Our analysis of precipitation frequencies in the CPM ensemble compared to observations indicates that the sub-hourly 5-min CPM outputs adequately reproduce the observed precipitation frequency distribution over Germany, although the CPMs underestimate the frequency of the most extreme precipitation intensities compared to the station observations but are in agreement with the frequency distribution from the radar dataset. The representation of extreme precipitation events in the CPM simulations is dependent on the temporal aggregation and modelled extreme intensities are higher at longer duration compared to the observations. This leads to an overestimation of extreme precipitation at low temporal resolutions by the CPMs. Our findings imply that the CPM precipitation bias depends on the aggregation duration; this points towards a systematic bias in the temporal representation of precipitation in the CPM time series. We conclude therefore, that it is crucial to retain the natural temporal correlation structure of the precipitation sequence to evaluate the precipitation bias in CPM simulations; thus, not using a typical ranked analytical approach. We propose to use an event-based analysis to help to improve the understanding of precipitation biases in CPM simulations.

6.4 The representation of precipitation events in CPM

6.4.1 Inter-arrival time

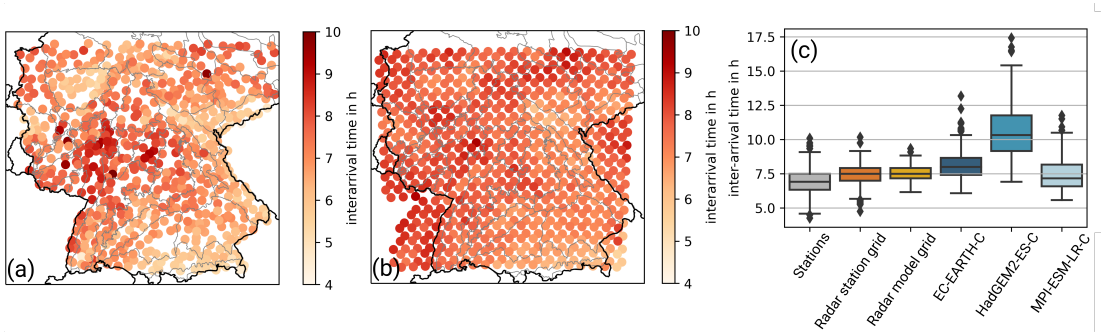

Figure 6.5: Spatial distribution of the inter-arrival time in (a) station and (b) radar datasets. (c) shows the distribution of inter-arrival time over the German part of the domain for the observed datasets and the CPM simulations. Reprinted from Hundhausen et al. (2025).

The minimum inter-arrival time over the study area shows a spatial pattern related to the altitude or the mean annual precipitation, which correlates with the former (Fig. 6.5a-b). The higher the altitude (or the higher the mean annual precipitation), the shorter the detected inter-arrival time. This observed spatial pattern is reproduced by the CPM ensemble members (Supplementary Information Fig. C.2 and Fig. C.3). The inter-arrival time in the station data is typically between 6.3 h to 6.9 h (25th and 75th

percentile). The inter-arrival time for the radar dataset is significantly higher, from 7.2 h (7.0 h) to 7.9 h (7.9 h) (25th and 75th percentile for radar on model grid and for station grid in brackets) and shows lower overall variance. The spatial resolution of the radar data seems to have little effect on the result, with the higher resolution of 1 km×1 km being slightly closer to the station results than the coarser 2.8 km×2.8 km model grid. The observations of inter-arrival time over Germany agree well with the results of Villalobos Herrera et al. (2023b) for south-west Britain, where they found an inter-arrival time predominantly between 6 and 9 h. CPM ensemble members EC-EARTH-C and HadGEM2-ES-C tend to show higher inter-arrival times than the observations (Fig. 6.5c). In particular, HadGEM2-ES-C appears to overestimate the inter-arrival time. MPI-ESM-LR-C has the shortest inter-arrival time in the CPM ensemble and therefore the best agreement with the observations. To enable comparability of the event-based analysis for the 6 datasets, a constant inter-arrival time was chosen for the analysis across all datasets. The average radar inter-arrival time of 7.5 h was chosen as a compromise to best represent all datasets.

6.4.2 Event distribution

Table 6.2: Annual mean precipitation for the different datasets over the model domain and overview of statistics for the event-based analysis.

Data	Precipitation in mm	Precipitation from events >5 mm in mm	number of events >5 mm
Stations	800	592	43
Radolan station grid	721	507	39
Radolan model grid	721	506	40
EC-EARTH-C	914	709	48
HadGEM2-ES-C	816	624	43
MPI-ESM-LR-C	1143	915	59

The event-based analysis divides the precipitation time series into rain events. The averaged precipitation sum in the station data is 800 mm per year, of which 592 mm (74 %) falls in events with a total of at least 5 mm of precipitation (Tab. 6.2). These rain events of at least 5 mm are hereafter referred to as significant events, thus excluding rain falling in the form of light showers or drizzle which contain only small amounts of precipitation that are presumably of little importance for the immediate hydrological response. Such significant precipitation occurs on average 43 times per year in the station measurements. The total annual precipitation is underestimated in the radar dataset compared to the *in-situ* measurements. The proportion of rain coming from significant events is also slightly lower (70 %), with a range of 39 to 40 significant events per year (Tab. 6.2). The results of the radar on the station grid and the model grid are consistent.

All CPM simulations overestimate total precipitation, which is a known outcome for CPMs (e.g., Prein et al., 2015). Depending on the forcing data, this overestimation

varies strongly, with particularly high overestimation for MPI-ESM-LR-C (Tab. 6.2). The proportion of rain from significant events is from 76 to 80 %, thus slightly higher in the CPMs than for observations. The number of significant events also varies between forcing models. With 43 significant events per year, the HadGEM2-ES driven simulation is in agreement with the station measurements. The EC-EARTH and MPI-ESM-LR driven runs show more significant events than observed, with 48 and 59 events per year.

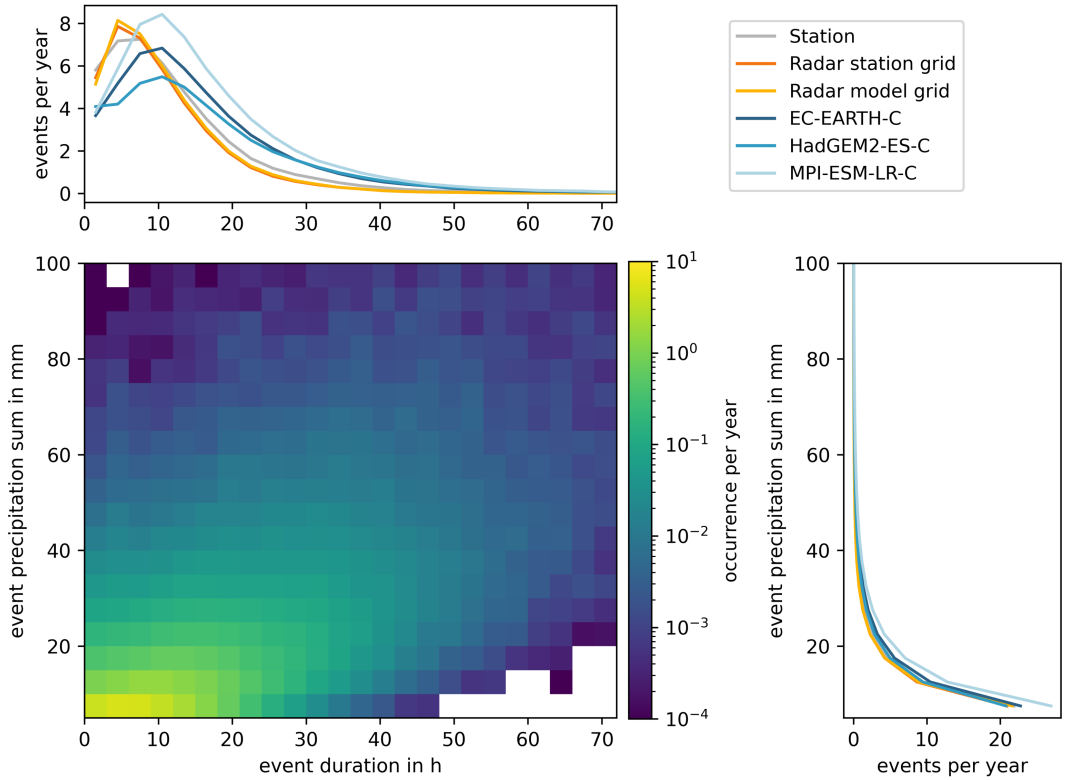

Figure 6.6: The distribution of annual mean event frequency regarding event duration and event precipitation sum averaged over the station measurements is shown. The marginal distribution on the x-axis shows the respective frequency distribution for station, radar and the CPM ensemble members over the event duration, the marginal distribution on the y-axis shows the distribution over the event precipitation sum. Reprinted from Hundhausen et al. (2025).

In general, significant events have most often relatively low intensities and their frequency decreases with event precipitation sum (Fig. 6.6). Significant event duration peaks at 6-9 h for the station measurements. Short-duration significant events are mainly associated with small event precipitation sums and their frequency decreases with event precipitation sum (Fig. 6.6). While the distribution patterns of event precipitation sum are largely in agreement between the radar observations and the CPM models, there are some discrepancies, as the radar tends to show shorter event durations. There is no notable difference between statistics for the radar dataset at the station grid and on the model grid. The CPM simulations tend to have longer event durations than observations. Fig. 6.7a-c shows that the occurrence of short events is consistently underestimated in the CPM ensemble. The underestimation is strongest for short events with low

precipitation totals up to about 15 mm. The occurrence of longer events however is overestimated by the CPMs. The normalized differences shown in Fig. 6.7d-f indicate that events with small precipitation totals are generally underestimated by the CPMs and not compensated for by longer events with the same precipitation totals. This leads to a general overestimation of event precipitation in all CPM ensemble members compared to observations.

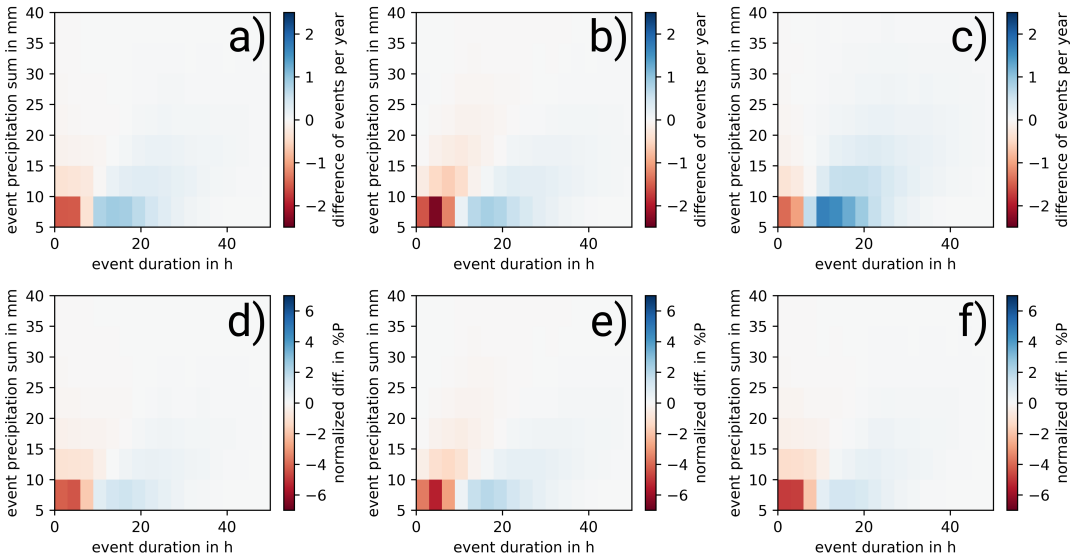

Figure 6.7: The difference in event occurrence in the CPM simulations from the observed station distribution is shown in the first row for (a) EC-EARTH-C, (b) HadGEM2-ES-C, (c) MPI-ESM-LR-C. In the second row, the normalized differences are shown for (d) EC-EARTH-C, (e) HadGEM2-ES-C, (f) MPI-ESM-LR-C. For the normalization, the mean annual event occurrence is scaled to 100 % and the differences are displayed in percentage points. Reprinted from Hundhausen et al. (2025). The respective comparison of station and radar observations is provided in the supporting information Fig. C.4.

Our results provide evidence that the precipitation bias in the ensemble CPM simulations is attributable to two factors. First, the occurrence of significant events seems to be overestimated in the CPM ensemble members that show strong total precipitation overestimates. Second, the event-based analysis reveals an underestimation of the proportion of short and small precipitation events, but a tendency to overestimate the occurrence of longer events. This finding suggests that the CPM ensemble members analysed here have deficiencies in reproducing significant short precipitation events, which are likely to contain significant convection.

6.5 Profile characteristics of extreme events

The following section on the analysis of extreme events includes all events detected above that lead to an AM of either 1 h or 6 h duration at the respective station or grid point. Almost all of these hourly (Fig. 6.8a) and 6 h (Fig. 6.8b) AM occur in the

summer half-year (April to September). The peak of the observed AM occurrence is in June and July. The CPM simulations reproduce this seasonal pattern well, except for the ensemble member driven by HadGEM2-ES. We expect that due to a significantly too dry July in HadGEM2-ES-C compared to the observations, the probability of AM-generating precipitation event in July is too low. On the contrary, the probability of June extremes is overestimated in HadGEM2-ES-C. This strong seasonality implies that the AM-generating events of interest analysed below are a sub-sample of events in the annual cycle, and the following characterisation of AM extremes describes predominantly events in the warm season.

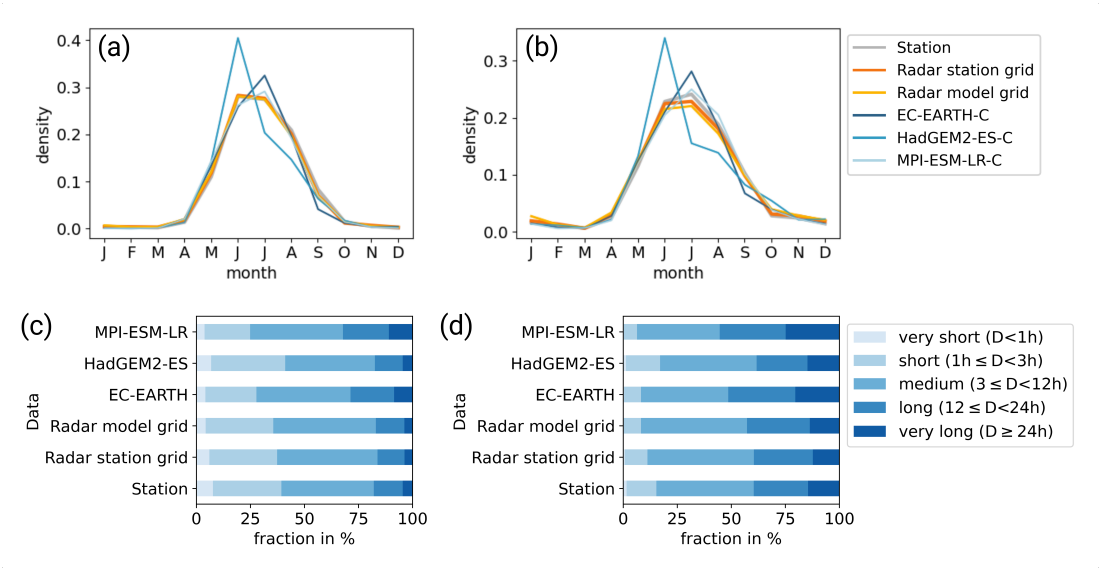

Figure 6.8: The density distribution of AM-generating events over the year in the study area for (a) 1 h-AM-generating events and (b) 6 h-AM-generating events is shown. The distribution of the duration, divided into five sub-categories, of (c) 1 h-AM-generating and (d) 6 h-AM-generating events is shown on the bottom. Reprinted from Hundhausen et al. (2025).

The event duration of AM-generating precipitation events reaches from the sub-hourly event duration to multi-day events (Fig. 6.8c,d). Comparing the two sets of observations for events leading to hourly annual maxima (AM), it is apparent that the larger the areal coverage of the measurement – from station data, a point measurement, to the radar station grid (1 km×1 km) to the radar on the model grid (2.8 km×2.8 km) – the lower the proportion of very short and short events (Fig. 6.8c). The same is seen for short events leading to 6 h AM (Fig. 6.8d). The proportion of very long events is also slightly larger in the station measurements compared to the radar dataset.

The CPM ensemble members MPI-ESM-LR-C and EC-EARTH-C show similar behaviour, underestimating the proportion of short events and overestimating the proportion of long events for hourly AM-generating events. Since the CPM simulations produce average precipitation over a 2.8 km×2.8 km grid, the hypothesis is that they may under-represent the occurrence of short convective events or their intensities. We

find that for 6 h AM-generating events, the proportion of short events is well represented in MPI-ESM-LR-C and EC-EARTH-C, but the occurrence of medium-length events is underestimated, and very long events are overestimated. The HadGEM2-ES-C simulation is characterized by significantly more very short and short events that generate AM. Therefore, the results for HadGEM2-ES-C are in good agreement with the station measurements for 1 h and 6 h AM-generating events.

In order to ensure comparability between statistics, we divide extreme events into three sub-groups: short events (1 h to 3 h), medium-length events (3 h to 12 h) and long events (12 h to 24 h). These categories cover the majority of events, as most events containing hourly and 6 h AM have a duration of 1 h to 24 h. The small proportion of very short (<1 h) and very long (>24 h) extreme events are not considered due to lower data availability and hence large variance. We analyse event precipitation sum, peak intensity and D50 for the three duration categories (short, medium, long) based on the visualization of the characteristics of hourly (Fig. 6.9) and 6 h AM-generating events (Fig. 6.10).

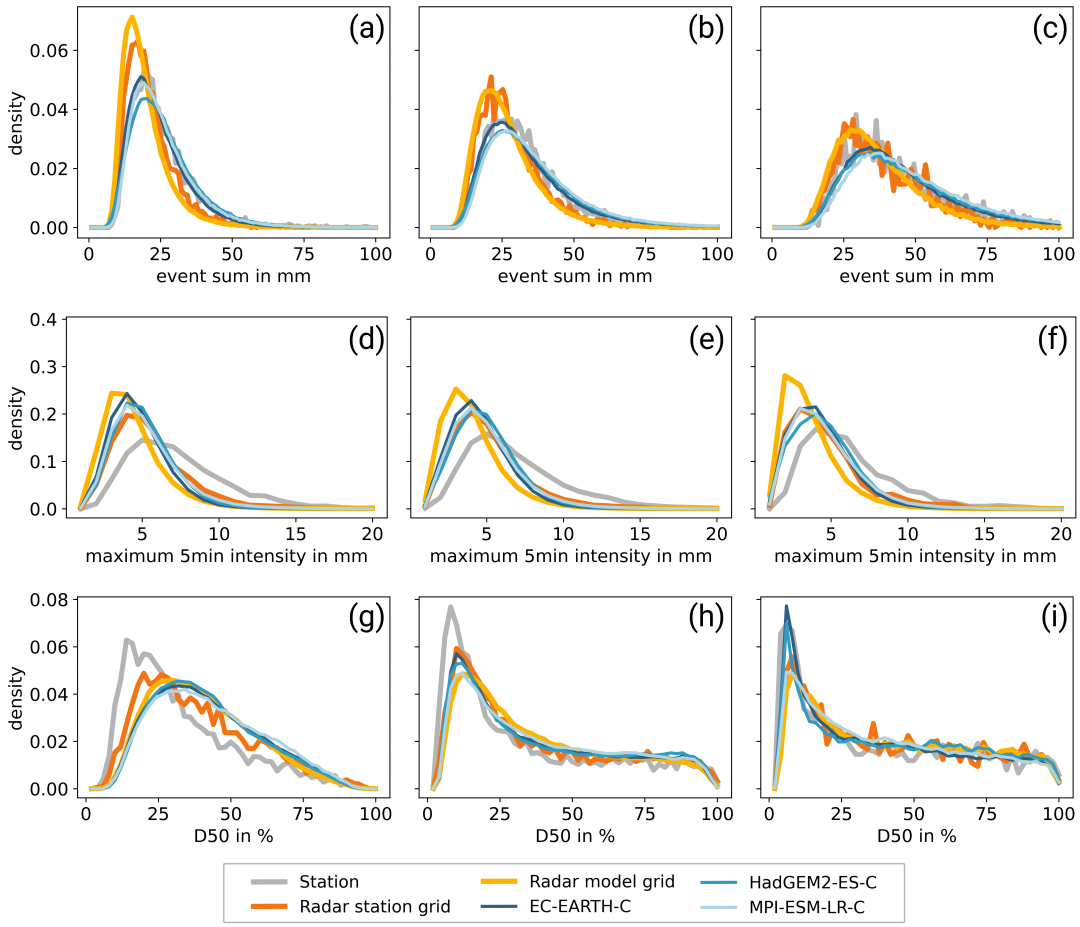

Figure 6.9: Event precipitation sum (first row), maximum 5-min intensity (second row), and D50 (third row) for 1 h AM-generating events of different duration categories of short (first column), medium (second column) and long events (third column). Reprinted from Hundhausen et al. (2025).

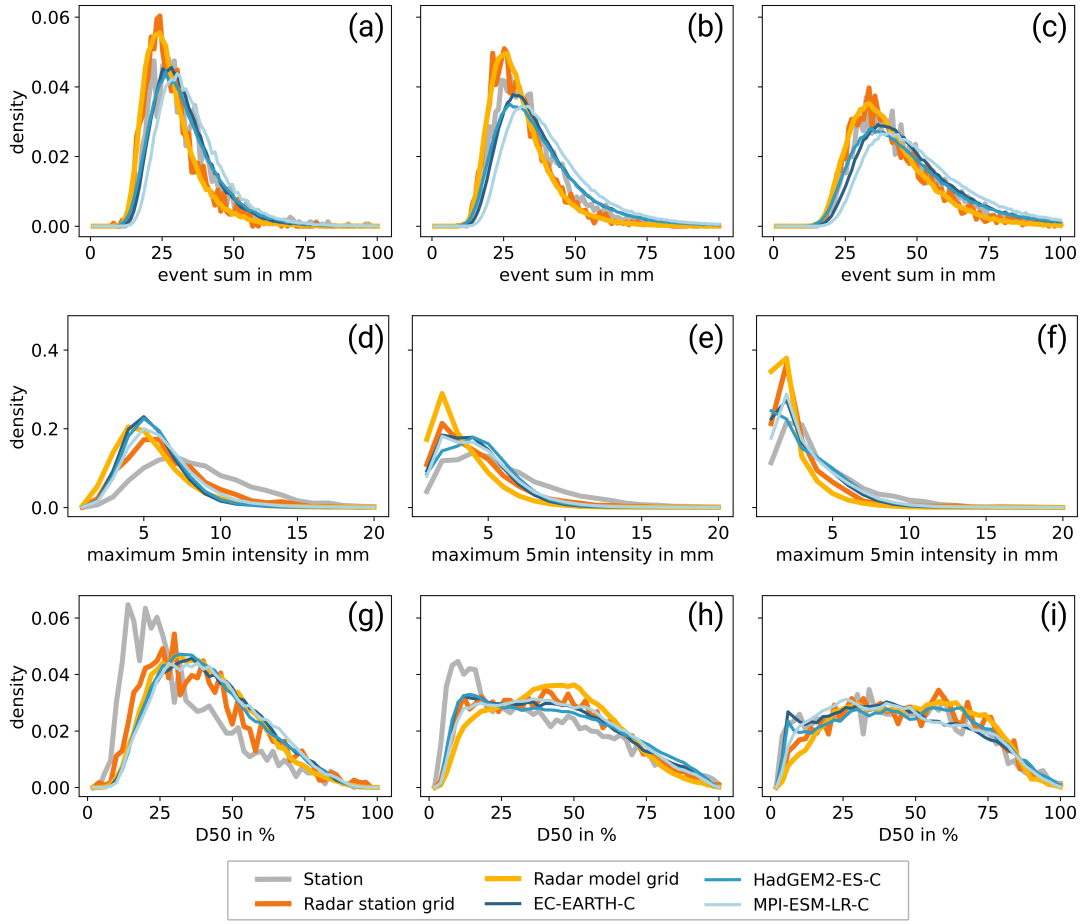

Figure 6.10: Event precipitation sum (first row), maximum 5-min intensity (second row), and D50 (third row) for 6 h AM-generating events of different duration categories of short (first column), medium (second column) and long events (third column). Reprinted from Hundhausen et al. (2025).

Event precipitation sum

The event precipitation sum in the station data for 1 h AM-generating events (and 6 h AM-generating events in brackets) typically ranges from 17.1 to 29.4 mm (23.3 to 36.7 mm) for short events, from 22.2 to 38.0 mm (24.8 to 39.9 mm) for medium events, and from 29.0 to 42.9 mm (32.0 to 52.0 mm) for long events (inter-quartile range). Two relationships are apparent; the longer the event generally the larger the event precipitation sum, and that events generating 6 h AM have generally more rain than 1 h AM-generating events. Both of these are reproduced by the other observational datasets as well as by the CPM simulations (Fig. 6.9a-c and 6.10a-c). In general, the radar data shows lower event precipitation sums compared to the station measurements, especially for short and medium events, with a similar result, on the model grid (2.8 km×2.8 km) and the station grid (1 km×1 km). Only for short events generating hourly AM is there a visible difference between the two radar resolutions, with a higher event sum on the 1 km grid (Fig. 6.9a). The underestimation of event precipitation sums in the radar

data compared to the station measurements is in accordance with an overall dry bias in the radar dataset (see Table 6.2).

There is generally good agreement within the CPM ensemble members. For 6 h AM-generating events, the event precipitation sum in MPI-ESM-LR-C is slightly higher than in EC-EARTH-C and HadGEM2-ES-C, which is in accordance with higher total annual precipitation in the MPI-ESM-LR driven simulation (see Tab. 2, Fig. 6.9a-c and 6.10a-c). The CPM simulations' event precipitation sum for short events and hourly AM is in good agreement with the station observations. The CPM simulations tend to overestimate the event precipitation sum slightly for medium events, and this overestimation is even stronger for long events. For 6 h AM-generating events there is a slightly more pronounced overestimation by the CPMs.

Peak intensity

A comparison of the different observational datasets shows a strong dependence on the measurement footprint. For the examined 1 h and 6 h AM-generating events, the 5-min peak intensity is lowest for the radar 2.8 km×2.8 km grid. The 1 km radar resolution shows higher intensities (Fig. 6.9d-f and 6.10d-f). The 95th percentile of 1 h (6 h) AM-generating events recorded by the station gauges is 12.8 mm (14.0 mm) for short events, 12.5 mm (12.0 mm) for medium events, 11.1 mm (9.2 mm) for long events; these are lower in the radar observation. In addition to the effects of areal reduction, it is expected that the general underestimation of precipitation in the radar data compared to station data contributes to the bias in peak intensity.

The 5-min peak intensity distribution in the CPM simulations show good agreement within ensemble members. The CPM peak intensity is, in general, higher than the radar on the model grid and, for the 1 h AM-generating event, agrees well with the 1 km×1 km radar data. Therefore, the CPM simulations of 5 min peak intensity are within the range of the two observational datasets (Fig. 6.9d-f and 6.10d-f). Although the 5-min maximum intensities in CPM simulations are below the station measurements, they agree well with the radar product.

D50

In the station data, the dominant fraction of 1 h AM- generating events is front-loaded (Fig. 6.9g-i). The mode of the distribution is below 20 % for the 1 h AM- generating events, which classifies as very front-loaded. For 1 h AM-generating events, the longer the event, the more pronounced the peak at the very front-loaded end of the distribution. For medium and long events, there are only a low and roughly equal proportion of centred to back-loaded events. For 6 h AM-generating events, the D50 distribution for short events shows a similar distribution to the 1 h AM-generating events of mainly (very) front-loaded events (Fig. 6.10g-i). However, in the station measurements the proportion of very front-loaded events becomes smaller with increasing event duration,

such that for long events the distribution has a slightly higher proportions of centred events compared to very front-loaded and front-loaded events. The smallest fraction are very back-loaded events.

Comparing station and radar data for 1 h AM-generating events, radar tends to show higher D50 and a lower fraction especially of very front-loaded events, with the largest differences found for short events. For 6 h AM-generating events, a similar positive bias in the radar data compared to the station data is visible. In addition, for medium events, the radar data show the highest proportion of centred events, while most of the station events are (very) front-loaded. The D50 for radar on the station grid is generally within the distribution of the station and radar on the model grid for both 1 h and 6 h AM-generating events. We therefore attribute the bias, at least in part, to differences in the spatial footprint of the measurement.

A dominant (very) front-loaded fraction of events is reproduced by the CPM ensemble members with low ensemble spread. For short 1 h and 6 h AM-generating events, the CPM projections agree well with the radar on the model grid. For medium events, the CPM simulation appears to be in best agreement with the radar on the station grid, and is thus well within the range of radar and station observations (Fig. 6.9g-i and 6.10g-i). For long events, the ensemble spread is slightly higher and the agreement with both station and radar data, with a relatively similar distribution for long events, is good.

In summary, most 1 h and 6 h AM-generating events in southern Germany occur in summer. With an event duration typically ranging from 1 to 24 h, the AM-generating events are generally longer than the AM duration for 1 h, and for 6 h AM both cases are common, an event shorter than 6 h or longer than 6 h. Event precipitation sum in CPM simulations of AM-generating events is generally in good agreement with station measurements, but tends to be overestimated, especially for long events, which is consistent with the overestimation of precipitation totals in the CPM simulations (Tab. 6.2). The maximum 5-min peak intensity in the CPM simulations is in agreement with the radar data, but compared to station measurements the observed extreme intensities are not reached. A dominant (very) front-loaded fraction of events is reproduced by the CPM historical simulations and the probability distributions of D50 are mostly within the station and radar observations.

6.6 Discussion and conclusions

In this chapter, we investigate sub-hourly precipitation in the KIT-KLIWA ensemble and compare extreme precipitation down to 5-min resolution for the historical simulations (1971-2000) with the dense radar and raingauge observation network in Germany. A method for detection and characterization of precipitation event profiles was developed to improve the understanding of the precipitation bias in CPM simulations and in

particular, characterize extreme precipitation events leading to 1 h and 6 h annual maxima. We can draw three main findings:

1. 5-min CPM precipitation data adequately reproduces the observed precipitation frequency distribution, with an underestimation of the most extreme intensities compared to the station observations but in agreement with the radar data. However, for longer temporal aggregation (6 h) there is an overestimation of the most extreme intensities, revealing a mismatch of the temporal correlation of simulated precipitation time series.

2. The event-based analysis reveals an underestimation of the proportion of short precipitation events by the CPM, but a tendency to overestimate the occurrence of longer events. This implies that the CPM has deficiencies in reproducing strong and short, likely convective, precipitation events.

3. Events leading to 1 h and 6 h AM in Germany mostly occur in summer and usually have an event duration between 1 and 24 h. CPM simulations generally reproduce event precipitation sums of those extremes of short and medium duration but tend to overestimate event precipitation sums for long events. Maximum peak intensity simulated by CPMs is in agreement with spatially aggregated radar data but well below intensity maxima in station data. A dominant (very) front-loaded fraction of extreme precipitation events leading to 1 h AM is reproduced by the CPM ensemble.

By investigating 5-min precipitation in a 30-year CPM simulation ensemble, we take a step towards closing the knowledge gap on sub-hourly CPM precipitation, an area where previous studies have been limited. Chan et al. (2016b) derived climate change signals of sub-hourly precipitation from CPM projections, however, no evaluation could be made due to lack of adequate observational data. The first evaluations of a sub-hourly CPM simulation compared to station observations were made with a decade-long COSMO-CLM simulation over Switzerland (Vergara-Temprado et al., 2021), and a 22-year simulation over Barcelona (Meredith et al., 2020) that found adequate representation of precipitation on sub-hourly resolution and indications of a similar error in sub-hourly precipitation as for hourly resolution precipitation. With our study, we for the first time extend the analysis to a multi-GCM ensemble of CPM simulations and with a comparison with radar data in addition to station measurements. In the analysis of the 30-year historical period, we found that sub-hourly precipitation characteristics are reasonably represented by the CPM simulations on a 2.8 km grid for all intensities. The most extreme values at 5-min resolution are within the range of radar measurements, albeit well below the highest intensities measured at the stations. The lack of observations at high temporal resolution constrains the validation of CPMs at high temporal resolution and, as emphasised by Chan et al. (2016b), stresses the need for more quality-controlled high-resolution observational data products.

We find a dependence of the bias for the extremes on the temporal resolution of the CPM simulation data, in agreement with Meredith et al. (2020), as the extreme intensities in the CPM simulations seem to increase relative to the observations with longer duration. This leads to an overestimation of extreme precipitation at low temporal resolutions. Based on this dependence of the precipitation bias on resolution, we conclude that it is crucial to preserve the natural temporal correlation structure of the precipitation sequence in the evaluation of the precipitation bias. Therefore, we propose an event-based analysis to improve the understanding of the precipitation bias in CPM simulations instead of typical ranked analytical approaches.

Event-based approaches have been applied previously on sub-hourly observational data, e.g. by Villalobos Herrera et al. (2023b); Visser et al. (2023); Wasko and Sharma (2015). For CPM data, the approach has been applied e.g. in Kendon et al. (2012); Fosser et al. (2015); Müller et al. (2023). However, these studies were limited to hourly data. The application of event-based analysis to multi-decadal CPM 5-min outputs showed an underestimation of the proportion of short and small precipitation events by the CPMs, but a tendency to overestimate the occurrence of longer events. The overestimation of event duration is likely caused by low-intensity precipitation in the model, which aggregates precipitation episodes into excessively long events (Fosser et al., 2015). Moreover, the analysis indicates that the CPMs are deficient in reproducing strong and short, probably convective, precipitation events, in agreement with Kendon et al. (2012). The attribution of precipitation biases to events shows the potential for model development. In our application we were able to attribute errors to the forcing data, hence, for model development CPM simulations driven by reanalysis should be pursued.

Precipitation profiles of extreme events are of particular interest because of their importance for a range of practical applications. For engineering applications, such as urban drainage design, stress testing of infrastructure, and risk management, it is common to rely on design rainfall profiles, which are artificial profiles produced, often based on observations. Updating these profiles is clearly needed for resilient planning that considers future extreme events, given climate change and its potential changes on extreme precipitation. Realistic modelling of such extremes has been limited in the past by inadequate spatial resolution of climate models. Deep convection processes and related extremes in coarser climate simulations using parametrized convection were found to be, in general too spatially diffuse, too persistent in time and showing too low intensity maxima of extremes (Kendon et al., 2012).

Our study shows that the characteristics of extreme precipitation events are well represented in a convection-permitting simulation. In particular, for 1 h-AM-generating storms, the features of event precipitation sum, maximum peak intensity, and event shape are within the observational range. Also for longer 6 h-AM-generating events, the features of maximum intensity and shape are within the observational range. For longer events, a slight overestimation of the event precipitation sum is found. Overall,

the analysis of precipitation profile features shows that CPMs are able to represent the decisive features embedded in the design rainfall profiles, thus providing confidence in sub-hourly CPM simulations for future projections. This study is thus an important step towards the applicability of CPMs as a tool for studying future sub-hourly extreme precipitation and paves the way for the application of CPMs for hydrological modelling in a warmer world.

7 | THE CLIMATOLOGY OF PRECIPITATION EVENTS IN CLIMATE CHANGE

This chapter is based on the following article in preparation for re-submission to Geophysical Research Letters:

> Hundhausen, M., H. J. Fowler, H. Feldmann, & J. G. Pinto (in preparation). Unprecedented precipitation events and seasonal shifts over Germany revealed by sub-hourly ensemble. Geophysical Research Letters – in preparation for re-submission.

Minor changes have been made to make the article coherent in the context of this thesis.

7.1 Introduction

Climate projections for Central Europe show a trend towards less precipitation, and thus drier summer months, accompanied by wetter winter months under climate change (IPCC, 2021[1]). In addition to the total precipitation depth, global warming is expected to lead to changes in the intensity, frequency, and duration of precipitation events (Trenberth et al., 2003). While moderate rains infiltrate into the soil, the same amount of rainfall over a short period of time can lead to local flooding and surface runoff (Trenberth et al., 2003). To understand the implications of these changes for the hydrological cycle, it is therefore essential to assess the precipitation climatology at the event scale.

Previous event-based analyses using CPM projections have been limited to hourly resolution (Kendon et al., 2012; Chan et al., 2023a; Fosser et al., 2020; Müller et al., 2023; Fosser et al., 2024; Caillaud et al., 2024), yet this limits the accuracy of event-based analysis, especially for short-duration events. Multi-decadal CPM simulations of sub-hourly resolution are rare but first datasets provide promising results (Chan

[1]IPCC Working Group I Interactive Atlas, the seasonal change signal of precipitation totals is provided in Supplementary Fig. D.1

et al., 2016b; Meredith et al., 2020; Purr et al., 2021). Purr et al. (2021) showed that sub-hourly precipitation in a convection-permitting downscaling of EC-EARTH adequately represents convective cell characteristics including precipitation sum, area, and peak intensity. Analysis of 5-min CPM downscaling in the KIT-KLIWA ensemble in the previous chapter showed good representation of extreme precipitation event characteristics, precipitation sums, and profile shape.

This chapter extends the event-based analysis of the KIT-KLIWA ensemble to the projection period and investigates the climate change signal in the climatology of precipitation events, based on event intensity and event duration. Specifically, we address the research question: What is the projected climate change signal for the frequency of precipitation events and how does the climate change signal manifest seasonally? We approach the topic in two steps:

a) Evaluation of mean intensity in the ensemble in the historical CPM simulations and projection of the climate change signal of the mean event intensity with a focus on record-breaking events.

b) Assessment of the seasonality of the climate change signal.

This chapter is structured as follows: First, the methodology is outlined, including a description of the event catalogue and the approach to evaluating climate change signals throughout the chapter (Section 7.2). Section 7.3 investigates the mean intensity of precipitation events in the CPM ensemble and projected changes in the event frequency. The seasonality of the climate change signal is the subject of Section 7.4. Section 7.5 synthesizes the results and relates the results to the existing literature.

7.2 Methods

7.2.1 The event catalogue

The event-based analysis is based on the method of precipitation event extraction presented in the previous Chapter 6. Here, we analyse all events which meet the criteria of a minimum event precipitation total of 5 mm and a minimum event duration of 1 h. These events are considered "significant" events with potential impact on the local water cycle. In addition to the previous chapter, the minimum available percentage of station data in a year to be considered in the analysis is increased to 95% (compared to 80% in the analysis of annual maxima in Chapter 6). This decision was made because we are analysing the distribution of all events in this chapter - not focusing on events that generate AMs as in Chapter 6. This modification slightly alters the data availability for station and radar observations.

The event catalogue analysed here is derived from the observational data at (1) the measurement stations, (2) the radar data in the original grid resolution of 1 km $\times$ 1 km for the grid point closest to the station locations and (3) the radar data interpolated to

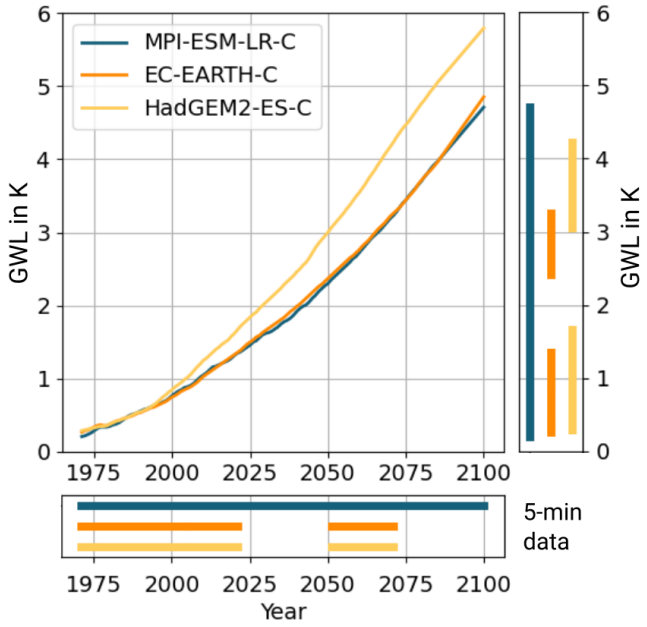

Figure 7.1: GWL in the driving GCMs, with the data availability of 5-min precipitation analysed in the event catalogue on the marginal axis. See Chapter 4 for details on the calculation of GWLs.

the simulation grid of the KIT-KLIWA ensemble. In addition, we analyse precipitation events in the ensemble members EC-EARTH-C, HadGEM2-ES-C, and MPI-ESM-LR-C of the KIT-KLIWA ensemble. The available years with 5-min precipitation output subject to this evaluation are MPI-ESM-LR-C with 1971-2100, HadGEM2-ES & MPI-ESM-LR-C with 1971-2021 & 2051-2071. An overview of the data availability in the event catalogue analysed here is in Table 7.1, with detailed information on the specific years analysed available in Supplementary Fig. D.2. For details regarding the precipitation datasets, refer to Chapter 4.

The classification of extreme events

We characterise events by their mean intensity, Imean, which is defined as the total precipitation of the event divided by the duration of the event. Events with a high Imean are considered to be heavy precipitation events. Specifically, we analyse events exceeding the 90th percentile of the Imean (Imean $>$ p90) and the 99th percentile of the Imean (Imean $>$ p99) as extreme events.

The p90 and p99 thresholds of Imean are calculated for each dataset to account for the systematic bias in the different datasets. The thresholds are based on the pooled results of all stations/grid points without taking into account regional differences in the domain. For the CPM simulations, the 90th or 99th percentile (p90(hist) or p99(hist)) is always evaluated over the 30-year historical time slice (1971-2000), to enable the analysis of frequency changes. The resulting thresholds are in Table D.1 for p90 and Table D.2 for p99.

Table 7.1: Overview of the event catalogue analysed. The data availability for the observational data indicates the total number of analysed years and does not reflect sub-annual data gaps (by definition <5 %). Data coverage in the radar model grid is calculated as analysed years at all grid points / (18 years in the full dataset × number of grid points). Data coverage in the radar model grid is calculated as analysed years at all grid points / (18 years in the full dataset × number of grid points).

Event dataset	Period	Data availability
Stations	2003-2022	686 stations, on average 16.2 years analysed
Radar station location	2003-2022	677 grid cells, on average 15.4 years analysed
Radar model grid	2003-2022	96 % data coverage
EC-EARTH-C	1971-2021 & 2051-2071	100%
HadGEM2-ES-C	1971-2021 & 2051-2071	100%
MPI-ESM-LR-C	1971-2100	100%

7.2.2 The calculation of the climate change signal

We analyse the climate change signal of event frequency in relation to the GWL in the CPM projection. As shown in Fig. 7.1, the analysed projection period in the ensemble spans a range of GWL from 0.46 K to slightly above 4.5 K.

To derive projected frequency changes of precipitation events in Section 7.4, we evaluate annual statistics for each available year in each ensemble member. The rate of change with GWL is then determined from the slope of a linear regression on the annual frequency of events over GWL.

In order to make best use of a larger data pool for the distribution-based evaluation of Imean in the ensemble projection, where annual statistics are not robust, we compare in Section 7.3.2 the historical time slice (30 years from 1971 to 2000) with the common future time slice (21 years from 2051 to 2071) corresponding to a level of global warming between 2.5 and about 4 K (see details in Fig.7.1).

7.3 The climate change signal of mean event intensity

7.3.1 Evaluation of mean event intensity

We find that most observed precipitation events over Germany have a short, sub-daily, duration and tend to have a low Imean < 1 mm/h. There is an expected dependency of Imean on event duration: Imean is highest for short events and decreases for longer events (Fig. 7.2a). This pattern agrees with observations from both stations and radar.

However, comparing the different observational datasets, a systematic positive bias of very short, heavy precipitation events in radar data on its original grid resolution

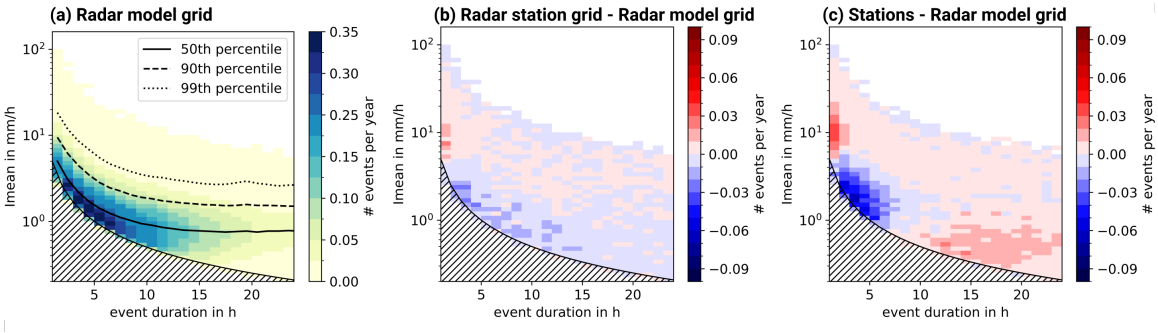

Figure 7.2: (a) the frequency distribution in the event dataset derived from Radar on the model grid is shown normalized as events per year per grid point. Note the logarithmic y-axis. (b) shows the difference between the event frequencies in the observational datasets radar at the station grid - radar at model grid. (c) shows the difference between the event frequencies in the observational datasets stations - radar at model grid. The bin size is 1 h for the duration and increases exponentially by an increment of $\times 10^{0.05}$ for Imean. The hatched area marks where no events are possible by the event definition.

of 1km (radar station locations) and station data compared to the radar on the model grid with a resolution of 2.8 km (Fig. 7.2b & c). In general, event frequencies of high Imean are consistently higher in station data and 1 km radar observations. We primarily attribute this bias to differences in spatial resolution. Conversely, the radar data at the coarser 2.8 km resolution exhibits a higher frequency of events with low intensity, with approximately 2 to 7 h duration. The most extreme events for each duration are typically observed in the radar data on the model grid, which is likely due to the larger data coverage provided in the gridded dataset.

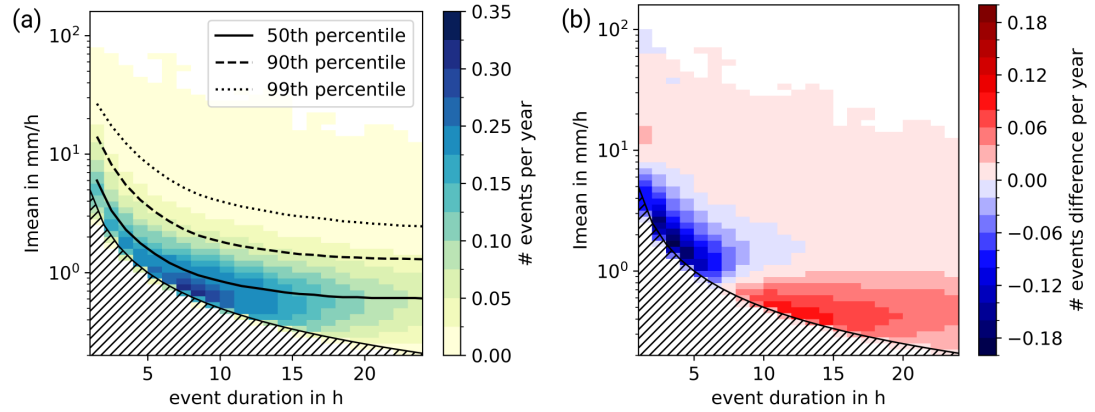

Figure 7.3: (a) The frequency distribution of events per year per grid point in the historical ensemble average (1971-2000). (b) The bias of frequency distribution (a) compared to radar data (ensemble - radar) of events per year and grid point. The bin size is 1 h for duration and increases exponentially by an increment of $\times 10^{0.05}$ for Imean. The hatched area marks where no events are possible by the event definition.

The CPM simulations reproduce the underlying pattern of the Imean distribution (Fig. 7.3a). However, the CPM shows a systematic overestimation of long precipitation events of ~ 9 h and an underestimation of short events compared to the radar dataset

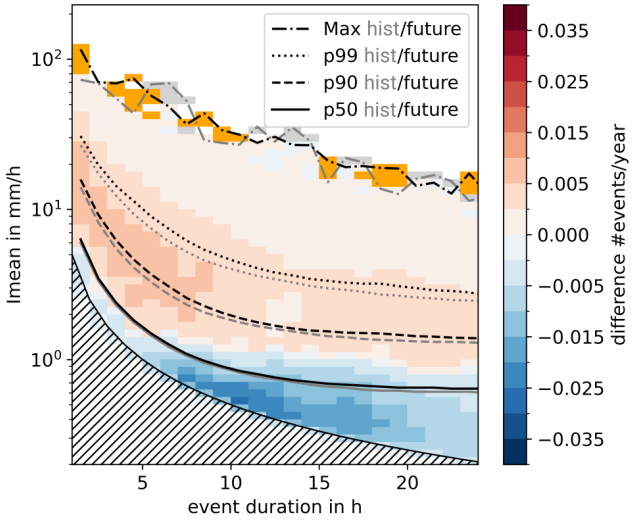

Figure 7.4: Difference in the event frequency per year and grid point from historical to future time slice is shown. The bin size is 1 h for duration and increases exponentially by an increment of $\times 10^{0.05}$ for Imean. Orange shading marks areas that occur in the future time slice but were absent in the historical, grey shading vice versa. Grey lines show percentiles in the historical, and black lines the respective percentiles in the future time slice.

(Fig. 7.3b). The pattern is similar in the three ensemble members, with the largest overestimation of long events found in MPI-ESM-LR-C and the largest underestimation of short events in HadGEM2-ES-C (Supporting Fig. D.3). Hence, the analysis reveals that precipitation events are too persistent in the CPM, in agreement with Kendon et al. (2012). In addition, the CPM ensemble overestimated the frequency of events with high Imean (>p99).

In summary, we find that Imean declines with event duration, and events with very high Imean are predominantly of short-duration. Even though the CPM reproduces the observed range of Imean with respect to event duration, the CPM has limitations in the representation of short events and has a bias towards too persistent precipitation events. The intensity of extreme Imean is overestimated in the CPM compared to the radar data.

7.3.2 Projected event intensity changes and unprecedented events

Changing event occurrence with global warming is shown in Fig. 7.4, which compares Imean in 1971-2000 with the future time slice from 2051-2071. The CPM ensemble projects a reduced number of events with low Imean (below approximately 1 mm/h) and an increased frequency of events with higher Imean. All percentiles analysed shift to higher Imean for the future simulation, for all event durations. The strongest absolute increase is found for events with short duration, and the increase is stronger for higher percentiles of Imean (note the logarithmic axis in Fig. 7.4). These results refer to the composite over all grid points and years.

To support the approach of spatial composites, we tested different subselections of summer-only events, winter-only events, and grid points above and below 400 m altitude in all ensemble members (Fig. 7.5). Similar results were found for different altitudes. However, the change signal in summer and winter differs, showing that Imean above which an increase in frequency is projected are higher in summer than in winter.

The orange shading in Fig. 7.4 and Fig. 7.5 highlights events that did not occur in the historical 30 years but are present in the future ensemble projection (2051-2071). Our detection of these unprecedented events indicates that the future increase in the most extreme events is accompanied by future record-breaking events. The ensemble mean, as well as all ensemble members (Fig. 7.5), show record-breaking events of short duration (<5 h). For longer durations, the number of record-breaking events in the ensemble composite is less evident.

In summary, we find that the CPMs project a decreasing frequency of events with low Imean in the future time slice. However, we find that events with high Imean increase across all event durations, and global warming is projected to lead to unprecedented events with record-breaking Imean.

7.4 Seasonality of the climate change signal

Our assessment of the annual cycle of precipitation events in observations shows that while events of medium to long duration occur throughout the year, long events are found predominantly in winter, while medium events dominate in the summer half year. The occurrence of short events is mainly restricted to summer. Extreme events are most likely to occur in the summer half year, with the most extreme events (Imean>p99) concentrated almost exclusively in the warmest months from May to September (Fig. 7.6c-d).

The CPM ensemble represents these seasonal patterns of short, medium, and long events. Bias in the representation of the annual cycle in the CPM ensemble appears connected to the too high persistence of precipitation events: the frequency of long events is overestimated in all ensemble members, but short events are underestimated throughout the year (Fig. 7.6b). The maximum frequency of events of all durations in summer is reproduced by MPI-ESM-LR-C and EC-EARTH-C. Only HadGEM2-ES-C does not show this, due to excessively hot and dry summers within its simulation. In contrast, the seasonality of extreme events is represented well in all members (Fig. 7.6c-d), although in HadGEM2-ES-C the frequency peaks too early in summer and has a deficit in late summer. Supporting information for the single ensemble members is in Supplementary Fig. D.4.

We find that all CPMs project a decreasing number of precipitation events over Germany with global warming (Fig. 7.6e). This pattern is dominated by a decreasing frequency of summer events, while winter event frequency tends to increase. Decomposed

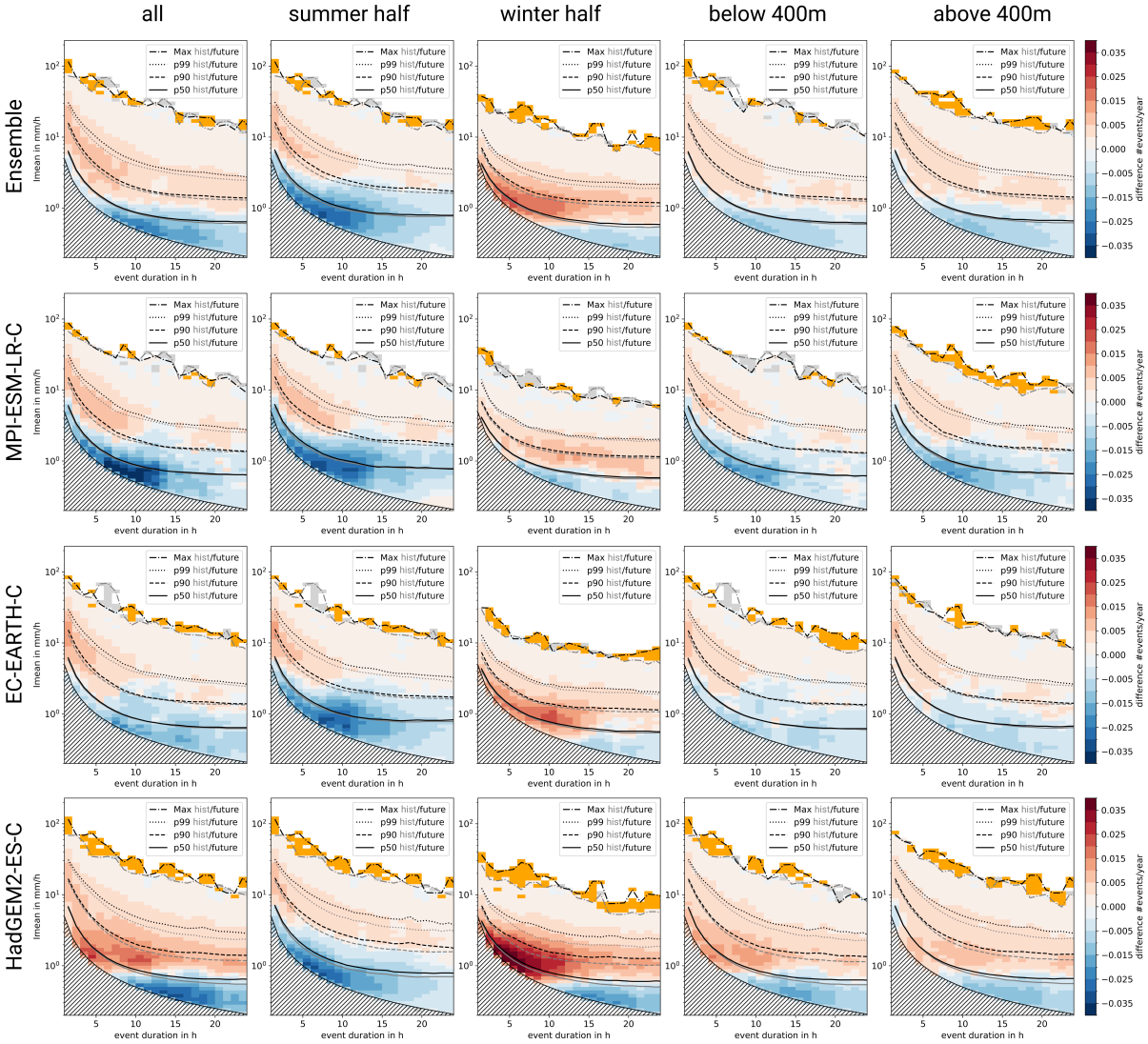

Figure 7.5: The difference of the event frequency per year and grid point from historical (1971-2000) to future time slice (2051-2071) is shown for the ensemble and the single ensemble members (rows) and for different configurations (columns). The bin size is 1 h for duration and increases exponentially by an increment of $\times 10^{0.05}$ for I_{mean}. Orange shading marks areas that occur in the future time slice but were absent in the historical, grey shading vice versa. Grey lines show percentiles in the historical, and black lines the respective percentiles in the future time slice.

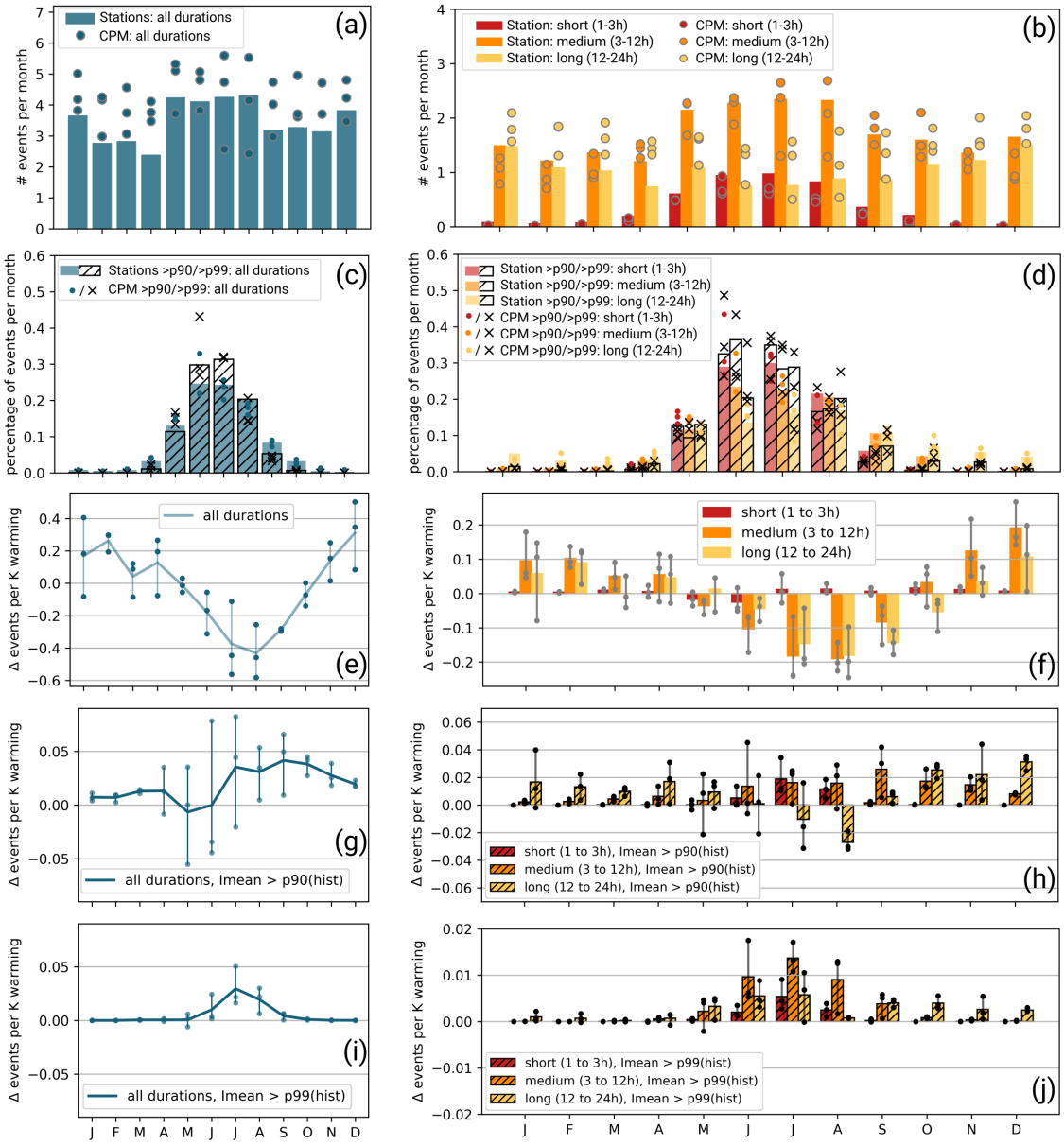

Figure 7.6: Bar plots show the number of events in the respective month per year and station derived from the station measurement, for all events (a) and for the sub-groups of short events, medium events, and long events in (b). Dots in (a) and (b) show results from ensemble members for event frequency per month and grid points averaged over the historical period 1971-2000. (c) and (d) show the above for all events exceeding the threshold of p90 and p99. The percentiles are evaluated over the respective duration class. The climate change signal of the number of events per K global warming is provided in (e) for all events, and in (f) for all events sub-divided into the three duration classes (dots ensemble members, lines ensemble average). (g) and (h) show the above for extremes with Imean > p90(hist), (i) and (j) for extremes with Imean > p99(hist).

into different durations (Fig. 7.6f), these changes are driven by modifications primarily to the frequency of medium to long-duration events. The frequency of short events is less affected by the climate change signal and increases only slightly in late summer. The results of the single ensemble members and the statistical significance of the change signal are provided in Supplementary Fig. D.5.

In contrast, we find that all CPMs project an increasing number of extreme events (Fig. 7.6g and i). For events above p90, the increase is projected to be strongest in late summer and the early winter half-year, which agrees with the strongest projected temperature increases in the KIT-KLIWA ensemble during that time of the year (Hundhausen et al., 2023). The increase in the summer is mainly reflected in extreme events with a duration of <12 h. We also find a projected increase in the frequency of long extreme events above p90, primarily in the winter half-year (Fig. 7.6h).

For very extreme events (>p99), an increase in frequency is projected throughout the year, but concentrated in the summer months from May to September and peaking in July (Fig. 7.6i). This result applies mostly to short and medium-duration events (significant increase in all ensemble members in July; Supplementary Fig. D.5); only in the case of long events does the ensemble show an increase in these extremely rare events extending into the winter (Fig. 7.6j).

In summary, the observations show distinct seasonal patterns in precipitation events across different durations. Long-duration events dominate in winter, medium-duration events prevail in the summer half-year, and short-duration events occur primarily in summer. Extreme events are concentrated in the summer. The CPM ensemble captures these seasonal patterns but exhibits biases, overestimating long events and underestimating short ones. All models represent the seasonality of extreme events reasonably well, despite a late summer bias in HadGEM2-ES-C. With global warming, the CPM ensemble projects a reduction in summer events and an increase in winter events. The frequency of extreme events is projected to increase across all CPM simulations. Short to medium duration events exceeding p90 (p99) are expected to rise most notably in late summer (summer), while long-duration extremes increase in the winter months (throughout the year).

7.5 Discussion and conclusion

We have analysed precipitation events in the projections from the KIT-KLIWA ensemble to study the climate change response of precipitation events with respect to Imean, and seasonality. The chapter has revealed the following key results:

1. The CPMs reproduce the link between Imean and event duration across sub-daily events in Germany as found in observations with a bias of too persistent events. The projections reveal increasing Imean in the future across all event durations, leading to unprecedented events with record-breaking Imean.

2. The event frequency changes affect the annual cycle so that longer events increase in winter but decrease in summer, whereas short duration events show a slight increase in frequency, mainly in late summer and winter. Extreme events of short to medium duration mostly increase in frequency in summer. Long duration extreme events (>p90) increase in winter and the most extreme events (>p99) throughout the year.

The dynamical downscaling in the CPM ensemble demonstrated an expected increase in Imean under climate change, corroborating previous studies which also found more significant and larger changes for short, sub-daily, and extreme events (e.g. Berg et al., 2019; Rajczak and Schär, 2017; Ban et al., 2020, 2015; Hundhausen et al., 2024). Importantly, we find that our CPM projections show that unprecedented events with extremely high mean intensity occur under future conditions, similar to record-breaking events in transient CPM projections for the UK (Kendon et al., 2023). The identification of unprecedented events in all three ensemble members' analyses, despite examining only 21 years (compared to 30 years in the historical reference) for Germany, reinforces that these events are expected to occur in a warmer world. This finding underscores the need for climate adaptation to address record-breaking events, in agreement with Fowler et al. (2021b). We note that follow-up studies are necessary to understand the atmospheric conditions leading to these events and to assess their impacts.

Our event-based analysis of the CPM projections reveals that changes in precipitation event frequency affect the annual cycle, leading to fewer long precipitation events in summer and further reduced water availability, since a larger fraction of the precipitation occurs in an increasing number of extreme events. This complements results from previous CPM studies for Germany (Ban et al., 2020; Hundhausen et al., 2024). Such extreme precipitation events lead to increased surface run-off, water may be unsuitable for drinking due to contamination by pollutants (e.g. Kistemann et al., 2002), and the risk of flash floods from short, intense rainfall is increased (Fowler et al., 2021b). To cope with the changing distribution of water resources in the future, adaptive water management strategies are needed.

Our analysis demonstrates the potential of CPM simulations to assess changes in the climatology of precipitation events. We argue that the event-based approach produces tailored information to support successful climate adaptation, such as risk assessment and water management. The identification of unprecedented events as well as the declining water availability in summer events presents a valuable interface with impact models, such as data-driven hydrological modelling.

8 | THE SCALING OF PRECIPITATION EVENT PROFILE CHARACTERISTICS

8.1 Introduction

Design rainfall profiles for hydrological modelling are typically based on ranked analytical approaches using long observational time series. Currently, it is assumed that the same design profiles, based on past observations, can be used to design systems in a warming climate (Dale, 2021). However, there are indications that the temporal profile of precipitation events changes with warming temperatures (Wasko and Sharma, 2015; Visser et al., 2023; Ghanghas et al., 2024, , details in Chapter 2), posing a significant challenge for design flow estimation in a changed climate. Reliable projection of temporal precipitation profiles is crucial to address this challenge.

We have established in Chapter 6, that the simulation of sub-hourly precipitation in the KIT-KLIWA ensemble adequately represents the features of observed precipitation event temporal profiles. Further, we showed in Chapter 7, that there is an intensification of mean event precipitation intensity with global warming and changes to the frequency of events. In this chapter, we extend the analysis to investigate precipitation event profile characteristics; intensity – specifically the event 5-min peak intensity (Imax), the 1-h peak intensity (I1h) and mean event intensity (Imean) – and the timing of the bulk precipitation, parametrised over D50 for summer precipitation events. Specifically, this chapter assesses the research question: How do the precipitation event profile characteristics Imax, I1h, Imean, and D50 depend on temperature and does this apparent scaling relationship translate into a climate change signal? We approach the research question in three steps:

a) Evaluation of the apparent scaling rates for Imax, I1h, Imean, and D50 in the historical CPM simulations.

b) Comparison of the established apparent scaling relations in the historical time slice with the apparent scaling rates in the future time slice to test whether the relationships hold in a warmer future.

c) Assessment of the climate change signal of Imax, I1h, Imean, and D50 in the CPM projection.

The chapter is structured as follows: First, the methodology is outlined, including a description of the event catalogue and the approach to estimating scaling rates for both the apparent and climate scaling of precipitation event characteristics (Section 8.2). Section 8.3 investigates the apparent scaling relationship for the event characteristics Imax, I1h, Imean, and D50. In Section 8.4, the apparent scaling rates in the historical and future time slices are compared. Section 8.5 focuses on the climate scaling of the precipitation event characteristics. The chapter concludes with Section 8.6, synthesizing the results and setting them within the context of the existing literature.

8.2 Methods

8.2.1 The event catalogue

The event-based analysis is based on the method presented in Chapter 6. In this chapter, we analyse precipitation events in the following datasets: Station observations, Radar data at the station locations (1 km×1 km resolution grid point closest to the station location), Radar data interpolated onto the model grid (2.8 km×2.8 km resolution), and the three ensemble members EC-EARTH-C, HadGEM2-ES-C, and MPI-ESM-LR-C. The criteria for the event selection for analysis are the same as in Chapter 7 (analysis of event climatology): precipitation sum ≥ 5 mm, duration ≥ 1 h. In agreement with Chapter 7, the available observational data in a year to be considered within the analysis is $\geq$95 %.

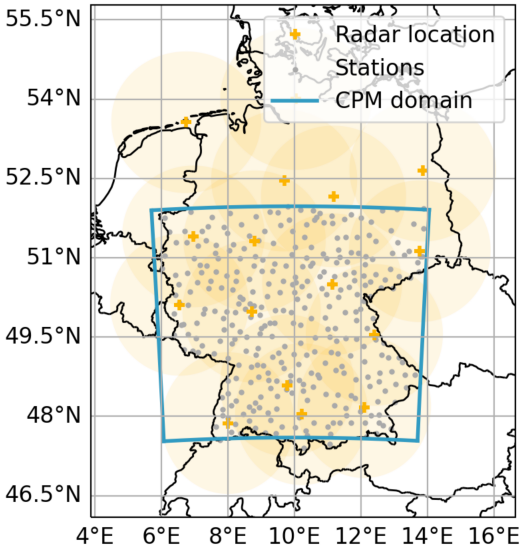

Figure 8.1: Overview of the data used for the event catalogue. The CPM data is only analysed in the German part of the domain.

For the analysis, each precipitation event is associated with a representative temperature for that event. Temperature recordings are available from an observational

dataset from DWD at 340 stations that also record sub-hourly precipitation within the analysis domain (Fig. 8.1). Gridded Tmax data that are associated with radar data is available in the HYRAS dataset until 2020. An overview of the data availability in the event catalogue analysed here is in Table 8.1, with detailed information on the specific years analysed available in Supplementary Fig. E.1; for details of the datasets, refer to Chapter 4. Analogously to the previous chapters, the analysis is restricted to the German part of the domain. In addition, we restrict the analysis to precipitation events in the summer half-year (April to September).

Table 8.1: Overview of the event catalogue analysed. The data availability for the observational data indicates the total number of analysed years, and does not reflect sub-annual data gaps (by definition <5%). Data coverage in the radar model grid is calculated as analysed years at all grid points / (18 years in the full dataset × number of grid points). The Tmax dataset "CPM" indicates that Tmax is taken from the simulation's output. Hourly station datasets and the CPMs also provide dew point temperature data.

Event dataset	Tmax dataset	Period and data availability
Stations	Hourly station observations	2003-2022, 340 stations, in average 15.8 years analysed
Radar station location	Hourly station observations	2003-2022, 336 grid cells, in average 15.0 years analysed
Radar model grid	HYRAS	2003-2020 with data coverage of 95%
EC-EARTH-C	CPM	Historical 1971-2000, projection: 2001-2020, 2051-2070
HadGEM2-ES-C	CPM	Historical 1971-2000, projection: 2001-2020, 2051-2070
MPI-ESM-LR-C	CPM	Historical 1971-2000, projection: 2001-2100

Subsample of extreme events

The analysis covers an assessment of the composite of all events as well as two subsets of heavy precipitation events. A heavy precipitation event is defined over the mean intensity of the event, Imean (compare with Chapter 7). The subset of heavy-10% events comprises an analysis of all events that exceed the 90th percentile (p90) of Imean in the respective dataset. The subset of heavy-1% events comprises an analysis of all events that exceed the 99th percentile (p99) of Imean in the respective dataset.

The Imean thresholds are evaluated based on the pooled results of all stations or radar/model grid points without consideration of regional patterns. This threshold is specific for each dataset (Station, radar station grid, radar model grid, and ensemble member) as well as for each duration category. The thresholds are provided in Table E.1. We also use this definition of heavy precipitation for the analysis of future projected time slices in the CPM simulations, with a specific threshold set for each 20-year time slice (Tab. E.3 and Tab. E.4).

The approach of using a flexible threshold allows the assessment of the top 10 % of events in each dataset and time slice independently of bias in event frequency assessed in Chapter 7. Even though the method is analogous to that used in Chapter 7, the different threshold values here are due to the consideration of only the summer half-year in this Chapter.

8.2.2 Temperature covariate

Apparent scaling relationships for precipitation intensities, first introduced in the pioneering work of Lenderink and Van Meijgaard (2008), have become widely used for analysing precipitation, particularly precipitation intensities, in relation to temperature (e.g. Berg et al., 2013; Ali et al., 2022; Da Silva and Haerter, 2024). The covariate used to assess this scaling is typically an "event-associated" temperature. Different approaches have been used for determining this temperature. Commonly, mean daily surface temperature, Tmean, is used as a practical proxy for atmospheric moisture capacity (Berg et al., 2009).

However, apparent scaling relationships based on maximum daily surface temperature, Tmax, have been previously assessed in Lenderink and Van Meijgaard (2008) and Berg et al. (2013) and were found to result in a similar apparent scaling relationship for precipitation extremes as the more commonly used Tmean. A thorough evaluation of the use of different scaling variables in the here presented CPM dataset is provided in the supporting section E.1. Since using Tmax as the scaling variable effectively captures precipitation variability while minimizing the impact of the cooling effect from the rainfall itself, and it is available in daily datasets, we choose Tmax on the day of the event as the associated event temperature within our analysis, referred to as event-T_{max} in the following.

In addition, daily maximum dew point temperature was extracted for the CPM simulations and for observations (event-$\mathrm{TD}_{\mathrm{max}}$). However, we restrict our discussion of dew point temperature scaling of precipitation in this chapter to contextualising the behaviour of event-T_{max} scaling at high-temperature ranges.

8.2.3 Apparent temperature scaling

Apparent scaling relations with event-T_{max} are derived for the following event characteristics: maximum 5-min intensity (Imax), maximum 1 h-intensity (I1h), mean intensity of the event (Imean), and the percentage of event duration at which 50 % of precipitation event total is reached (D50, see Chapter 6 for details). There are several approaches used for deriving scaling relationships within the literature, which can be grouped into binning and quantile regression methods (Ali et al., 2022). In this study, we adopt the widely-used binning method, which groups samples into temperature bins of equal size. Following Lenderink and Van Meijgaard (2008), we apply a bin width of 2 °C. We then estimate the 50th percentile (p50) of each characteristic (Imax, I1h, Imean, and D50)

for each temperature bin, as well as the 90th percentile (p90) for the intensity measures (Imax, I1h, Imean).

To quantify the apparent scaling, the scaling rate for the intensity measures (Imax, I1h, Imean) is approximated using an exponential relationship with temperature, while D50 – based on Visser et al. (2023) – is approximated with a linear relationship. A least squares polynomial fit is used to fit the data according to the following relationships.

To assess the exponential scaling of the intensity characteristics, a linear regression is fitted to the logarithm of p50 and p90 of the distribution in each temperature bin as a function of temperature:

$$\log(p_x) = a + bT_{\max}, \quad \text{with } p_x \in \{p50, p90\} \tag{8.1}$$

a and b are the fit parameters. The apparent scaling rate, SR, in %/°C is given by:

$$\mathrm{SR} = 100(e^b - 1) \tag{8.2}$$

To evaluate the dependence on D50, we use a linear regression to the median D50 (p50) over temperature as in Visser et al. (2023):

$$p50 = a + \mathrm{slope} \cdot T_{\max} \tag{8.3}$$

The slope of the linear regression is the apparent linear scaling signal.

The analysis of apparent scaling is based on pooled data over the regional domain, similar to the previous analysis of apparent scaling in Berg et al. (2013) over a similar domain in Germany. A threshold of at least 50 data points was set for each temperature bin to be included in the fit. In addition, temperature bins below the coldest 5 % and warmest 5 % events were excluded from the calculation of scaling rates or linear change signals, similar to Ali et al. (2022). A sensitivity analysis showed that the magnitude of the scaling rate is sensitive to this cut-off threshold, consistent with Ali et al. (2022). The 5 % threshold largely excludes the previously assessed "hook" structure of negative apparent scaling at high surface air temperatures in many regions (e.g. Hardwick Jones et al., 2010; Utsumi et al., 2011; Panthou et al., 2014; Ali et al., 2018). Due to the dependence of the scaling rate on the temperature range, the scaling plots of Imax, I1h, Imean, or D50 versus temperature are always given for context, rather than scaling rates alone. The sensitivity analysis is provided in the Supporting Section E.1 for further details.

We assess apparent scaling rates for events of different durations based on the same categories as in the previous chapters: short events from 1 h to < 3 h, medium events from 3 h to < 12 h, and long events from 12 h to < 24 h.

8.2.4 Climate scaling rates

The calculation of the climate change signal is based on projected 20-year time slices, the longest available period in the projection of all ensemble members. Each 20-year time slice is assigned the GWL of the middle, 10th, year. For EC-EARTH and HadGEM2-ES, the calculation includes the 30-year historical time slice (GWL = 0.46 °C) and the projected time slices 2001-2020 and 2051-2070. For the transient 5-min time series in MPI-ESM-LR-C, the analysis is extended to the nine overlapping time slices 2001-2020, 2011-2030, 2021-2040, 2031-2050, 2041-2060, 2051-2070, 2061-2080, 2071-2090, 2081-2100. For details regarding the GWL calculation refer to Chapter 4.

Analogous to the apparent scaling, the climate change signal of intensity measures – Imean, Imax, I1h – is approximated by an exponential function which is fitted to the 50th, 90th and 99th percentiles (p50, p90, p99) of the distribution in the respective time slice:

$$\log(p_x) = a + b\text{GWL}, \quad \text{with } p_x \in \{p50, p90, p99\} \tag{8.4}$$

The climate scaling rate (CSR) in % is given by:

$$\text{CSR} = 100(e^b - 1) \tag{8.5}$$

The climate change signal of event-$T_{\max}$ and D50 is evaluated using a linear regression across the different GWLs. We evaluate the 10th, 50th and 90th percentiles (p10, p50, p90) of the distributions of event-$T_{\max}$ and D50 in each time slice. The climate change signal, CCS, is given by the slope of a regression to the percentiles:

$$p_x = a + \text{CCS} \cdot \text{GWL}, \quad \text{with } p_x \in \{p50, p90, p99\} \tag{8.6}$$

CCSs are evaluated for the full event data as well as the heavy-10% events and heavy-1% events.

8.3 Apparent temperature scaling

This section assesses the apparent scaling of precipitation event characteristics in observations under current climate conditions and evaluates the ability of CPM simulations to reproduce these features in their historical simulation (1971–2000). We start with an evaluation of event-$T_{\max}$, then assess the apparent scaling of intensity measures Imax, I1h, and Imean and conclude with an assessment of the apparent scaling of D50.

8.3.1 Evaluation of the temperature covariate, event-$T_{\max}$

Event-$T_{\max}$ from the HYRAS dataset that is associated with precipitation events the gridded radar data (radar model grid) aligns well with the station observations for

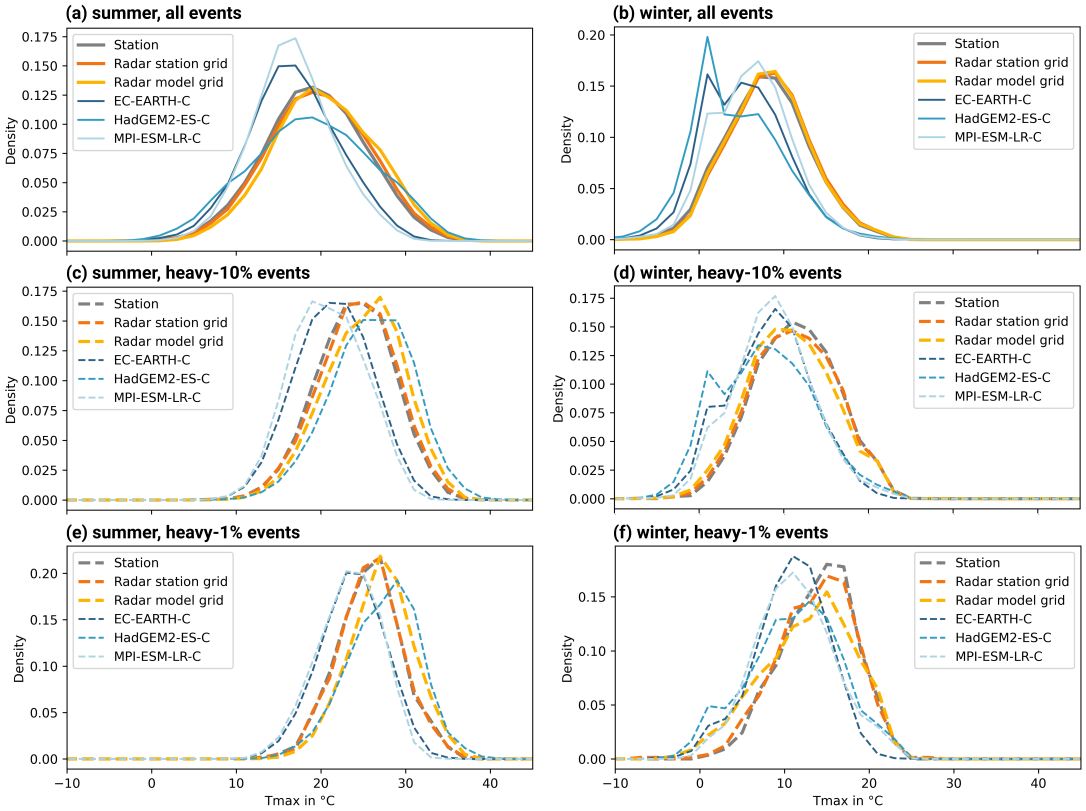

Figure 8.2: Distribution of event-$T_{\max}$ associated with precipitation events of 1 h-24 h duration for the full event set in (a) the summer half-year and (b) in the winter half-year, heavy-10% events in (c) the summer half-year and in (d) the winter half-year, heavy-1% events in (e) the summer half-year and in (d) the winter half-year.

all events in both summer and winter (Fig. 8.2a and b). For heavy-10% and heavy-1% events, however, discrepancies become evident. In summer, event-$T_{\max}$ associated with radar data (radar model grid) exhibits a systematic positive bias compared to station measurements of temperature associated with events in station data and radar data on the station grid (Fig. 8.2c and e), whereas, in winter, the deviations are smaller, with a slight negative bias (Fig. 8.2d and f). These biases are attributed to differences in event selection and sampling locations between the two datasets. Minor differences in event-$T_{\max}$ distribution between the station measurements and radar measurements at the station location indicate variations in event detection, likely due to lower detection frequency of precipitation events in the radar data, associated with a negative precipitation bias in the radar data compared to the station data.

Simulated event-$T_{\max}$ associated with summer precipitation shows a systematic cold bias in the EC-EARTH-C and MPI-ESM-LR-C runs (Fig. 8.2a). The simulation driven by HadGEM2-ES overestimates the variance in the summer temperature distribution, resulting in an exaggerated occurrence of cold and hot conditions. This extends to event-$T_{\max}$ associated with heavy-10% and heavy-1% events, where high temperatures are overestimated by HadGEM2-ES. During winter, HadGEM2-ES-C exhibits a cold bias similar to that of the other ensemble members (Fig. 8.2b, d, f). This cold bias

in event-$T_{\max}$ associated with precipitation events aligns with the general cold bias observed in the KIT-KLIWA ensemble (Hundhausen et al., 2023).

A further bias in the simulations comes from an overestimation of frequencies near to the freezing point. All ensemble members display a pronounced peak at event-$T_{\max}$ ≈ 0°C, a feature absent from observational data (Fig. 8.2b). This model deficiency is expected to be reduced in more recent versions of COSMO-CLM, which incorporate an updated formulation of skin temperature in the Land Surface Scheme TERRA (Schulz and Vogel, 2020). The temperature bias in the CPM simulation is discussed in detail in Hundhausen et al. (2023).

Given the biases in modelled event-$T_{\max}$, particularly around freezing point, our analysis of apparent and climate scaling is restricted to the summer half-year. This restriction minimises the impact of the unrealistic CPM behaviour on the results.

8.3.2 Intensity

Apparent scaling rates for Imean, I1h, Imax

To comprehensively capture the different characteristics of precipitation event intensity, this analysis includes a range of intensity measures: Imax, I1h, and Imean. The following patterns are derived from the scaling relationship provided in Fig. 8.3 and the associated apparent scaling rates in Fig. 8.4.

Imax The observed scaling of Imax with event-$T_{\max}$ reveals an increase of Imax with rising temperatures, with the strongest rate of increase occurring between 10 °C and 25 °C (Fig. 8.3a-d). Below and, especially, above this range, the rate of increase flattens, before levelling off and scaling even becomes negative in station data at temperatures above 28 °C. This distinctive hook pattern, a common feature of apparent scaling rates in many regions when using surface air temperature, aligns well with findings from previous studies (e.g. Hardwick Jones et al., 2010; Utsumi et al., 2011; Panthou et al., 2014). In station observations, the scaling of p50 of Imax ranges from approximately 5 % for short events to around 8.5 % for longer duration events, thus the apparent scaling of Imax generally shows an increase with event duration (Fig. 8.4a). For events above p90, the scaling rate is higher than for p50, with maximum values close to 10 %/°C at the longest event durations (12-24 h). Radar observations generally show a lower scaling rate for Imax with temperature than found for station observations, except for short duration events (Fig. 8.4a). For p50, the scaling rate is 5 to 6 %/°C which is below CC-scaling. The higher apparent scaling rates for p90 exceed the CC-rate except for short duration events: this agrees well with relative scaling rates for station observations. The increase in apparent scaling rate with event duration is also present for p90 in the radar data.

The CPM ensemble simulations capture the main characteristics of this approximately exponential temperature scaling at moderate temperatures, with a pronounced flattening

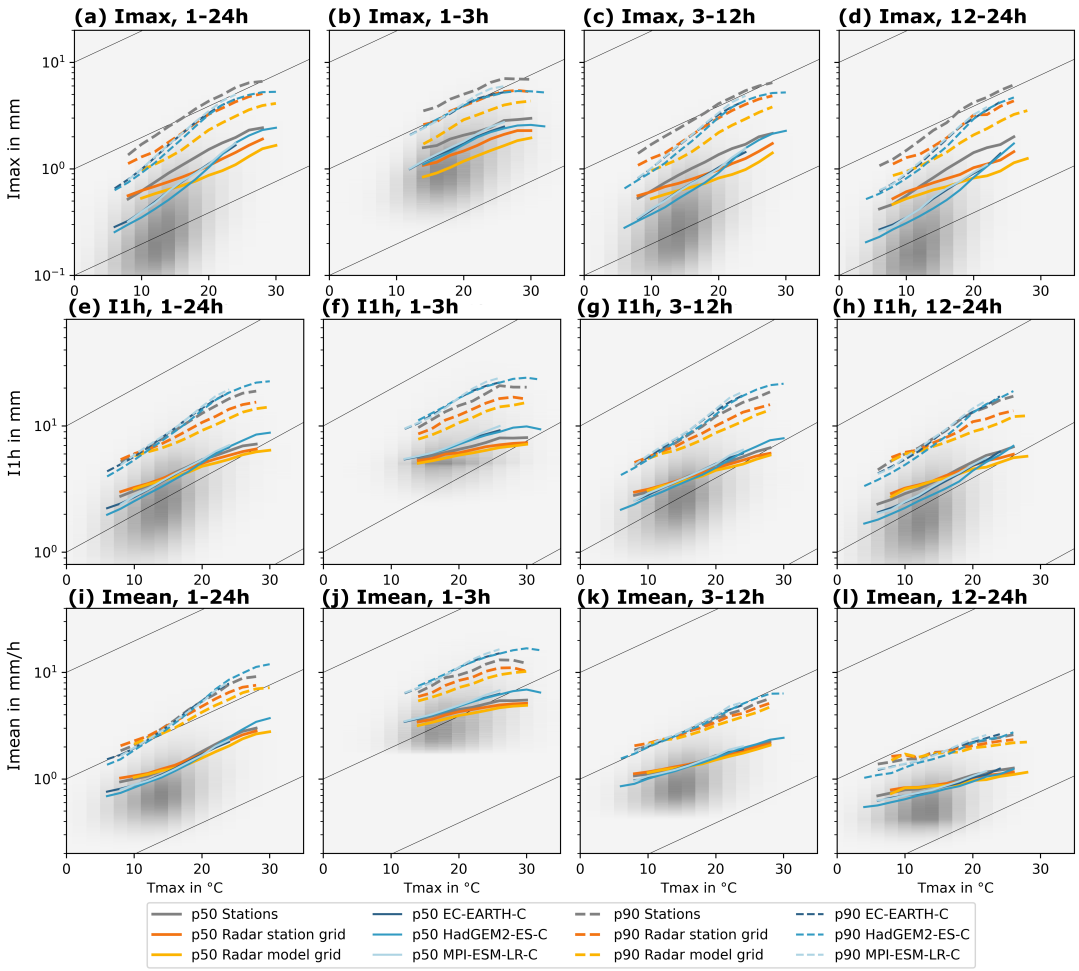

Figure 8.3: Apparent scaling relations in observation and historical CPM simulation of median and p90 of the three intensity measures (a-d) Imax, (e-h) I1h, and (i-l) Imean. Columns refer to the different duration categories: 1-24 h (1st column), 1-3 h (2nd column), 3-12 h (3rd column), 12-24 h (4th column). Grey shading indicates the frequency distribution in the CPM ensemble, diagonal lines indicate CC-scaling with a slope of 7 %/°C.

at both lower, and especially higher, temperatures (represented in blue in Fig. 8.3a-d). This levelling-off at higher event-T_{max} is most notable in the ensemble member driven by HadGEM2-ES, which reaches higher event-T_{max} values than other ensemble members. We find the increase in Imax in the CPM ensemble simulations is steeper than for observations, resulting in higher apparent scaling rates (Fig. 8.4a). This model overestimation is somewhat reduced for p90 compared to p50. The CPM simulations also replicate the increase in apparent scaling rate with event duration found in observations for both p50 and p90, as well as an enhanced scaling of p90 relative to p50. Scaling rates beyond CC are found for simulated Imax at p50 and p90, with a maximum p90 scaling rate in MPI-ESM-LR, exceeding 12%/°C. The lowest scaling rate for p90 is found for short duration events in the ensemble member HadGEM2-ES-C due to its pronounced hook pattern, leading to an apparent scaling rate below CC-scaling rate. However, this ensemble member shows a stronger scaling of p50 compared to p90. The

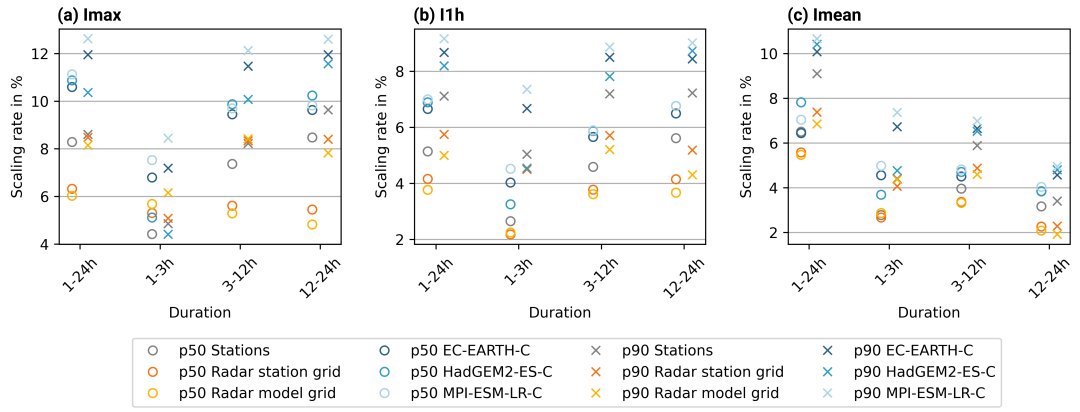

Figure 8.4: Apparent scaling rates for (a) Imax, (b) I1h, and (c) Imean.

ensemble spread is found to be larger for short duration events and for p90 compared to p50 and tends to increase with event duration.

I1h I1h shows similar apparent scaling to Imax, with exponential scaling from approximately 10 to 25 °C and a levelling-off above this temperature (Fig. 8.3e-h). Scaling is higher for p90 compared to p50, and scaling increases with event duration. However, the magnitude of the apparent scaling rates for I1h is consistently lower than for Imax (Fig. 8.4b). Although the observed scaling rate for p50 is below CC-scaling, the scaling for p90 approaches the CC-rate for long duration events for the station observations but stays below the CC-rate for the radar observations. The CPM simulations reproduce this enhanced scaling for p90 compared to p50 found in observations, and the stronger scaling found for longer duration events. Again, the CPMs show an overestimation of apparent scaling rates compared to observations, especially for p50. The apparent scaling rates for p90 of I1h are well above the CC-rate for medium and long duration events.

Imean The shape of the scaling curve for Imean is similar to that for Imax and I1h, discussed above (Fig. 8.3i-l). Scaling rates for Imean are strongest for the event pool of all events from 1 h to 24 h duration, which highlights the influence of event duration here (Fig. 8.4c). For the station observations, the apparent scaling for 1-24 h events is slightly below 7 %/°C for p50 and above the CC-rate for p90 at approximately 9 %/°C. Scaling rates are significantly lower when considering single duration categories and the observed scaling rate ranges from ~2 to ~4 % for p50 and up to 6 %/°C for medium events for p90. In general, the apparent scaling rate for Imean is less dependent on event duration. The CPM simulations reproduce the observed characteristics of Imean scaling well, but the overestimation of observed scaling rates is evident.

There are some commonalities among the analysis of the three intensity measures: for example, the scaling rate shows the strongest increase in the moderate temperature range and levels off at higher temperatures. At high temperatures, even a negative scaling with temperature is observed for short events. This finding of a “hook” pat-

tern is typically observed when investigating scaling based on surface air temperature (e.g. Hardwick Jones et al., 2010; Utsumi et al., 2011; Panthou et al., 2014). This hook pattern can be explained by a limitation in moisture at high temperatures. To support the explanation of negative apparent scaling resulting from limited moisture availability, we performed the analogous apparent scaling analysis using maximum dew point temperature, event-TD_{max}, instead of event-T_{max}. Shown for the example of Imax in Fig. 8.5, the apparent scaling relationship with event-TD_{max} reveals that the hook structure is removed and that a continuing exponential scaling rate at high temperatures is more pronounced. The magnitude of the intensity scaling is strongest in the range of event-TD_{max} between approximately 6 °C - 14 °C and the slope of the scaling relation is lower below and above that range. No negative apparent scaling of intensity with event-TD_{max} is observed. This is shown for the example of Imax in Fig. 8.5, and provided for the other intensity measures in the Supporting Information in Fig. E.5. In addition, the apparent scaling rates derived from the scaling with event-TD_{max} are higher than the apparent scaling rates based on event-T_{max} resulting from limited moisture availability in the apparent scaling relation with event-T_{max} (Fig. E.6).

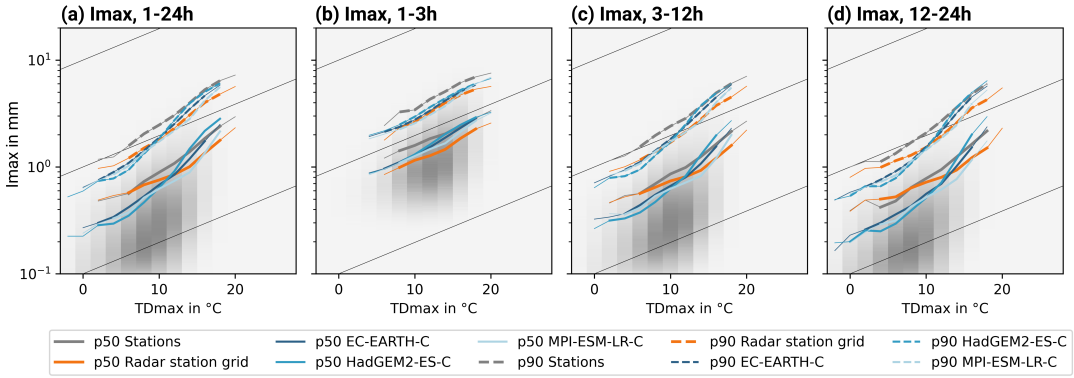

Figure 8.5: Apparent scaling of Imax over event-TD_{max} in observation and historical CPM simulation of p50 and p90 for (a) 1-24 h, (b) short events 1-3 h, (c) medium events 3-12 h, and (d) long events 12-24 h. Grey shading indicates the frequency in the simulation ensemble, diagonal lines indicate CC-scaling with a slope of 7 %/°C. Thick lines show the scaling relation with a cut-off of 5 %, and thin lines with a cut-off of 1 %. Apparent scaling rates are always calculated with 5 % cut-off.

Apparent scaling of profile steepness for extreme precipitation events

Combining the findings from the intensity measures reveals a stronger apparent scaling of Imax compared to I1h and Imean. This indicates that the temporal profiles of events under warmer conditions are steeper (more peaked) than under colder conditions. Assessment down to the 5 min resolution suggests that this increased steepness extends to scales shorter than an hour. To investigate this relationship not only across independent samples in the dataset but also within individual precipitation events, we analyse the scaling of the ratio Imax/I1h - termed the “peak ratio”.

We find that the peak ratio in the full event catalogue increases with event-T_{max} (Fig. 8.6a-d). The radar observations at the station locations (1 km resolution) show a

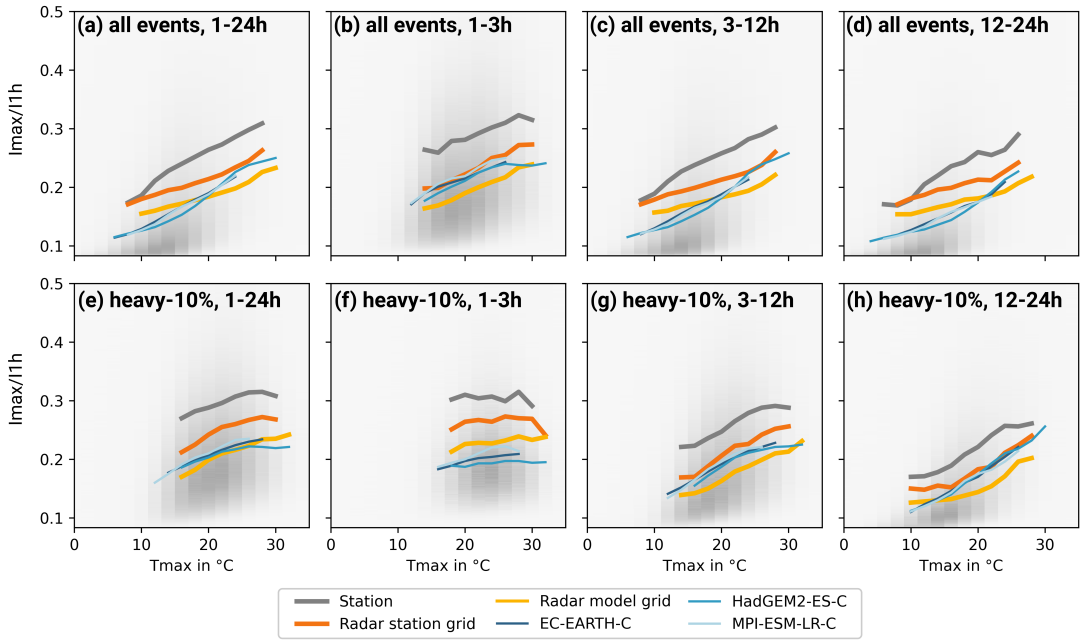

Figure 8.6: Scaling of p50 of the peak ratio Imax/I1h for all events (1st row) and heavy-10% events (2nd row). Columns refer to the different duration categories: 1-24 h (1st column), 1-3 h (2nd column), 3-12 h (3rd column), 12-24 h (4th column). Grey shading indicates the frequency distribution in the CPM ensemble.

significantly higher magnitude of the peak ratio than radar observations on the model grid (2.8 km resolution), highlighting the importance of grid resolution for the assessment of peak intensity - this finding holds for all event durations assessed. The rate of apparent scaling with temperature does not seem to be subject to this difference in resolution and is consistent between the two radar datasets. However, the rate of increase is higher in the station data compared to the radar data, except for short events (Fig. 8.6a, c, d).

To assess the peak ratio in extreme precipitation events, the same analysis is conducted for the heavy-10% events (Fig. 8.6e-h). The scaling of increasing peak ratio with higher temperatures is preserved for the heavy-10% events. In addition, the subdivision into short, medium and long duration events indicates that the scaling is weak for short duration events that are relatively peaked in nature, and also for colder temperatures. Scaling for longer duration events is stronger suggesting that these events undergo a more notable transformation in their characteristics from colder to warmer conditions.

We include an analysis of the peak ratio in the CPM simulations for completeness (Fig. 8.6). However, the bias discussed in the scaling of Imax and I1h leads to low confidence in the CPM result. All CPM simulations reproduce the observed scaling of increasing peak ratio with temperature for the full event catalogue (Fig. 8.6a-d). The scaling rate is overestimated in comparison to observations, originating from too low peak ratios at low temperatures. However, this bias is reduced for heavy precipitation events (heavy-10% events in Fig. 8.6e-h) and the pattern of increased scaling rate with an increase in event duration is reproduced by the CPM simulations. Yet, the assessment

of heavy-10% events reveals a bias of peak intensity which depends on event duration, with the CPM simulations underestimating the scaling rate for short duration events but not for long duration events. This indicates a bias in the representation of short and strong precipitation events by the CPMs, in agreement with Chapter 6 and Chapter 7.

Implication

To conclude the analysis of apparent intensity scaling in precipitation events, we discuss the following key points from the analysis above: unexpectedly high apparent scaling rates for peak intensities in extreme and average precipitation events, and the bias in the representation of apparent intensity scaling for precipitation within the CPM simulations.

The event-based analysis (compared to commonly assessed percentiles of the whole wet fraction) has shown that super-CC scaling of sub-hourly peak intensities is not tied only to extreme precipitation events, but in contrast, is observed in station observations also for more moderate events. This increase in peak intensity is attributed to a shift from predominantly stratiform precipitation under colder conditions, to an increase in convective fraction in warmer conditions, as previously proposed by Berg et al. (2013) or Da Silva and Haerter (2024). The shift in rainfall type is further supported by the scaling of the event peak ratio, which indicates that precipitation events become more peaked (steeper in temporal profile) at higher temperatures. This suggests that at higher temperatures a larger proportion of the precipitation is convective, with more rapid moisture release occurring as temperatures rise. This key result from the event-based analysis thus indicates that high scaling rates, up to super-CC scaling, need not be tied to thermodynamic constraints but can arise from changes in rainfall type.

Further, the event-based analysis revealed a dependence of Imax apparent scaling rates on the event duration, with longer events generally showing a stronger scaling of peak intensity. We interpret this to be because short events are generally more convective by nature with already high peak intensities, while longer events tend to be more stratiform in nature under colder conditions, with a greater potential for an increase in convective fraction under warmer temperatures. This finding highlights one of the benefits of using event-based intensity sampling, for a better exploration of changes to the underlying processes.

The evaluation of apparent scaling in the CPM simulations revealed that, while the models capture the main features of apparent intensity scaling – such as stronger scaling for Imax compared to I1h and Imean, stronger scaling of Imax and I1h for longer events compared to short duration events, and generally above-CC scaling for the p90 of Imax and I1h – they systematically overestimate the magnitude of scaling rates compared to observations. This overestimation was less pronounced when analysing the higher percentile p90 compared to p50, suggesting that biases in event representation within the simulated event catalogue may contribute to this uncertainty.

In summary, we find that apparent scaling rates are higher for extreme intensities than for more moderate quantiles of the distribution. The scaling rate for precipitation intensity depends on the representative period over which intensity is sampled, and we find stronger apparent scaling for embedded peaks in a precipitation event than for the mean intensity of the event. This translates into an increased steepness of the temporal profile of events for warmer temperatures. The rate of scaling was found to be dependent on event duration. While short-duration events scale strongest in Imean, long duration events scale strongest for embedded peak intensities, for Imax and I1h. The CPM simulations overestimate the scaling rates for Imax and I1h and show better agreement with the observed scaling rates for Imean. CC-scaling is found to be exceeded in the station observations of Imax, while apparent scaling rates for I1h is approximately at the CC-rate for p90.

8.3.3 D50

The parameter D50 is used to assess the timing of bulk precipitation during the event. For a detailed description of D50, refer back to Chapter 6. In this chapter, we first analyse the co-dependence of D50 on Imean, and then derive the apparent temperature scaling of D50 for all events and the heavy-10% events.

Dependence of D50 on precipitation intensity

The median D50 dependence on Imean for all events reveals predominantly centred profiles (D50 $\approx$ 50 %) at low Imean values (Fig. 8.7a-c). As Imean increases, the median D50 tends to decrease, indicating that higher Imean values are associated with more front-loaded event profiles. The decrease in D50 with increasing Imean is strongest in the station observations throughout the different event durations. For short events at Imean above approximately 10 mm/h, D50 rises in the observation datasets (mainly for the radar), though events remain predominantly front-loaded (Fig. 8.7a). This increase for high Imean is explained as short-duration events of very high Imean are generally events with high precipitation rates throughout the event and thus without pronounced peak structure. As a result, the very high Imean range does not exhibit strong front-loading inherently.

To clarify the relationship at high precipitation intensities, the same analysis of D50 with dependence on peak intensity Imax instead of Imean was conducted (Fig. 8.7d-f). The results show consistent centered profiles at low Imax and increasing front-loading with increasing at all durations.

The CPM simulations capture the general patterns observed for different event durations. However, limitations become apparent for short duration events. The CPM slope of median D50 over Imean is less steeply declining with increasing Imean than in the observations, indicating a limitation in representing front-loaded short and intense events.

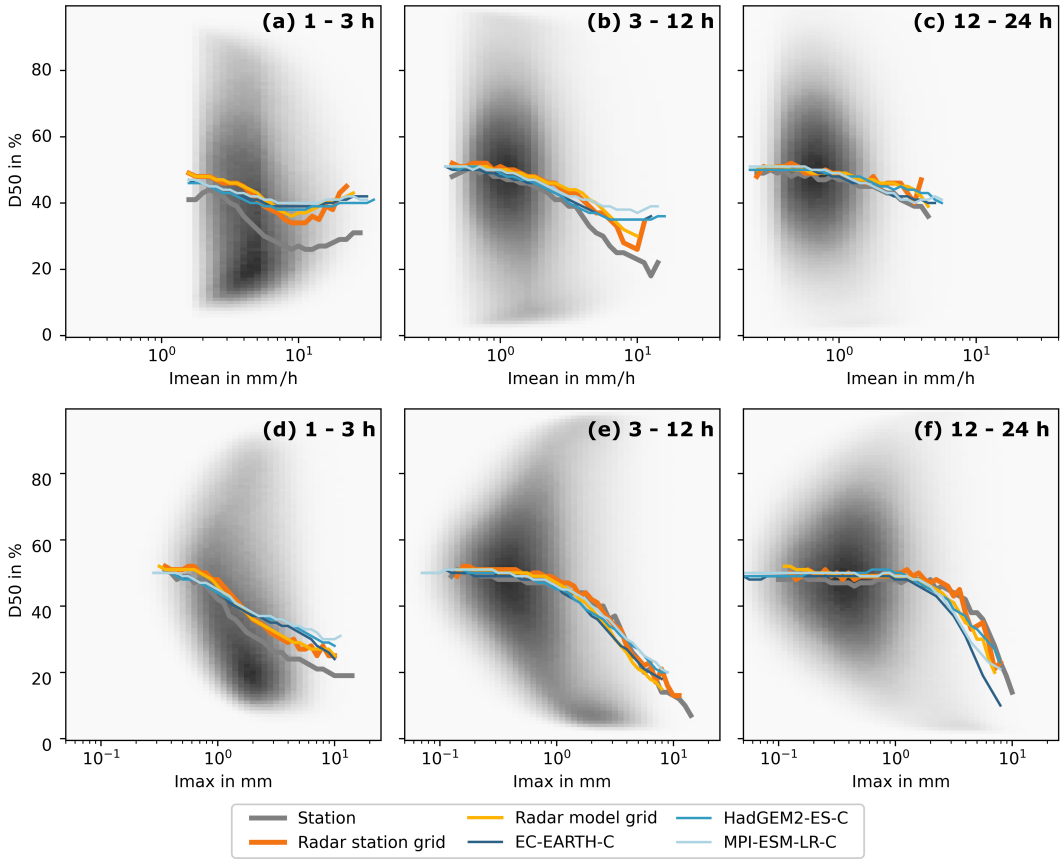

Figure 8.7: Solid lines show the median of D50 in the respective Imean bin for event durations of (a) 1-3 h, (b) 3-12 h, (c) 12-24 h and the median of D50 in the respective Imax bin for event durations of (d) 1-3 h, (e) 3-12 h, (f) 12-24 h. The bin width of Imean or Imax increases exponentially with an increment of $\times 10^{0.05}$. The 0.1 % highest and 0.1 % lowest Imean or Imax are excluded from the analysis of the median in each dataset to remove the range with low data availability. Grey shading indicates the normalised frequency in the simulation ensemble.

In summary, the findings show that the D50 is tied to intensity and there is a trend of increasing front-loading with higher Imean. However, for short events with very high Imean, precipitation events do not have a distinct front-loaded temporal profile. These findings are consistent with the analysis in Visser et al. (2023) for Australia, who attribute increased front-loading to an increase in convective proportion.

Scaling of D50 with temperature

A negative apparent scaling of median D50 with event-T_{max} is observed, indicating more front-loaded events in warmer conditions for all events. This negative scaling is strongest for short duration events and much weaker for longer duration events (Fig. 8.8a-c). Quantifying this relationship through linear regression, the scaling ranges from approximately -0.8 %/°C for short duration events to -0.3 % for longer duration events in the station data (Fig. 8.9). The scaling is weaker in the radar observations than in the station observations. Closer inspection of the scaling curve reveals that the

regression slope varies across the temperature range. For all events except the shortest ones, the curve tends to be flatter at colder temperatures (up to around 15-20 °C) and becomes steeper as temperatures rise beyond this point. The apparent scaling of D50 with event-T_{max} for heavy-10% events is weakest for short duration events, which tend to be relatively front-loaded over the whole temperature range (Fig. 8.8a). In contrast, the scaling for medium and long duration events is generally stronger (more negative) for the heavy-10% events than for all events (Fig. 8.8e-f). Station observations show the steepest scaling for D50 of nearly -1.2 %/°C for long duration events.

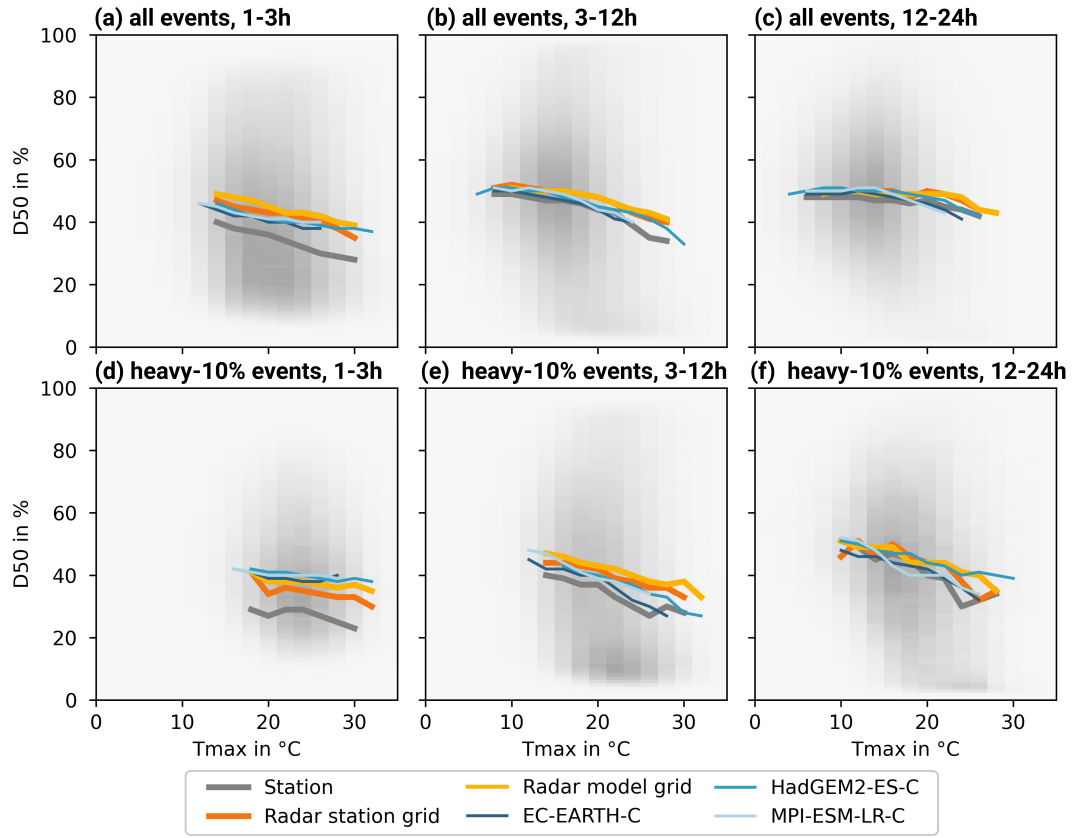

Figure 8.8: Scaling relation of D50 over event-T_{max} in the different datasets in colour. The top row shows the relationship over all events with an event duration of (a) 1 h - 3 h duration, (b) 3 h - 12 h duration, (c) 12 h - 24 h duration. The bottom row shows the relationship for the heavy-10% events: (d) 1 h - 3 h duration, (e) 3 h - 12 h duration, (f) 12 h - 24 h duration. Grey shading indicates the normalised frequency in the simulation ensemble.

The CPM simulations reproduce the observed negative scaling of D50 with event-T_{max}. The CPMs underestimate the scaling for short duration precipitation events but are within the observational range for medium and long duration events. The CPM simulations also reproduce the observed enhanced apparent scaling for heavy-10% events compared to all events for medium and long duration events. The ensemble spread is especially high for long duration events and generally higher for higher temperature ranges.

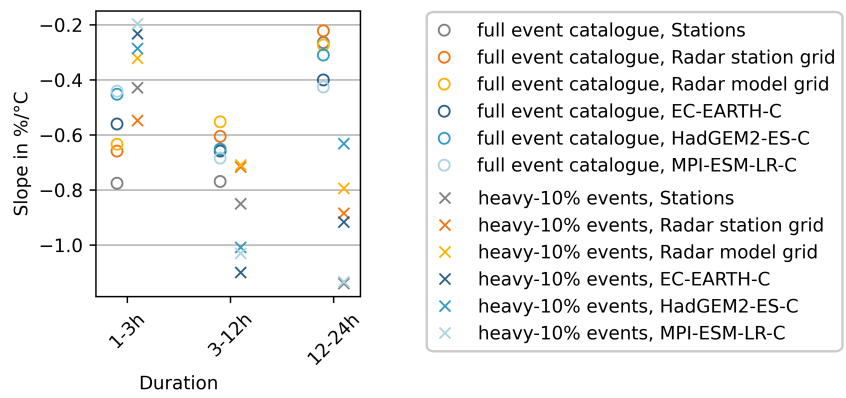

Figure 8.9: Slope of the linear regression of the D50 dependence on event-$T_{\max}$ in all events and heavy-10% events.

In summary, the apparent scaling of D50 with event-$T_{\max}$ varies with both event duration and precipitation intensity. Our results generally show a decline in D50 at higher temperatures, meaning that events become more front-loaded in warmer conditions. The strength of this scaling is more pronounced for heavy precipitation events (heavy-10% events) – except for events of short duration; these are already predominantly front-loaded throughout the temperature range. The steepest decline of D50 with event-$T_{\max}$ is found for long duration, heavy precipitation events. The CPM simulations reproduced this negative scaling of D50 with event-$T_{\max}$ as well as the observed dependence on event duration, and the strongest scaling of heavy-10% events for long duration events. The simulated magnitude of the apparent scaling relation for the full event catalogue is in relatively good agreement with the observations. However, a larger bias is apparent for heavy-10% events.

We hypothesize that changes in D50 are linked to shifts in precipitation type; convective events tend to be more front-loaded, with the majority of precipitation released at the start of the event, while stratiform events are more uniform in their temporal distribution. As suggested by Visser et al. (2023), the temperature dependence of D50 indicates that the thermodynamically-increased water vapour at higher temperatures precipitates preferentially at the beginning of an event, leading to a shift in the temporal precipitation event profile.

8.4 Day-to-day variability in historical and future simulations

The previous section evaluated the apparent scaling rates for summer precipitation events in CPM simulations for the historical period. This section investigates whether the same scaling relationships hold in a warmer future climate. We compare the apparent scaling rates derived from the CPM historical simulation (1971-2000) with those derived from the future time slice (2051-2070). The future time slice comprises only 20 years, in

contrast to 30 years in the historical period. Despite the shorter duration, pooling data across grid points results in a sufficiently large sample size for deriving robust scaling rates. However, the shorter future time slice may limit the representation of the internal variability of the climate system.

8.4.1 Intensity

Figure 8.10 shows the ensemble mean of the temperature scaling for Imax, I1h, and Imean for the historical (blue) and future (red) time slices respectively. The ensemble mean is presented for clarity, as the individual ensemble members largely overlap. Results for each ensemble member are included in the Appendix for reference (Fig. E.7-E.9).

We find that the distribution of event-$T_{\max}$ in the future time slice shifts toward higher temperatures (Fig. 8.10a-d). In addition, there is a decreasing frequency of summer events in the future time slice. Note that this is not the focus of this Chapter: frequency changes of events are detailed in Chapter 7.

The key features of the scaling for intensity in the historical time slice – an approximately exponential increase below 25°C, and curve flattening at higher temperatures – are reproduced in the future projection (Fig. 8.10). The future time slice shows an extension of the scaling curve along the same slope toward higher temperatures and the threshold at which scaling flattens due to moisture limitations shifts to higher temperatures. The extension of the future scaling curve for intensity along its slope results in only minor changes in the future scaling rate compared to the historical apparent scaling rate for short duration events (Fig. 8.11). For long duration events, the scaling rate increases slightly in the future time slice, for both the ensemble mean and the individual members (See Fig. 8.11 for the ensemble composite and Fig. E.7-E.9 for the single ensemble members).

This comparison suggests that past and future scaling curves largely align, particularly for a moderate temperature range below ~25 °C where the scaling is an approximately exponential increase. However, we find slight positive lateral displacements in the p50 scaling for Imax and I1h, especially for long duration events (Fig. 8.10h and l). The displacement mainly stems from the ensemble members EC-EARTH-C and MPI-ESM-LR-C (Fig. E.7-E.8). This finding suggests that additional factors, possibly dynamic changes or changes in moisture availability, may affect moderate events more than extreme events, whose peak intensities are largely governed by thermodynamic constraints.

In summary, this analysis indicates that future intensity scaling closely follows historical scaling rates, with an approximately exponential increase at moderate temperatures and a levelling-off at higher temperatures due to moisture limitations. However, in future projections, the exponential scaling is generally extended towards a higher tem-

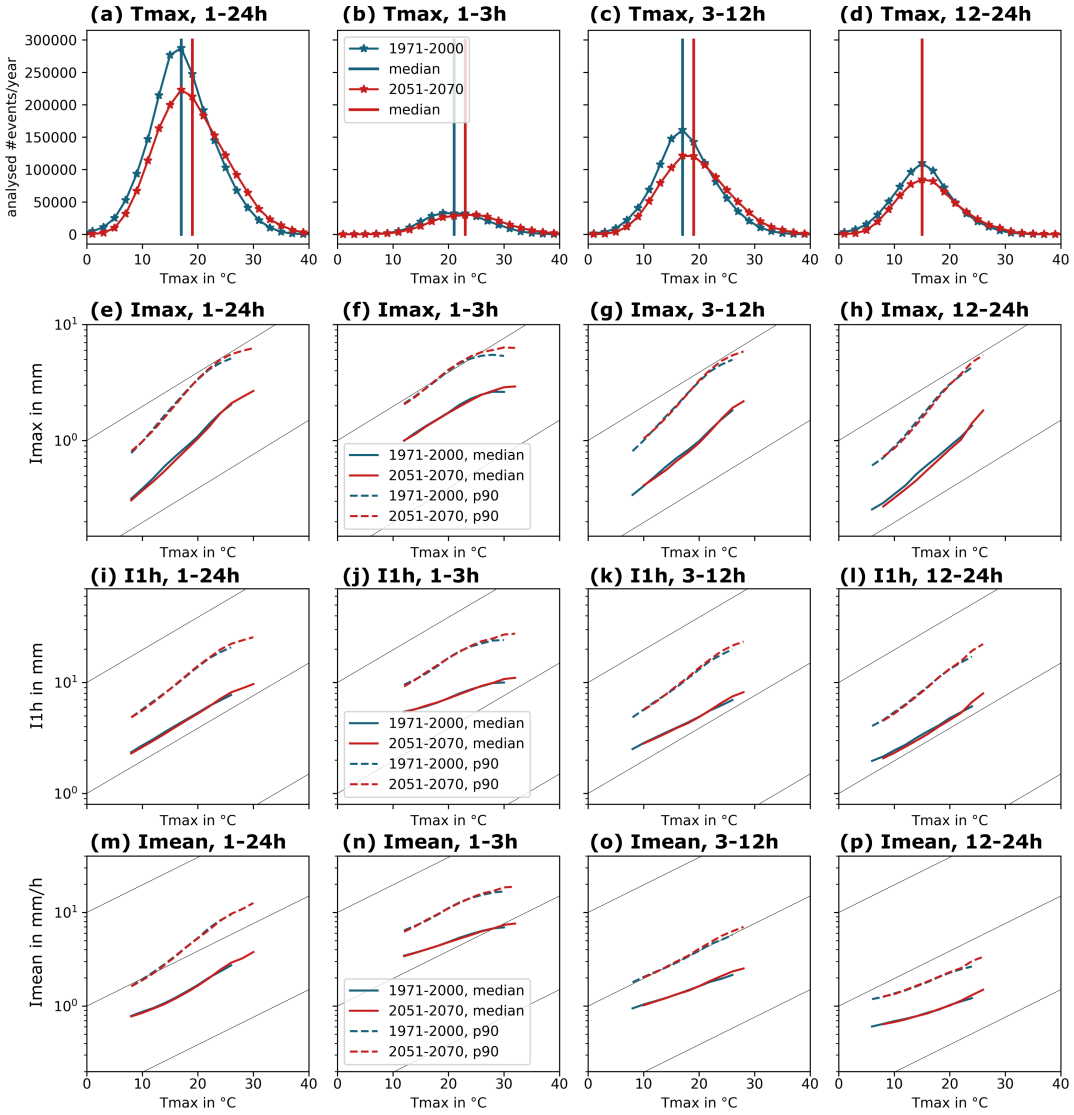

Figure 8.10: Projected apparent scaling relations in the reference (1971-2000) and future time slice (2051-2070) of p50 and p90 of the three intensity measures Imax (e-h), I1h (i-l), and Imean (m-p). Columns refer to the different duration categories: 1-24 h (1st column), 1-3 h (2nd column), 3-12 h (3rd column), 12-24 h (4th column). (a-d) show the underlying temperature distribution to the according samples. The diagonal lines indicate CC-scaling with a slope of 7 %/°C.

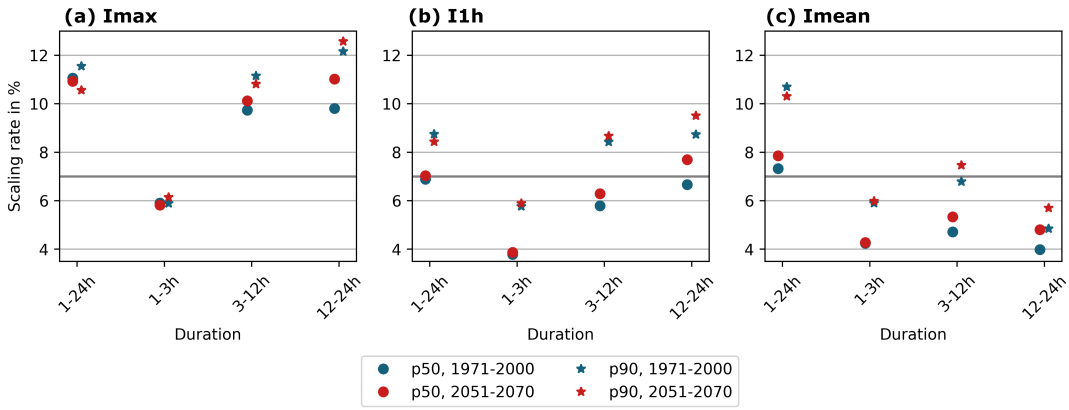

Figure 8.11: Apparent scaling rates for intensity in reference (1971-2000) and projection (2051-2070) for the p50 and the p90 of the distributions. The intensity measures (a) Imax, (b) I1h, and (c) Imean are shown. The gray horizontal line marks CC-scaling with a rate of 7 %.

perature range. Slightly higher apparent scaling rates in the future than in the historical simulations agree with findings in Prein et al. (2016) for low-elevation regions in the US.

8.4.2 D50

We compare the CPM simulated scaling of D50 in the future and historical time slices for the entire event catalogue as well as for heavy-10% events. Due to differences in the D50 scaling curves among the three ensemble members for the historical period, results are presented individually for each member rather than as an ensemble average (Fig. 8.12-8.14).

The future scaling reproduces the key features identified for historical apparent scaling of D50 with event-T_{max} – specifically, a general decline of D50, and a more pronounced decline for heavy-10% events for longer event durations. Scattering in the results of HadGEM2-ES-C for long duration events is attributed to dry summers in this ensemble member, which tends to simulate fewer long duration events, potentially leading to a biased occurrence in the spatially pooled dataset (Fig. 8.13d).

The dominant pattern across all ensemble members is a lateral shift of the scaling curve towards higher event-T_{max} (Fig. 8.12-8.14). This implies that median D50 is not expected to remain constant under similar temperature conditions in a future climate, with the same event-T_{max} leading to fewer front-loaded events in the future compared to historical period under similar temperature conditions. The strongest lateral shift is found for heavy-10% events for medium and long duration events. For short duration heavy-10% events, the ensemble does not consistently show a positive shift. The shift could not be attributed to a reduction in moisture, as the same pattern is apparent in the scaling with event-TD_{max} (Supplementary Fig. E.10-E.12).

The quantification of scaling by the slope of a linear regression indicates a similar magnitude of scaling in the historical and future time slice for all events (Fig. 8.15). For

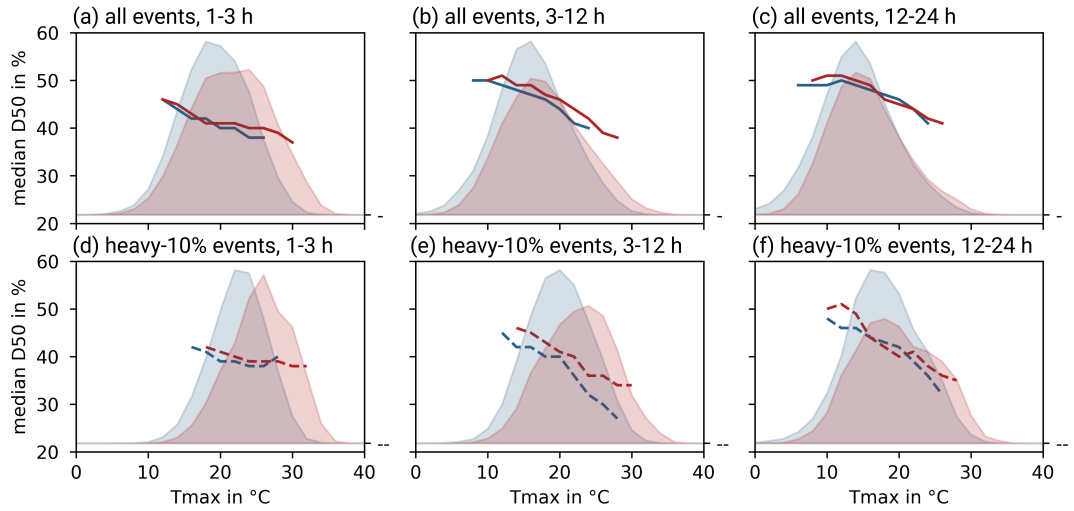

Figure 8.12: Projected apparent scaling by EC-EARTH-C in reference (blue, 1971-2000) and future time slice (red, 2051-2070) of the median of D50 over event-$T_{\max}$ for all events (1st row), and heavy-10% events (2nd row). Different duration categories are displayed in columns: 1-3 h (1st column), 3-12 h (2nd column), 12-24 h (3rd column). The temperature distribution is provided in the background normalised with the number of events in the historical period.

short duration heavy-10% events, the lateral shift does not strongly impact the slope of the apparent scaling relationship. The uncertainty was assessed using bootstrapping over the simulation years, and the resulting uncertainty is indicated by the whiskers in the figure. Indeed, the estimates indicate no significant change in scaling for short events. However, for medium and long duration heavy-10% events, the magnitude of the scaling is lower in the future compared to the historical period. The ensemble spread increases from historical to future time slice, particularly for longer duration events. We attribute this increase to the shorter 20-year future time slice, a reduction in event frequency, and potentially varying signals in the driving GCMs.

In summary, although the scaling curves of D50 with event-$T_{\max}$ do not align precisely across the three ensemble members, they consistently show similar patterns when comparing historical and future time slices. The primary pattern of change in future projections is a lateral shift of the scaling curve towards higher temperatures, suggesting that median D50 at similar temperature conditions is less front-loaded in the future compared to the historical simulations. This shift is most evident for medium- and long-duration heavy events. These findings suggest that, while certain scaling behaviours of D50 appear robust under future climate conditions, the misalignment of past and future scaling curves and the uncertainty in future scaling from different ensemble members require cautious interpretation of projected D50 patterns.

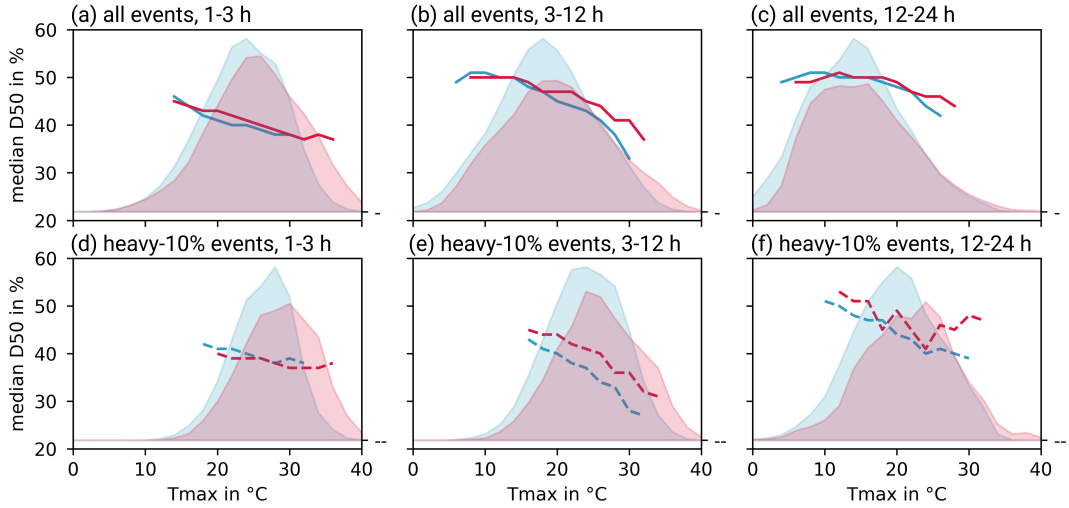

Figure 8.13: Projected apparent scaling by HadGEM2-ES-C in reference (blue, 1971-2000) and future time slice (red, 2051-2070) of the median of D50 over event-$T_{\max}$ as in Fig. 8.12.

8.5 Climate change signal

We now analyse the climate change signal: first, by assessing changes to event-$T_{\max}$; second, by evaluating changes to intensity measures and peak proportions; and third, by investigating changes to event profile shape using D50.

8.5.1 Temperature event-$T_{\max}$

To assess changes in the event-$T_{\max}$ temperature distribution with global warming, we examine the percentiles p10, p50, and p90 of the event-$T_{\max}$ distribution in each time slice (Fig. 8.16). The corresponding linear climate change signal (CCS) for these percentiles is shown in Fig. 8.17. The analysis is presented first for the full dataset, followed by an assessment for the heavy-10% and heavy-1% events.

Projected event-$T_{\max}$ for all events

We find that the increase in p50 of event-$T_{\max}$ associated with summer precipitation events is generally below the increase in GWL (Fig. 8.16a-d, solid lines): the linear change signal for the full event dataset is below 1°C/(°C GWL), except for short duration events in the EC-EARTH driven simulations (Fig. 8.17a, solid lines). However, the magnitude of the increase in event-$T_{\max}$ is dependent on the driving GCM. The highest change signals are generally projected by EC-EARTH, and the lowest by HadGEM2-ES. To contextualize the low increase in HadGEM2-ES-C, it should be noted that absolute values of event-$T_{\max}$ are highest in HadGEM2-ES-C throughout the projection (Fig. 8.16a-d). All ensemble members agree on a stronger change signal for event-$T_{\max}$ of short duration events compared to longer events.

The change signal of p90 of the event-$T_{\max}$ distribution is systematically higher than the change in p50, across all ensemble members (Fig. 8.17a, dashed lines). Again, the

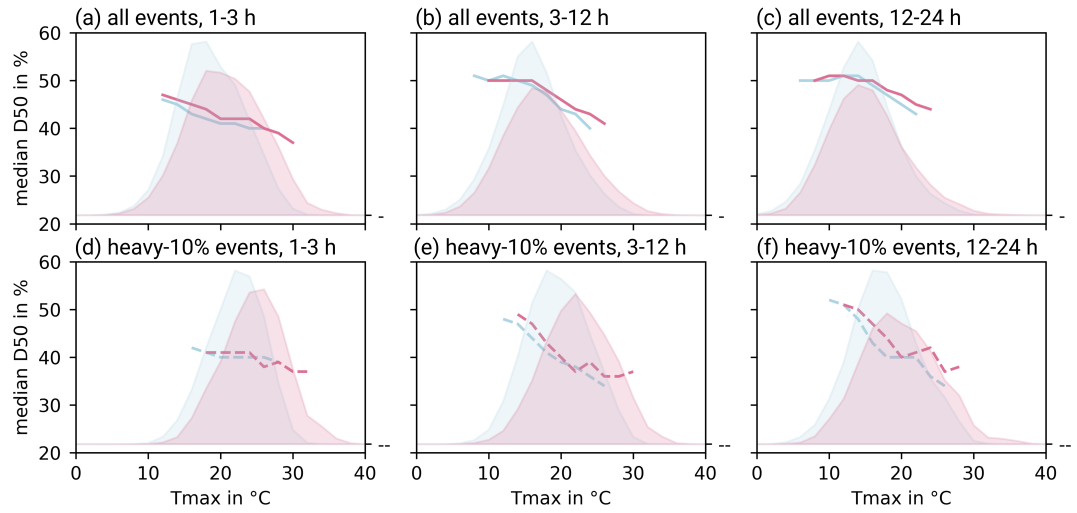

Figure 8.14: Projected apparent scaling by MPI-ESM-LR-C in reference (blue, 1971-2000) and future time slice (red, 2051-2070) of the median of D50 over event-$T_{\max}$ as in Fig. 8.12.

change signal is strongest for short duration events. For p90, CCS is above 1 °C/(°C GWL) for short duration events and is around 1 °C/(°C GWL) for medium duration events. In contrast, for p10 of the event-$T_{\max}$ distribution – describing the behaviour of the coldest 10 % of events – increases are generally below the increase in the median, except for long duration events. These contrasting results indicate increasing spread in the event-$T_{\max}$ distribution in a warmer future climate. We find a similar, although less pronounced increasing spread in the distribution of event-$\mathrm{TD}_{\max}$ (Supplementary Fig. E.13).

Projected event-$T_{\max}$ for heavy-10% and heavy-1% events

We find that event-$T_{\max}$ associated with heavy-10% events and heavy-1% events has a higher ensemble spread compared to the full event catalogue, indicating considerable uncertainty in the projections. In heavy-10% events and heavy-1% events, an increase above 1 °C/(°C GWL) is generally found for the median in EC-EARTH-C, and MPI-ESM-LR-C, whereas HadGEM2-ES projects an increase in event-$T_{\max}$ below GWL increase (Fig. 8.17b & c). The overestimation of projected event-$T_{\max}$ in HadGEM2-ES-C compared to the ensemble is more pronounced for heavy precipitation events compared to the full event catalogue (Fig. 8.16e-l). The ensemble members converge towards high GWL.

The change signal of heavy-10% events and heavy-1% events is generally higher than for the full event dataset (Fig. 8.17b & c). Similar to the behaviour for all events, also for heavy-10% events, the event-$T_{\max}$ distribution widens in the future projection, derived from a larger change signal of p90 compared to p50 and p10 (Fig. 8.17b). A similar pattern is projected for heavy-1% events, though it is less pronounced (Fig. 8.17c).

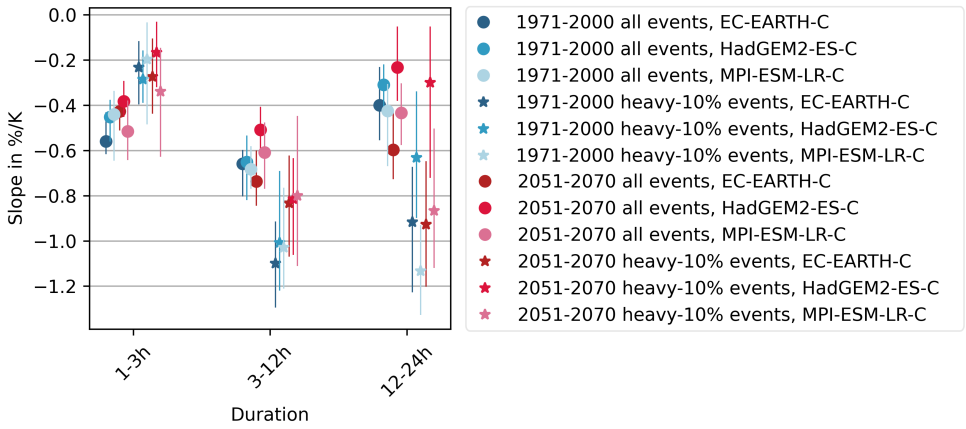

Figure 8.15: Magnitude of the apparent linear scaling of D50 with event-$T_{\max}$ in the reference (1971-2000, blue) and future time slice (2051-2070, red). Whiskers represent the range from the 25th to the 75th percentile of the apparent linear scaling. The uncertainty was estimated using bootstrapping over the simulation years with 1000 repetitions with replacement.

In summary, we find that event-$T_{\max}$ increase is strongest for short duration events and generally higher for higher percentiles (hotter conditions) than for lower percentiles (colder conditions). The magnitude of the climate change signal of event-$T_{\max}$ is variable across the CPM ensemble. It is generally below the change signal in GWL (<1 °C/(°C GWL)) for the full event dataset, but mostly above the GWL change signal for heavy precipitation events. The findings suggest that the event-$T_{\max}$ of extreme precipitation events is more sensitive to an increase in global warming compared to event-$T_{\max}$ of moderate events.

8.5.2 Intensity

We examine changes to Imax, I1h, and Imean. For each intensity measure, we specifically assess changes to the percentiles p50, p90, and p99 of the distributions.

Imax The p50 of Imax increases at below the CC-rate for all ensemble members (Fig. 8.18a-d and Fig. 8.19a). The increase is more pronounced for higher percentiles of the distribution (p90 and p99), with this pattern being consistent across the ensemble. For EC-EARTH-C and MPI-ESM-LR-C, climate scaling rates (CSR) of p99 exceed the CC-rate for all event durations and maximum climate scaling rates of approximately 9%/°C are projected. HadGEM2-ES-C projects a lower CSR for p90 and p99 (below CC). This weaker climate change signal in HadGEM2-ES aligns with the weaker signal in event-$T_{\max}$ discussed above. The CSR is found to depend on event duration, particularly for p50 of Imax which is generally larger for short duration events. For higher percentiles (p90 and p99), there is no pattern of duration dependence.

I1h The CSR is similar for I1h. The CSR of p50 is below CC and is strongest for short duration events, while the CSRs for the extremes are higher and exceed the CC-rate mainly in the EC-EARTH-C simulation (Fig. 8.18e-h and Fig. 8.19b). The

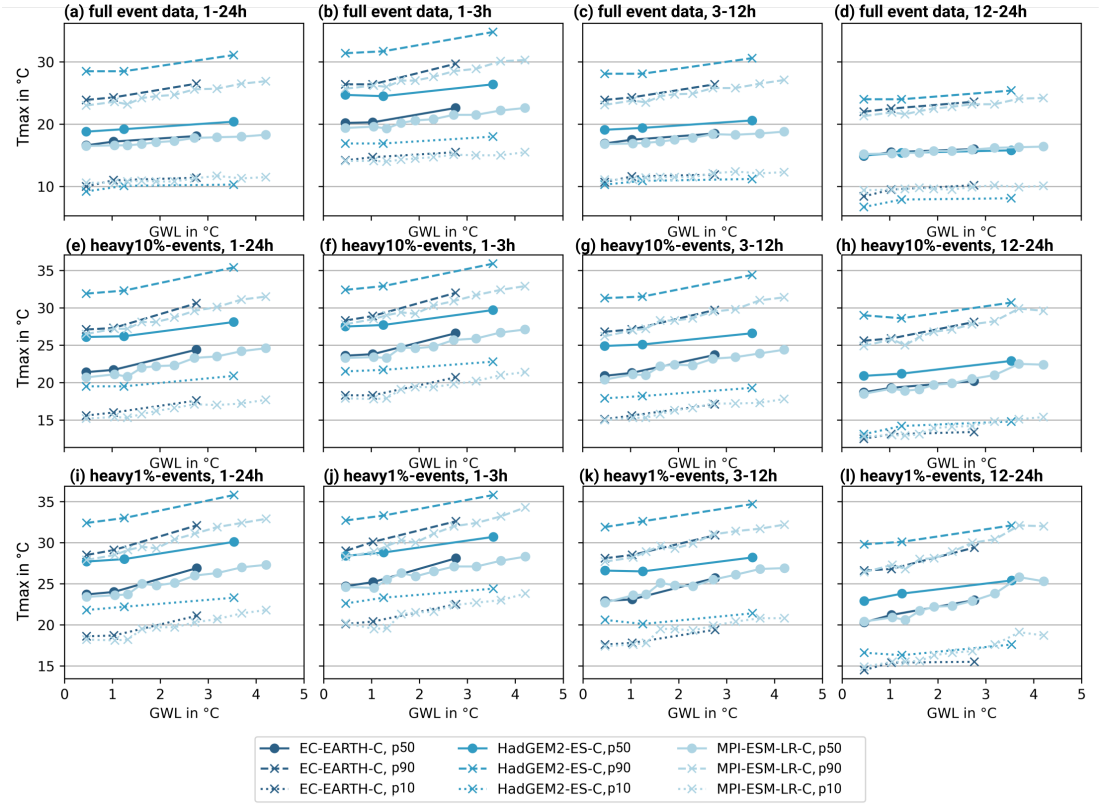

Figure 8.16: Projected event-$T_{\max}$ associated with the all events in the first row, heavy-10% events in the second row, and heavy-1% events in the second row. Different duration categories are displayed in columns: 1-24h (1st column), 1-3h (2nd column), 3-12h (3rd column), 12-24h (4th column). The p10, p50, and p90 of the event-$T_{\max}$ distribution in each 20-year time slice are shown over the GLW associated with that time slice.

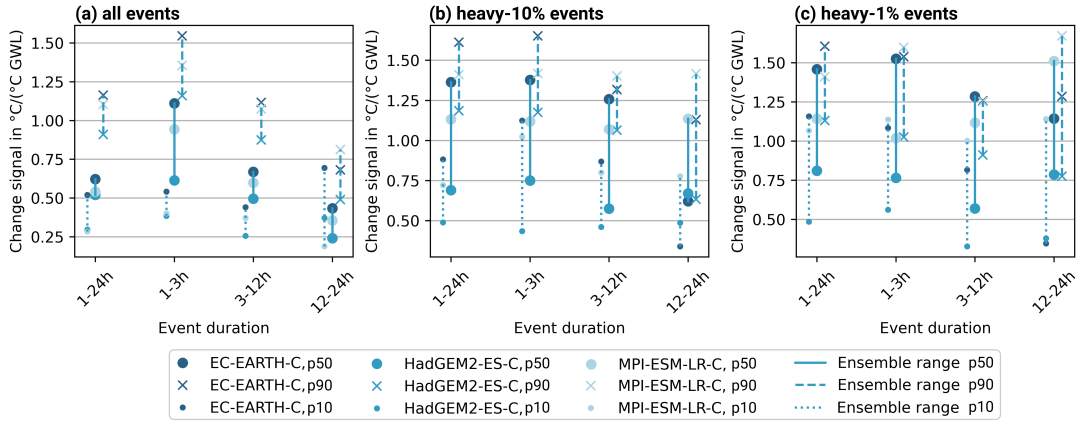

Figure 8.17: Slope of the linear regression of event-$T_{\max}$ over GWL in (a) the full event dataset and (b) heavy-10% events, (c) heavy-1% events

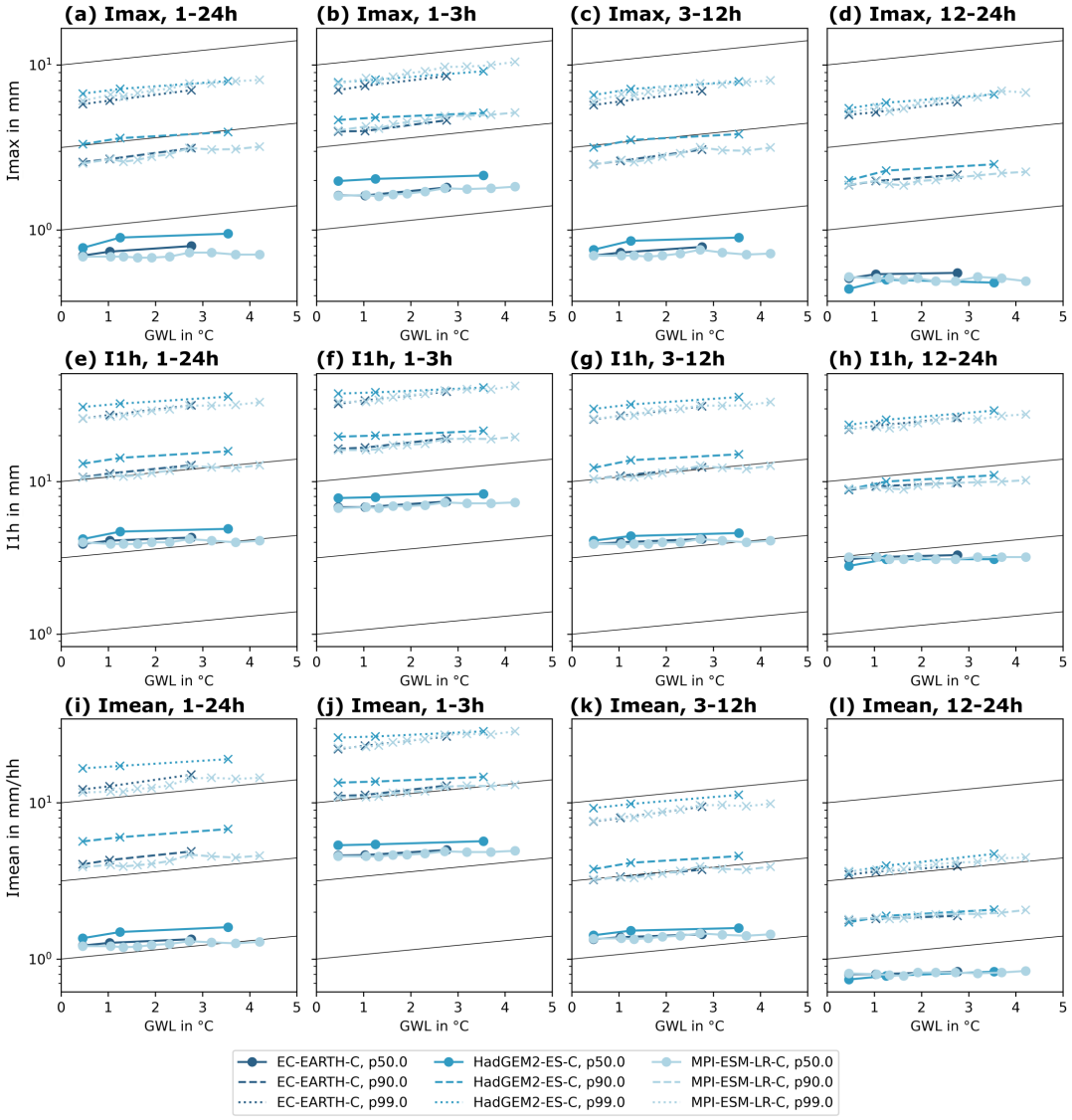

Figure 8.18: The p50, p90, and p99 percentile of the distribution of (a-d) Imax, (e-h) I1h, and (i-l) Imean in each 20-year time slice are shown over the GWL associated with that time slice. Different duration categories are displayed in columns: 1-24 h (1st column), 1-3 h (2nd column), 3-12 h (3rd column), 12-24 h (4th column).

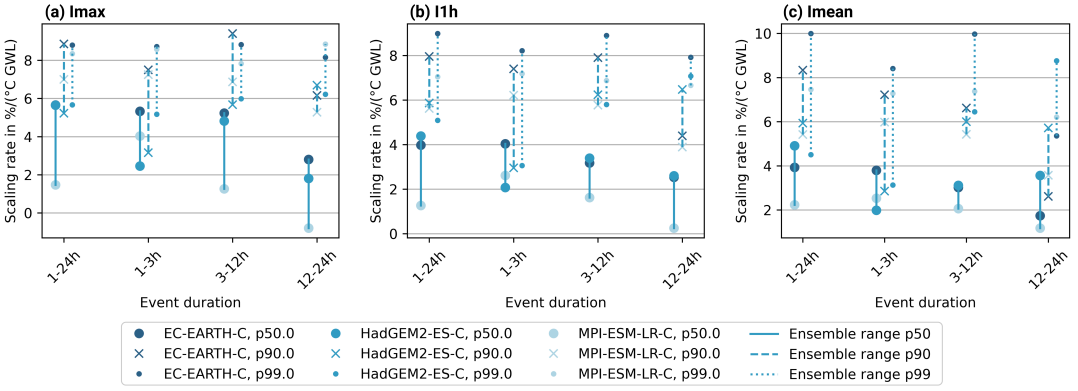

Figure 8.19: CSR of the intensity measures (a) Imax, (b) I1h, and (c) Imean.

strongest CSRs are projected for p99 in EC-EARTH-C, reaching approximately 9%/°C. Compared to Imax, the CSR in I1h is slightly lower for p50, suggesting a slight increase in peak ratio. However, this is not found for p90 or p99.

Imean Imean increases across all event durations (Fig. 8.18i-l and Fig. 8.19c). The increase is stronger for p90 and p99 than for p50. The highest CSRs, of up to 10 %/°C, are projected for EC-EARTH-C. However, the CSRs must be interpreted with caution, as an increase in Imean can result from either a genuine rise in intensity or a shortening of event duration. These results imply that, in general, rainfall in future rain events will fall in more concentrated bursts.

In summary, the assessment of climate scaling for intensity measures indicates that while p50 of Imax and I1h increases at a rate below CC, higher percentiles (p90 and p99) of Imax and I1h can increase at a super-CC rate mostly in the ensemble members EC-EARTH-C and MPI-ESM-LR-C. A comparison across the scaling of p90 and p99 of the different intensity measures does not show consistently stronger scaling of Imax relative to I1h or Imean. This finding suggests no fundamental change to the peak proportion of extreme precipitation; with both historic and future extremes likely to be convective.

8.5.3 D50

To assess changes in the D50 distribution with global warming, we examine the percentiles p10, p50, and p90 for each time slice (Fig. 8.20). The corresponding linear climate change signal (CCS) for these percentiles is shown in Fig. 8.21.

Using the full event dataset reveals no climate change signal in the distribution of D50 (Fig. 8.20a-d). This is consistent across all ensemble members, duration categories and assessed percentiles and is reflected in a CCS that is around zero for p50 and shows only minor fluctuations for p10 and p90 (Fig. 8.21a). The largest deviations from CCS ≈ 0 are projected by the member EC-EARTH-C. Specifically, a negative CCS of D50 for p10 in EC-EARTH-C (approximately -0.4 %/°C) suggests a slight projected increase in the proportion of very front-loaded events. Conversely, p90 exhibits a positive scaling, indicating a decreased proportion of back-loaded events. Given the minimal projected climate change signal overall, no consistent patterns emerge with respect to event duration.

The assessment in Fig. 8.20e-h for heavy-10% events and Fig. 8.20i-l for heavy-1% events, reveals that also for heavy precipitation events, no distinct climate change signal is detected for D50. In both heavy-10% and heavy-1% events, larger fluctuations in CCS are evident for longer duration events (Fig. 8.21b&c). However, these fluctuations are accompanied by the largest ensemble spread, and no clear trend emerges. We attribute these variations at longer event durations to changes in event frequency, as the occurrence of long summer events is significantly reduced, potentially impacting the regionally pooled statistics (see Chapter 7).

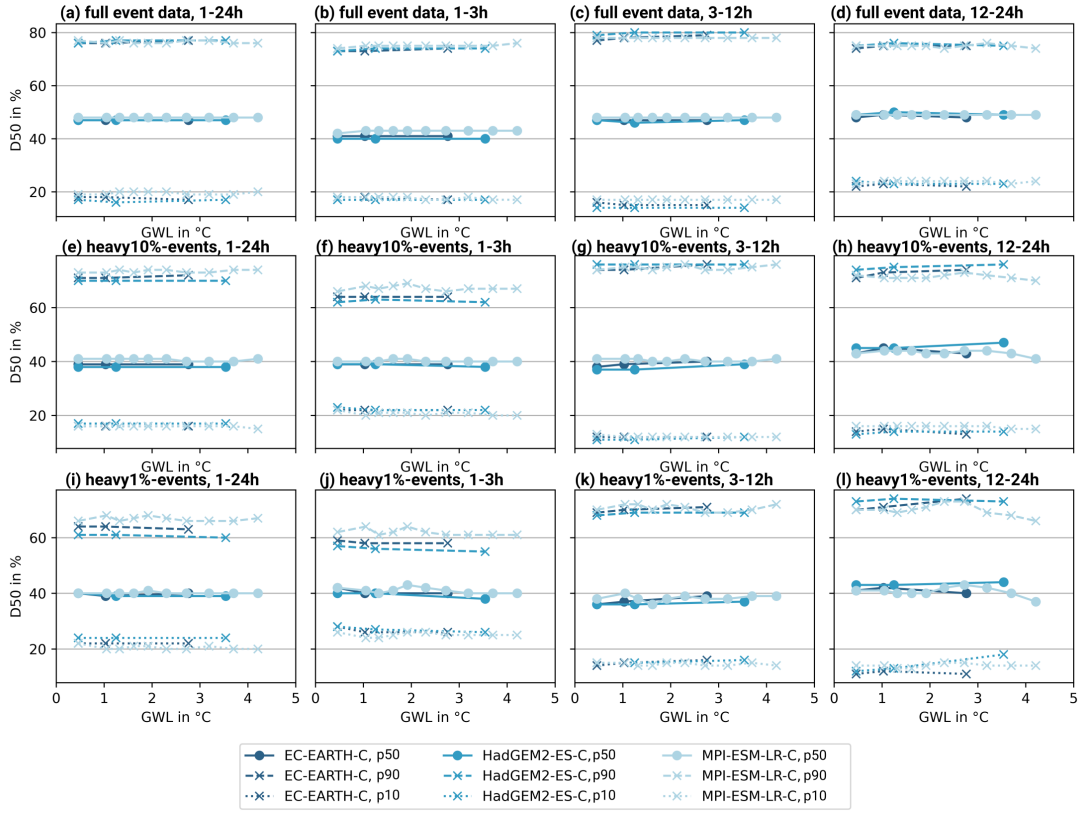

Figure 8.20: Projected D50 associated with the full event dataset in the first row, heavy-10% events in the second row, and heavy-1% events in the third row. Different duration categories are displayed in columns: 1-24 h (1st column), 1-3 h (2nd column), 3-12 h (3rd column), 12-24 h (4th column). The p10, p50, and p90 of the D50 distribution in each 20-year time slice are shown over the GLW associated with that time slice.

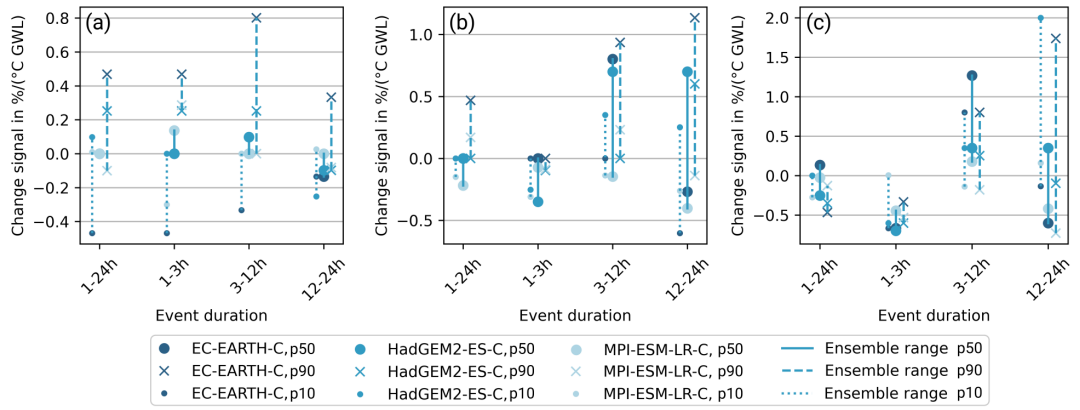

Figure 8.21: Slope of the linear regression of D50 over GWL in (a) the full event dataset and (b) heavy-10% events, (c) heavy-1% events.

In summary, the simulations do not project a climate change signal of D50. The finding of no clear climate change signal in D50 seems to contradict the apparent scaling results which indicate more front-loading with higher event-$T_{\max}$. This implies that D50 may not be closely tied to thermodynamic changes, highlighting the limitations of apparent scaling relations.

8.6 Discussion and conclusion

This chapter has assessed the precipitation event characteristics of peak intensity, mean intensity and timing of bulk precipitation and their sensitivity to temperature. The analysis comprises three steps: first, the apparent scaling rates for the historical period were evaluated and compared to those from the observational datasets; second, apparent scaling rates were compared for the historical and future climate; and third, the climate scaling from historical to future climate was assessed. The key results of the analysis are:

- The apparent scaling rates with event-$T_{\max}$ are higher for Imax than for I1h or Imean. This implies an increased steepness of the temporal event profile with event-$T_{\max}$. Maximum observed scaling rates for Imax exceed the CC-rate and approach 9%/°C. The CPM simulations systematically overestimate the apparent scaling rates for Imax, I1h, and Imean. D50 shows a decrease with event-$T_{\max}$, indicating more front-loaded events with warmer conditions, a trend adequately captured in the CPM simulations.

- Apparent scaling relations for Imax, I1h, and Imean from historical simulations are preserved in the future simulations, with scaling curves extending towards higher event-$T_{\max}$. However, there is a misalignment of past and future scaling curves for D50.

- The CPM simulations indicate that the increase in event-$T_{\max}$ for the full event dataset is generally below the projected increase in GWL but the increase in event-$T_{\max}$ for heavy precipitation events exceeds the GWL increase. The climate scaling rate for the median Imax and I1h is well below the CC-rate. However, the climate scaling rate is higher for p90 and p99 of Imax and I1h and can exceed the CC-rate. No climate change signal in the projected distribution of D50 is detected.

Our finding of super-CC scaling in the apparent scaling rates supports previous literature which documents this enhanced temperature scaling, particularly for sub-hourly and short-duration events (Lenderink and Van Meijgaard, 2008; Loriaux et al., 2013; Panthou et al., 2014; Fowler et al., 2021a). The overestimation of scaling rates by the CPMs is consistent with the findings of Lenderink et al. (2021) using the CPM HCLIM-AROME, which showed too strong dew point temperature dependencies. Moreover, in agreement with our findings with COSMO-CLM, they also concluded that

overestimation is more pronounced for moderate percentiles of precipitation intensity, while the most extreme events exhibited only slight overestimation.

Our results showing consistent precipitation intensity scaling rates with surface air temperature from past to future climates are similar to Prein et al. (2016) for the US but diverge from studies such as Lenderink et al. (2021) and Zhang et al. (2017), who report a downward shift of the scaling curves of precipitation intensities with dew point temperature in the future climate compared to present-day climate. In addition, Lenderink et al. (2021) and Prein et al. (2016) note significant regional differences.

To our knowledge, apparent scaling rates for D50 have only been evaluated in observations by Visser et al. (2023) for Australia. They report similar negative apparent scaling rates for D50 as observed in our study for Germany. In addition, Visser et al. (2023) found systematic shifts towards more front-loaded precipitation events over the last decades. However, our CPM-based projections for Germany do not replicate this pattern for a future climate. This finding indicates the importance of considering different climate zones. The finding of different regional signals of change in event-loading is supported by Ghanghas et al. (2024) who use satellite data in a global analysis. They showed that precipitation events in areas south of 30°N are becoming generally more front-loaded, while those north of 30°N are becoming generally more back-loaded with higher temperatures.

We further note that changes in D50 are dependent on event duration and frequency changes. A decrease in the frequency of medium and long duration events in the future as assessed in Chapter 7 might impact the assessment of the projected climate change signal of D50. We propose that follow-up studies should investigate absolute measures of the timing of the onset of peak intensity in the temporal precipitation profile, such as the time to peak or the precipitation in the first hour. In addition, our study, based on a regional composite, does not account for regional differences or frequency changes, which might further impair the findings. Further, our assessment of the temporal profile from an Eulerian perspective may obscure changes to the underlying storm structures (Purr et al., 2021).

We find that the main future change to precipitation events is an overall increase in intensity. However, changes to event frequency complicate the statistical analysis. The issue has been discussed by Schär et al. (2016) and Ban et al. (2015), who suggest that super-CC scaling rates may arise due to the use of percentiles conditional on rainfall occurrence in scenarios where the frequency of wet days is changing. The analysis of percentile thresholds can consequently lead to misleading results "where a decrease in wet days can mimic an artificial increase in the intensity of heavy events" (Ban et al., 2015).

The event-based analysis presented here encounters challenges in addressing the statistical issue highlighted in the literature regarding the use of wet-conditioned percentiles. To mitigate this issue, we propose basing future analyses of event characteristics on

relevant return levels to eliminate dependence on event frequency, allowing for a more robust characterization of changes to precipitation extremes.

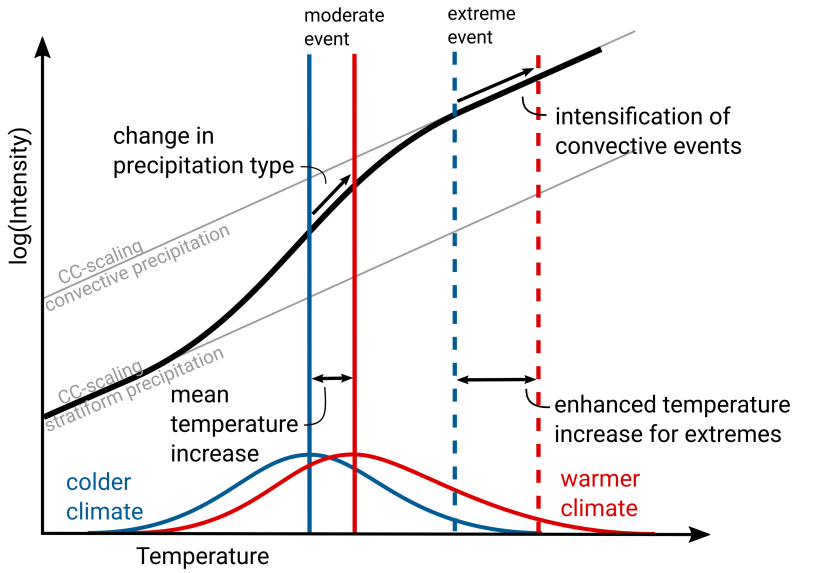

Figure 8.22: Schematic of the role of event temperature increase in the climate scaling of precipitation events, suggesting that super-CC climate scaling can be driven by the disproportionate increase in temperatures associated with extreme precipitation in contrast to super-CC scaling for peak intensities of moderate events, which can be driven by a transition from stratiform to convective precipitation.

However, the event-based analysis did provide valuable insights into the mechanisms driving super-CC climate scaling. Specifically, the analysis of event-$T_{\max}$ in the CPM projections revealed that the projected increase in event-$T_{\max}$ for extreme precipitation events exceeds the general event-$T_{\max}$ increase observed across the entire event catalogue and event-$T_{\max}$ increases above GWL increase for extremes. This non-linearity raises the question of whether the super-CC scaling observed in the climate scaling arises from the same mechanisms as those responsible for super-CC scaling in apparent scaling rates (Fig. 8.22): While super-CC in apparent scaling rate is generally attributed to a shift in rainfall type (while still under debate and potentially also intensification of convection can cause super-CC scaling), this finding suggests that super-CC scaling in a climate change context may instead be driven by the disproportionate increase in temperatures associated with extreme precipitation. This finding adds valuable context to the understanding of super-CC scaling that we also find in the projection for summer precipitation extremes, which are expected to be predominantly convective in both past and future climates. If super-CC scaling were driven solely by shifts in rainfall types, it would not manifest in these events. Even though the analysis is based on event-Tmax, and a thorough assessment of humidity has not yet been conducted, our findings highlight the role of disproportionate event-associated temperature changes in increased intensities of extreme rainfall events in a warming climate.

In conclusion, this chapter provides insight into the temperature dependence of precipitation event characteristics, suggesting a clear relationship between temperature and precipitation profile towards steeper, more front-loaded events with higher event-$T_{\max}$. In line with Visser et al. (2023) and Ghanghas et al. (2024), we hypothesize that this shift in temporal precipitation profile is linked to a change to precipitation type. Long duration, stratiform precipitation events tend to have more uniform, centred profiles, while short duration, convective precipitation events exhibit a more peaked structure, with rapid local atmospheric moisture release. In general, the results in this chapter support the use of CPM outputs for data-driven hydrological modelling as precipitation characteristics and their relation to temperature, including the timing of bulk precipitation, are well reproduced in CPM simulations. Our analysis of the CPM projections revealed that apparent temperature dependence of temporal event profiles (profile peakedness and D50) may not result in a distinct climate change signal for extreme summer precipitation events, potentially because such events are already largely convective in nature. However, shifts in precipitation type may have a greater impact on moderate rather than extreme events. To build on these findings, future studies should include an analysis of precipitation events in other seasons.

9 | CONCLUSION

In this thesis, we have conducted an in-depth analysis of the novel KIT-KLIWA ensemble, a high-resolution, convection-permitting climate ensemble consisting of four members driven by four CMIP5 GCMs, covering the period from 1971 to 2100 over southern Germany. By exploiting the ensemble's unique transient projections and high-resolution precipitation data, this study improves our understanding of precipitation extremes in CPMs and identifies future climate change signals in Germany, with a particular focus on high temporal resolution.

This concluding chapter summarises the thesis (Section 9.1), synthesizes the implications of the analysis (Section 9.2), and provides an outlook of the work (Section 9.3).

9.1 Summary

The thesis is motivated by the evidence that extreme precipitation is intensifying due to climate change, posing significant risks to infrastructure and society. Contextualized in Chapter 2, extreme precipitation changes due to climate change arise from an interplay of thermodynamic and dynamic contributions, with dynamic contributions amplifying or dampening the change signal regionally. The literature review underscores the complexity of these changes, including regional variations, stronger scaling for short-duration events, and a more pronounced increase in the most extreme events compared to moderate extremes. Specifically, at short temporal resolutions, missing data is often a challenge and uncertainty is high. Existing literature indicates that emerging high-resolution CPM simulations offer an improved representation of extreme precipitation compared to coarser, convection-parameterising models. However, CPM projections are often limited to single realizations and time slice approaches, with assessments of the sub-hourly scale being rare. The analysis of climate change signals in temporal precipitation profile characteristics remains in its infancy.

Chapter 3 condenses the identified challenges and research gaps to define research questions for the thesis. Specifically, four research topics were addressed. The schematic

overview of the results is shown in Fig. 9.1. Below, we summarize the findings of each part, addressing the research questions posed.

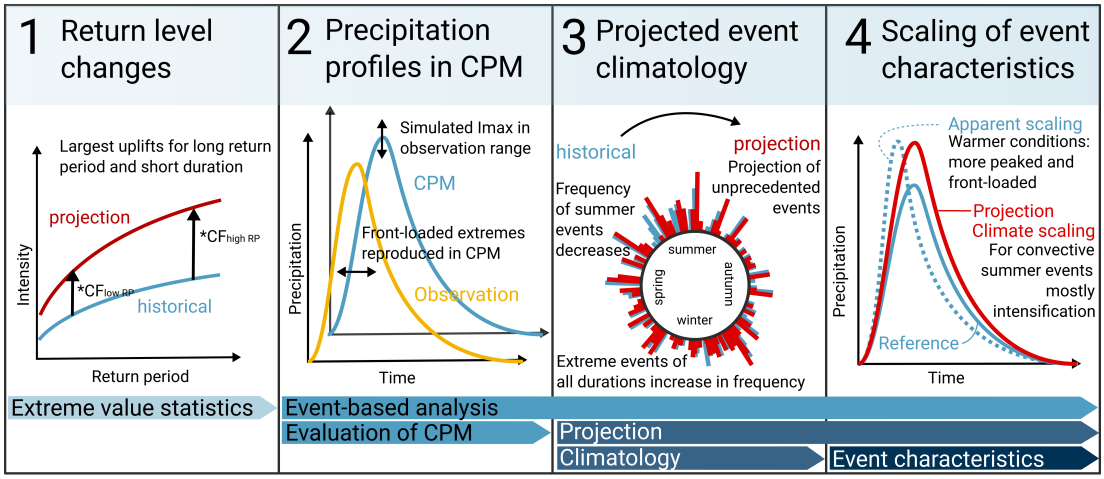

Figure 9.1: Schematic summary of the thesis.

Topic 1: Return level changes

In Chapter 5, we examined return levels (RLs) of extreme precipitation events in intensity-duration-frequency curves. We analysed RLs based on fixed durations (ED) ranging from 1 hour to 3 days and return periods (RP) from 1 to 100 years. The statistical analysis is based on a method originally developed for practical applications in the DWA-A guideline (DWA, 2012), widely applied to observational data. We apply the method to the four ensemble members in the KIT-KLIWA ensemble, spanning the period from 1971 to 2100, to address the research question:

> **How do precipitation return levels evolve under global warming as a function of duration and return period?**

To address this question, we first evaluated the CPM simulations against observational data and the KOSTRA rainfall risk product. The CPM simulations showed better agreement with observed RLs for short EDs, but tended to overestimate RLs for durations longer than 1 hour. Following this evaluation, we assessed RLs during the transient projection period and derived climate change uplifts relative to GWL. The CPM ensemble projects maximum climate change uplifts of 6 % to 8.5 % for each 1 °C increase in GWL, depending on the ensemble member. These uplifts vary for both ED and RP, with the strongest climate change signals for short ED and long RPs. The sensitivity analysis of the climate change signal revealed that the model spread is significantly smaller for short ED than for long ED. Analysis of spatial uncertainty indicated that estimates for long RPs are only feasible with pooled spatial information. Furthermore, the spatial variance is found to increase with climate change. A substantial residual standard deviation of the approximation of the change signal across the projection period highlights the added value of considering a transient ensemble, thus avoiding the sampling uncertainty typically associated with time slice approaches.

Topic 2: Precipitation profiles in CPM

Motivated by the finding in Chapter 5 that the strongest intensification with global warming was found for extreme precipitation over a short duration, we extend the analysis of precipitation in Chapter 6 to the sub-hourly resolution – a resolution where limited knowledge on the performance of CPMs exists. Specifically, we analyse 5-min precipitation output in the KIT-KLIWA ensemble for the three ensemble members EC-EARTH-C, HadGEM2-ES-C, and MPI-ESM-LR-C. The 5-min CPM output in the historical simulation period (1971-2000) is compared with the observational data from station and radar measurements. Moreover, an event-based analysis using the 5-min data is used to answer the posed research question:

> **How well does the CPM ensemble reproduce the temporal profiles of extreme precipitation events compared to observations?**

To approach the research question, we start with an analysis of the 5-min precipitation frequency distribution in the CPM simulations. We find that 5-min CPM precipitation data adequately reproduces the observed precipitation frequency distribution, with an underestimation of the most extreme intensities compared to the station observations, but in agreement with the radar data. Compared to the precipitation frequency distributions over longer temporal aggregation, the analysis reveals an increasing overestimation of extreme intensities. This indicates a mismatch in the precipitation temporal correlation structure of the CPM precipitation output.

In the second step, an event-based analysis method is developed that extracts independent precipitation events from the 5-min time series and characterises event precipitation profiles according to their duration, precipitation sum, 5-min peak intensity (Imax), 1-h peak intensity (I1h), and D50, a metric for the timing of the bulk precipitation (with D50 $< 50\%$ indicating a front-loaded event and D50 $> 50\%$ indicating a back-loaded event). The event-based analysis reveals a tendency for the CPMs to overestimate the persistence of precipitation events compared to radar and station observations.

In the third part of the analysis, we focus on the representation of extreme events in the CPM ensemble, specifically those leading to 1 h and 6 h annual maxima. The CPM simulations generally reproduce event precipitation sums of those extremes of short (1 h - 3 h) and medium (3 h - 12 h) duration but tend to overestimate event precipitation sums for long events (12 h - 24 h). Imax simulated by CPMs aligns with the radar observation but is well below Imax observed in station data. The observed dominant front-loaded fraction of extreme precipitation events leading to 1 h annual maximum precipitation intensities is reproduced by the CPM ensemble.

In essence, the evaluation of the event-based method demonstrats that the CPM ensemble effectively captures the temporal features of precipitation profiles, including sub-hourly precipitation peaks. This establishes the event-based analysis as a tool to explore climate change signals in Chapter 7 and 8.

Topic 3: Projected event climatology

In Chapter 7, we extend the event-based analysis method to the available 5-minute precipitation projection data in the ensemble (1971–2100 for MPI-ESM-LR-C, and 1971–2021 & 2051–2071 for EC-EARTH-C and HadGEM2-ES-C). This analysis investigates the projected climate change signal in the frequency of precipitation events. The study hereby focused on all precipitation events exceeding a 5 mm threshold, with particular attention to extremes – defined as events with a mean intensity (Imean) above the 90th percentile of Imean in the historical simulations (1971-2000) – and very extreme events, exceeding the corresponding 99th percentile. The analysis herein addresses the posed research question:

> **What is the projected climate change signal for the frequency of precipitation events and how does the climate change signal manifest seasonally?**

Comparing historical simulations to future projections, the CPM ensemble reveals a declining frequency of events with low Imean and an increasing frequency of high Imean events across all event durations. Furthermore, unprecedented events with record-breaking Imean values are identified for all event durations and across all ensemble members in a warmer future climate.

We find that the projected changes in event frequency show a clear seasonal pattern. Long duration events are projected to increase in frequency in winter but to decrease in summer, while short duration events show a slight increase in frequency, mainly in late summer and winter. Short- to medium-duration extreme events (>p90 and >p99) are projected to increase mainly in summer, while long-duration extreme events >p90 will increase in winter and the most extreme events (>p99) will increase throughout the year. The study highlights the critical role of seasonality, attributing much of the intensification of extreme precipitation to summer events. This intensification coincides with a projected decrease in the overall frequency of summer events, implying a shift towards a larger proportion of summer precipitation occurring in extreme events.

Topic 4: Scaling of event characteristics

Building on the event-based analysis and the future climate event catalogue from Chapter 7, the analysis in Chapter 8 examines the characteristics of summer precipitation events as a function of temperature and the evolution of the event characteristics in the ensemble projection. In particular, the chapter evaluates the characteristics Imax, I1h, Imean, and D50 of the temporal precipitation event profile. To analyse the dependence on temperature, each event is associated with the daily maximum temperature on the day of the event, the event-$T_{\max}$. The analysis in Chapter 8 answers the research question:

How do the precipitation event profile characteristics Imax, I1h, Imean, and D50 depend on the event-associated temperature and does this apparent scaling relationship translate into a climate change signal?

The question is approached by first evaluating the apparent scaling relationships in the historical CPM period (1971-2000) with radar and station observations. Apparent scaling rates reveal an enhanced scaling of Imax with event-$T_{\max}$ compared to I1h or Imean, suggesting a clear relationship towards steeper precipitation profiles with higher event-$T_{\max}$. Maximum apparent scaling rates for Imax in the observations exceed CC-scaling. The CPM simulations systematically overestimate the intensity scaling. The apparent scaling of D50 shows a decrease in D50 with event-$T_{\max}$, indicating more front-loaded events under warmer conditions. This trend is captured in the CPM simulations.

Secondly, the consistency of the apparent scaling between the historical (1971-2000) and the future period (2051-2070) in the CPM ensemble is assessed. Apparent intensity scaling relations from historical simulations are preserved in a future climate, with scaling extending towards higher event-$T_{\max}$. While certain scaling behaviours of D50 appear robust under future climate conditions, there is a misalignment of past and future scaling curves, and events with the same event-$T_{\max}$ tend to be less front-loaded in the future time slice compared to the historical simulations.

Finally, the climate scaling of the event characteristics is analysed over 20-year time slices in the CPM projection associated with the respective GWLs. The analysis of future characteristics showed that the increase in event-$T_{\max}$ is generally below the increase in GWL for average events, but exceeds the increase in GWL for extreme events. The 50th percentile, p50, of Imax and I1h increase at a rate well below 6-7% (CC-scaling) per degree increase in the GWL. The scaling rates for the high percentiles p90 and p99 of Imax and I1h exceed CC-rate in some ensemble members and for some event durations. No climate change signal is detected in the projected distribution of D50.

We hypothesise that the shift in precipitation profiles with event-$T_{\max}$ – increased steepness and increased front-loading – is due to a change in precipitation types from stratiform precipitation, predominantly during colder conditions, to convective precipitation, predominantly occurring under warmer conditions. Our analysis of a CPM ensemble showed that the apparent temperature dependence of temporal precipitation event profiles may not lead to a clear climate change signal for extreme events, at least in the summer extreme events studied, possibly because such events are already largely convective in nature under recent climate conditions. The analysis also highlights the importance of assessing the climate change signal of event-associated temperature: For extreme events (Imean>p90 or Imean>p99), event-$T_{\max}$ increases faster with global warming than for moderate events (all events).

In essence, we have conducted a comprehensive study of precipitation extremes under climate change using the novel KIT-KLIWA ensemble. The thesis provides valuable insights into the intensification of precipitation extremes with global warming, highlighting how the magnitude of the intensification varies with duration and return periods. By exploiting the 5-min resolution precipitation simulation in the ensemble, the thesis advances the current understanding of the representation of sub-hourly precipitation in CPM simulations. An event-based analysis highlights the occurrence of unprecedented future events and seasonal shifts in event frequency. Further, we establish a relationship between different types of precipitation profiles and their dependence on duration, intensity, and temperature.

9.2 Implication

This section synthesises the implications of the broad analysis across the four research topics. It first discusses the implications for future simulation strategies in CPMs, followed by the implications for the transfer of climate information for climate adaptation and engineering applications.

The added value of transient data and sub-hourly CPM data

The KIT-KLIWA ensemble provides a unique transient CPM projection for Germany. We showed that transient simulations significantly reduce uncertainties in the projection of future climate change signals of extreme precipitation compared to conventional time-slice approaches, with a reduction of uncertainty due to internal variability of the climate system. Our findings also indicate that extreme precipitation will become more variable in the future compared to the past, further highlighting the growing importance of addressing these uncertainties. In addition, by assessing climate change signals based on GWLs, we have documented that transient simulations allow for a wider range of analysis methods. This opens up the possibility of facilitating improved intercomparisons between models driven by GCMs with different climate sensitivities. We therefore argue for the inclusion of more transient simulations in future CPM ensemble setups.

By examining 5-min precipitation from a 30-year CPM simulation ensemble, this study takes an important step towards addressing the knowledge gap in sub-hourly CPM precipitation. The assessment of different temporal resolutions of precipitation in the thesis improves the understanding of precipitation biases in CPM. In particular, we highlight the tendency for overly persistent precipitation events leading to an overestimation of the intensity of longer, e.g. daily precipitation extremes but not for shorter, e.g. hourly precipitation extremes. In essence, the precipitation bias depends crucially on the temporal resolution, and the finding implies that there is a bias in the temporal correlation structure of simulated precipitation time series.

This finding is expected to have important implications for the implementation of bias correction methods. Currently, quantile mapping approaches are commonly used

for bias correction in regional climate models (Cannon et al., 2015). Such approaches do not take into account the temporal correlation structure in the correction of the bias. Based on our findings, event-based bias correction methods are needed to improve the accuracy of corrected precipitation data.

In general, our results show that simulated 5-min precipitation extremes are within the observed range of radar and station observations. This supports the reliability of CPM data at sub-hourly resolutions, and the results argue for the inclusion of more sub-hourly output in future CPM simulation designs. However, in addition, the wide range of precipitation intensities in different observational products encountered in the analysis also highlights the need for further quality controlled sub-hourly precipitation data and assessment of bias in remote sensing based precipitation products (Villarini et al., 2008).

Need for updated rainfall risk products

The results of this thesis have substantial implications for improving societal resilience to extreme precipitation. The projected increase in extreme precipitation intensities across all durations, from sub-hourly to multi-day scales, suggests that existing infrastructure is moving towards a state of maladaptation. This underscores the urgent need for updated precipitation hazard products and engineering frameworks that account for these climate change-driven changes.

In response to the intensification of precipitation extremes, some countries have incorporated so-called climate uplifts into regulations for sustainable drainage design (Dale et al., 2017). The results of Chapter 5 emphasise that climate uplifts for extreme precipitation intensities should be of different magnitudes for different return periods and durations. The finding supports the strategy that is e.g. used at the national level by Denmark for rainfall design implementing different safety factors based on the return period (Arnbjerg-Nielsen, 2008). We find that intensities over short durations and long return periods are particularly sensitive to global warming. This is of concern because such events can trigger flash floods, which develop rapidly with little warning and can cause soil erosion and debris flows. This is critical, especially for urban areas, that are particularly vulnerable to flash floods due to their high proportion of impermeable surfaces (Archer and Fowler, 2018).

While transient ensemble data have improved the assessment of the climate change signal of precipitation extremes, substantial uncertainties remain. This highlights the critical need to incorporate uncertainty ranges in climate change uplifts. An example is the framework used in the UK, where the Environment Agency provides a range of allowances and the choice of allowance depends on the specific use case (UK Environment Agency, 2022).

In addition, the analysis projects record-breaking events under future climate scenarios. This finding reinforces the inadequacy of relying on historical observations to

estimate flood risk. The flood of 2021 in western Germany and neighbouring countries tragically exemplified the devastating impact of such unprecedented precipitation events for the region (Mohr et al., 2023; Ludwig et al., 2023; Kreienkamp et al., 2021). The projected record-breaking events highlight the urgent need for climate adaptation strategies to incorporate new, future "plausible worst-case" scenarios to ensure resilience to unprecedented extremes.

Further, the event-based analysis revealed a shift towards fewer prolonged precipitation events in summer, coupled with an increase in extreme precipitation events with global warming. This pattern exacerbates the risk of both pluvial floods and droughts, aligning with the IPCC (2021)'s broader climate projections. As extreme precipitation events lead to increased surface runoff, the findings suggest that water availability in summer is further reduced, posing a growing challenge in maintaining stable water supplies for agriculture, industry, and households. In addition, water associated with extreme events may be unsuitable for drinking due to contamination by pollutants (e.g. Kistemann et al., 2002). To cope with the changing distribution of water resources in the future, adaptive water management strategies are needed.

Implications for engineering applications, including precipitation design profiles

Temporal profiles of extreme precipitation events are particularly important due to their relevance for numerous practical applications. For engineering applications, such as urban drainage design, infrastructure stress testing, and risk management, it is common practice to rely on design rainfall profiles, which are artificially constructed profiles often derived from observational data.

The study highlights significant limitations in runoff estimation methods that depend on single design rainstorm profiles, as they disregard significant sources of variability and uncertainty. We stress that real extreme precipitation events in Germany have a number of different temporal profiles and we can attribute their frequency to event duration as well as intensity similar to Villalobos Herrera et al. (2023a). Additionally, we emphasize that the occurrence of these profiles depends on temperature conditions.

In the context of climate change, updating design rainstorm profiles is needed for resilient planning that considers future extreme events (Dale, 2021). Realistic modelling of such extreme precipitation event profiles has been limited in the past by inadequate spatial resolution of climate models. Deep convection processes and related extremes in coarser climate simulations using parametrized convection were found to be in general too spatially diffuse, too persistent in time and showing too low intensity maxima of extremes (Kendon et al., 2021).

With the use of 5-min precipitation data, we were able to evaluate simulated temporal profiles in CPMs with observational data. A key finding is that CPM simulations adequately reproduce critical features of peak intensity and event loading. Limitations were

found in the simulation of strong, short-duration precipitation events from convective precipitation events. This evaluation is an important step towards the applicability of CPMs for hydrological and hydraulic modelling.

Specifically, there is a knowledge gap for practitioners in understanding how temporal profiles evolve under global warming. Our analysis of temperature scaling of the temporal precipitation profile reveals that the frequency of different profile shapes in Germany is closely linked to temperature conditions. Specifically, we find that warmer conditions are associated with more peaked and more front-loaded precipitation profiles, consistent with findings from other climate zones (e.g. Visser et al., 2023; Wasko and Sharma, 2015). This dependence of the temporal precipitation profile on temperature is attributed to a shift from predominantly stratiform precipitation under colder conditions to predominantly convective precipitation under warmer conditions in agreement with Visser et al. (2023) and Ghanghas et al. (2024).

The results emphasise the importance of accurately reproducing precipitation types in the simulations to capture the climate change signal in future projections. This implies the need to assess the climate change signal of extreme precipitation using high-resolution simulations that can resolve these processes. Conversely, it advises against relying on commonly performed convection-parameterised simulations for the detailed information required at the regional scale.

When assessing the CPM projections for extreme summer precipitation events, we find little to no change in profile shape in future climate scenarios, probably because these events are already largely convective in nature. For these extreme precipitation events, the results therefore support the use of uniform climate uplifts for climate adaptation, provided in the form of a percentage increase in the total depth of the precipitation event to reflect the impact of climate change (Dale, 2021). However, we anticipate that shifts in precipitation type may have a greater impact on moderate events than on extreme events and/or in the winter half year.

The findings underscore the critical need for updated rainfall risk assessments and engineering frameworks to address the intensification of extreme precipitation due to climate change, particularly for short-duration events. Additionally, the results suggest that water resource management must adapt to changes in precipitation distribution. Assessments of the temporal event profile reveal shortcomings in frameworks that rely on single-event design rainstorms and indicate that generally warmer conditions lead to more peaked and front-loaded temporal precipitation event profiles.

9.3 Outlook

The work presented in this thesis serves as an initial exploration of extreme precipitation in the KIT-KLIWA ensemble with a focus on the event scale to provide meaningful

products for future resilient impact modelling. This final section of the thesis discusses follow-up studies on the KIT-KLIWA ensemble, that were left unexplored in the thesis and concludes with the potential transfer of the methods developed in the thesis to future studies and using further CPM simulations.

Use of regression model

The comprehensive uncertainty analysis in Chapter 5 revealed significant spatial uncertainties in the climate change signal of RLs across the simulation domain. Specifically, the study was unable to identify a robust spatial pattern of the climate change signal, with the spatial pattern of RLs being particularly uncertain for short-duration intensities. A previous study on extreme precipitation in CPMs demonstrated that spatial patterns of short-duration events could be more effectively resolved using a regression model (Chan et al., 2023b). The method employed in this study is implemented through the R package "evgam" (Youngman, 2020), which is publicly available via the R CRAN repository. Preliminary analysis applying the regression model to the KIT-KLIWA ensemble, using the covariates of latitude, longitude, altitude, and GWL as well as a regional warming level, was conducted in collaboration with the UK Met Office and the University of Newcastle. The results indicated that the regression model effectively reduced uncertainty in the extreme value statistics.

Follow-up studies on the KIT-KLIWA ensemble should focus on assessing the change signal derived from the regression model and comparing these results with those obtained from the current grid-point-based method.

Follow-up studies on the established event catalogue of the CPM ensemble

In the thesis, we assessed the climate change signal in event-based precipitation climatology in the KIT-KLIWA ensemble. Our analysis in Chapter 7 revealed unprecedented events across all ensemble members, highlighting critical implications for climate adaptation, particularly in assessing the maximum precipitation expected for high-risk applications.

Follow-up studies based on the event catalogue established in Chapter 7 should focus on further examining these unprecedented events in detail to understand the atmospheric conditions leading to these unprecedented events.

In Chapter 8, we attribute the shape of precipitation event profiles to the prevailing temperature conditions. In line with the studies of Visser et al. (2023) and Ghanghas et al. (2024), we hypothesise that the dependence of temporal precipitation profiles on temperature is driven by shifts in precipitation type, specifically a transition from stratiform to convective precipitation. To further strengthen this argument, a distinction between convective and stratiform events could prove advantageous in the assessment of the event profile characteristics. Assessing the precipitation type would add further

complexity to the study and requires additional data such as synoptic observations, lightning data (Molnar et al., 2015) or cloud observations (Berg and Haerter, 2013).

We derived apparent scaling rates based on event-$T_{\max}$, a surface parameter available in both model and observational data at a daily resolution. Extending the analysis to include atmospheric stability, CAPE, or precipitable water could provide a deeper understanding of the scaling relation of the extracted temporal precipitation profiles, similar to Prein et al. (2016).

These proposed follow-up studies are expected to improve the understanding of the projected changes in precipitation events with global warming we have analysed in the thesis.

Application of the event-based analysis method to further data

With the development of an event-based analysis method for CPM application, a variety of new research topics can be pursued. First and foremost the method can be applied to other CPM simulations with sub-hourly data to assess the robustness of the results.

Motivated by the finding that the bias in the CPM ensemble compared to the observation often depends on the driving GCM, with the most pronounced discrepancies observed in the analysis of event frequency (Chapter 7), a COSMO-CLM downscaling of the ERA5 reanalysis dataset was performed with 5-min precipitation output. The application of the event-based analysis method to the reanalysis downscaling in future work will potentially help to unravel the source of the observed biases in the CPM ensemble compared to the observations.

So far, the event-based analysis method has been evaluated for the CPM COSMO-CLM over Germany. Extending the method to other regions and models is essential for further validation and to explore regional patterns in frequency changes (compare to Chapter 7) and the scaling behaviour of temporal precipitation profiles (see Chapter 8). Current efforts at the University of Newcastle are focused on applying the method to convection-permitting 1.5 km simulations with the Met Office Unified Model at a temporal resolution of 10 min for the UK (Chan et al., 2013). Further extension of the evaluation of sub-hourly data in coordinated multi-model CPM simulations should be pursued in order to systematically assess the robustness of the results.

A key implication of this work is that 5-min CPM data provide valuable input for data-driven hydrological simulations. Tests of this integration will be pursued in the second phase of the ISAP project, where the coupling of hydrological models with selected precipitation events from the KIT-KLIWA simulations will be explored for the Stuttgart region in southern Germany.

In summary, this thesis presents an initial exploration of precipitation extremes in the novel KIT-KLIWA ensemble. The established precipitation event catalogue offers

potential for further exploration. In addition, the developed event-based analysis method is versatile and applicable to a wide range of datasets, providing valuable opportunities for further research.

ACKNOWLEDGEMENTS

First and foremost, I would like to express my gratitude to my supervisors, Joaquim Pinto, Hayley Fowler, and Hendrik Feldmann for their great supervision. Joaquim, thank you for believing in me and giving me the opportunity and freedom to explore my research interests. Hayley, thank you for the great opportunity to work with your group. The inspiring time at Newcastle University and your input have been invaluable. Hendrik, thank you for sharing your knowledge, the many discussions, and for supporting me in so many ways. I further thank Lizzie Kendon and Steven Chan for the inspiring time during my research stay at the UK Met Office.

I am grateful to my colleagues in the regional climate modelling group at KIT for creating a great working environment, and to my Newcastle colleagues in the Cassie Building for their warm welcome during both of my research stays. Special thanks to my fellow PhD students Katharina, Kim, and Selina, who started this PhD journey with me during the challenging COVID times, for their support, discussions, and friendship.

I thank the ISAP-Team for the inspiring discussions during the project meetings, which greatly benefited my work through interdisciplinary exchange.

I acknowledge funding from the Federal Ministry of Education and Research (BMBF) as part of the ISAP project under grant numbers 01LR2007B and 01LR2007B1. Data processing and climate modelling were conducted at the High-Performance Computing Center Stuttgart (HLRS) and Deutsches Klimarechenzentrum (DKRZ). I also acknowledge funding from the GRACE graduate school, which enabled my research stays at the UK Met Office in Exeter and Newcastle University.

I would like to take this opportunity to thank my family for their unwavering support, with special thanks to my mother for her support with the thesis.

Above all, thank you, Tobi, for supporting me throughout this challenging journey. I could not have done it without your support.

Appendices

A | APPENDIX TO CHAPTER 4

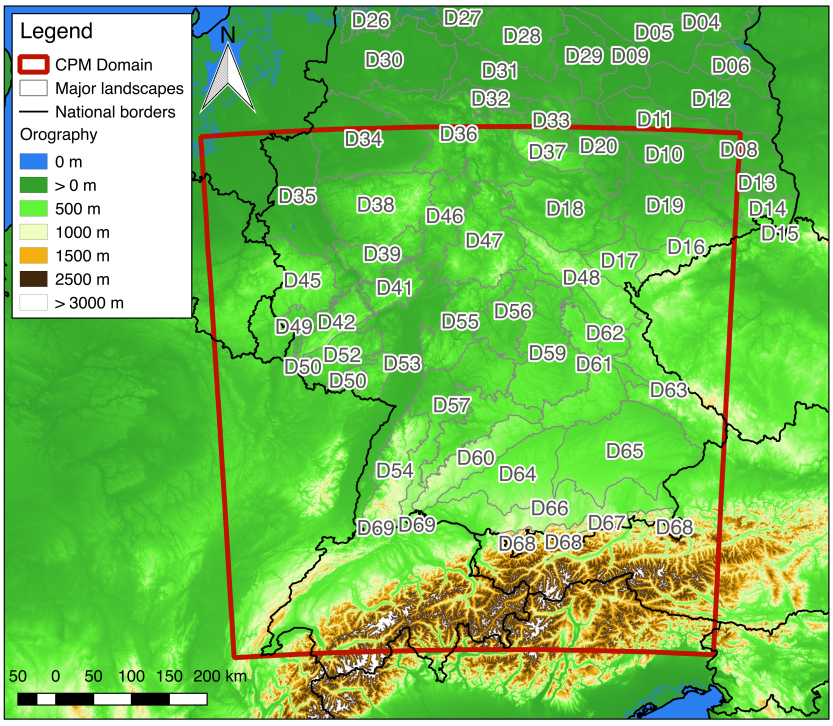

Northern Lowlands
D04 Mecklenburgische Seenplatte
D05 Mecklenburg-Brandenburgisches Platten- und Hügelland sowie Luchland
D06 Ostbrandenburgische Platte
D07 Odertal
D08 Spreewald und Lausitzer Becken- und Heideland
D09 Elbtalniederung
D10 Elbe-Mulde-Tiefland
D11 Fläming
D12 Mittelbrandenburgische Platten und Niederungen sowie Ostbrandenburgisches Heide- und Seengebiet
D13 Oberlausitzer Heideland
D19 Erzgebirgsvorland und Sächsisches Hügelland
D20 Mitteldeutsches Schwarzerdegebiet
D21 Schleswig-Holsteinische Marschen und Nordseeinseln
D22 Schleswig-Holsteinische Geest
D23 Schleswig-Holsteinisches Hügelland
D24 Unterelbeniederung (Elbmarsch)
D25 Ems-Weser-Marsch
D26 Ostfriesisch-Oldenburgische Geest
D27 Stader Geest
D28 Lüneburger Heide
D29 Wendland und Altmark
D30 Dümmer Geestniederung und Ems-Hunte-Geest
D31 Weser-Aller-Tiefland
D32 Niedersächsische Börden
D33 Nördliches Harzvorland
D34 Westfälische Tieflandsbucht
D35 Kölner Bucht und Niederrheinisches Tiefland

Central Uplands
D14 Oberlausitz
D15 Sächsisch-Böhmisches Kreidesandsteingebiet
D16 Erzgebirge
D17 Vogtland
D18 Thüringer Becken und Randplatten
D36 Unteres Weserbergland und Oberes Weser-Leinebergland
D37 Harz
D38 Bergisches Land, Sauerland (Süderbergland)
D39 Westerwald
D40 Lahntal und Limburger Becken
D41 Taunus
D42 Hunsrück
D43 Moseltal
D44 Mittelrheingebiet (mit Siebengebirge)
D45 Eifel und Vennvorland
D46 Westhessisches Berg- und Beckenland
D47 Osthessisches Bergland (Vogelsberg und Rhön)
D48 Thüringisch-Fränkisches Mittelgebirge
D49 Gutland (Bitburger Land)
D50 Pfälzisch-Saarländisches Muschelkalkgebiet
D51 Pfälzer Wald (Haardtgebirge)
D52 Saar-Nahe-Berg- und Hügelland
D63 Oberpfälzer und Bayerischer Wald

South German Scarplands
D53 Oberrheinisches Tiefland und Rhein-Main-Tiefland
D54 Schwarzwald "*Black Forest*"
D55 Odenwald, Spessart und Südrhön
D56 Mainfränkische Platten
D57 Neckar- und Tauberland, Gäuplatten
D58 Schwäbisches Keuper-Liasland
D59 Fränkisches Keuper-Liasland
D60 Schwäbische Alb
D61 Fränkische Alb
D62 Oberpfälzisch-Obermainisches Hügelland
D69 Hochrheingebiet und Dinkelberg

Alpine Foreland
D64 Donau-Iller-Lech-Platten
D65 Unterbayerisches Hügelland und Isar-Inn-Schotterplatten
D66 Voralpines Hügel- und Moorland

Alps
D67 Schwäbisch-Oberbayerische Voralpen
D68 Nördliche Kalkalpen

Figure A.1: Major landscapes according to Ssymank (1994) in the CPM domain of the KIT-KLIWA ensemble. The model domain with the sponge area truncated is displayed in red. Shapefiles of the major landscapes: Bundesamt für Naturschutz (BfN) (2011), digital elevation model, EarthEnv-DEM90: Robinson et al. (2014).

A.1 Simulation setup

This section provides the parameters for the CPM simulations in the KIT-KLIWA ensemble that were set in addition to the default in the COSMO_DE setup (Schättler et al., 2013).

Parameters for the adiabatic model:

DYN:
itype_turb=3,
imode_turb=1,
icldm_turb=2,
itype_tran=2,
imode_tran=1,
itype_wcld=2,
icldm_tran=0,
itype_synd=2,
lprfcor=.FALSE.,
lsoil=.TRUE.,
itype_evsl=2,
itype_trvg=2,
lmulti_layer=.TRUE.,
lmelt=.TRUE.,
lmelt_var=.TRUE.,
czbot_w_so=2.5,
ke_soil = 9,
czml_soil = 0.005, 0.025, 0.07, 0.16, 0.34, 0.7, 1.42, 2.86, 5.74, 11.5,
lconv=.TRUE.,
nincconv=10,
itype_conv=3,
lconv_inst=.TRUE.,
lcape=.FALSE.,
lsso=.FALSE.,
lseaice=.FALSE.,

Parameters for the diabatic model:

PHY
lgsp=.TRUE.,
ldiniprec=.FALSE.,
itype_gscp=4,
lrad=.TRUE.,
nradcoarse=2,
lradf_avg=.TRUE.,
hincrad=0.25,
lforest=.TRUE.,
ico2_rad=10,
icldm_rad=4,
ltur=.TRUE.,
limpltkediff=.TRUE.,
ninctura=1,
ltkesso=.TRUE.,
lexpcor=.FALSE.,
ltmpcor=.FALSE.,
lnonloc=.FALSE.,
lcpfluc=.FALSE.,
itype_turb=3,
imode_turb=1,
icldm_turb=2,
itype_tran=2,
imode_tran=1,
itype_wcld=2,
icldm_tran=0,
itype_synd=2,
lprfcor=.FALSE.,
lsoil=.TRUE.,
itype_evsl=2,
itype_trvg=2,
lmulti_layer=.TRUE.,
lmelt=.TRUE.,
lmelt_var=.TRUE.,
czbot_w_so=2.5,
ke_soil = 9,
czml_soil = 0.005, 0.025, 0.07, 0.16, 0.34, 0.7, 1.42, 2.86, 5.74, 11.5,
lconv=.TRUE.,
nincconv=10,
itype_conv=3,
lconv_inst=.TRUE.,
lcape=.FALSE.,
lsso=.FALSE.,
lseaice=.FALSE.,

Parameters for the model run:

RUNCTL
dt=25.0,
itype_timing=4,
lreorder=.FALSE.,
lreproduce=.TRUE.,
ldatatypes=.FALSE.,
ncomm_type=3,
ltime_barrier=.FALSE.,
luseobs=.FALSE.,

luse_rttov=.FALSE.,
ldump_ascii=.FALSE.,
hincmxt=24.0,
hincmxu=1.0,
ldiagnos=.TRUE.,
ldebug_io=.FALSE.,
idbg_level=2,
nboundlines=3,
linit_fields=.FALSE.,
lartif_data=.FALSE.

Parameters for tuning dynamics and physics:

TUNING
clc_diag = 0.5,
pat_len= 500.0,
tur_len= 150.0,
rlam_heat = 1.0,
rlam_mom = 0.0,
rat_lam = 1.0,
rat_can = 1.0,
rat_sea = 20.0,
c_lnd = 2.0,
c_soil = 1.0,
c_sea = 1.5,
z0m_dia = 0.2,
crsmin = 150.0,
qc0 = 0.0002,
qi0 = 0.0,
q_crit = 1.600,
wichfakt = 0.00,
mu_rain = 0.5,
v0snow = 20.0,
rain_n0_factor=0.1,
tkhmin = 0.4,
tkmmin = 0.4

B | APPENDIX TO CHAPTER 5

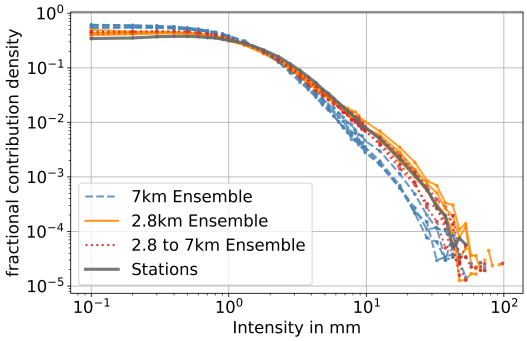

Figure B.1: Density distribution of fractional contributions of hourly precipitation from station measurements and the results in the according cells of the simulation output of 2.8 km, 7 km, and the 2.8 km resolution interpolated to the 7 km grid. The bin width for both panels is 0.1 mm for the intensity range from 0 to 1 mm aligned with the resolution of the station measurement. Bin width is 0.5 mm for the intensity range from 1 to 10 mm and 5 mm for the intensity range from 10 to 100 mm.

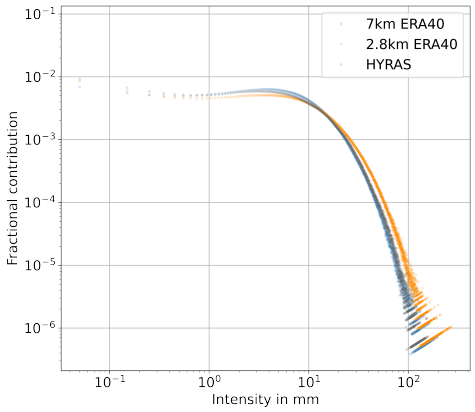

(a) Fractional contribution of HYRAS compared to the downscaled ERA40 results in 7 km and 2.8 km.

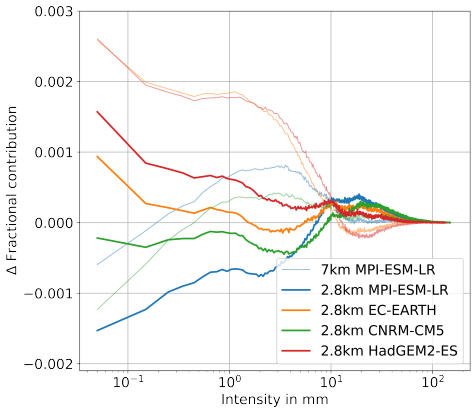

(b) Fractional contribution of HYRAS compared to the CPM ensemble median in the historical period in 7 km and 2.8 km.

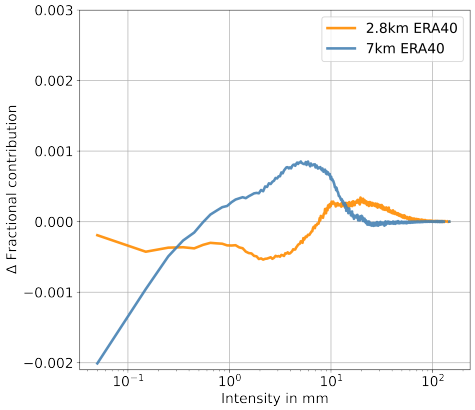

(c) Difference of fractional contribution of the downscaled ERA40 results in 7 km and 2.8 km to HYRAS.

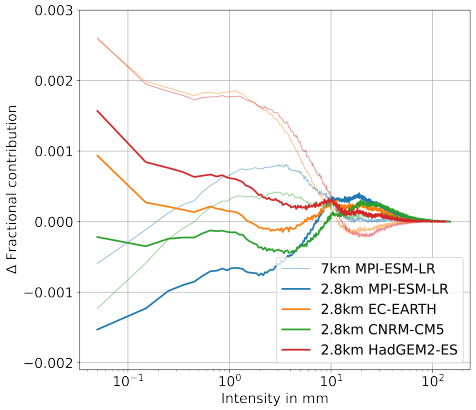

(d) Difference of fractional contribution of the CPM ensemble median in the historical period in 7 km and 2.8 km to HYRAS.

Figure B.2: Fractional contribution of daily rainfall from HYRAS dataset and the simulation results from the historical period both for 1971-2005. The bin width is 0.1 mm, in agreement with the resolution of HYRAS.

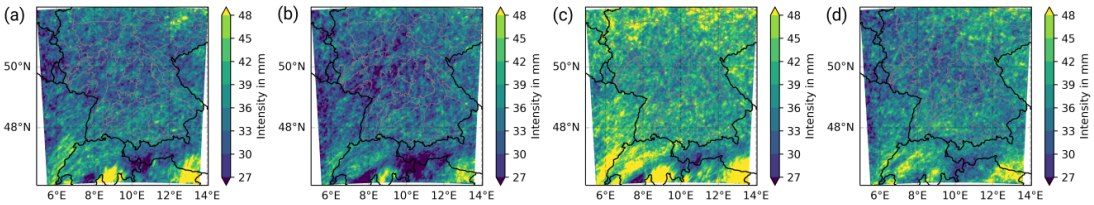

Figure B.3: Spatial distribution of the RL with RP=10 a, ED=1 h in the single ensemble members (a) MPI-ESM-LR-C, (b) EC-EARTH-C, (c) CNRM-CM5-C, (d) HadGEM2-ES-C.

Table B.1: Relative difference between KOSTRA and CPM simulations in percent for different RP-ED combinations for the four ensemble members.

MPI-ESM-LR-C		ED in h 1	2	3	4	6	9	12	24	48	72
RP in a	100	-5	6	8	11	12	16	19	27	24	23
	50	-4	6	9	11	12	17	20	27	24	23
	30	-3	7	9	12	13	17	20	27	23	22
	20	-3	7	10	12	13	17	20	27	23	22
	10	-2	8	11	13	14	18	20	26	23	21
	5	0	10	12	14	15	19	21	26	22	20
	3	1	11	13	15	16	19	22	26	22	19
	2	3	12	14	16	17	20	22	26	21	18
	1	8	15	17	18	18	21	23	24	18	15

CNRM-CM5-C		ED in h 1	2	3	4	6	9	12	24	48	72
RP in a	100	12	25	27	29	30	34	37	47	47	46
	50	13	26	28	30	30	34	37	46	46	44
	30	14	26	28	30	31	35	37	46	45	43
	20	14	27	28	30	31	34	37	45	44	42
	10	16	28	29	31	31	34	37	44	42	39
	5	18	29	30	32	32	35	36	42	40	37
	3	20	30	31	33	32	35	37	41	38	34
	2	22	31	32	34	33	35	36	40	36	32
	1	27	35	35	35	34	35	36	37	30	25

EC-EARTH-C		ED in h 1	2	3	4	6	9	12	24	48	72
RP in a	100	-7	2	3	4	3	6	8	16	15	14
	50	-7	2	3	4	4	6	8	16	15	14
	30	-6	3	3	5	4	7	8	16	14	13
	20	-6	3	4	5	4	7	9	16	14	13
	10	-5	4	4	5	5	7	9	15	13	12
	5	-3	5	5	7	6	8	10	15	12	10
	3	-2	6	7	8	7	9	11	15	12	9
	2	0	7	7	9	8	10	11	15	11	8
	1	3	9	9	10	9	11	12	14	9	5

HadGEM2-ES-C		ED in h 1	2	3	4	6	9	12	24	48	72
RP in a	100	2	11	10	10	7	8	8	12	9	8
	50	3	11	10	10	7	8	8	11	9	7
	30	3	12	11	10	7	8	8	11	8	7
	20	3	12	11	10	7	8	8	11	8	6
	10	4	12	11	10	7	8	8	10	7	5
	5	5	13	11	11	7	7	7	9	6	4
	3	6	13	11	10	7	7	7	8	5	3
	2	8	13	11	11	7	7	7	8	4	1
	1	10	13	11	10	6	5	5	5	0	-2

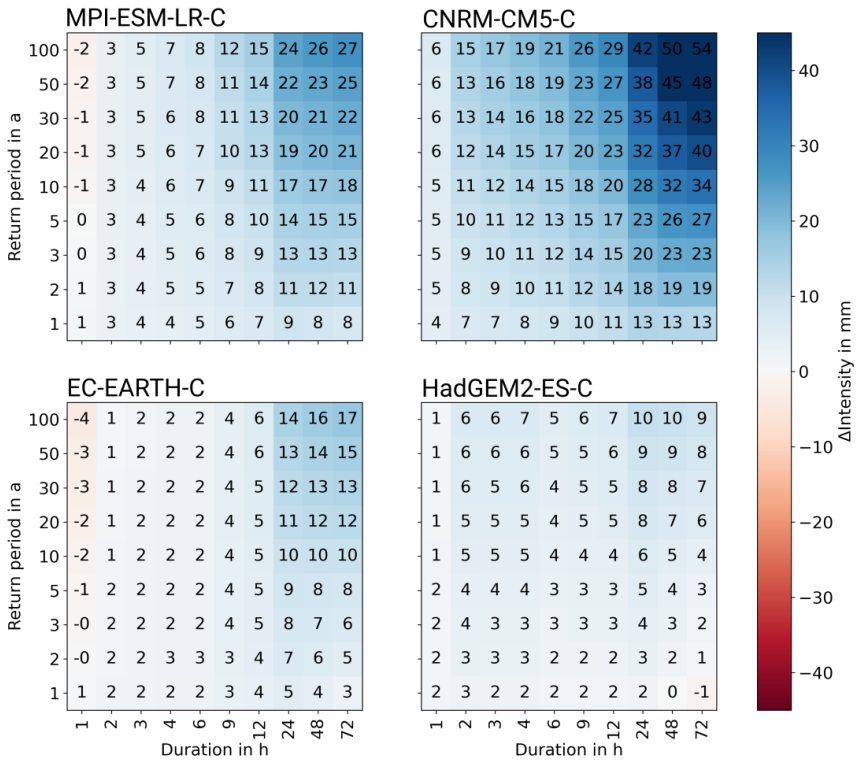

Figure B.4: The absolute differences in RLs for all analysed RPs and EDs are shown for the four ensemble members separately – top left: MPI-ESM-LR-C, top right: CNRM-CM5-C, bottom left: EC-EARTH-C, bottom right: HadGEM2-ES-C.

Table B.2: The relative CF of RL with global warming in percent for different RP-ED combinations for the four ensemble members.

MPI-ESM-LR-C		ED in h 1	6	12	24	72	CNRM-CM5-C		ED in h 1	6	12	24	72
RP in a	100	5.9	5.7	4.9	3.3	0.8	RP in a	100	6.9	8.1	7.4	6.5	6.8
	50	5.8	5.5	4.8	3.2	0.8		50	6.9	8.0	7.2	6.4	6.7
	30	5.7	5.4	4.6	3.2	0.8		30	6.9	7.9	7.1	6.3	6.6
	20	5.7	5.4	4.5	3.1	0.9		20	6.9	7.8	7.0	6.2	6.5
	15	5.6	5.3	4.4	3.1	0.9		15	6.9	7.7	6.9	6.1	6.5
	10	5.5	5.1	4.2	3.0	0.9		10	6.9	7.5	6.8	6.0	6.3
	5	5.4	4.8	3.9	2.8	1.0		5	6.9	7.2	6.5	5.7	6.1
	3	5.2	4.5	3.5	2.6	1.1		3	6.8	6.9	6.2	5.4	5.7
	2	5.1	4.1	3.1	2.4	1.2		2	6.8	6.6	5.8	5.1	5.3
	1	4.7	3.2	2.4	2.2	1.6		1	6.8	5.8	4.9	4.4	4.6

EC-EARTH-C		ED in h 1	6	12	24	72	HadGEM2-ES-C		ED in h 1	6	12	24	72
RP in a	100	8.5	8.4	6.4	3.8	2.3	RP in a	100	6.1	5.7	5	4.1	4.3
	50	8.4	8.3	6.3	3.9	2.3		50	6.1	5.7	5.0	4.1	4.3
	30	8.4	8.1	6.2	3.9	2.4		30	6.0	5.6	4.9	4.2	4.4
	20	8.3	8.0	6.1	3.9	2.5		20	6.0	5.6	4.9	4.2	4.4
	15	8.2	7.9	6	3.9	2.5		15	5.9	5.5	4.9	4.2	4.4
	10	8.2	7.7	5.9	3.9	2.6		10	5.9	5.5	4.8	4.2	4.5
	5	8.0	7.4	5.7	4.0	2.8		5	5.8	5.4	4.8	4.2	4.6
	3	7.8	7.0	5.4	4.0	3.0		3	5.7	5.2	4.7	4.2	4.7
	2	7.7	6.7	5.3	4.1	3.2		2	5.7	5.1	4.6	4.2	4.8
	1	7.3	6.0	4.9	4.2	3.5		1	5.5	4.8	4.5	4.3	5.1

Table B.3: Statistics over the distribution of different RL sampled over all grid points in the domain for additional ED and RP configurations.

Configuration	Member	Median in mm			Interquartile range in mm			Skewness		
		hist	GWL2	GWL3	hist	GWL2	GWL3	hist	GWL2	GWL3
ED=1 h, RP=5 a	MPI-ESM-LR-C	28.6	31.9	33.4	3.7	4.3	4.4	0.62	0.54	0.36
	EC-EARTH-C	27.7	30.4	32.9	3.7	4.6	5	0.26	0.22	0.27
	CNRM-CM5-C	33.7	34.7	37.5	4.3	4.8	5.3	0.47	0.5	0.59
	HadGEM2-ES-C	30.2	32	33.5	4.1	4.5	4.6	0.34	0.43	0.37
ED=1 h, RP=10 a	MPI-ESM-LR-C	33.5	37.4	39.2	4.7	5.5	5.6	0.68	0.52	0.38
	EC-EARTH-C	32.4	35.7	38.6	4.7	5.7	6.2	0.32	0.29	0.33
	CNRM-CM5-C	39.4	40.6	43.8	5.4	6.1	6.7	0.5	0.55	0.63
	HadGEM2-ES-C	35.5	37.5	39.3	5.1	5.6	5.8	0.37	0.43	0.4
ED=1 h, RP=30 a	MPI-ESM-LR-C	41.1	46.1	48.4	6.3	7.3	7.6	0.73	0.51	0.41
	EC-EARTH-C	39.9	44	47.7	6.3	7.6	8.3	0.37	0.34	0.4
	CNRM-CM5-C	48.4	50	53.9	7.3	8.1	9	0.54	0.6	0.68
	HadGEM2-ES-C	43.8	46	48.4	6.8	7.3	7.7	0.44	0.45	0.44
ED=24 h, RP=5 a	MPI-ESM-LR-C	69.5	73.5	76.8	12.4	11.6	13.7	2.04	2.5	2.1
	EC-EARTH-C	63.7	67.2	69.6	10.5	12.5	13.1	1.55	1.9	1.6
	CNRM-CM5-C	78.5	83.9	88.2	14.7	15.3	15.7	1.08	1.2	1
	HadGEM2-ES-C	60.2	69.5	72.7	10.4	12.5	14.2	2.43	2.3	2.1
ED=24 h, RP=10 a	MPI-ESM-LR-C	79.8	84.5	88.5	15.1	14.2	16.7	1.8	2.4	1.8
	EC-EARTH-C	73.1	77.4	80.2	12.6	15.1	16.2	1.3	1.7	1.4
	CNRM-CM5-C	90.9	97.4	102.6	18.2	19.2	19.3	1	1.1	0.8
	HadGEM2-ES-C	69.5	80.4	84.3	12.5	15.3	17.3	2.2	2	1.8
ED=24 h, RP=30 a	MPI-ESM-LR-C	96.1	101.8	107	19.4	18.5	21.6	1.5	2.1	1.6
	EC-EARTH-C	87.8	93.4	96.8	16	19.5	21.2	1.1	1.5	1.2
	CNRM-CM5-C	110.4	118.6	125.2	23.6	25.5	25.4	0.9	1	0.8
	HadGEM2-ES-C	84.1	97.5	102.6	16.2	20	22.7	1.9	1.7	1.5

C | APPENDIX TO CHAPTER 6

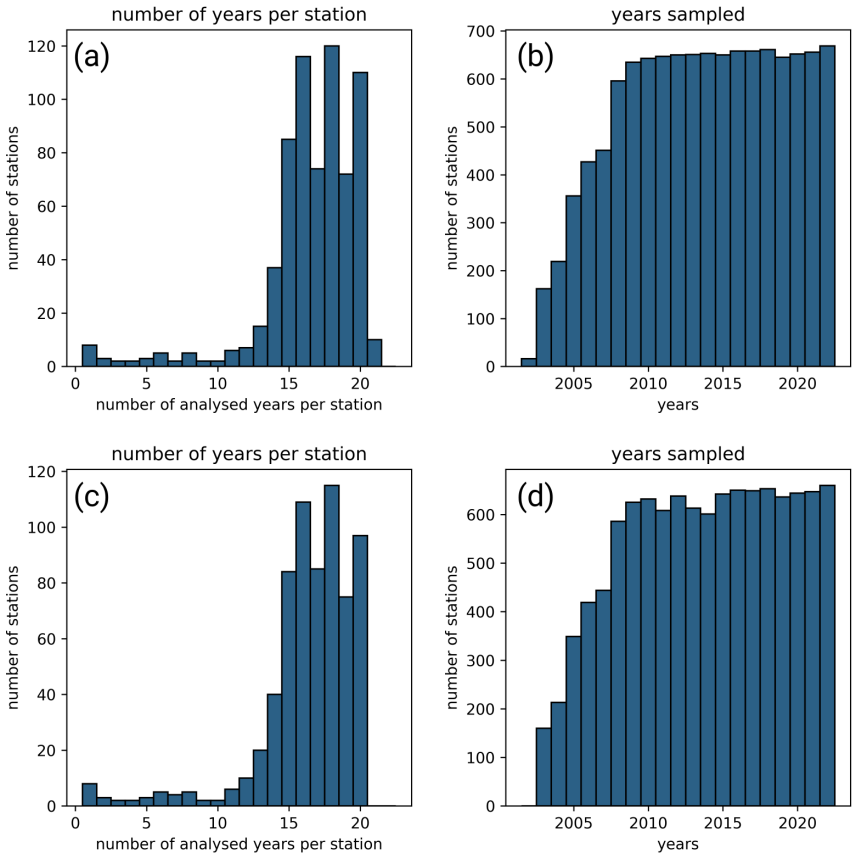

Figure C.1: Data availability of the observational data in the event catalogue used in Chapter 6. (a) and (b) show the data availability for the stations, (c) and (d) for the radar data at station locations.

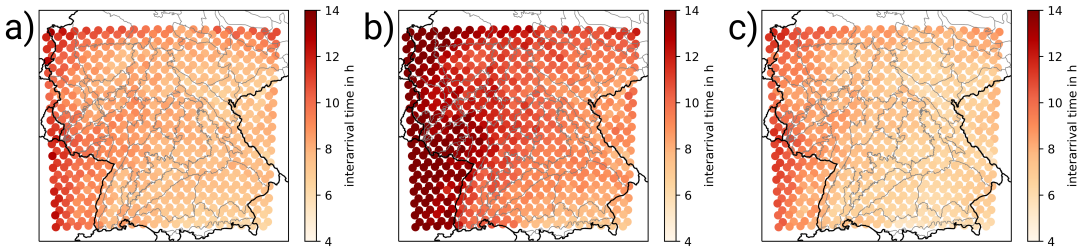

Figure C.2: Spatial distribution of the inter-arrival time in the CPM ensemble members: a) EC-EARTH-C, b) HadGEM2-ES-C, c) MPI-ESM-LR-C.

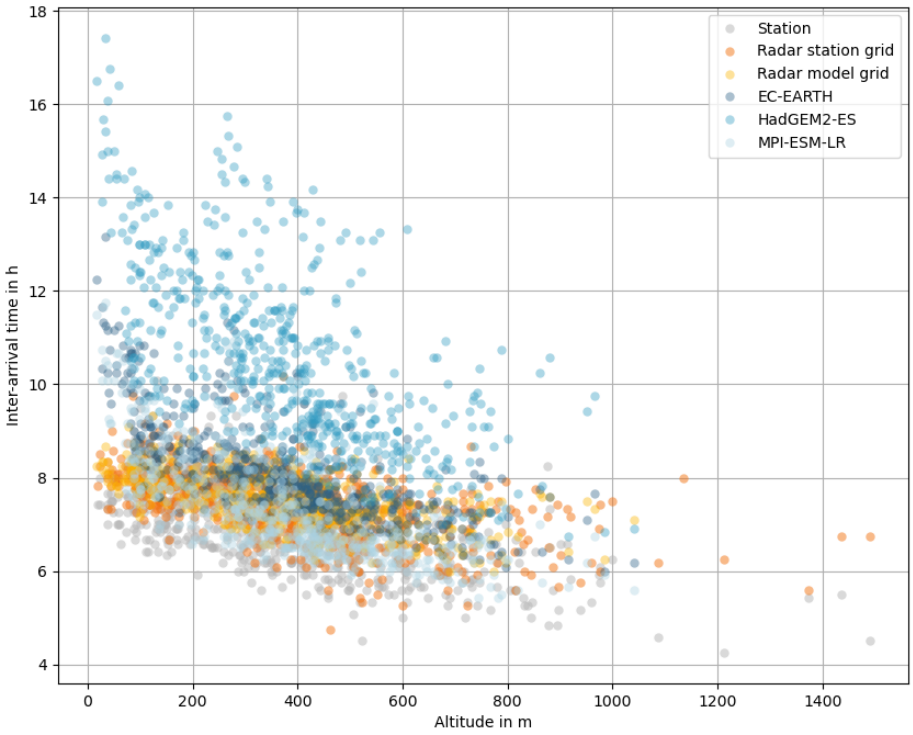

Figure C.3: Relationship between altitude and inter-arrival time.

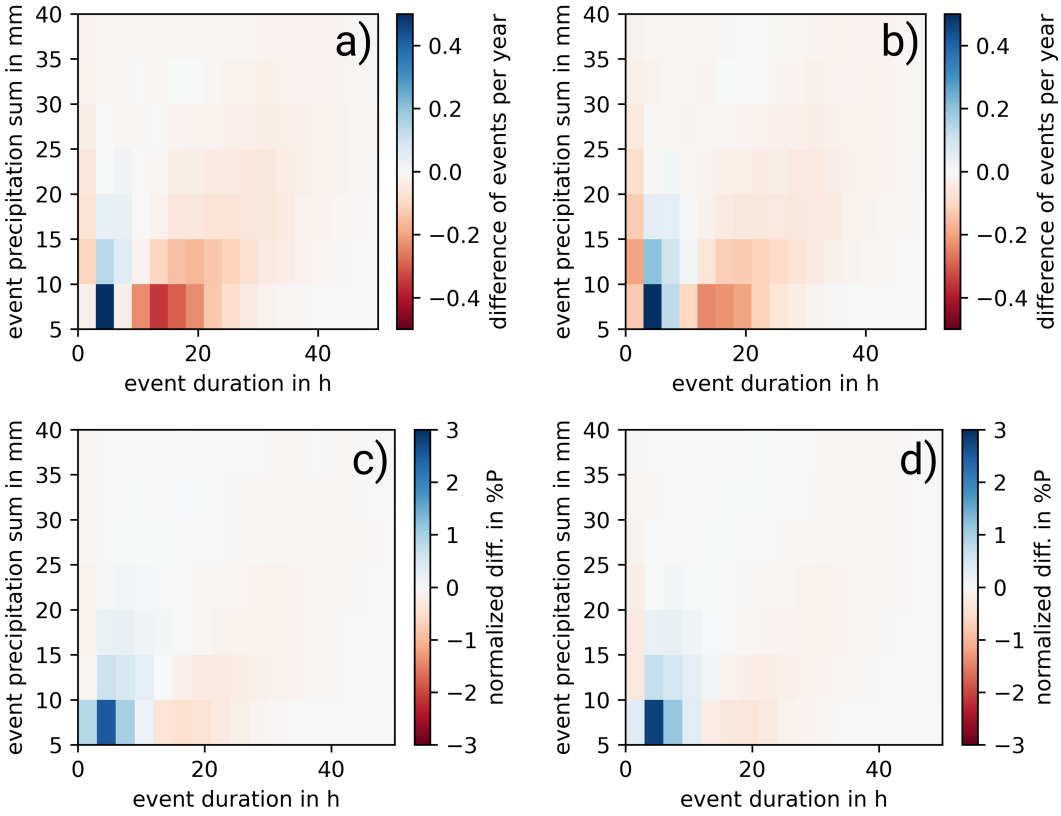

Figure C.4: The difference in event occurrence in the radar and station data is shown in the first row for (a) the radar at the station locations, (b) the radar interpolated to the model grid. In the second row, the normalised differences are shown for (c) the radar at the station locations, (d) the radar interpolated to the model grid. For the normalization, the mean annual event occurrence is scaled to 100 % and the differences are displayed in percentage points.

D | APPENDIX TO CHAPTER 7

Evaluation Imean

Table D.1: Thresholds of p90 of Imean in mm in the different event datasets.

Dataset	>1 h	1-3 h	3-12 h	12-24 h
Stations	3.442	10.034	2.791	1.550
Radar station location	3.535	8.523	2.793	1.608
Radar model grid	3.364	7.816	2.749	1.579
EC-EARTH-C	2.626	10.758	2.748	1.459
HadGEM2-ES-C	2.890	13.200	2.974	1.303
MPI-ESM-LR-C	2.447	10.474	2.685	1.467

Table D.2: Thresholds of p99 of Imean in mm in the different event datasets.

Dataset	>1 h	1-3 h	3-12 h	12-24 h
Stations	10.641	21.498	6.592	2.934
Radar station location	9.355	17.390	6.056	2.891
Radar model grid	8.424	15.533	5.780	2.826
EC-EARTH-C	9.131	21.699	6.670	2.955
HadGEM2-ES-C	11.834	25.862	7.876	2.775
MPI-ESM-LR-C	8.333	22.048	6.550	3.011

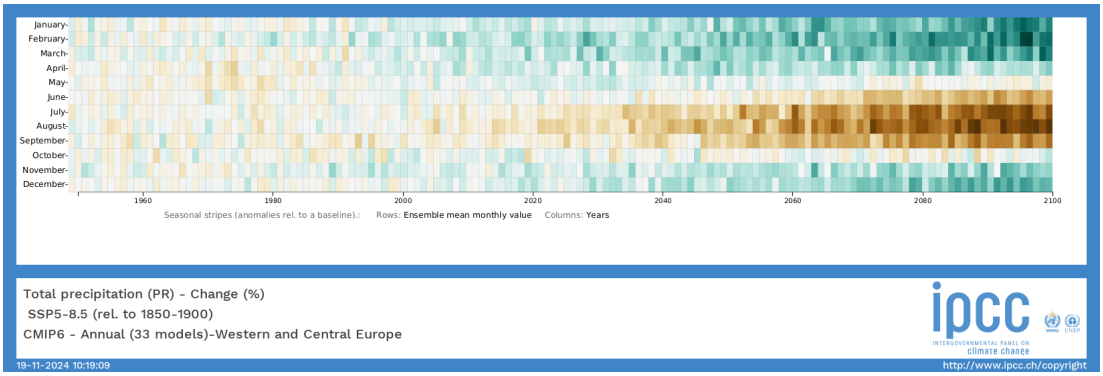

Figure D.1: Change signal in total monthly precipitation relative to 1850-1900 in Western and Central Europe. The data is based on 33 CMIP6 simulations with the emission scenarios SSP5-8.5. Green indicates an increase in total precipitation, brown a decrease (©IPCC Working Group I (WGI): Sixth Assessment Report, IPCC WGI Interactive Atlas, URL: `https://interactive-atlas.ipcc.ch/`, last access November 2024).

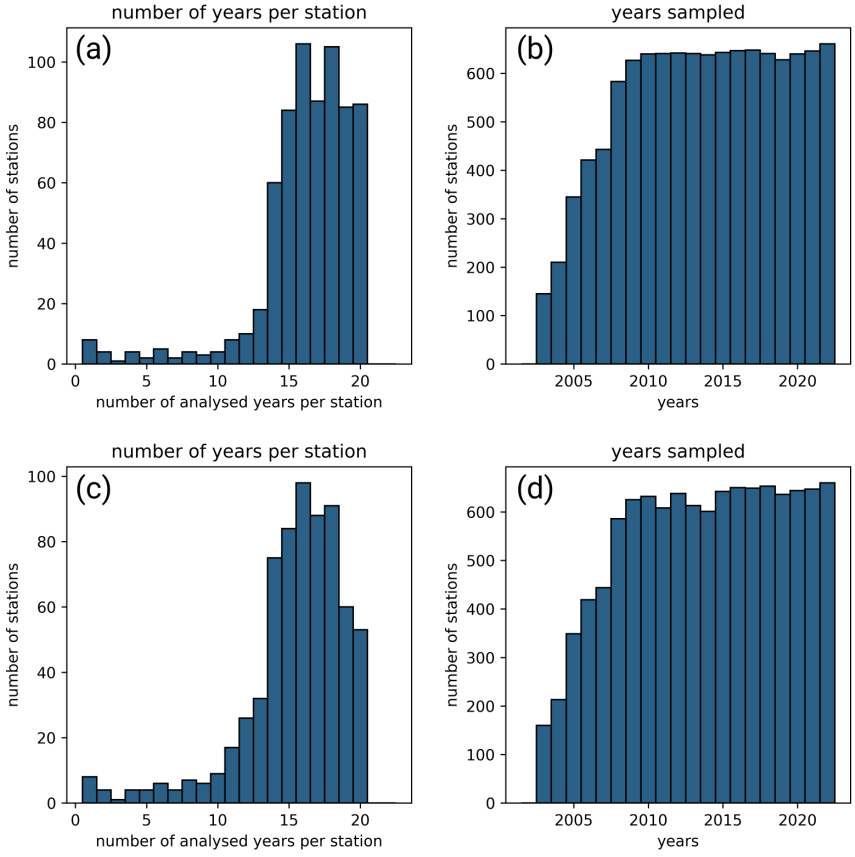

Figure D.2: Data availability of the observational data in the event catalogue used in Chapter 7. (a) and (b) show the data availability for the stations, (c) and (d) for the radar data at station locations.

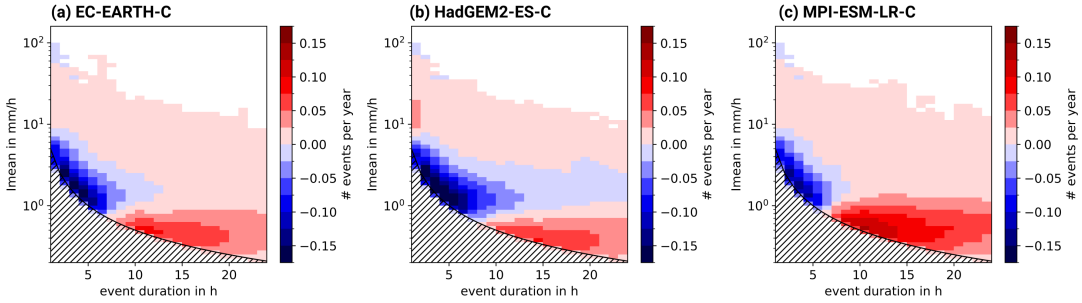

Figure D.3: The bias of the frequency distribution of events in the simulation compared to radar data (ensemble - radar) of events per year and grid point analogously to Fig. 7.3. The bin size is 1 h for the duration and increases exponentially by an increment of $\times 10^{0.05}$ for Imean. The hatched area marks where no events are possible by the event definition.

D.1 Seasonality in the ensemble and significance

The significance of the climate change signal in the frequency of precipitation events is assessed by testing the null hypothesis that the slope of the linear regression to annual event occurrences is zero (Fig. D.5). The calculation is performed using the function *stats.linregress* from the Python package *scipy*. The method applies a Wald Test with a t-distribution for the test statistic. Statistical significance is evaluated at a 0.05 significance level.

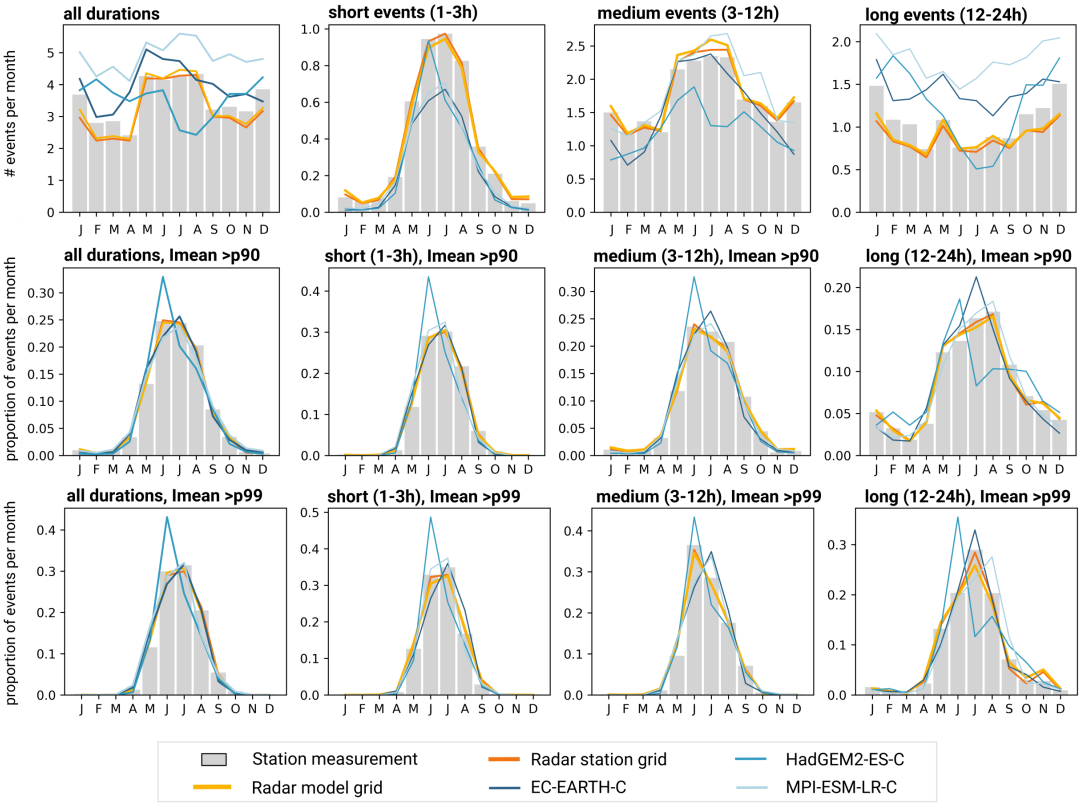

Figure D.4: The bar plots show the number of events in each respective month per year and station, derived from the station measurements, for all events (first column), short duration events (1-3 h, second column), medium duration events (3-12 h, third column), and long duration events (12-24 h, fourth column). The first row shows the distribution for events of all intensities, the second (third) row shows events of Imean>p90 (Imean>p99). Line plots show the equivalent results for the radar dataset (2003-2022) and the CPM ensemble in the historical period (1971-2000).

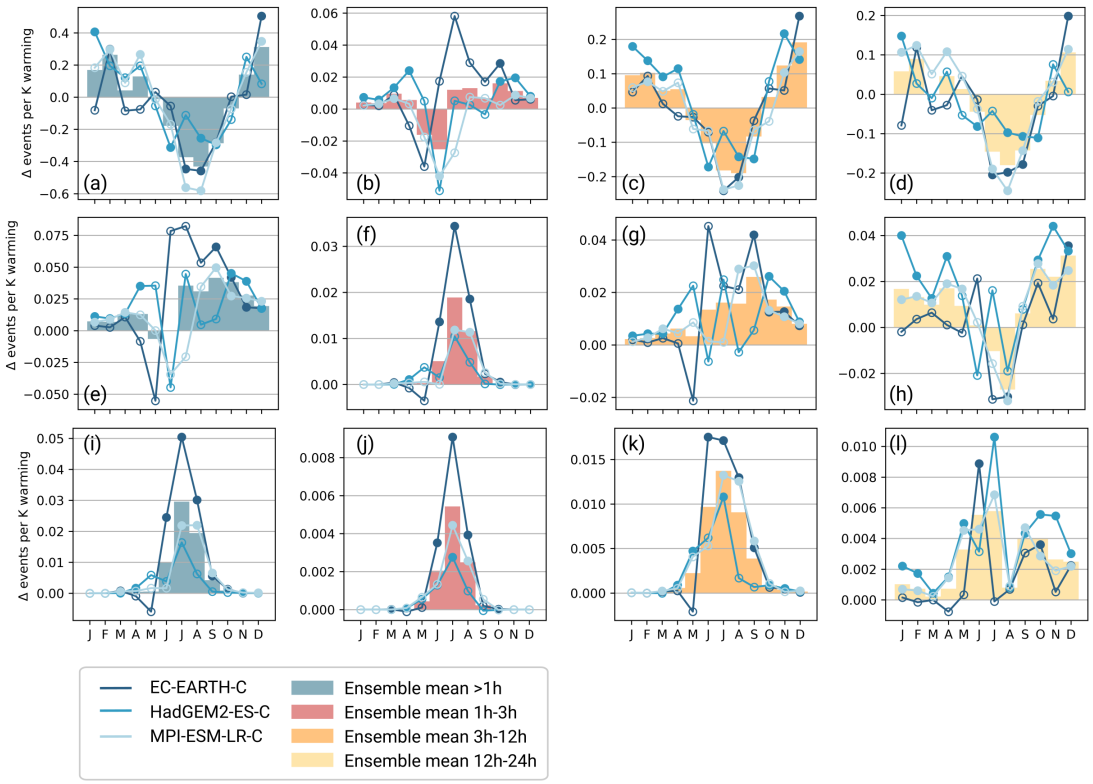

Figure D.5: Climate change signal of the frequency of precipitation events for all events in the first row, events above p90(Imean) in the second row, and events above p99(Imean) in the third row. Columns refer to the event durations: (a, e, i) events duration $\geq$1 h, (b, f, j) event duration of 1 h - 3 h, (c, g, k) duration of 3 h - 12 h, and (d, h, l) 12 h - 24 h. Line plots show the results from the single ensemble members. Filled markers indicate a significant change signal, empty markers indicate the months without significant change (See Section D.1 for further information). The bar plots show the ensemble mean.

E | APPENDIX TO CHAPTER 8

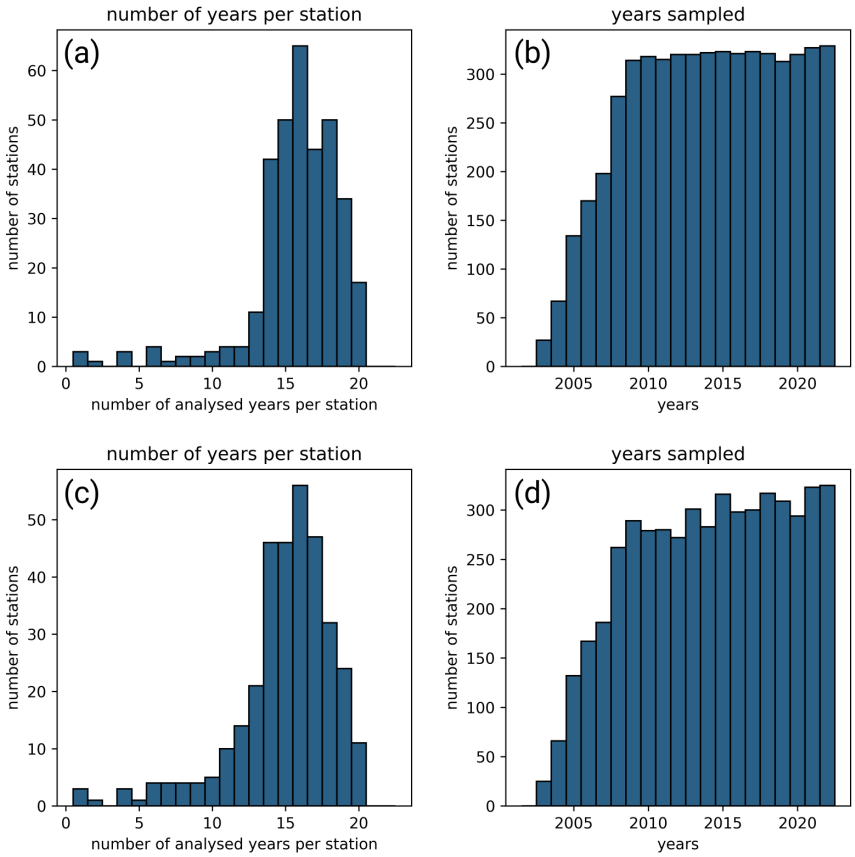

Figure E.1: Data availability of the observational data in the event catalogue used in Chapter 8. (a) and (b) show the data availability for the stations, (c) and (d) for the radar data at station locations.

Table E.1: Thresholds of Imean in mm for heavy-10% events in the observational datasets and the historical model simulations (1971-2000).

Dataset	1-24h	1-3h	3-12h	12-24h
Stations	5.155	10.504	3.423	1.917
Radar station location	4.799	9.078	3.336	1.914
Radar model grid	4.461	8.261	3.225	1.842
EC-EARTH-C	4.048	11.069	3.218	1.781
HadGEM2-ES-C	5.668	13.468	3.764	1.725
MPI-ESM-LR-C	3.896	10.853	3.243	1.807

Table E.2: Thresholds of Imean in mm for heavy-1% events in the observational datasets and the historical model simulations (1971-2000).

Dataset	1-24 h	1-3 h	3-12 h	12-24 h
Stations	13.748	22.831	7.969	3.475
Radar station location	11.507	18.344	7.059	3.323
Radar model grid	10.213	16.283	6.561	3.169
EC-EARTH-C	12.186	22.042	7.598	3.470
HadGEM2-ES-C	16.618	26.126	9.24	3.611
MPI-ESM-LR-C	11.661	22.484	7.652	3.654

Table E.3: Thresholds of Imean in mm for heavy-10% events in the CPM projections.

Dataset	time slice	1-24 h	1-3 h	3-12 h	12-24 h
EC-EARTH-C	2001-2020	4.303	11.225	3.366	1.816
	2051-2070	4.887	12.895	3.737	1.890
HadGEM2-ES-C	2001-2020	6.028	13.672	4.133	1.892
	2051-2070	6.792	14.65	4.562	2.078
MPI-ESM-LR-C	2001-2020	4.000	10.875	3.349	1.846
	2011-2030	3.915	10.972	3.316	1.818
	2021-2040	3.996	11.561	3.421	1.822
	2031-2050	4.063	11.64	3.528	1.9
	2041-2060	4.249	11.877	3.668	1.931
	2051-2070	4.661	12.671	3.917	1.953
	2061-2080	4.549	12.864	3.783	1.947
	2071-2090	4.462	12.784	3.734	1.98
	2081-2100	4.593	13.038	3.906	2.06

Table E.4: Thresholds of Imean in mm for heavy-1% events in the CPM projections.

Dataset	time slice	1-24 h	1-3 h	3-12 h	12-24 h
EC-EARTH-C	2001-2020	12.764	23.182	8.003	3.637
	2051-2070	15.137	26.576	9.447	3.937
HadGEM2-ES-C	2001-2020	17.223	26.576	9.836	3.966
	2051-2070	19.031	28.668	11.249	4.712
MPI-ESM-LR-C	2001-2020	11.778	22.83	8.101	3.736
	2011-2030	11.754	23.274	8.036	3.702
	2021-2040	12.309	24.335	8.482	3.766
	2031-2050	12.439	24.993	8.747	3.922
	2041-2060	12.933	25.633	9.074	4.049
	2051-2070	14.281	27.258	9.657	4.155
	2061-2080	14.478	27.634	9.673	4.186
	2071-2090	14.214	27.354	9.509	4.425
	2081-2100	14.46	28.683	9.874	4.476

E.1 Evaluation of the scaling temperature variable

The apparent scaling of precipitation is generally related to an "event-associated" temperature, though different approaches exist for determining this temperature. Surface air temperature is commonly used as a practical proxy for atmospheric moisture capacity (Berg et al., 2009). Early studies of the apparent scaling of extreme precipitation often employed daily mean temperature, Tmean (Lenderink and Van Meijgaard, 2008; Berg et al., 2009, 2013). Similarly, Wasko and Sharma (2015) used 24 h mean centred to the start of the event. However, as discussed in Visser et al. (2020), the event-associated temperature should not include the cooling effect of the rainfall event itself. To avoid this, they suggested averaging the temperature over the 24 h preceding the event.

Further approaches use a temperature from a specific period before the event but often focus on dew point temperature rather than air temperature to include the effects of moisture availability. For example, Lenderink et al. (2011) used the 2 m dew point temperature from 4 h before the event, while Da Silva and Haerter (2024) examined the maximum dew point temperature within the 3 h window before the event. The daily maximum temperature on the day of the event (event-$T_{\max}$) was previously tested by Berg et al. (2013) and Lenderink and Van Meijgaard (2008) in supporting materials and was found to provide results comparable to those based on daily mean temperature.

We here present an evaluation of the different approaches for one example simulation year, the year 1971 in the simulation driven by MPI-ESM-LR. We here compare event-$T_{\max}$ to traditional methods using Tmean (e.g. Lenderink and Van Meijgaard, 2008; Berg et al., 2009, 2013, Fig. E.2a), the mean temperature over the 24 hours preceding the event (Visser et al., 2020, Fig. E.2b), and an approach similar to a recent study in Da Silva and Haerter (2024) – even though on dew point temperature of the maximum temperature 3 h before the event (Fig. E.2c). As expected, Tmean is consistently lower than event-$T_{\max}$. Similar deviations are found for the mean deviation when applying the 24 h averaged temperature before the event. The closest agreement with event-$T_{\max}$ is achieved using the method analogous to (Da Silva and Haerter, 2024), adapted for air

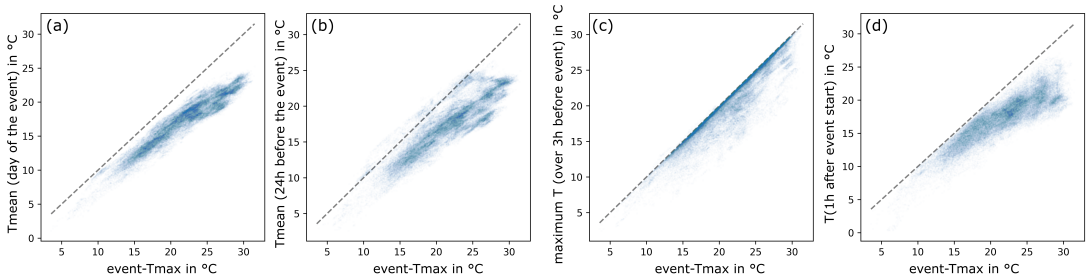

Figure E.2: Comparison of event-$T_{\max}$ with alternative event-associated temperatures: (a) Tmean of the day of the event, (b) Tmean averaged temperature before the event, (c) maximum temperature within the 3 h period prior to the event, (d) temperature 1 h after the event start. The analysis is for heavy-10% events in MPI-ESM-LR-C in the year 1971.

temperature, which extracts the maximum temperature within the 3 h period prior to the event.

To assess the impact of cooling of the temperature during the event itself, we compared event-T_{max} with the temperature observed within the event (Fig. E.2d). The temperature in the event decreases and is generally lower than event-T_{max}. The deviations are similar to the comparison of event-T_{max} and Tmean.

In conclusion, event-T_{max}, in contrast to daily mean temperature, better represents the high temperatures typically observed before precipitation events and yields results similar to those obtained using the maximum temperature from the 3 h window prior to the event. A key advantage of using event-T_{max} is that it does not rely on sub-daily data, which is largely unavailable for gridded observations in Germany. A limitation of this approach is that it does not per definition ensure that the temperature is sampled before the event, particularly if the event starts in the morning. However, as shown in Fig. E.2c, this is generally not an issue for summer precipitation events.

In essence, we chose event-T_{max} as the covariate for the analysis in Chapter 8, as it effectively captures precipitation variability while minimizing the impact of the cooling effect from the rainfall itself and is available in daily datasets.

E.2 Sensitivity to of apparent scaling rates to temperature range and outliers

Although assessing scaling rates has become a common practice for investigating the relationship between precipitation and temperature, there remains no consensus on the exact methodology for deriving these rates. Scaling rates are known to be sensitive to the choice of data, as well as to statistical assumptions and methods applied (Ali et al., 2022).

In this section, we present the preliminary sensitivity analysis of the assessment of apparent scaling rates in Chapter 8, with a focus on (1) the selection of temperature range (2) the impact of sampling uncertainty.

The sensitivity of scaling rates to the temperature ranges for assessment

The sensitivity analysis of the temperature range for the apparent scaling is illustrated using the variable Imax in the event dataset derived from station observations (Fig. E.3). The example shows a positive scaling of the 90th percentile of Imax with event-T_{max}. Scaling appears to follow an exponential relationship, represented by a linear increase in the logarithmic plot (Fig. E.3a), for temperatures between 5 and 25 °C, beyond which the curve flattens. The flattening of the apparent scaling curve with increasing air temperature is typically attributed to limited moisture availability (e.g., Ali et al., 2022).

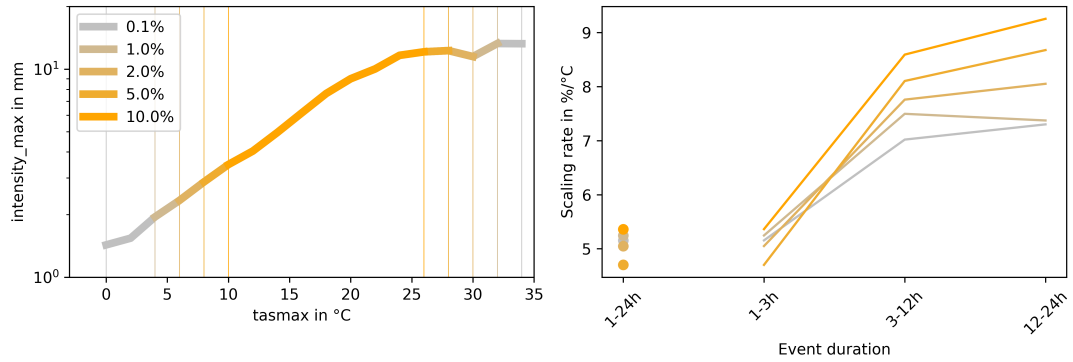

Figure E.3: Apparent scaling of p90 of Imax in the station observations.

Moreover, flattening of the scaling curve has also been observed to result from a residual effect of pooling data from different locations (Visser et al., 2021).

The scaling rate is estimated with an exponential regression to the scaling curve (Details are in Chapter 8). The lower slope at both low and especially high temperatures indicates that the fit is sensitive to the chosen temperature range. In Fig. E.3b, we examine results using different temperature cut-offs ranging from 0.1% to 10%. The pattern observed is that higher cut-off leads to higher scaling rates, as the sampling primarily reflects the steepest increase in the central part of the temperature distribution. Similar analyses were conducted for other parameters and event subsets (not shown here) and yielded consistent results.

Further investigation of the scaling with dew point temperature revealed that the flattening at high temperatures is reduced compared to the scaling using event-$T_{\max}$. Nonetheless, the scaling rate still depends similarly on the choice of temperature cut-off thresholds, with higher cut-off generally leading to higher scaling rates.

In conclusion, the sensitivity analysis shows that the scaling rate is highly dependent on the temperature range considered, particularly when the quantity does not follow an exponential pattern. To mitigate the influence of extreme cases that do not follow exponential scaling, we apply a cut-off of 5% for both the lower and upper temperature boundaries. The approach is similar to the applied procedure in Ali et al. (2022). To still account for this sensitivity in the scaling rate output, we not only provide the scaling rates in Chapter 8 but also always provide the figures showing the scaling curves over temperature.

Uncertainty in the estimated scaling rates

To estimate the variance due to sampling uncertainty, a bootstrapping approach with 100 realisations was applied. The largest variance is anticipated for samples with small sample sizes, which is in our analysis the case for the dataset derived from station observations. Thus, Fig. E.4 illustrates this effect for the station dataset, focusing on Imax.

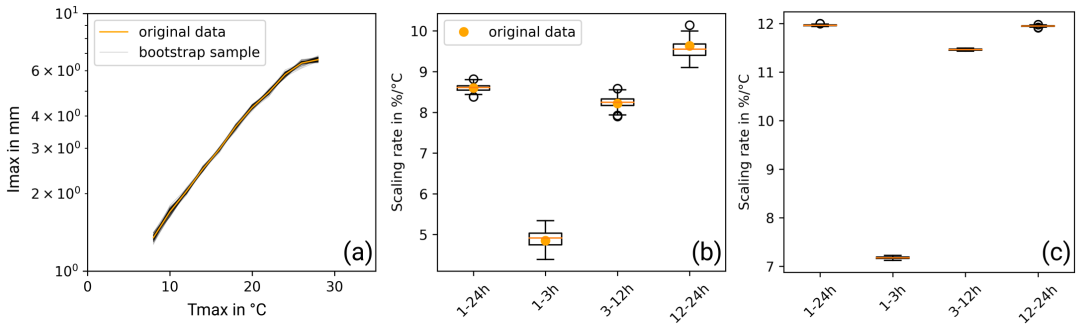

Figure E.4: (a) Scaling relation of p90 of Imax over event-$T_{\max}$ in the station data with 100 bootstraps. (b) Scaling rates derived from (a), with orange dots showing the results without bootstrapping. (c) Scaling rates derived from the analogous approach as for the station data in (b), but for EC-EARTH-C in the historical period (1971-2000).

The assessment of Imax reveals an interquartile range up to approximately 0.5 %/°C. The uncertainty is highest for shorter events, which is also associated with the smallest data availability for this duration category (Fig. E.4b). The same assessment in the simulation data showed, that due to large data availability in the pooled gridded data, here no significant deviation is expected from the bootstrapping (Fig. E.4c).

In conclusion, the highest uncertainties are expected in the station data and radar data at station locations, where data availability is low. The expected range of uncertainty remains smaller than the observed patterns targeted for different durations. Due to the large sample size in the gridded model data, there is only minimal uncertainty due to the sampling expected and no additional benefit from a bootstrapping approach is anticipated.

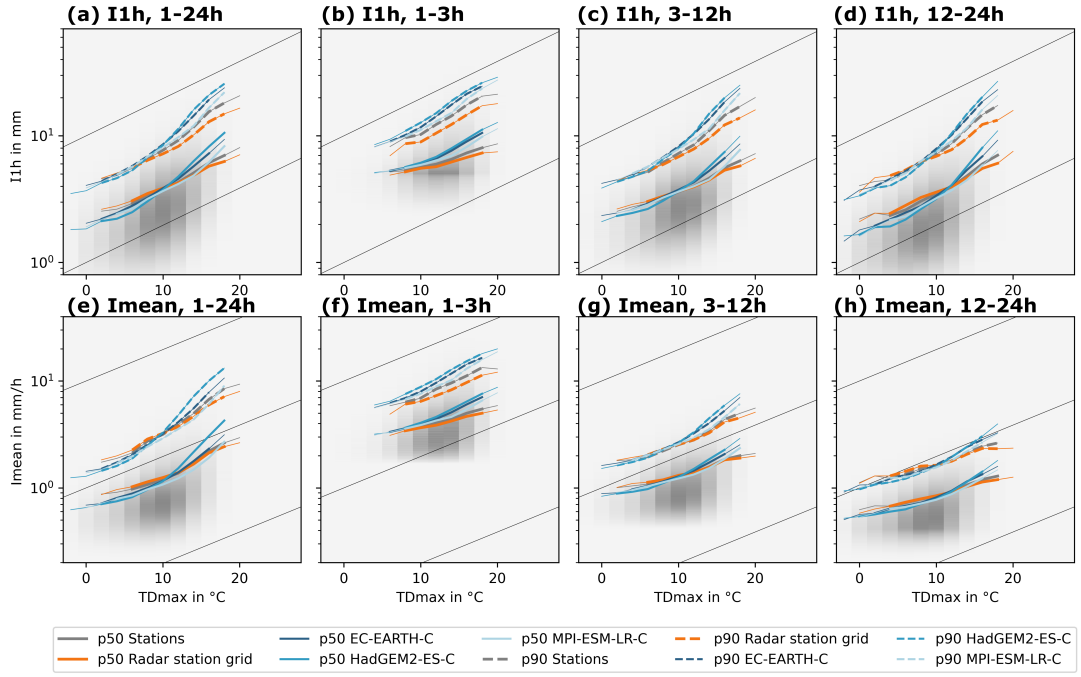

Figure E.5: Apparent scaling with event-TD_{max} in observation and historical CPM simulation of p50 and p90 for (a-d) I1h, (e-h) Imean. Columns refer to the different duration categories: 1-24 h (1st column), 1-3 h (2nd column), 3-12 h (3rd column), 12-24 h (4th column). Grey shading indicates the frequency in the simulation ensemble, diagonal lines indicate CC-scaling with a slope of 7 %/°C. Thick lines show the scaling relation with a cut-off of 5 %, and thin lines with a cut-off of 1 %. Apparent scaling rates are always calculated with 5 % cut-off.

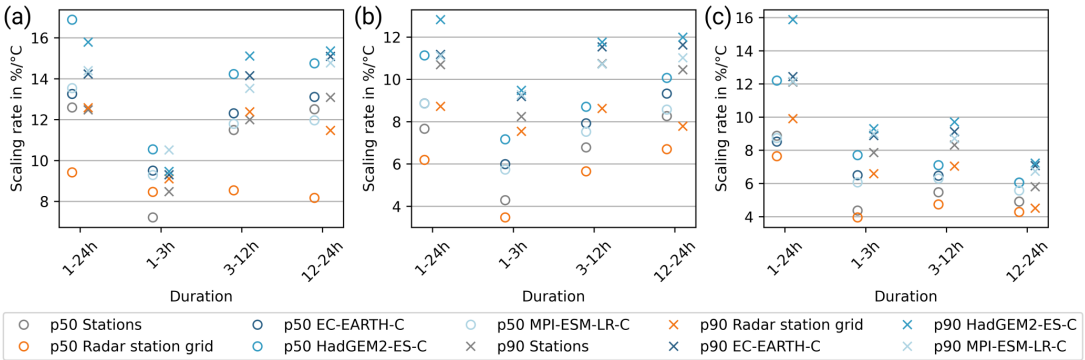

Figure E.6: Apparent scaling rates of intensity with event-TD_{max} for (a) Imax, (b) I1h, and (c) Imean.

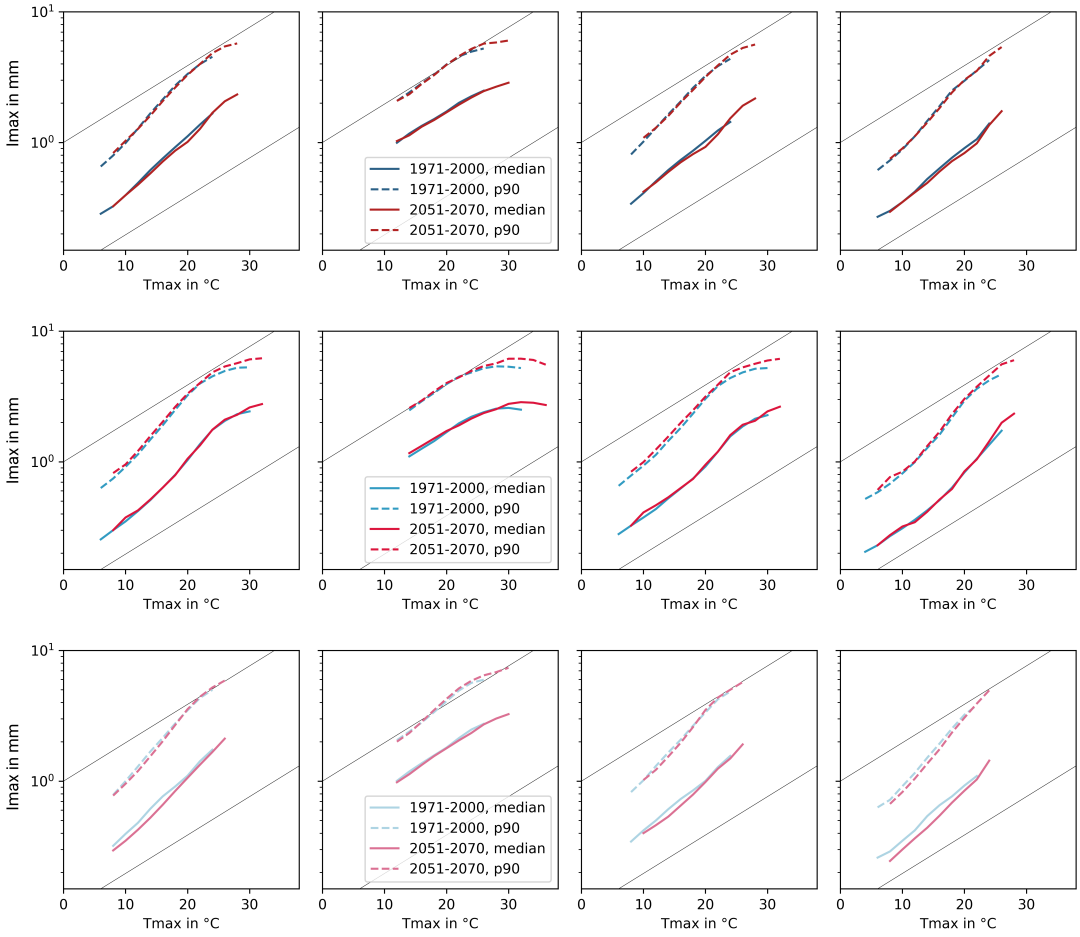

Figure E.7: Projected apparent scaling of Imax in the reference (1971-2000) and future time slice (2051-2070) of p50 and p90 in (a-d) EC-EARTH-C, (e-h) HadGEM2-ES-C, and (i-l) MPI-ESM-LR-C. Columns refer to the different duration categories: 1-24 h (1st column), 1-3 h (2nd column), 3-12 h (3rd column), 12-24 h (4th column).

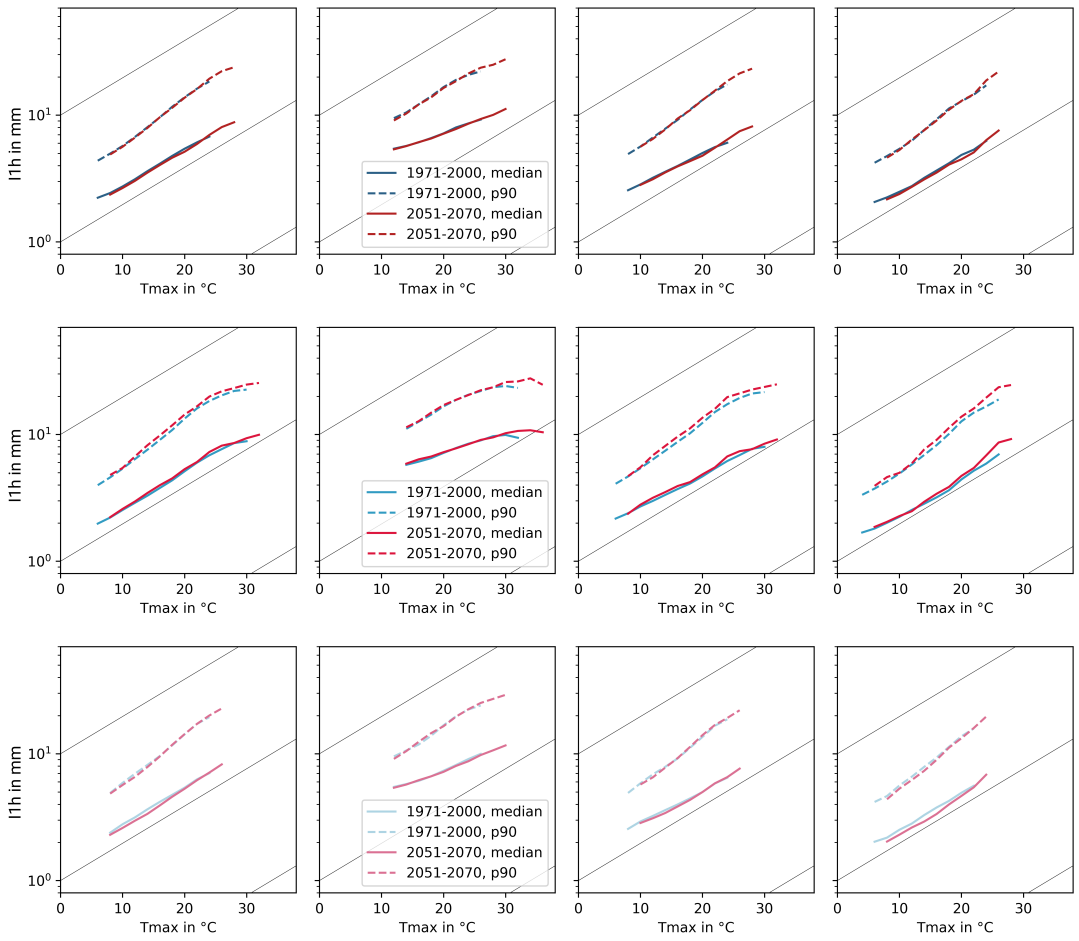

Figure E.8: Projected apparent scaling of I1h in the reference (1971-2000) and future time slice (2051-2070) of p50 and p90 in (a-d) EC-EARTH-C, (e-h) HadGEM2-ES-C, and (i-l) MPI-ESM-LR-C. Columns refer to the different duration categories: 1-24 h (1st column), 1-3 h (2nd column), 3-12 h (3rd column), 12-24 h (4th column).

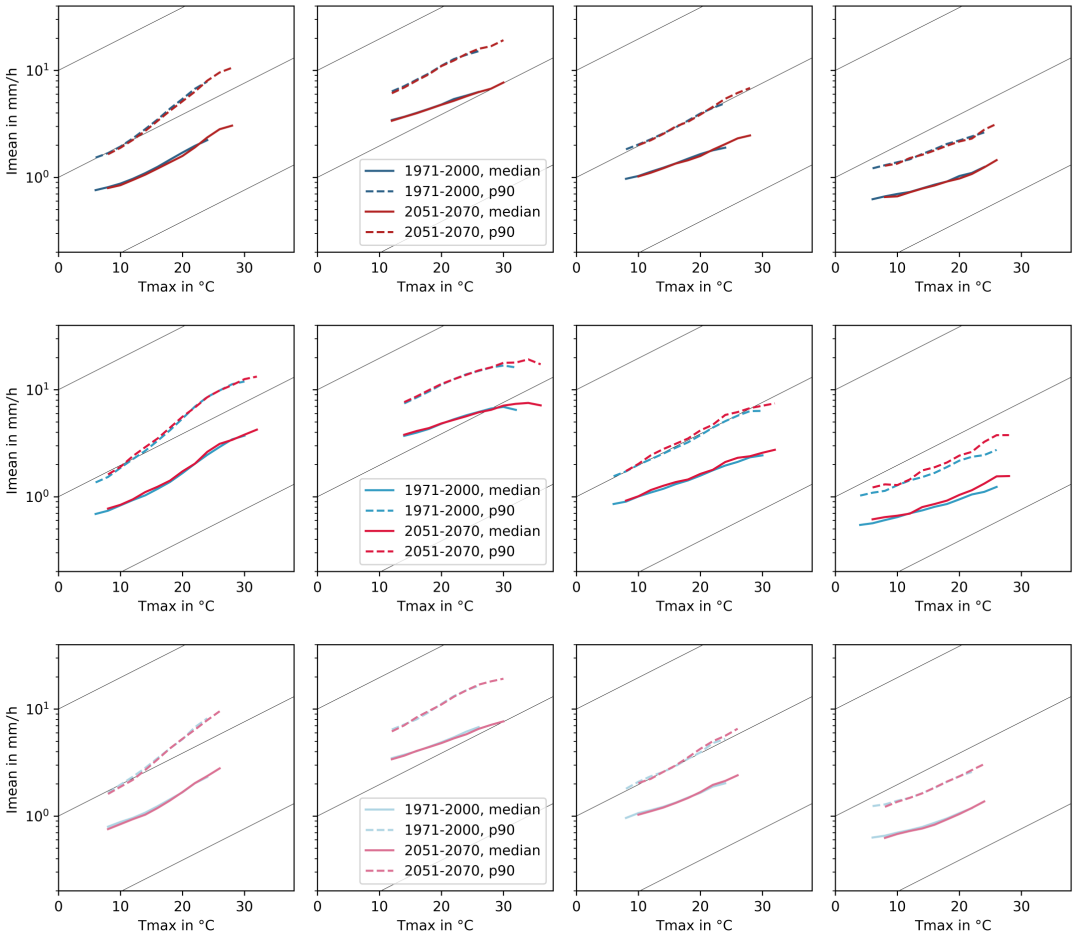

Figure E.9: Projected apparent scaling of Imean in the reference (1971-2000) and future time slice (2051-2070) of p50 and p90 in (a-d) EC-EARTH-C, (e-h) HadGEM2-ES-C, and (i-l) MPI-ESM-LR-C. Columns refer to the different duration categories: 1-24 h (1st column), 1-3 h (2nd column), 3-12 h (3rd column), 12-24 h (4th column).

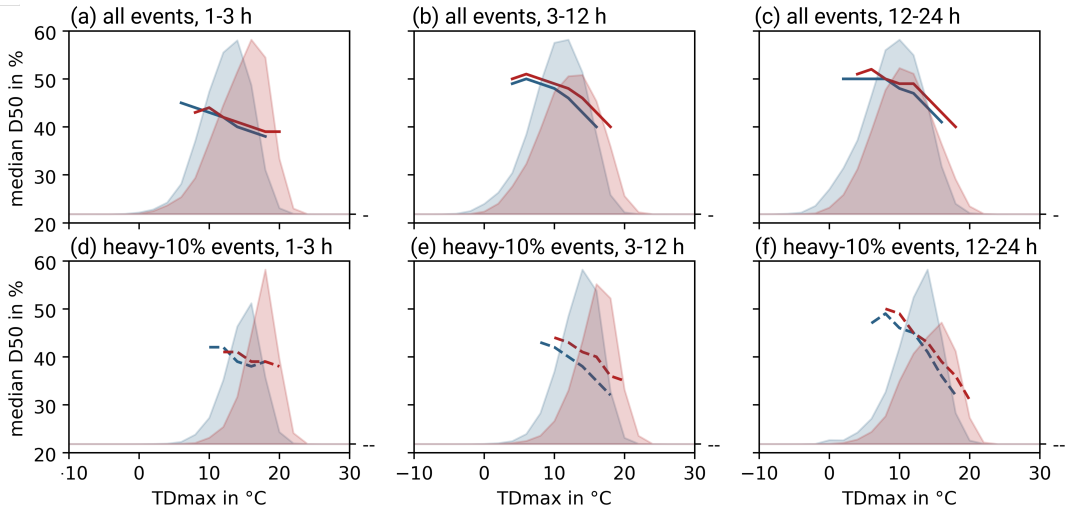

Figure E.10: Projected apparent scaling in EC-EARTH-C in reference (blue, 1971-2000) and future time slice (red, 2051-2070) of the median of D50 over event-TD_{max} for all events (1st row), and heavy-10% events (2nd row). Different duration categories are displayed in columns: 1-3 h (1st column), 3-12 h (2nd column), 12-24 h (3rd column). The event-TD_{max} distribution is provided in the background normalised with the number of events in the historical period.

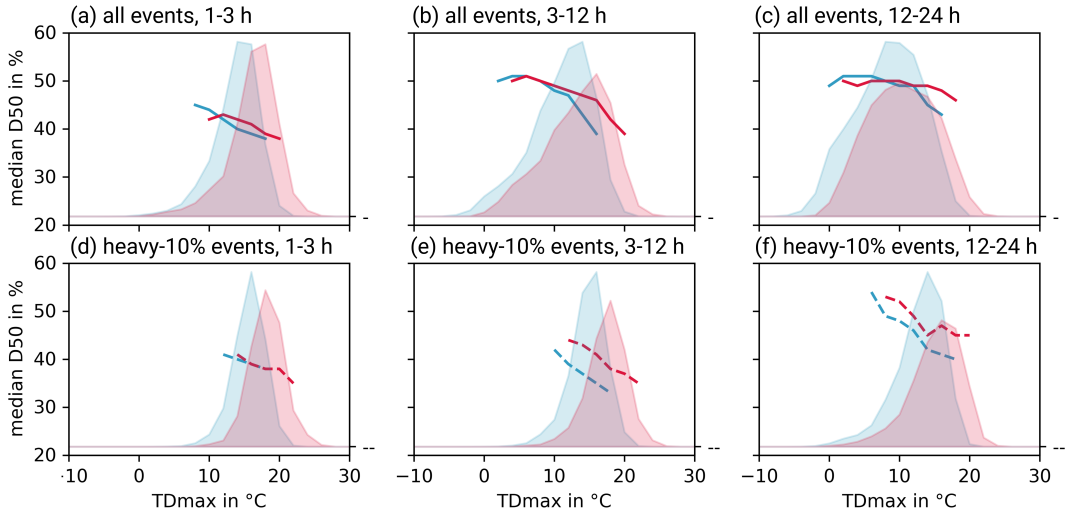

Figure E.11: Projected apparent scaling in HadGEM2-ES-C in reference (blue, 1971-2000) and future time slice (red, 2051-2070) of the median of D50 over event-TD_{max} as in Fig. E.10.

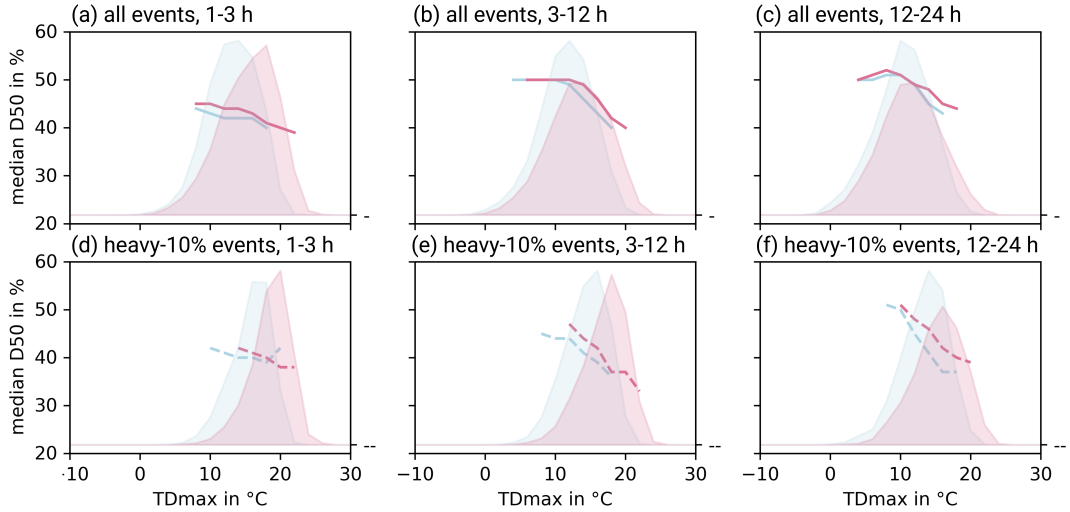

Figure E.12: Projected apparent scaling in MPI-ESM-LR-C in reference (blue, 1971-2000) and future time slice (red, 2051-2070) of the median of D50 over event-TD_{max} as in Fig. E.10.

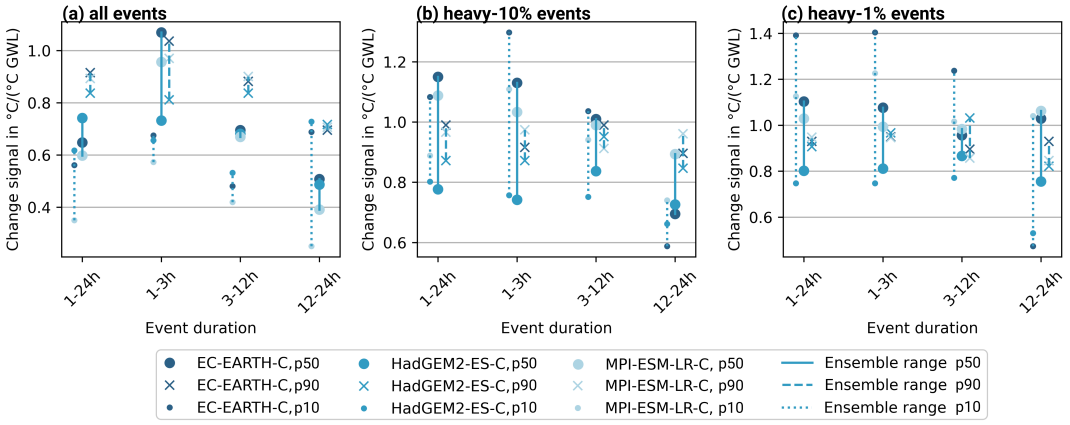

Figure E.13: Slope of the linear regression of event-TD_{max} over GWL in (a) all events, (b) heavy-10% events, and (c) heavy-1% events.

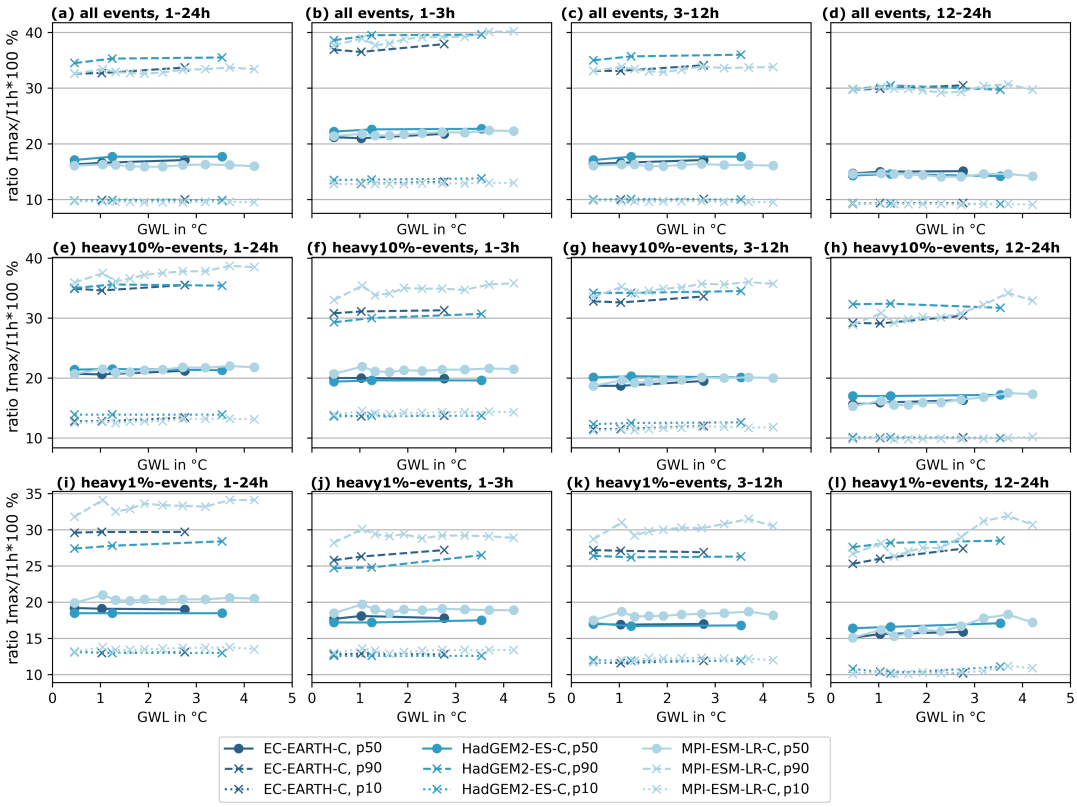

Figure E.14: Projected ratio of Imax/I1h×100 % in % for all events in the first row, heavy-10% events in the second row, and heavy-1% events in the third row. Different duration categories are displayed in columns: 1-24 h (1st column), 1-3 h (2nd column), 3-12 h (3rd column), 12-24 h (4th column). p10, p50, and p90 of the Imax/I1h×100 in % distribution in each 20-year time slice are shown over the GLW associated with that time slice.

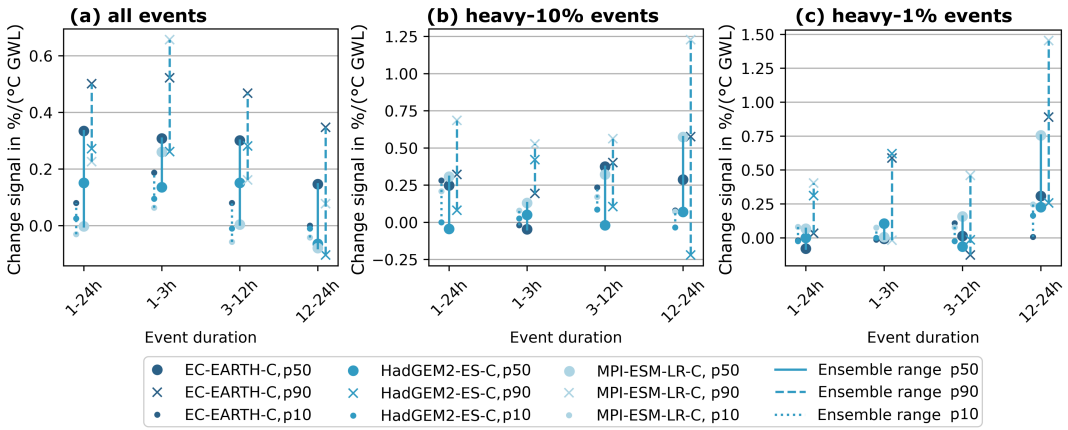

Figure E.15: Slope of the linear regression of Imax/I1h×100 % in %/(°C GWL) for (a) all events, (b) heavy-10% events, and (c) heavy-1% events.

BIBLIOGRAPHY

Alduchov, O. A., and R. E. Eskridge, 1996: Improved Magnus Form Approximation of Saturation Vapor Pressure. *Journal of Applied Meteorology (1988-2005)*, **35 (4)**, 601–609, URL `http://www.jstor.org/stable/26187406`.

Ali, H., H. J. Fowler, and V. Mishra, 2018: Global observational evidence of strong linkage between dew point temperature and precipitation extremes. *Geophysical Research Letters*, **45 (22)**, 12–320, doi: 10.1029/2018gl080557.

Ali, H., H. J. Fowler, D. Pritchard, G. Lenderink, S. Blenkinsop, and E. Lewis, 2022: Towards Quantifying the Uncertainty in Estimating Observed Scaling Rates. *Geophysical Research Letters*, **49 (12)**, e2022GL099 138, doi: 10.1029/2022gl099138.

Ali, H., N. Peleg, and H. J. Fowler, 2021: Global scaling of rainfall with dew-point temperature reveals considerable ocean-land difference. *Geophysical Research Letters*, **48 (15)**, doi: 10.1029/2021gl093798, URL `http://dx.doi.org/10.1029/2021GL093798`.

Allen, M. R., and W. J. Ingram, 2002: Constraints on future changes in climate and the hydrologic cycle. *Nature*, **419 (6903)**, 224–232, doi: 10.1038/nature01092.

Archer, D., and H. Fowler, 2018: Characterising flash flood response to intense rainfall and impacts using historical information and gauged data in Britain. *Journal of Flood Risk Management*, **11**, S121–S133, doi: 10.1111/jfr3.12187.

Argüeso, D., J. P. Evans, A. J. Pitman, and A. Di Luca, 2015: Effects of City Expansion on Heat Stress under Climate Change Conditions. *PLOS ONE*, **10 (2)**, e0117 066, doi: 10.1371/journal.pone.0117066.

Arnbjerg-Nielsen, K., 2008: Forventede ændringer i ekstremregn som følge af klimaændringer. *Spildevandskomiteen Skrift*, **29**, 37.

Balbastre-Soldevila, R., R. García-Bartual, and I. Andrés-Doménech, 2019: A Comparison of Design Storms for Urban Drainage System Applications. *Water*, **11 (4)**, 757, doi: 10.3390/w11040757.

Baldauf, M., A. Seifert, J. Förstner, D. Majewski, M. Raschendorfer, and T. Reinhardt, 2011: Operational Convective-Scale Numerical Weather Prediction with the COSMO Model: Description and Sensitivities. *Monthly Weather Review*, **139 (12)**, 3887 – 3905, doi: 10.1175/MWR-D-10-05013.1.

Ball, J., M. Babister, R. Nathan, P. Weinmann, W. Weeks, M. Retallick, and I. Testoni, 2019: Australian Rainfall and Runoff-A guide to flood estimation. Commonwealth of Australia (Geoscience Australia), Version 4.2, URL `https://aha.net.au/article/australian-rainfall-runoff-guide-flood-estimation/`.

Ball, J. E., 1994: The influence of storm temporal patterns on catchment response. *Journal of Hydrology*, **158 (3)**, 285–303, doi: 10.1016/0022-1694(94)90058-2.

Ban, N., J. Rajczak, J. Schmidli, and C. Schär, 2020: Analysis of Alpine precipitation extremes using generalized extreme value theory in convection-resolving climate simulations. *Climate Dynamics*, **55 (1)**, 61–75, doi: 10.1007/s00382-018-4339-4.

Ban, N., J. Schmidli, and C. Schär, 2014: Evaluation of the convection-resolving regional climate modeling approach in decade-long simulations. *Journal of Geophysical Research: Atmospheres*, **119 (13)**, 7889–7907, doi: 10.1002/2014JD021478.

Ban, N., J. Schmidli, and C. Schär, 2015: Heavy precipitation in a changing climate: Does short-term summer precipitation increase faster? *Geophysical Research Letters*, **42 (4)**, 1165–1172, doi: 10.1002/2014GL062588.

Ban, N., C. Caillaud, E. Coppola, E. Pichelli, S. Sobolowski, M. Adinolfi, B. Ahrens, A. Alias et al., 2021: The first multi-model ensemble of regional climate simulations at kilometer-scale resolution, part I: evaluation of precipitation. *Climate Dynamics*, **57**, 275–302, doi: 10.1007/s00382-021-05708-w.

Barbero, R., H. J. Fowler, S. Blenkinsop, S. Westra, V. Moron, E. Lewis, S. Chan, G. Lenderink et al., 2019: A synthesis of hourly and daily precipitation extremes in different climatic regions. *Weather and Climate Extremes*, **26**, 100 219, doi: 10.1016/j.wace.2019.100219.

Bartels, H., E. Weigl, T. Reich, P. Lang, A. Wagner, O. Kohler, and N. Gerlach, 2004: Projekt RADOLAN-Routineverfahren zur Online-Aneichung der Radarniederschlagsdaten mit Hilfe von automatischen Bodenniederschlagsstationen (Ombrometer): zusammenfassender Abschlussbericht für die Projektlaufzeit von 1997 bis 2004. 111, URL `www.dwd.de/DE/leistungen/radolan/radolan_info/abschlussbericht_pdf.html`.

Bechtold, P., 2017: Atmospheric moist convection. *ECMWF Meteorological training course lecture series*, 1–78, URL `https://www.ecmwf.int/node/16953`.

Berg, P., O. B. Christensen, K. Klehmet, G. Lenderink, J. Olsson, C. Teichmann, and W. Yang, 2019: Summertime precipitation extremes in a EURO-CORDEX 0.11

ensemble at an hourly resolution. *Natural hazards and earth system sciences*, **19 (4)**, 957–971, doi: 10.5194/nhess-19-957-2019.

Berg, P., and J. Haerter, 2013: Unexpected increase in precipitation intensity with temperature—A result of mixing of precipitation types? *Atmospheric Research*, **119**, 56–61, doi: 10.1016/j.atmosres.2011.05.012.

Berg, P., J. Haerter, P. Thejll, C. Piani, S. Hagemann, and J. Christensen, 2009: Seasonal characteristics of the relationship between daily precipitation intensity and surface temperature. *Journal of Geophysical Research: Atmospheres*, **114 (D18)**, doi: 10.1029/2009JD012008.

Berg, P., C. Moseley, and J. O. Haerter, 2013: Strong increase in convective precipitation in response to higher temperatures. *Nature Geoscience*, **6 (3)**, 181–185.

Berthou, S., E. J. Kendon, S. C. Chan, N. Ban, D. Leutwyler, C. Schär, and G. Fosser, 2020: Pan-European climate at convection-permitting scale: a model intercomparison study. *Climate Dynamics*, **55**, 35–59, doi: 10.1007/s00382-018-4114-6.

Brisson, E., K. Van Weverberg, M. Demuzere, A. Devis, S. Saeed, M. Stengel, and N. P. M. van Lipzig, 2016: How well can a convection-permitting climate model reproduce decadal statistics of precipitation, temperature and cloud characteristics? *Climate Dynamics*, **47 (9–10)**, 3043–3061, doi: 10.1007/s00382-016-3012-z.

Bundesamt für Naturschutz (BfN), 2011: Naturräumliche Gliederung Deutschland. *Geodienste*, URL `https://metadaten.bfn.de/BfN-MetaCat/?lang=de#/datasets/iso/685e36cd-87a7-4e7c-a780-ab7b19d54115`, (accessed: 2024-12-04).

Caillaud, C., S. Somot, H. Douville, A. Alias, S. Bastin, S. Brienen, M. Demory, A. Dobler et al., 2024: Northwestern Mediterranean Heavy Precipitation Events in a Warmer Climate: Robust Versus Uncertain Changes With a Large Convection-Permitting Model Ensemble. *Geophysical Research Letters*, **51 (6)**, doi: 10.1029/2023gl105143.

Cannon, A. J., S. R. Sobie, and T. Q. Murdock, 2015: Bias Correction of GCM Precipitation by Quantile Mapping: How Well Do Methods Preserve Changes in Quantiles and Extremes? *Journal of Climate*, **28 (17)**, 6938–6959, doi: 10.1175/jcli-d-14-00754.1.

Carvalho, D., A. Rocha, M. Gómez-Gesteira, and C. Santos, 2012: A sensitivity study of the WRF model in wind simulation for an area of high wind energy. *Environmental Modelling & Software*, **33**, 23–34, doi: 10.1016/j.envsoft.2012.01.019.

Chan, S., E. Kendon, H. J. Fowler, B. D. Youngman, M. Dale, and C. Short, 2022: New Extreme Rainfall Projections for Improved Climate Resilience of Urban Drainage Systems. *Available at SSRN 4303999*, doi: 10.1016/j.cliser.2023.100375.

Chan, S. C., E. J. Kendon, H. J. Fowler, S. Blenkinsop, C. A. T. Ferro, and D. B. Stephenson, 2013: Does increasing the spatial resolution of a regional climate model improve the simulated daily precipitation? *Climate Dynamics*, **41 (5–6)**, 1475–1495, doi: 10.1007/s00382-012-1568-9.

Chan, S. C., E. J. Kendon, H. J. Fowler, S. Blenkinsop, and N. M. Roberts, 2014a: Projected increases in summer and winter UK sub-daily precipitation extremes from high-resolution regional climate models. *Environmental Research Letters*, **9 (8)**, 084 019.

Chan, S. C., E. J. Kendon, H. J. Fowler, S. Blenkinsop, N. M. Roberts, and C. A. Ferro, 2014b: The value of high-resolution Met Office regional climate models in the simulation of multihourly precipitation extremes. *Journal of Climate*, **27 (16)**, 6155–6174, doi: 10.1175/JCLI-D-13-00723.1.

Chan, S. C., E. J. Kendon, H. J. Fowler, A. Kahraman, J. Crook, N. Ban, and A. F. Prein, 2023a: Large-scale dynamics moderate impact-relevant changes to organised convective storms. *Communications Earth & Environment*, **4 (1)**, 8, doi: 10.1038/s43247-022-00669-2.

Chan, S. C., E. J. Kendon, H. J. Fowler, B. D. Youngman, M. Dale, and C. Short, 2023b: New extreme rainfall projections for improved climate resilience of urban drainage systems. *Climate Services*, **30**, 100 375, doi: 10.1016/j.cliser.2023.100375.

Chan, S. C., E. J. Kendon, N. M. Roberts, H. J. Fowler, and S. Blenkinsop, 2016a: Downturn in scaling of UK extreme rainfall with temperature for future hottest days. *Nature Geoscience*, **9 (1)**, 24–28, doi: 10.1038/ngeo2596.

Chan, S. C., E. J. Kendon, N. M. Roberts, H. J. Fowler, and S. Blenkinsop, 2016b: The characteristics of summer sub-hourly rainfall over the southern UK in a high-resolution convective permitting model. *Environmental Research Letters*, **11 (9)**, 094 024, doi: 10.1088/1748-9326/11/9/094024.

Chow, V. T., D. R. Maidment, and L. W. Mays, 1988: Applied hydrology. McGraw-Hill.

Coles, S., J. Bawa, L. Trenner, and P. Dorazio, 2001: *An introduction to statistical modeling of extreme values*, Vol. 208. Springer.

Coppola, E., S. Sobolowski, E. Pichelli, F. Raffaele, B. Ahrens, I. Anders, N. Ban, S. Bastin et al., 2018: A first-of-its-kind multi-model convection permitting ensemble for investigating convective phenomena over Europe and the Mediterranean. *Climate Dynamics*, **55 (1–2)**, 3–34, doi: 10.1007/s00382-018-4521-8.

Cristiano, E., M.-C. ten Veldhuis, and N. van de Giesen, 2017: Spatial and temporal variability of rainfall and their effects on hydrological response in urban areas -– a review. *Hydrology and Earth System Sciences*, **21 (7)**, 3859–3878, doi: 10.5194/hess-21-3859-2017.

Da Silva, N. A., and J. O. Haerter, 2023: The Precipitation Characteristics of Mesoscale Convective Systems Over Europe. *Journal of Geophysical Research: Atmospheres*, **128 (23)**, e2023JD039 045, doi: 10.1029/2023jd039045.

Da Silva, N. A., and J. O. Haerter, 2024: Non super-Clausius-Clapeyron scaling of convective precipitation extremes. *preprint*, doi: 10.21203/rs.3.rs-3777860/v1.

Dale, M., 2021: Managing the effects of extreme sub-daily rainfall and flash floods—a practitioner's perspective. *Philosophical Transactions of the Royal Society A: Mathematical, Physical and Engineering Sciences*, **379 (2195)**, 20190 550, doi: 10.1098/rsta.2019.0550.

Dale, M., B. Luck, H. J. Fowler, S. Blenkinsop, E. Gill, J. Bennett, E. Kendon, and S. Chan, 2017: New climate change rainfall estimates for sustainable drainage. *Proceedings of the Institution of Civil Engineers - Engineering Sustainability*, **170 (4)**, 214–224, doi: 10.1680/jensu.15.00030.

Darwish, M. M., H. J. Fowler, S. Blenkinsop, and M. R. Tye, 2018: A regional frequency analysis of UK sub-daily extreme precipitation and assessment of their seasonality. *International Journal of Climatology*, **38 (13)**, 4758–4776, doi: 10.1002/joc.5694.

DIN 1986-100, 2016: Entwässerungsanlagen für Gebäude und Grundstücke.

DIN EN 752, 2008: Entwässerungssysteme außerhalb von Gebäuden.

Doms, G., and M. Baldauf, 2013: COSMO-Model Version 5.00: A Description of the Nonhydrostatic Regional COSMO-Model - Part I: Dynamics and Numerics. URL `https://www.dwd.de/DE/leistungen/cosmo_dokumentation/pdf_doku_v5_0/1_cosmo_dynamics_5_00.pdf;jsessionid=C0BF7C1944BF03255536F193B850F8B4.live31093?__blob=publicationFile&v=5`.

Doms, G., J. Förstner, E. Heise, H.-J. Herzog, D. Mironov, M. Raschendorfer, T. Reinhardt, B. Ritter et al., 2013: COSMO-Model Version 5.00: A Description of the Nonhydrostatic Regional COSMO-Model - Part II: Physical Parameterizations. doi: 10.5676/DWD_PUB/NWV/COSMO-DOC_5.00_II.

Dougherty, E., and K. L. Rasmussen, 2020: Changes in Future Flash Flood–Producing Storms in the United States. *Journal of Hydrometeorology*, **21 (10)**, 2221–2236, doi: 10.1175/jhm-d-20-0014.1.

Dullo, T. T., A. J. Kalyanapu, and R. S. V. Teegavarapu, 2017: Evaluation of Changing Characteristics of Temporal Rainfall Distribution within 24-Hour Duration Storms and Their Influences on Peak Discharges: Case Study of Asheville, North Carolina. *Journal of Hydrologic Engineering*, **22 (11)**, 05017 022, doi: 10.1061/(asce)he.1943-5584.0001575.

DWA, 2012: *Starkregen in Abhängigkeit von Wiederkehrzeit und Dauer*. DWA-Regelwerk, Dt. Vereinigung für Wasserwirtschaft, Abwasser u. Abfall e.V., URL `https://d-nb.info/1025556631`.

EC-Earth Consortium (EC-Earth), 2014a: EC-EARTH model output prepared for CMIP5 historical, served by ESGF. World Data Center for Climate (WDCC) at DKRZ, URL `https://hdl.handle.net/21.14106/f793786fff08239c2ed4da9e6bfa21c73222c13b`.

EC-Earth Consortium (EC-Earth), 2014b: EC-EARTH model output prepared for CMIP5 rcp85, served by ESGF. World Data Center for Climate (WDCC) at DKRZ, URL `https://hdl.handle.net/21.14106/073343da4a6a11bc544567e497a1ce1e73194db1`.

Eggert, B., P. Berg, J. Haerter, D. Jacob, and C. Moseley, 2015: Temporal and spatial scaling impacts on extreme precipitation. *Atmospheric Chemistry and Physics*, **15 (10)**, 5957–5971, doi: 10.5194/acp-15-5957-2015.

Fadhel, S., M. A. Rico-Ramirez, and D. Han, 2018: Sensitivity of peak flow to the change of rainfall temporal pattern due to warmer climate. *Journal of Hydrology*, **560**, 546–559, doi: 10.1016/j.jhydrol.2018.03.041.

Fernández-González, S., M. L. Martín, E. García-Ortega, A. Merino, J. Lorenzana, J. L. Sánchez, F. Valero, and J. S. Rodrigo, 2018: Sensitivity Analysis of the WRF Model: Wind-Resource Assessment for Complex Terrain. *Journal of Applied Meteorology and Climatology*, **57 (3)**, 733–753, doi: 10.1175/jamc-d-17-0121.1.

Formayer, H., and A. Fritz, 2016: Temperature dependency of hourly precipitation intensities–surface versus cloud layer temperature. *International Journal of Climatology*, **37 (1)**, 1–10, doi: 10.1002/joc.4678.

Fortak, H., 1982: *Meteorologie*. Reimer, Berlin.

Fosser, G., E. J. Kendon, D. Stephenson, and S. Tucker, 2020: Convection-permitting models offer promise of more certain extreme rainfall projections. *Geophysical Research Letters*, **47 (13)**, e2020GL088 151, doi: 10.1029/2020GL088151.

Fosser, G., S. Khodayar, and P. Berg, 2015: Benefit of convection permitting climate model simulations in the representation of convective precipitation. *Climate Dynamics*, **44**, 45–60, doi: 10.1007/s00382-014-2242-1.

Fosser, G., M. Gaetani, E. J. Kendon, M. Adinolfi, N. Ban, D. Belušić, C. Caillaud, J. A. M. Careto et al., 2024: Convection-permitting climate models offer more certain extreme rainfall projections. *npj climate and atmospheric science*, **7 (1)**, 51, doi: 10.1038/s41612-024-00600-w.

Fowler, H. J., G. Lenderink, A. F. Prein, S. Westra, R. P. Allan, N. Ban, R. Barbero, P. Berg et al., 2021a: Anthropogenic intensification of short-duration rainfall extremes. *Nature Reviews Earth & Environment*, **2 (2)**, 107–122, doi: 10.1038/s43017-020-00128-6.

Fowler, H. J., H. Ali, R. P. Allan, N. Ban, R. Barbero, P. Berg, S. Blenkinsop, N. S. Cabi et al., 2021b: Towards advancing scientific knowledge of climate change impacts on short-duration rainfall extremes. *Philosophical Transactions of the Royal Society A*, **379 (2195)**, 20190 542, doi: 10.1098/rsta.2019.0542.

Gatzen, C. P., A. H. Fink, D. M. Schultz, and J. G. Pinto, 2020: An 18-year climatology of derechos in germany. *Natural Hazards and Earth System Sciences*, **20 (5)**, 1335–1351, doi: 10.5194/nhess-20-1335-2020.

Ghanghas, A., A. Sharma, and V. Merwade, 2024: Unveiling the Evolution of Extreme Rainfall Storm Structure Across Space and Time in a Warming Climate. *Earth's Future*, **12 (9)**, e2024EF004 675, doi: 10.1029/2024ef004675.

Gillett, N. P., and J. C. Fyfe, 2013: Annular mode changes in the CMIP5 simulations. *Geophysical Research Letters*, **40 (6)**, 1189–1193, doi: 10.1002/grl.50249.

Giorgetta, M., J. Jungclaus, C. Reick, S. Legutke, V. Brovkin, T. Crueger, M. Esch, K. Fieg et al., 2012a: CMIP5 simulations of the Max Planck Institute for Meteorology (MPI-M) based on the MPI-ESM-LR model: The historical experiment, served by ESGF. World Data Center for Climate (WDCC) at DKRZ, doi: 10.1594/WDCC/CMIP5.MXELhi.

Giorgetta, M., J. Jungclaus, C. Reick, S. Legutke, V. Brovkin, T. Crueger, M. Esch, K. Fieg et al., 2012b: CMIP5 simulations of the Max Planck Institute for Meteorology (MPI-M) based on the MPI-ESM-LR model: The rcp85 experiment, served by ESGF. World Data Center for Climate (WDCC) at DKRZ, doi: 10.1594/WDCC/CMIP5.MXELr8.

Hackenbruch, J., G. Schädler, and J. W. Schipper, 2016: Added value of high-resolution regional climate simulations for regional impact studies. *Meteorol. Z.*, **25 (3)**, 291–304, doi: 10.1127/metz/2016/0701.

Haerter, J. O., and P. Berg, 2009: Unexpected rise in extreme precipitation caused by a shift in rain type? *Nature Geoscience*, **2 (6)**, 372–373, doi: 10.1038/ngeo523.

Hardwick Jones, R., S. Westra, and A. Sharma, 2010: Observed relationships between extreme sub-daily precipitation, surface temperature, and relative humidity. *Geophysical Research Letters*, **37 (22)**, doi: 10.1029/2010gl045081.

Helsen, S., N. P. M. van Lipzig, M. Demuzere, S. Vanden Broucke, S. Caluwaerts, L. De Cruz, R. De Troch, R. Hamdi et al., 2020: Consistent scale-dependency of

future increases in hourly extreme precipitation in two convection-permitting climate models. *Climate Dynamics*, **54 (3)**, 1267–1280, doi: 10.1007/s00382-019-05056-w.

Henn, B., A. J. Newman, B. Livneh, C. Daly, and J. D. Lundquist, 2018: An assessment of differences in gridded precipitation datasets in complex terrain. *Journal of hydrology*, **556**, 1205–1219, doi: 10.1016/j.jhydrol.2017.03.008.

Hennegriff, W., 2007: Climate change and floods – findings and adaptation strategies for flood protection in baden-württemberg. *Water Science and Technology*, **56 (4)**, 35–44, doi: 10.2166/wst.2007.534.

Hettiarachchi, S., C. Wasko, and A. Sharma, 2018: Increase in flood risk resulting from climate change in a developed urban watershed–the role of storm temporal patterns. *Hydrology and Earth System Sciences*, **22 (3)**, 2041–2056, doi: 10.5194/hess-22-2041-2018.

Ho, C. K., D. B. Stephenson, M. Collins, C. A. Ferro, and S. J. Brown, 2012: Calibration strategies: a source of additional uncertainty in climate change projections. *Bulletin of the American Meteorological Society*, **93 (1)**, 21–26, doi: 0.1175/2011BAMS3110.1.

Hodnebrog, Ø., L. Marelle, K. Alterskjær, R. R. Wood, R. Ludwig, E. M. Fischer, T. Richardson, P. Forster et al., 2019: Intensification of summer precipitation with shorter time-scales in Europe. *Environmental Research Letters*, **14 (12)**, 124 050, doi: 10.1088/1748-9326/ab549c.

Hohenegger, C., P. Brockhaus, and C. Schar, 2008: Towards climate simulations at cloud-resolving scales. *Meteorologische Zeitschrift*, **17 (4)**, 383–394, doi: 0.1127/0941-2948/2008/0303.

Houze, R. A., 1993: *Cloud dynamics*. International geophysics series, Academic Press, San Diego.

Hundhausen, M., H. Feldmann, R. Kohlhepp, and J. G. Pinto, 2024: Climate change signals of extreme precipitation return levels for Germany in a transient convection-permitting simulation ensemble. *International Journal of Climatology*, doi: 10.1002/joc.8393.

Hundhausen, M., H. Feldmann, N. Laube, and J. G. Pinto, 2023: Future heat extremes and impacts in a convection-permitting climate ensemble over Germany. *Natural Hazards and Earth System Sciences*, **23 (8)**, 2873–2893, doi: 10.5194/nhess-23-2873-2023.

Hundhausen, M., H. J. Fowler, H. Feldmann, and J. G. Pinto, 2025: Sub-hourly precipitation and rainstorm event profiles in a convection-permitting multi-GCM ensemble. *Weather and Climate Extremes*, **48**, 100 764, doi: 10.1016/j.wace.2025.100764.

Hundhausen, M., H. J. Fowler, H. Feldmann, and J. G. Pinto, in preparation for re-submission: Unprecedented precipitation events and seasonal shifts over Germany revealed by sub-hourly ensemble. *Geophysical Research Letters – in preparation for re-submission.*

IPCC, 2021: *Climate Change 2021 – The Physical Science Basis: Working Group I Contribution to the Sixth Assessment Report of the Intergovernmental Panel on Climate Change.* Cambridge University Press, doi: 10.1017/9781009157896.

Jimenez, P. A., J. P. Hacker, J. Dudhia, S. E. Haupt, J. A. Ruiz-Arias, C. A. Gueymard, G. Thompson, T. Eidhammer, and A. Deng, 2016: WRF-Solar: Description and Clear-Sky Assessment of an Augmented NWP Model for Solar Power Prediction. *Bulletin of the American Meteorological Society*, **97 (7)**, 1249–1264, doi: 10.1175/bams-d-14-00279.1.

Jones, C., J. Hughes, G. Jones, N. Christidis, F. Lott, A. Sellar, M. Webb, A. Bodas-Salcedo et al., 2014: HadGEM2-ES model output prepared for CMIP5 historical, served by ESGF. World Data Center for Climate (WDCC) at DKRZ, doi: 10.1594/WDCC/CMIP5.MOGEhi.

Junghänel, T., H. Ertel, and T. Deutschländer, 2017: Bericht zur Revision der koordinierten Starkregenregionalisierung und -auswertung des Deutschen Wetterdienstes in der Version 2010. *German Meteorological Service, Department of Hydrometeorology, Offenbach am Main.*

Kahraman, A., E. J. Kendon, S. C. Chan, and H. J. Fowler, 2021: Quasi-Stationary Intense Rainstorms Spread Across Europe Under Climate Change. *Geophysical Research Letters*, **48 (13)**, e2020GL092 361, doi: 10.1029/2020gl092361.

Kaspar, F., G. Müller-Westermeier, E. Penda, H. Mächel, K. Zimmermann, A. Kaiser-Weiss, and T. Deutschländer, 2013: Monitoring of climate change in Germany–data, products and services of Germany's National Climate Data Centre. *Advances in Science and Research*, **10 (1)**, 99–106, doi: 10.5194/asr-10-99-2013.

Kautz, L.-A., O. Martius, S. Pfahl, J. G. Pinto, A. M. Ramos, P. M. Sousa, and T. Woollings, 2022: Atmospheric blocking and weather extremes over the Euro-Atlantic sector–a review. *Weather and Climate Dynamics*, **3 (1)**, 305–336, doi: 10.5194/wcd-3-305-2022.

Kay, A., A. Rudd, H. Davies, E. Kendon, and R. Jones, 2015: Use of very high resolution climate model data for hydrological modelling: baseline performance and future flood changes. *Climatic Change*, **133**, 193–208, doi: 10.1007/s10584-015-1455-6.

Keifer, C. J., and H. H. Chu, 1957: Synthetic storm pattern for drainage design. *Journal of the hydraulics division*, **83 (4)**, 1332–1, doi: 10.1061/JYCEAJ.0000104.

Kendon, E., A. Prein, C. Senior, and A. Stirling, 2021: Challenges and outlook for convection-permitting climate modelling. *Philosophical Transactions of the Royal Society A*, **379 (2195)**, 20190 547, doi: 10.1098/rsta.2019.0547.

Kendon, E. J., E. M. Fischer, and C. J. Short, 2023: Variability conceals emerging trend in 100yr projections of uk local hourly rainfall extremes. *Nature Communications*, **14 (1)**, 1133, doi: 10.1038/s41467-023-36499-9.

Kendon, E. J., N. M. Roberts, G. Fosser, G. M. Martin, A. P. Lock, J. M. Murphy, C. A. Senior, and S. O. Tucker, 2020: Greater future UK winter precipitation increase in new convection-permitting scenarios. *Journal of Climate*, **33 (17)**, 7303–7318, doi: 10.1175/JCLI-D-20-0089.1.

Kendon, E. J., N. M. Roberts, H. J. Fowler, M. J. Roberts, S. C. Chan, and C. A. Senior, 2014: Heavier summer downpours with climate change revealed by weather forecast resolution model. *Nature Climate Change*, **4 (7)**, 570–576, doi: 10.1038/nclimate2258.

Kendon, E. J., N. M. Roberts, C. A. Senior, and M. J. Roberts, 2012: Realism of rainfall in a very high-resolution regional climate model. *Journal of Climate*, **25 (17)**, 5791–5806, doi: 10.1175/JCLI-D-11-00562.1.

Kendon, E. J., N. Ban, N. M. Roberts, H. J. Fowler, M. J. Roberts, S. C. Chan, J. P. Evans, G. Fosser, and J. M. Wilkinson, 2017: Do convection-permitting regional climate models improve projections of future precipitation change? *Bulletin of the American Meteorological Society*, **98 (1)**, 79–93, doi: 10.1175/BAMS-D-15-0004.1.

Kistemann, T., T. Claßen, C. Koch, F. Dangendorf, R. Fischeder, J. Gebel, V. Vacata, and M. Exner, 2002: Microbial load of drinking water reservoir tributaries during extreme rainfall and runoff. *Applied and environmental microbiology*, **68 (5)**, 2188–2197, doi: 10.1128/AEM.68.5.2188-2197.20.

Knight, C. G., S. H. E. Knight, N. Massey, T. Aina, C. Christensen, D. J. Frame, J. A. Kettleborough, A. Martin et al., 2007: Association of parameter, software, and hardware variation with large-scale behavior across 57,000 climate models. *Proceedings of the National Academy of Sciences*, **104 (30)**, 12 259–12 264, doi: 10.1073/pnas.0608144104.

Knist, S., K. Goergen, and C. Simmer, 2018: Evaluation and projected changes of precipitation statistics in convection-permitting WRF climate simulations over Central Europe. *Climate Dynamics*, **55 (1–2)**, 325–341, doi: 10.1007/s00382-018-4147-x.

Kreienkamp, F., S. Y. Philip, J. S. Tradowsky, S. F. Kew, P. Lorenz, J. Arrighi, A. Belleflamme, T. Bettmann et al., 2021: Rapid attribution of heavy rainfall events leading to the severe flooding in Western Europe during July 2021. *World Weather Attribution*, URL `http://hdl.handle.net/1854/LU-8732135`.

Krvavica, N., and J. Rubinić, 2020: Evaluation of Design Storms and Critical Rainfall Durations for Flood Prediction in Partially Urbanized Catchments. *Water*, **12 (7)**, 2044, doi: 10.3390/w12072044.

Kurz, M., 1990: *Synoptische Meteorologie*. Selbstverlag des Deutschen Wetterdienstes Offenbach.

Lackmann, G. M., 2013: The South-Central U.S. Flood of May 2010: Present and Future. *Journal of Climate*, **26 (13)**, 4688–4709, doi: 10.1175/jcli-d-12-00392.1.

Lambourne, J. J., and D. Stephenson, 1987: Model study of the effect of temporal storm distributions on peak discharges and volumes. *Hydrological sciences journal*, **32 (2)**, 215–226, doi: 10.1080/02626668709491179.

Langendijk, G. S., T. Halenka, P. Hoffmann, M. Adinolfi, A. Aldama Campino, O. Asselin, S. Bastin, B. Bechtel et al., 2024: Towards better understanding the urban environment and its interactions with regional climate change - The WCRP CORDEX Flagship Pilot Study URB-RCC. *Urban Climate*, **58**, 102 165, doi: 10.1016/j.uclim.2024.102165.

Laube, N., 2019: Predictability of European Heat Waves. Ph.D. thesis, Dissertation, Karlsruhe, Karlsruher Institut für Technologie (KIT), 2019.

Lavin-Gullon, A., J. Milovac, M. García-Díez, and J. Fernández, 2022: Spin-up time and internal variability analysis for overlapping time slices in a regional climate model. *Climate Dynamics*, **61 (1–2)**, 47–64, doi: 10.1007/s00382-022-06560-2.

Lee, M.-H., D.-H. Bae, and E.-S. Im, 2019: Effect of the horizontal resolution of climate simulations on the hydrological representation of extreme low and high flows. *Water Resources Management*, **33**, 4653–4666, doi: 10.1007/s11269-019-02359-9.

Lenderink, G., R. Barbero, J. Loriaux, and H. Fowler, 2017: Super-Clausius–Clapeyron scaling of extreme hourly convective precipitation and its relation to large-scale atmospheric conditions. *Journal of Climate*, **30 (15)**, 6037–6052.

Lenderink, G., H. de Vries, H. J. Fowler, R. Barbero, B. van Ulft, and E. van Meijgaard, 2021: Scaling and responses of extreme hourly precipitation in three climate experiments with a convection-permitting model. *Philosophical Transactions of the Royal Society A*, **379 (2195)**, 20190 544, doi: 10.1098/rsta.2019.0544.

Lenderink, G., H. Mok, T. Lee, and G. Van Oldenborgh, 2011: Scaling and trends of hourly precipitation extremes in two different climate zones–Hong Kong and the Netherlands. *Hydrology and Earth System Sciences*, **15 (9)**, 3033–3041, doi: 10.5194/hess-15-3033-2011.

Lenderink, G., and E. Van Meijgaard, 2008: Increase in hourly precipitation extremes beyond expectations from temperature changes. *Nature Geoscience*, **1 (8)**, 511–514, doi: 10.1038/ngeo262.

Lenderink, G., and E. Van Meijgaard, 2010: Linking increases in hourly precipitation extremes to atmospheric temperature and moisture changes. *Environmental Research Letters*, **5 (2)**, 025 208, doi: 10.1088/1748-9326/5/2/025208.

Lengfeld, K., T. Winterrath, T. Junghänel, M. Hafer, and A. Becker, 2019: Characteristic spatial extent of hourly and daily precipitation events in Germany derived from 16 years of radar data. *Meteorologische Zeitschrift*, **28 (5)**, 363–378, doi: 10.1127/metz/2019/0964.

Leutwyler, D., O. Fuhrer, X. Lapillonne, D. Lüthi, and C. Schär, 2016: Towards European-scale convection-resolving climate simulations with GPUs: A study with COSMO 4.19. *Geoscientific Model Development*, **9 (9)**, 3393–3412, doi: 10.5194/gmd-9-3393-2016.

Lewis, E., H. Fowler, L. Alexander, R. Dunn, F. McClean, R. Barbero, S. Guerreiro, X.-F. Li, and S. Blenkinsop, 2019: GSDR: A Global Sub-Daily Rainfall Dataset. *Journal of Climate*, **32 (15)**, 4715–4729, doi: 10.1175/jcli-d-18-0143.1.

Li, C., F. Zwiers, X. Zhang, G. Chen, J. Lu, G. Li, J. Norris, Y. Tan et al., 2019: Larger increases in more extreme local precipitation events as climate warms. *Geophysical Research Letters*, **46 (12)**, 6885–6891, doi: 10.1029/2019GL082908.

Long, K., D. Wang, G. Wang, J. Zhu, S. Wang, and S. Xie, 2021: Higher Temperature Enhances Spatiotemporal Concentration of Rainfall. *Journal of Hydrometeorology*, **22 (12)**, 3159–3169, doi: 10.1175/jhm-d-21-0034.1.

Loriaux, J. M., G. Lenderink, S. R. De Roode, and A. P. Siebesma, 2013: Understanding convective extreme precipitation scaling using observations and an entraining plume model. *Journal of the Atmospheric Sciences*, **70 (11)**, 3641–3655, doi: 10.1175/JAS-D-12-0317.1.

Losada Carreño, I., M. T. Craig, M. Rossol, M. Ashfaq, F. Batibeniz, S. E. Haupt, C. Draxl, B.-M. Hodge, and C. Brancucci, 2020: Potential impacts of climate change on wind and solar electricity generation in Texas. *Climatic Change*, **163**, 745–766, doi: 10.1007/s10584-020-02891-3.

Lucas-Picher, P., D. Argüeso, E. Brisson, Y. Tramblay, P. Berg, A. Lemonsu, S. Kotlarski, and C. Caillaud, 2021: Convection-permitting modeling with regional climate models: Latest developments and next steps. *Wiley Interdisciplinary Reviews: Climate Change*, **12 (6)**, e731, doi: 10.1002/wcc.731.

Ludwig, P., F. Ehmele, M. J. Franca, S. Mohr, A. Caldas-Alvarez, J. E. Daniell, U. Ehret, H. Feldmann et al., 2023: A multi-disciplinary analysis of the exceptional flood event of July 2021 in central Europe – Part 2: Historical context and relation to climate change. *Natural Hazards and Earth System Sciences*, **23 (4)**, 1287–1311, doi: 10.5194/nhess-23-1287-2023.

Lutgens, F. K., and E. J. Tarbuck, 2019: *The atmosphere*. 14th ed., Pearson, New York.

Madsen, H., K. Arnbjerg-Nielsen, and P. S. Mikkelsen, 2009: Update of regional intensity–duration–frequency curves in Denmark: Tendency towards increased storm intensities. *Atmospheric Research*, **92 (3)**, 343–349, doi: 10.1016/j.atmosres.2009.01.013.

Malitz, G., and H. Ertel, 2015: KOSTRA DWD 2010: Starkniederschlagshöhen für Deutschland (Bezugszeitraum 1951 bis 2010), Abschlussbericht, Deutscher Wetterdienst. Offenbach: Abteilung Hydrometeorologie.

Markolf, S. A., M. V. Chester, A. M. Helmrich, and K. Shannon, 2021: Re-imagining design storm criteria for the challenges of the 21st century. *Cities*, **109**, 102 981, doi: 10.1016/j.cities.2020.102981.

Martel, J.-L., F. P. Brissette, P. Lucas-Picher, M. Troin, and R. Arsenault, 2021: Climate Change and Rainfall Intensity–Duration–Frequency Curves: Overview of Science and Guidelines for Adaptation. *Journal of Hydrologic Engineering*, **26 (10)**, doi: 10.1061/(asce)he.1943-5584.0002122.

McKenna, C. M., and A. Maycock, 2022: The role of the North Atlantic Oscillation for projections of winter mean precipitation in Europe. *Geophysical Research Letters*, **49 (19)**, e2022GL099 083, doi: 10.1029/2022GL099083.

Meredith, E. P., U. Ulbrich, and H. W. Rust, 2020: Subhourly rainfall in a convection-permitting model. *Environmental Research Letters*, **15 (3)**, 034 031, doi: 10.1088/1748-9326/ab6787.

Meredith, E. P., U. Ulbrich, H. W. Rust, and H. Truhetz, 2021: Present and future diurnal hourly precipitation in 0.11 EURO-CORDEX models and at convection-permitting resolution. *Environmental Research Communications*, **3 (5)**, 055 002, doi: 10.1088/2515-7620/abf15e.

Mohr, S., U. Ehret, M. Kunz, P. Ludwig, A. Caldas-Alvarez, J. E. Daniell, F. Ehmele, H. Feldmann et al., 2023: A multi-disciplinary analysis of the exceptional flood event of July 2021 in central Europe – Part 1: Event description and analysis. *Natural Hazards and Earth System Sciences*, **23 (2)**, 525–551, doi: 10.5194/nhess-23-525-2023.

Molnar, P., S. Fatichi, L. Gaál, J. Szolgay, and P. Burlando, 2015: Storm type effects on super Clausius–Clapeyron scaling of intense rainstorm properties with air temperature. *Hydrology and Earth System Sciences*, **19 (4)**, 1753–1766, doi: 10.5194/hess-19-1753-2015.

Moseley, C., P. Berg, and J. O. Haerter, 2013: Probing the precipitation life cycle by iterative rain cell tracking. *Journal of Geophysical Research: Atmospheres*, **118 (24)**, doi: 10.1002/2013jd020868.

Müller, S. K., E. Pichelli, E. Coppola, S. Berthou, S. Brienen, C. Caillaud, M.-E. Demory, A. Dobler et al., 2023: The climate change response of alpine-mediterranean heavy precipitation events. *Climate Dynamics*, **62 (1)**, 165–186, doi: 10.1007/s00382-023-06901-9.

Müller, S. K., C. Caillaud, S. Chan, H. De Vries, S. Bastin, S. Berthou, E. Brisson, M.-E. Demory et al., 2023: Evaluation of Alpine-Mediterranean precipitation events in convection-permitting regional climate models using a set of tracking algorithms. *Climate Dynamics*, **61 (1-2)**, 939–957, doi: 10.1007/s00382-022-06555-z.

Müller, T., M. Schütze, and A. Bárdossy, 2017: Temporal asymmetry in precipitation time series and its influence on flow simulations in combined sewer systems. *Advances in Water Resources*, **107**, 56–64, doi: 10.1016/j.advwatres.2017.06.010.

Myhre, G., K. Alterskjaer, C. W. Stjern, O. Hodnebrog, L. Marelle, B. H. Samset, J. Sillmann, N. Schaller et al., 2019: Frequency of extreme precipitation increases extensively with event rareness under global warming. *Scientific Reports*, **9 (1)**, doi: 10.1038/s41598-019-52277-4.

Ng, J. Y., S. Fazlollahi, and S. Galelli, 2020: Do design storms yield robust drainage systems? How rainfall duration, intensity, and profile can affect drainage performance. *Journal of Water Resources Planning and Management*, **146 (3)**, 04020 003, doi: 10.1061/(ASCE)WR.1943-5452.0001167.

Nijsse, F. J., P. M. Cox, and M. S. Williamson, 2020: Emergent constraints on transient climate response (TCR) and equilibrium climate sensitivity (ECS) from historical warming in CMIP5 and CMIP6 models. *Earth System Dynamics*, **11 (3)**, 737–750, doi: 10.5194/esd-11-737-2020.

Ochoa-Rodriguez, S., L.-P. Wang, A. Gires, R. D. Pina, R. Reinoso-Rondinel, G. Bruni, A. Ichiba, S. Gaitan et al., 2015: Impact of spatial and temporal resolution of rainfall inputs on urban hydrodynamic modelling outputs: A multi-catchment investigation. *Journal of Hydrology*, **531**, 389–407, doi: 10.1016/j.jhydrol.2015.05.035.

Panthou, G., A. Mailhot, E. Laurence, and G. Talbot, 2014: Relationship between Surface Temperature and Extreme Rainfalls: A Multi-Time-Scale and Event-Based Analysis. *Journal of Hydrometeorology*, **15 (5)**, 1999–2011, doi: 10.1175/jhm-d-14-0020.1.

Peel, M. C., B. L. Finlayson, and T. A. McMahon, 2007: Updated world map of the Köppen-Geiger climate classification. *Hydrology and Earth System Sciences*, **11 (5)**, 1633–1644, doi: 10.5194/hess-11-1633-2007.

Peleg, N., D. B. Wright, H. J. Fowler, J. P. Leitão, A. Sharma, and F. Marra, 2024: A simple and robust approach for adapting design storms to assess climate-induced changes in flash flood hazard. *Advances in Water Resources*, **193**, 104 823, doi: 10.1016/j.advwatres.2024.104823.

Pendergrass, A. G., 2018: What precipitation is extreme? *Science*, **360 (6393)**, 1072–1073, doi: 10.1126/science.aat1871.

Peterson, T. C., and M. J. Manton, 2008: Monitoring changes in climate extremes: a tale of international collaboration. *Bulletin of the American Meteorological Society*, **89 (9)**, 1266–1271, doi: 10.1175/2008BAMS2501.1.

Pfahl, S., P. A. O'Gorman, and E. M. Fischer, 2017: Understanding the regional pattern of projected future changes in extreme precipitation. *Nature Climate Change*, **7 (6)**, 423–427, doi: 10.1038/nclimate3287.

Pichelli, E., E. Coppola, S. Sobolowski, N. Ban, F. Giorgi, P. Stocchi, A. Alias, D. Belušić et al., 2021: The first multi-model ensemble of regional climate simulations at kilometer-scale resolution part 2: historical and future simulations of precipitation. *Climate Dynamics*, **56 (11–12)**, 3581–3602, doi: 10.1007/s00382-021-05657-4.

Pichler, M., 2024: idf_analysis: Intensity duration frequency analysis with python based on KOSTRA. Zenodo, doi: 10.5281/ZENODO.10559992.

Piper, D., M. Kunz, F. Ehmele, S. Mohr, B. Mühr, A. Kron, and J. Daniell, 2016: Exceptional sequence of severe thunderstorms and related flash floods in May and June 2016 in Germany–Part 1: Meteorological background. *Natural Hazards and Earth System Sciences*, **16 (12)**, 2835–2850, doi: 10.5194/nhess-16-2835-2016.

Pochwat, K., D. Słyś, and S. Kordana, 2017: The temporal variability of a rainfall synthetic hyetograph for the dimensioning of stormwater retention tanks in small urban catchments. *Journal of Hydrology*, **549**, 501–511, doi: 10.1016/j.jhydrol.2017.04.026.

Poschlod, B., R. Ludwig, and J. Sillmann, 2021: Ten-year return levels of sub-daily extreme precipitation over Europe. *Earth System Science Data*, **13 (3)**, 983–1003, doi: 10.5194/essd-13-983-2021.

Prein, A., A. Gobiet, M. Suklitsch, H. Truhetz, N. Awan, K. Keuler, and G. Georgievski, 2013: Added value of convection permitting seasonal simulations. *Climate Dynamics*, **41**, 2655–2677, doi: 10.1007/s00382-013-1744-6.

Prein, A. F., R. M. Rasmussen, K. Ikeda, C. Liu, M. P. Clark, and G. J. Holland, 2016: The future intensification of hourly precipitation extremes. *Nature Climate Change*, **7 (1)**, 48–52, doi: 10.1038/nclimate3168.

Prein, A. F., W. Langhans, G. Fosser, A. Ferrone, N. Ban, K. Goergen, M. Keller, M. Tölle et al., 2015: A review on regional convection-permitting climate modeling: Demonstrations, prospects, and challenges. *Reviews of geophysics*, **53 (2)**, 323–361, doi: 10.1002/2014RG000475.

Pritchard, D., E. Lewis, S. Blenkinsop, L. Patino Velasquez, A. Whitford, and H. J. Fowler, 2023: An observation-based dataset of global sub-daily precipitation indices

(gsdr-i). *Scientific Data*, **10 (1)**, doi: 10.1038/s41597-023-02238-4, URL `http://dx.doi.org/10.1038/s41597-023-02238-4`.

Purr, C., E. Brisson, and B. Ahrens, 2021: Convective rain cell characteristics and scaling in climate projections for Germany. *International Journal of Climatology*, **41 (5)**, 3174–3185, doi: 10.1002/joc.7012.

Rajczak, J., and C. Schär, 2017: Projections of future precipitation extremes over Europe: a multimodel assessment of climate simulations. *Journal of Geophysical Research: Atmospheres*, **122 (20)**, 10–773, doi: 10.1002/2017JD027176.

Ramon, D., K. Allacker, F. De Troyer, H. Wouters, and N. P. van Lipzig, 2020: Future heating and cooling degree days for Belgium under a high-end climate change scenario. *Energy and Buildings*, **216**, 109 935, doi: 10.1016/j.enbuild.2020.109935.

Raschendorfer, M., 2001: The new turbulence parameterization of LM. *COSMO newsletter*, **1**, 89–97.

Rauthe, M., H. Steiner, U. Riediger, A. Mazurkiewicz, A. Gratzki et al., 2013: A Central European precipitation climatology–Part I: Generation and validation of a high-resolution gridded daily data set (HYRAS). *Meteorologische Zeitschrift*, **22 (3)**, 235–256, doi: 10.1127/0941-2948/2013/0436.

Razafimaharo, C., S. Krähenmann, S. Höpp, M. Rauthe, and T. Deutschländer, 2020: New high-resolution gridded dataset of daily mean, minimum, and maximum temperature and relative humidity for Central Europe (HYRAS). *Theoretical and Applied Climatology*, **142 (3–4)**, 1531–1553, doi: 10.1007/s00704-020-03388-w.

Restrepo-Posada, P. J., and P. S. Eagleson, 1982: Identification of independent rainstorms. *Journal of Hydrology*, **55 (1-4)**, 303–319, doi: 10.1016/0022-1694(82)90136-6.

Reszler, C., M. B. Switanek, and H. Truhetz, 2018: Convection-permitting regional climate simulations for representing floods in small- and medium-sized catchments in the Eastern Alps. *Natural Hazards and Earth System Sciences*, **18 (10)**, 2653–2674, doi: 10.5194/nhess-18-2653-2018.

Ritter, B., and J.-F. Geleyn, 1992: A Comprehensive Radiation Scheme for Numerical Weather Prediction Models with Potential Applications in Climate Simulations. *Monthly Weather Review*, **120 (2)**, 303–325, doi: 10.1175/1520-0493(1992)120<0303:acrsfn>2.0.co;2.

Robinson, N., J. Regetz, and R. P. Guralnick, 2014: EarthEnv-DEM90: A nearly-global, void-free, multi-scale smoothed, 90m digital elevation model from fused ASTER and SRTM data. *ISPRS Journal of Photogrammetry and Remote Sensing*, **87**, 57–67, doi: 10.1016/j.isprsjprs.2013.11.002.

Rockel, B., A. Will, and A. Hense, 2008: The regional climate model COSMO-CLM (CCLM). *Meteorologische Zeitschrift*, **17 (4)**, 347–348, doi: 0.1127/0941-2948/2008/0309.

Romps, D. M., 2016: Clausius–Clapeyron scaling of CAPE from analytical solutions to RCE. *Journal of the Atmospheric Sciences*, **73 (9)**, 3719–3737, doi: 10.1175/JAS-D-15-0327.1.

Rudd, A. C., A. L. Kay, S. C. Wells, T. Aldridge, S. J. Cole, E. J. Kendon, and E. J. Stewart, 2019: Investigating potential future changes in surface water flooding hazard and impact. *Hydrological Processes*, **34 (1)**, 139–149, doi: 10.1002/hyp.13572.

Saeed, S., E. Brisson, M. Demuzere, H. Tabari, P. Willems, and N. P. M. van Lipzig, 2016: Multidecadal convection permitting climate simulations over Belgium: sensitivity of future precipitation extremes. *Atmospheric Science Letters*, **18 (1)**, 29–36, doi: 10.1002/asl.720.

Sanderson, M., J. Hughes, and C. Jones, 2014: HadGEM2-ES model output prepared for CMIP5 RCP8.5, served by ESGF. World Data Center for Climate (WDCC) at DKRZ, doi: 10.1594/WDCC/CMIP5.MOGEr8.

Sangelantoni, L., S. Sobolowski, T. Lorenz, O. Hodnebrog, R. M. Cardoso, P. M. M. Soares, R. Ferretti, A. Lavín-Gullón et al., 2023: Investigating the representation of heatwaves from an ensemble of km-scale regional climate simulations within CORDEX-FPS convection. *Climate Dynamics*, **62 (6)**, 4635–4671, doi: 10.1007/s00382-023-06769-9.

Santos, J. A., M. Belo-Pereira, H. Fraga, and J. G. Pinto, 2016: Understanding climate change projections for precipitation over western Europe with a weather typing approach. *Journal of Geophysical Research: Atmospheres*, **121 (3)**, 1170–1189, doi: 10.1002/2015JD024399.

Sato, T., H. Miura, M. Satoh, Y. N. Takayabu, and Y. Wang, 2009: Diurnal cycle of precipitation in the tropics simulated in a global cloud-resolving model. *Journal of Climate*, **22 (18)**, 4809–4826, doi: 10.1175/2009JCLI2890.1.

Schädler, G., H.-J. Panitz, E. Christner, H. Feldmann, M. Karremann, and N. Laube, 2018: Regional Climate Simulations with COSMO-CLM: Ensembles, Very High Resolution and Paleoclimate. *High Performance Computing in Science and Engineering'17*, Springer, 411–429, doi: 10.1007/978-3-319-68394-2_24.

Schär, C., N. Ban, E. M. Fischer, J. Rajczak, J. Schmidli, C. Frei, F. Giorgi, T. R. Karl et al., 2016: Percentile indices for assessing changes in heavy precipitation events. *Climatic Change*, **137 (1–2)**, 201–216, doi: 10.1007/s10584-016-1669-2.

Schättler, U., G. Doms, and C. Schraff, 2013: COSMO-Model Version 5.00: A Description of the Nonhydrostatic Regional COSMO-Model - Part VII: User's Guide. doi: 10.5676/DWD_PUB/NWV/COSMO-DOC_5.00_VII.

Schiemann, R., P. Athanasiadis, D. Barriopedro, F. Doblas-Reyes, K. Lohmann, M. J. Roberts, D. V. Sein, C. D. Roberts et al., 2020: Northern Hemisphere blocking simulation in current climate models: evaluating progress from the Climate Model Intercomparison Project Phase 5 to 6 and sensitivity to resolution. *Weather and Climate Dynamics*, **1 (1)**, 277–292, doi: 10.5194/wcd-1-277-2020.

Schrodin, R., and E. Heise, 2001: The Multi-Layer Version of the DWD Soil Model TERRA-LM. *COSMO Technical Report*, URL `www.cosmo-model.org/content/model/cosmo/techReports/docs/techReport02.pdf`.

Schulz, J.-P., and G. Vogel, 2020: Improving the Processes in the Land Surface Scheme TERRA: Bare Soil Evaporation and Skin Temperature. *Atmosphere*, **11 (5)**, 513, doi: 10.3390/atmos11050513.

Seibert, P., A. Frank, and H. Formayer, 2006: Synoptic and regional patterns of heavy precipitation in austria. *Theoretical and Applied Climatology*, **87 (1–4)**, 139–153, doi: 10.1007/s00704-006-0198-8.

Seneviratne, S., N. Nicholls, D. Easterling, C. Goodess, S. Kanae, J. Kossin, Y. Luo, J. Marengo et al., 2012: Changes in climate extremes and their impacts on the natural physical environment. doi: 10.7916/D8-6NBT-S431.

Seneviratne, S. I., and M. Hauser, 2020: Regional climate sensitivity of climate extremes in CMIP6 versus CMIP5 multimodel ensembles. *Earth's future*, **8 (9)**, e2019EF001 474, doi: 10.1029/2019EF001474.

Shaw, T. A., M. Baldwin, E. A. Barnes, R. Caballero, C. I. Garfinkel, Y.-T. Hwang, C. Li, P. A. O'Gorman et al., 2016: Storm track processes and the opposing influences of climate change. *Nature Geoscience*, **9 (9)**, 656–664, doi: 10.1038/ngeo2783.

Sherwood, S. C., S. Bony, and J.-L. Dufresne, 2014: Spread in model climate sensitivity traced to atmospheric convective mixing. *Nature*, **505 (7481)**, 37–42, doi: 10.1038/nature12829.

Sieck, L. C., S. J. Burges, and M. Steiner, 2007: Challenges in obtaining reliable measurements of point rainfall. *Water Resources Research*, **43 (1)**, doi: 10.1029/2005WR004519.

Singh, M. S., and P. A. O'Gorman, 2014: Influence of microphysics on the scaling of precipitation extremes with temperature. *Geophysical Research Letters*, **41 (16)**, 6037–6044, doi: 10.1002/2014GL061222.

Soares, P. M. M., J. A. M. Careto, R. M. Cardoso, K. Goergen, E. Katragkou, S. Sobolowski, E. Coppola, N. Ban et al., 2022: The added value of km-scale simulations to describe temperature over complex orography: the CORDEX FPS-Convection multi-model ensemble runs over the Alps. *Climate Dynamics*, **62 (6)**, 4491–4514, doi: 10.1007/s00382-022-06593-7.

Sørland, S. L., R. Brogli, P. K. Pothapakula, E. Russo, J. Van de Walle, B. Ahrens, I. Anders, E. Bucchignani et al., 2021: COSMO-CLM regional climate simulations in the Coordinated Regional Climate Downscaling Experiment (CORDEX) framework: a review. *Geoscientific Model Development*, **14 (8)**, 5125–5154, doi: 10.5194/gmd-14-5125-2021.

Spiridonov, V., and M. Ćurić, 2021: *Fundamentals of Meteorology*. Springer International Publishing, doi: 10.1007/978-3-030-52655-9.

Ssymank, A., 1994: Neue Anforderungen im europäischen Naturschutz: das Schutzgebietssystem Natura 2000 und die FFH-Richtlinie der EU. *Natur und Landschaft*, **69 (9)**, 395–406.

Stephenson, D. B., V. Pavan, M. Collins, M. M. Junge, and R. Quadrelli, 2006: North Atlantic Oscillation response to transient greenhouse gas forcing and the impact on European winter climate: a CMIP2 multi-model assessment. *Climate Dynamics*, **27 (4)**, 401–420, doi: 10.1007/s00382-006-0140-x.

Stull, R. B., 2015: *Practical Meteorology: An Algebra-based Survey of Atmospheric Science*. University of British Columbia.

Sun, Q., X. Zhang, F. Zwiers, S. Westra, and L. V. Alexander, 2021: A global, continental, and regional analysis of changes in extreme precipitation. *Journal of Climate*, **34 (1)**, 243–258, doi: 10.1175/JCLI-D-19-0892.1.

Sénési, S., J. Richon, L. Franchistéguy, S. Tyteca, M.-P. Moine, A. Voldoire, E. Sanchez-Gomez, D. Salas y Mélia et al., 2014a: CNRM-CM5 model output prepared for CMIP5 historical, served by ESGF. World Data Center for Climate (WDCC) at DKRZ, doi: 10.1594/WDCC/CMIP5.CEC5HI.

Sénési, S., J. Richon, L. Franchistéguy, S. Tyteca, M.-P. Moine, A. Voldoire, E. Sanchez-Gomez, D. Salas y Mélia et al., 2014b: CNRM-CM5 model output prepared for CMIP5 rcp85, served by ESGF. World Data Center for Climate (WDCC) at DKRZ, doi: 10.1594/WDCC/CMIP5.CEC5R8.

Tebaldi, C., and R. Knutti, 2007: The use of the multi-model ensemble in probabilistic climate projections. *Philosophical Transactions of the Royal Society A: Mathematical, Physical and Engineering Sciences*, **365 (1857)**, 2053–2075, doi: 10.1098/rsta.2007.2076.

Teichmann, C., K. Bülow, J. Otto, S. Pfeifer, D. Rechid, K. Sieck, and D. Jacob, 2018: Avoiding extremes: Benefits of staying below +1.5 C compared to +2.0 C and +3.0 C global warming. *Atmosphere*, **9 (4)**, 115, doi: 10.3390/atmos9040115.

Tiedtke, M., 1989: A comprehensive mass flux scheme for cumulus parameterization in large-scale models. *Monthly weather review*, **117 (8)**, 1779–1800, doi: 10.1175/1520-0493(1989)117<1779:ACMFSF>2.0.CO;2.

Tölle, M. H., L. Schefczyk, and O. Gutjahr, 2018: Scale dependency of regional climate modeling of current and future climate extremes in Germany. *Theor. Appl. Climatology*, **134 (3)**, 829–848, doi: 10.1007/s00704-017-2303-6.

Trenberth, K. E., A. Dai, R. M. Rasmussen, and D. B. Parsons, 2003: The changing character of precipitation. *Bulletin of the American Meteorological Society*, **84 (9)**, 1205–1218, doi: 10.1175/BAMS-84-9-1205.

UK Environment Agency, 2022: Guidance flood risk assessments: climate change allowances. URL `www.gov.uk/guidance/flood-risk-assessments-climate-change-allowances`, (accessed: 01.12.2024).

Uppala, S. M., P. W. KÅllberg, A. J. Simmons, U. Andrae, V. D. C. Bechtold, M. Fiorino, J. K. Gibson, J. Haseler et al., 2005: The ERA-40 re-analysis. *Q. J. Roy. Meteor. Soc.*, **131 (612)**, 2961–3012, doi: https://doi.org/10.1256/qj.04.176.

Utsumi, N., S. Seto, S. Kanae, E. E. Maeda, and T. Oki, 2011: Does higher surface temperature intensify extreme precipitation? *Geophysical Research Letters*, **38 (16)**, doi: 10.1029/2011gl048426.

Vallis, G. K., 2017: *Atmospheric and Oceanic Fluid Dynamics*. Cambridge University Press, doi: 10.1017/9781107588417.

van den Besselaar, E. J. M., A. M. G. Klein Tank, and T. A. Buishand, 2012: Trends in European precipitation extremes over 1951–2010. *International Journal of Climatology*, **33 (12)**, 2682–2689, doi: 10.1002/joc.3619.

Van Vuuren, D. P., J. Edmonds, M. Kainuma, K. Riahi, A. Thomson, K. Hibbard, G. C. Hurtt, T. Kram et al., 2011: The representative concentration pathways: an overview. *Climatic change*, **109 (1)**, 5–31, doi: 10.1007/s10584-011-0148-z.

Vautard, R., A. Gobiet, S. Sobolowski, E. Kjellström, A. Stegehuis, P. Watkiss, T. Mendlik, O. Landgren et al., 2014: The European climate under a 2°C global warming. *Environmental Research Letters*, **9 (3)**, 034 006, doi: 10.1088/1748-9326/9/3/034006.

Vergara-Temprado, J., N. Ban, and C. Schär, 2021: Extreme sub-hourly precipitation intensities scale close to the Clausius-Clapeyron rate over Europe. *Geophysical Research Letters*, **48 (3)**, e2020GL089 506, doi: 10.1029/2020GL089506.

Villalobos Herrera, R., S. Blenkinsop, S. B. Guerreiro, M. Dale, D. Faulkner, and H. J. Fowler, 2023a: Towards new design rainfall profiles for the United Kingdom. *Journal of Flood Risk Management*, e12958, doi: 10.1111/jfr3.12958.

Villalobos Herrera, R., S. Blenkinsop, S. B. Guerreiro, and H. J. Fowler, 2023b: The creation and climatology of a large independent rainfall event database for Great Britain. *International Journal of Climatology*, **43 (13)**, 6020–6037, doi: 10.1002/joc.8187.

Villarini, G., P. V. Mandapaka, W. F. Krajewski, and R. J. Moore, 2008: Rainfall and sampling uncertainties: A rain gauge perspective. *Journal of Geophysical Research: Atmospheres*, **113 (D11)**, doi: 10.1029/2007jd009214.

Visser, J., C. Wasko, A. Sharma, and R. Nathan, 2020: Resolving inconsistencies in extreme precipitation-temperature sensitivities. *Geophysical Research Letters*, **47 (18)**, e2020GL089 723, doi: 10.1029/2020GL089723.

Visser, J. B., C. Wasko, A. Sharma, and R. Nathan, 2021: Eliminating the "hook" in precipitation–temperature scaling. *Journal of Climate*, **34 (23)**, 9535–9549, doi: 10.1175/JCLI-D-21-0292.1.

Visser, J. B., C. Wasko, A. Sharma, and R. Nathan, 2023: Changing storm temporal patterns with increasing temperatures across Australia. *Journal of Climate*, 1–26, doi: 10.1175/JCLI-D-22-0694.1.

Wasko, C., and A. Sharma, 2015: Steeper temporal distribution of rain intensity at higher temperatures within Australian storms. *Nature Geoscience*, **8 (7)**, 527–529, doi: 10.1038/ngeo2456.

Wasko, C., A. Sharma, and F. Johnson, 2015: Does storm duration modulate the extreme precipitation-temperature scaling relationship? *Geophysical Research Letters*, **42 (20)**, 8783–8790, doi: 10.1002/2015GL066274.

Wasko, C., S. Westra, R. Nathan, H. G. Orr, G. Villarini, R. Villalobos Herrera, and H. J. Fowler, 2021: Incorporating climate change in flood estimation guidance. *Philosophical Transactions of the Royal Society A*, **379 (2195)**, 20190 548, doi: 10.1098/rsta.2019.0548.

Westra, S., L. V. Alexander, and F. W. Zwiers, 2013: Global increasing trends in annual maximum daily precipitation. *Journal of climate*, **26 (11)**, 3904–3918, doi: 10.1175/JCLI-D-12-00502.1.

Westra, S., H. J. Fowler, J. P. Evans, L. V. Alexander, P. Berg, F. Johnson, E. J. Kendon, G. Lenderink, and N. Roberts, 2014: Future changes to the intensity and frequency of short-duration extreme rainfall. *Reviews of Geophysics*, **52 (3)**, 522–555, doi: 10.1002/2014RG000464.

Wilks, D. S., 2011: *Statistical methods in the atmospheric sciences*. Academic press.

Willems, P., 2011: Revision of urban drainage design rules based on extrapolation of design rainfall statistics. *12th International Conference on Urban Drainage*, 11–16.

Willems, P., 2013: Multidecadal oscillatory behaviour of rainfall extremes in Europe. *Climatic Change*, **120 (4)**, 931–944, doi: 10.1007/s10584-013-0837-x.

Winterrath, T., C. Brendel, M. Hafer, T. Junghänel, A. Klameth, K. Lengfeld, E. Walawender, E. Weigl, and A. Becker, 2018: RADKLIM version 2017.002: Reprocessed quasi gauge-adjusted radar data, 5-minute precipitation sums (YW). Deutscher Wetterdienst (DWD, http://www.dwd.de/EN/Home/home_node.html), doi: 10.5676/DWD/RADKLIM_YW_V2017.002.

Wouters, H., K. De Ridder, L. Poelmans, P. Willems, J. Brouwers, P. Hosseinzadehtalaei, H. Tabari, S. Vanden Broucke et al., 2017: Heat stress increase under climate change twice as large in cities as in rural areas: A study for a densely populated midlatitude maritime region. *Geophysical Research Letters*, **44 (17)**, 8997–9007, doi: 10.1002/2017GL074889.

Wright, D. B., J. A. Smith, and M. L. Baeck, 2014: Critical Examination of Area Reduction Factors. *Journal of Hydrologic Engineering*, **19 (4)**, 769–776, doi: 10.1061/(asce)he.1943-5584.0000855.

Youngman, B. D., 2020: evgam: An R package for Generalized Additive Extreme Value Models. arXiv, doi: 10.48550/ARXIV.2003.04067.

Zeder, J., and E. M. Fischer, 2020: Observed extreme precipitation trends and scaling in Central Europe. *Weather and Climate Extremes*, **29**, 100 266, doi: 10.1016/j.wace.2020.100266.

Zhang, X., F. W. Zwiers, G. Li, H. Wan, and A. J. Cannon, 2017: Complexity in estimating past and future extreme short-duration rainfall. *Nature Geoscience*, **10 (4)**, 255–259, doi: 10.1038/ngeo2911.

Zhu, Z., D. B. Wright, and G. Yu, 2018: The impact of rainfall space-time structure in flood frequency analysis. *Water Resources Research*, **54 (11)**, 8983–8998, doi: 10.1029/2018WR023550.